Modeling and design of a new generation of RF piezoelectric acoustic wave devices based on atomic monolayers of transition metal dichalcogenides.

Yang Yang

université de BORDEAUX

THÈSE PRÉSENTÉE

POUR OBTENIR LE GRADE DE

DOCTEUR DE

L'UNIVERSITÉ DE BORDEAUX

ÉCOLE DOCTORALE DES SCIENCES PHYSIQUES ET DE L'INGÉNIEUR

SPÉCIALITÉ : ÉLECTRONIQUE

Par Yang YANG

Modélisation et conception d'une nouvelle génération de dispositifs RF à ondes acoustiques à monocouches atomiques piézoélectriques de dichalcogénures de métaux de transition

Sous la direction de : Corinne DEJOUS
(co-directrice : Hamida HALLIL)

Soutenue le 09 juin 2023

Membres du jury :

Mme. LEBLOIS, Thérèse	Professeur, Université de Bourgogne Franche-Comté	Rapporteur
M. TALBI, Abdelkrim	Professeur, Université de Lille	Rapporteur et Président
M. DUCHAMP, Jean-Marc	Maître de Conférences, UGA /IUT RT Grenoble	Examinateur
Mme. DEJOUS, Corinne	Professeur, ENSEIRB-MATMECA / Bordeaux INP	Directrice
Mme. HALLIL, Hamida	Maître de Conférences, Université de Bordeaux	Co-directrice
M. ZHANG, Qing	Professeur, Nanyang Technological University	Invité

Acknowledgements

First and foremost, I wish to express my profound gratitude to my primary supervisor, Prof. Corinne Dejous, for her unparalleled expertise, invaluable guidance, and unwavering encouragement throughout the duration of my thesis. Her exceptional patience and unrelenting support have been instrumental in helping me overcome the challenges I faced during this research. I am also deeply indebted to my co-supervisor, Assoc. Prof. Hamida Hallil, whose visionary ideas and scientific creativity laid the foundation for this remarkable project. Furthermore, her global perspective has enabled me to benefit from numerous international exchanges, which have enriched my research experience beyond measure.

I extend my gratitude to Prof. Qing Zhang for his invaluable collaboration, exceptional research acumen, and profound expertise that enabled me to explore a nascent scientific field. Through this international collaboration, I gained a comprehensive understanding of the standards upheld by leading research institutions worldwide and the culture of Singapore. I would also like to acknowledge the unwavering support I received from Mr. Jiayi Sun, whose dedication and hard work played a pivotal role in the success of this challenging yet exciting research project. It was a pleasure working with you, and I am deeply appreciative of your critical contributions to this project. Without your efforts, this project would not have been as successful as it is today.

I would like to extend my heartfelt thanks to the other members of the MDA IMS Bordeaux research team. The numerous technical and scientific discussions that we engaged in during my thesis were immensely helpful in helping me grasp the intricacies of my research topic and provided me with invaluable inspiration to overcome a myriad of challenges. Moreover, the unforgettable after-work activities that we shared created a warm and welcoming atmosphere, which provided me with much-needed encouragement during difficult times. I will always cherish the memories of these moments, and I am deeply grateful for the support and camaraderie that you extended to me throughout my thesis.

I would like to express my sincere appreciation to the French National Centre for Scientific Research (CNRS) and the CNRS-International-NTU-Thales Research Alliance (CINTRA) for their generous financial support of this Joint Excellence Project. Your funding enabled me to pursue this research project and provided me with the necessary resources to conduct my research. Your commitment to promoting scientific research is truly commendable, and I am deeply grateful for your support.

Above all, I wish to express my profound gratitude to my family for their unwavering patience, encouragement, and understanding throughout my thesis. Their constant support has been the driving force behind my academic pursuits, and I am immensely grateful for the many exciting moments that they have shared with me along the way. Their unconditional love has given me the courage and motivation to take on this challenge, and it is with great pride and gratitude that I dedicate this thesis to them. I cannot thank them enough for their unwavering support and love, which have been the bedrock of my success.

To my family,
To all my beloved ones.

Abstract

Acoustic wave devices have played a key role in communication and sensing applications for several decades. They will continue to have a major impact on new generations of mobile technology, smart city development, and sensing applications for environmental monitoring and healthcare, etc.

The results of first-principles calculations show that the piezoelectric coefficients of transition metal dichalcogenides (TMDs) of 3R crystal structure, such as 3R-MoS_2, $MoSe_2$, WS_2 and WSe_2, are sufficiently large compared with those of conventional piezoelectric materials such as quartz, ZnO, AlN. Among them, 3R-MoS_2 has remarkable piezoelectric, thermal and mechanical properties, which makes it a very good candidate for the new generation of ultra-high frequency acoustic devices. Moreover, considered as an atomic layer material, 3R-MoS_2 is much more flexible than any other known piezoelectric semiconductor.

The objective of this thesis is to study the feasibility of developing a new generation of acoustic devices based on TMDs. A state of the art on acoustic resonators and their applications is first proposed, as well as on the properties of TMDs materials. Models and simulations based on analytical equations, finite element modeling and the Butterworth-Van Dyke (BVD) equivalent circuit are then described and used to design a SMR structure, in close collaboration with NTU Singapore, which led the fabrication. After characterization, the typical resonant frequency of 3R-MoS_2 flake-based SMR devices of ~200 nm reached over 25 GHz with good reproducibility. This work demonstrates for the first time that access to 2D piezoelectric nanomaterials enables the realization of high-performance piezoelectric devices for various promising applications.

Résumé

Les dispositifs à ondes acoustiques jouent un rôle clé dans les applications de communication et de détection depuis plusieurs décennies. Ils continueront à avoir un impact majeur sur les nouvelles générations de technologie mobile, le développement des villes intelligentes et les applications de détection pour la surveillance environnementale et les soins de santé, etc.

Les résultats des calculs de premiers principes montrent que les coefficients piézoélectriques des dichalcogénures de métaux de transition (TMDs) de 3R structure cristalline, comme 3R-MoS_2, $MoSe_2$, WS_2 et WSe_2, sont suffisamment grands par rapport à ceux des matériaux piézoélectriques conventionnels comme quartz, ZnO, AlN. Et parmi eux, le 3R-MoS_2 a des propriétés piézoélectriques, thermiques et mécaniques remarquables, qui en fait un très bon candidat pour la nouvelle génération des dispositifs acoustiques à ultra-haute fréquence. De plus, considéré comme un matériau en couches atomiques, le 3R-MoS_2 est beaucoup plus flexible que tout autre semi-conducteur piézoélectrique connu.

Cette thèse s'inscrit dans ce contexte et a comme objectif l'étude de la faisabilité du développement de la nouvelle génération des dispositifs acoustiques à base de matériaux TMDs. Un état de l'art sur les résonateurs acoustiques et leurs applications est d'abord proposé, ainsi que sur les propriétés des matériaux TMDs. Des modèles et des simulations basés sur des équations analytiques, la modélisation par éléments finis et le circuit équivalent Butterworth-Van Dyke (BVD) sont ensuite décrits et utilisés pour concevoir une structure SMR, en étroite collaboration avec NTU Singapour, qui a dirigé la fabrication. Après caractérisation, la fréquence de résonance typique des dispositifs SMR basés sur des flocons 3R-MoS_2 de ~200 nm a atteint plus de 25 GHz avec une bonne reproductibilité. Ce travail démontre pour la première fois que l'accès aux nanomatériaux piézoélectriques 2D permet de réaliser des dispositifs piézoélectriques de haute performance pour diverses applications prometteuses.

List of Symbols

$\mathbf{c}$: the elastic stiffness matrix

$\boldsymbol{c^E}$: the elastic stiffness coefficient matrix at constant electric field

$\boldsymbol{d}$: the piezoelectric strain coefficient matrix

$\boldsymbol{D}$: the electric charge density displacement

$\boldsymbol{e}$: the piezoelectric stress coefficient matrix

$\boldsymbol{E}$: electric-field intensity

$\boldsymbol{f_a}$: the anti-resonance frequency

$\boldsymbol{f_p}$: the parallel resonance frequency

$\boldsymbol{f_r}$: the resonance frequency

$\boldsymbol{f_s}$: the series resonance frequency

$\boldsymbol{I}$: the electric current

$\boldsymbol{k}$: the wavenumber

$\boldsymbol{k_t^2}$: the electromechanical coupling coefficient

$\boldsymbol{l}$: the propagating direction of a plane wave

$\boldsymbol{r}$: the position vector

$\boldsymbol{S}$: the strain

$\boldsymbol{s^E}$: the elastic compliance coefficient matrix

$\boldsymbol{t}$: the time

$\boldsymbol{T}$: the stress

$\boldsymbol{u}$: the displacement

$\boldsymbol{v}$: the velocity of the particle in the material

$\boldsymbol{v_l}$: the phase velocity of a longitudinal acoustic wave

$\boldsymbol{v_s}$: the phase velocity of a shear acoustic wave

$\boldsymbol{v_{z0}^-}$: the amplitudes of the waves in negative direction

$\boldsymbol{v_{z0}^+}$: the amplitudes of the waves in positive direction

$\boldsymbol{Z}$: the electrical impedance

$\mathbf{Z_a}$: the acoustic impedance

$\boldsymbol{Z_0}$: the transmission line characteristic impedance

$\boldsymbol{\lambda}$: the wavelength

$\boldsymbol{\rho}$: the mass density

$\boldsymbol{\omega}$: the angular frequency

$\boldsymbol{\phi}$: electric potential

$\boldsymbol{\varepsilon^S}$: the dielectric coefficient matrix at constant strain

$\boldsymbol{\varepsilon^T}$: dielectric coefficient matrix at constant stress

Table of contents

Introduction

Surface/bulk acoustic waves (SAW/BAW) are a form of mechanical vibration confined to solid surfaces or in volumes. SAW/BAW can couple efficiently to electromagnetic fields via the piezoelectric effect. Current acoustic devices have been used to filter signals for communications, modulate light via the acousto-optic effect and for sensing in liquid and gaseous medium, etc. Indeed, SAW/BAW devices have played a key role in communication and sensing applications for several decades. They will continue to make a substantial impact on the new generation of mobile technologies, development of smart cities and sensing applications for environmental monitoring and health care, etc.

However, limited by the resolution of interdigitated transducers (IDT), the working frequency of SAW devices can hardly go beyond 2.5 GHz. BAW devices, including FBAR, are limited by the fabrication technologies of the conventional piezoelectric materials such as AlN and ZnO, which limits their working frequency around 10 GHz. For the next-generation RF filters and high-sensitivity sensors, we are looking for acoustic devices with higher working frequency, among other features. To meet the wide spectrum of application demands, new acoustic devices have to be of not only the high performances, but also several unique functionalities that current acoustic devices do not have. To develop these new acoustic devices, new piezoelectric materials must be utilized.

Recent first-principles calculations suggest that the piezoelectric coefficients of bulk 3R- transition metal dichalcogenides, including $3R-MoS_2$, $MoSe_2$, WS_2, and WSe_2, are sufficiently large or comparable to those of conventional bulk piezoelectric materials such as α-quartz, wurtzite GaN, and wurtzite AlN. Let us take few-atomic layer $3R-MoS_2$ as an example. $3R-MoS_2$ has been successfully synthesized. The excellent piezoelectric, thermal and mechanical properties of $3R-MoS_2$ suggest that this material can be highly promising for the new acoustic devices. First of all, the atomic structure of $3R-MoS_2$ does not have a centrosymmetry of the trigonal 'building blocks' and, thus, $3R-MoS_2$ belongs to the space group of 3m. In sharp contrast, the conventional $2H-MoS_2$ shows the centrosymmetry of the hexagonal structure with the space group of 6mm. As a result, the non-centrosymmetric $3R-MoS_2$ flakes can induce strong piezoelectricity, regardless of the number of stacking layers. The measured piezoelectric constant d_{11} of MoS_2 flakes along the armchair direction is 1.5 times greater than that of quartz. Second, employment of the atomic-layer piezoelectric materials enables us to miniaturize acoustic devices, a key to boost the operation frequencies and reduce the footage of each acoustic device. Third, the atomic layered material is much more flexible than any other piezoelectric semiconductors known to us. $3R-MoS_2$ based acoustic devices could thus be easily integrated with other flexible electronic devices. This is genuinely ground-breaking as all conventional piezoelectric materials are in general very brittle and, thus, it is not feasible to have flexible acoustic devices that can be integrated with wearable electronics. Lastly, the thermal conductivity of MoS_2 flakes is found to be in between 40~70 $Wm^{-1}k^{-1}$, about an order of magnitude larger than that of crystalline quartz (4~6 $Wm^{-1}k^{-1}$), lithium niobate (3~5 $Wm^{-1}k^{-1}$) and lithium tantalate (8 $Wm^{-1}k^{-1}$). These attractive thermal properties make MoS_2 acoustic devices dissipate heat efficiently and enhance the devices' thermal stability and durability. After analysing the fabrication technologies of $3R-MoS_2$ flakes, we finally decided to develop SMR type of FBAR based on $3R-MoS_2$ flakes.

This thesis proposes a whole process of the design and fabrication of solidly mounted resonator (SMR) type of film-bulk acoustic resonator (FBAR) based on two-dimensional (2D) semiconducting transition metal dichalcogenides (TMDs), $3R-MoS_2$. It is a novel 2D ultra-thin materials with very interesting piezoelectric and elastic properties. The purpose of this thesis is to explore the feasibility of developing the next-generation acoustic devices based on this kind of 2D nanomaterial. These devices are expected to be used as high-performance radio-frequency (RF) filters in the fifth-generation networks (5G) wireless communication or high-sensibility sensors for gas, liquid, bio-sensing, etc.

The directions of the development of this next-generation acoustic devices are can be summarized as follows:

- Development of design tools and study of reference devices: The design of our devices is based on a good comprehension of acoustic theory and the simulation of the device in a finite element method (FEM) environment. Since $3R-MoS_2$ is a very novel material, its parameters are not all well-known yet. In this context, based on a state-of-the-art study, we firstly proposed a design and simulation of SMR based on ZnO as a reference. Such simulations based on 2D, 3D and 3D reduced FEM models were carried out and compared to the results of the literature. We also introduced the Butterworth-Van Dyke (BVD) equivalent circuit theory for further simple electrical model matching with FEM simulation results.
- Design of $3R-MoS_2$ based SMR: Based on the previous tools and design process for the reference ZnO based structure, we performed the design of targeted $3R-MoS_2$ based SMR, with thicknesses of $3R-MoS_2$ of 100 and 200 nm, which are often found in fabrication process. The material parameters were from the literature, mainly estimated from simulation works, and a few ones from characterization performed at NTU Singapore, who takes charge of the $3R-MoS_2$ and devices fabrication. We reported so far, the best experimental characterization of d_{33} of $3R-MoS_2$ with the value of 2.5-3.5 pm/V, and this characterization value was used to improve our design and simulations. The design was adapted to obtain simulated resonance frequencies around 20 GHz and confirm the desired longitudinal acoustic modes. A coplanar waveguide structure (CPW) for RF characterization access was then performed, based on the simulation results. The final mask design has been optimized with frequent exchanges with our collaborator, NTU Singapore Team.
- Characterization of fabricated samples: 5 samples have been successfully prepared, along with an exploration of improved fabrication process, though still very difficult and complex. The thicknesses of the $3R-MoS_2$ flakes range from 210 to 290 nm. RF characterization have been conducted and analyzed in comparison with simulations to put to evidence results beyond the state-of-the-art in terms of high resonance frequency above 20 GHz, electromechanical coupling coefficient (k_t^2) larger than that of conventional piezoelectric materials, such as AlN or ZnO.
- Retro-simulation and further analysis on the properties of $3R-MoS_2$: Discrepancies between experimental results and simulated ones led us to a retro-simulation approach. Based on some hypothesis, we proposed some "effective" $3R-MoS_2$ parameters, especially for the elastic constant C_{33} compared to the reported value in the literature, which is issued from first-principles density-

functional theory (DFT) calculations. The Butterworth-Van Dyke (BVD) equivalent circuit analysis was then introduced and, based on these characterized results, the BVD equivalent circuit was adapted by adding several other lumped elements. This analysis proposes a methodology for optimising BVD equivalent circuit to better fit the real characterization results.

This thesis shows the feasibility of the development 2D $3R - MoS_2$ based acoustic devices. The characterization results of these devices show some very interesting and promising performances. However, the classic acoustic theory is based on elastic and dense materials, whereas $3R - MoS_2$ has a layered-structure with Van der Waals force fields between flakes, which should involve a different behaviour of the wave propagation. This opens the way to further investigations for in-depth comprehension of $3R - MoS_2$ material properties and especially the physics underlying the acoustic wave propagation in such 2D layered-structure nanomaterials.

Chapter 1 State of art

1. From piezoelectricity to acoustic wave resonators and filters

Discovery and history of piezoelectricity

Piezoelectricity is one of the most exciting material properties that has also witnessed the development of human civilization. It derives from the Greek word piezein (to press) and is based on an interaction between electrical charge and mechanical stress [1, 2]. In 1880, the French scientists, the Curie brothers, discovered that applying pressure or tension in a certain direction to a quartz crystal results in the formation of electrical charges at the surface of the quartz crystal, and the density of the electrical charge is proportional to the magnitude of the applied external force [3]. This is the positive piezoelectric effect of the piezoelectric materials. Since then, the story of piezoelectricity began. In 1881, the Curie brothers proved the inverse piezoelectric effect by experiments and determined the direct and inverse piezoelectric coefficient of quartz crystal [4].

During World War 1, in 1917, P. Langevin and his French colleagues developed an ultrasonic transducer to detect German submarines [5]. This transducer has a sandwich structure, a thin quartz crystal is placed between two steel plates and can have a resonance frequency of 50 Hz, a hydrophone is also involved in this detector. By "listening" to an echo of the ultrasonic pulse emitted by the transducer and measuring the time it comes back, one can determine the distance of the underwater object in a specific direction. The successful application of piezoelectricity in sonar makes researchers and engineers realise the importance of piezoelectric devices. As a result, the development and analysis of components and systems based on piezoelectric materials has progressed rapidly [6].

Piezoelectricity, mechanical strain and acoustic wave

In general, piezoelectricity shows some relationships between the electrical and mechanical properties of materials [1, 2]. From the macroscopic point of view, as shown in Figure 1.1 (a), when a force (F_{Ext}) is applied to a piezoelectric material, a surface charge is induced and an electric field is generated, the direction of the electric field depends on whether the piezoelectric material is pressed or stretched. This phenomenon is called the direct piezoelectric effect. On the other hand, when an electric field (V_{Ext}) is applied to a piezoelectric material, this one is distorted and whether it is pressed or stretched depends on the direction of the applied electric field. This phenomenon is called the inverse piezoelectric effect [7], as shown in Figure 1.1 (b).

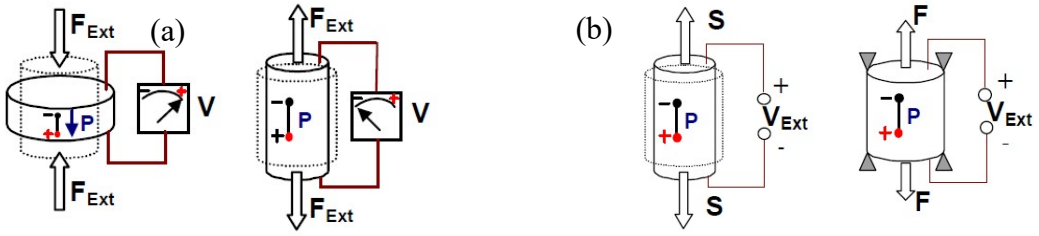

Figure 1.1 (a) Direct piezoelectric effect[8]; (b) Inverse piezoelectric effect [8].

The piezoelectric effect has a very important property: it is a linear effect [4]. For example, in the direct piezoelectric effect, the surface density of polarized charges induced by an external force is proportional to the strain of the piezoelectric material. The proportionality is quantified by the direct piezoelectric coefficient, usually expressed in $\frac{pC}{N}$. Similarly, the deformation of the material due to the applied electric field is also proportional to the applied electric field. The proportionality factor is called the inverse piezoelectric coefficient and the usual unit is $\frac{pm}{V}$. The two processes are mutually reversible, the direct and the inverse piezoelectric coefficients are the same, and the units can be converted into each other, for example, 1 $\frac{pC}{N}$ is equal to 1 $\frac{pm}{V}$ [9].

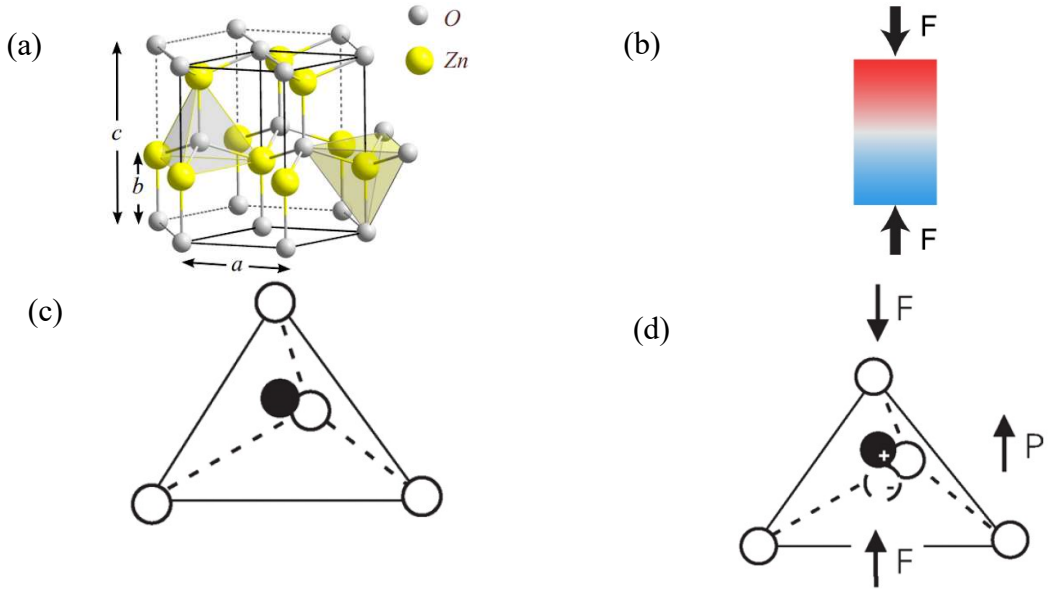

Figure 1.2 (a) The wurtzite crystal structure of ZnO[10]; (b) Applied compressive stress; (c) Regular tetrahedral structure of $Zn^{2+}[O^{2-}]_4$[10]; (d) The separation of positive and negative charge centres of $Zn^{2+}[O^{2-}]_4$[10]

From a microscopic point of view, the piezoelectric effect is due to the non-centrosymmetric crystal structure [11]. We take a traditional piezoelectric material, ZnO, as an example [12]. As shown in Figure 1.2 (a) and (c), in the atomic structure of ZnO, the O atoms form a bond with the adjacent Zn atoms to form two complementary regular tetrahedra. It is this tetrahedral coordination mode that accounts for the non-centrosymmetric structure of the wurtzite crystal structure of zinc oxide. Without loading, the $Zn^{2+}[O^{2-}]_4$ tetrahedron is a regular tetrahedron, the charge centres of the positive and negative ions coincide, and the external dipole moment is not displayed (as in Figure 1.2 (c)). A compressive stress along the c-axis acts on the $Zn^{2+}[O^{2-}]_4$ tetrahedron, induces asymmetric displacement of the positive and negative ions, due to the asymmetry of the positive tetrahedron in the c-axis direction (as in Figure 1.2 (d)). The centre of the charge forms a tiny dipole moment. When under stress, the dipole moments generated by all the crystal units within the piezoelectric material overlap, and a macro-level piezoelectric potential distribution is formed [11].

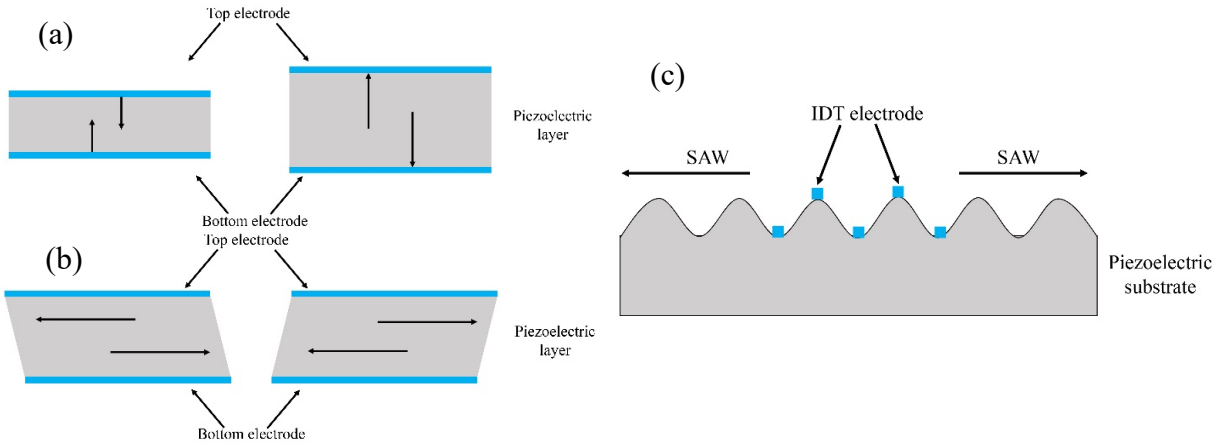

Figure 1.3 (a) Thickness-extensional mode and (b) Thickness-shear mode acoustic waves [13]; (c) Surface acoustic wave (SAW)[13];

As described above, the electric potential applied to the piezoelectric materials can deform the materials. As a consequence, the application of an alternating current (AC) signal can produce mechanical vibrations at the frequency of the AC signal. If the frequency of the mechanical oscillations is close to a resonance mode of the piezoelectric structure, a standing acoustic (mechanical) wave is produced. The amplitude of the mechanical displacement of this wave reaches its maximum when the maximum amount of energy of the electrical signal is converted into mechanical energy. This resonance depends on the material properties, dimensions, applied electrical excitation, etc. Such devices are called acoustic resonators and they are the basic building blocks for making oscillators and filters. They can be one-port devices as on Figure 1.3, or two-port devices with separate input/output dipoles for signal generation and reception, in which the signal comes through the input port and then undergoes a change at the output port [14].

Acoustic waves which are generated from the piezoelectric effect can be broadly classified into two types: “bulk acoustic waves” (BAW) [15] and “surface acoustic waves” (SAW)[16]. For bulk acoustic waves, the electrical signal is applied between the two sides of the piezoelectric material and the acoustic wave propagates through the thickness of the piezoelectric material. Due to the differences in crystalline orientation, sometimes the piezoelectric material expands and contracts perpendicularly to the surface (as in Figure 1.3(a)), which is called a thickness - extension mode, or the piezoelectric material deformations are in the horizontal direction, parallel to the surface and perpendicular to the wave propagation direction, which is called a thickness - shear mode (as in Figure 1.3 (b)) [17]. In the case of surface acoustic waves, the vibration propagates at the near surface of the material. By placing interdigitated transducers (IDTs) on the surface of the piezoelectric material (as in Figure 1.3 (c)), the propagating surface acoustic waves will be generated when an AC signal is applied, the resonance frequency, amplitude and propagation characteristics are determined by the design of the IDTs, the dimensions of the electrodes, the material properties and also the applied electrical signals. The wavelength λ of the propagating SAW is determined by the spatial periodicity of the IDTs and results in a resonance frequency depending on the acoustic wave velocity in the piezoelectric material ($f = \frac{v}{\lambda}$) [18].

Current acoustic devices and their applications

In recent decades, the rapid development of microwave wireless communication technology has led to very rapid development of other fields, such as mobile communication systems (like CDMA, UMTS, GSM, etc.), global positioning systems (GPS, Galileo, etc.), data transmission systems (WLAN, Bluetooth, etc.), satellite communication, and other military communication systems [19]. The most important parts of the components that make up these systems, such as filters, duplexers, voltage-controlled oscillators, frequency meters, and tuneable amplifiers, are microwave resonators [20]. With the remarkable advances in microelectronics and micromachining technology, researchers have paid more attention to miniaturization and integration of devices while improving device performance. Some ways of investigation focus on integrating multiple devices on a single chip or accommodating active and passive devices as well as MEMS in a single package [21].

Microwave resonators use electromagnetic waves as energy carriers. In the RF /microwave frequency range, the conventional resonators have important sizes and can hardly meet the integration requirements for current fifth-generation (5G) telecommunication standard. Therefore, the research has continued on acoustic waves, which have much lower wave velocities than electromagnetic waves. Indeed, since the velocity of acoustic wave is 4 to 5 orders of magnitude slower than that of electromagnetic wave, the size of the corresponding acoustic wave resonator is also 4 to 5 orders of magnitude smaller than that of the electromagnetic wave resonator, leading to dimensions that can meet the current miniaturization and integration requirements for 5G standard integrated circuits [22, 23].

As the integration technology of acoustic wave resonators is becoming more mature day after day, their application in the field of sensing has also gradually expanded. Currently, they are already used in mass [24], temperature [25], pressure [26], viscosity [27], and bio-chemical sensing [28]. Compared to conventional sensors, acoustic wave ones are passive, with shorter response time and wireless remote-control facilities. Therefore, they are used for applications in industrial, automotive, medical, consumer electronics, military and aerospace fields. In below, we will discuss in details about the theory, design and applications of SAW and BAW devices.

Surface acoustic wave devices (SAW)

In 1885, Lord Rayleigh discovered the "Waves Propagated along the Plane Surface of an Elastic Solid" and defined the firstly discovered SAW named as Rayleigh wave [29]. Rayleigh wave causes the surface particles to move elliptically in planes perpendicular to the surface and parallel to the propagation direction. They are typically involved in seismic movements. In 1911, Augustus Edward Hough Love mathematically predicted the existence of the so-called Love waves, which can propagate when the surface of a semi-infinitely thick elastic body is covered with a layer of a medium with lower sound velocity. The Love wave is a guided shear horizontal surface wave (SH-SAW) with a displacement of the particles parallel to the surface [30]. In 1965, Richard Manning White *et al.* proposed to deposit directly interdigital transducers (IDTs) onto the surface of piezoelectric materials in order to generate, transmit and receive SAW efficiently [31]. As represented in the Figure 1.4 (a), in a standard SAW resonator with delay-line, when the electrical signal arrives at the input IDT

(left side) through feedline, here with matching dipole, acoustic waves are generated by inverse piezoelectric effect and acoustic resonance occurs, at specific frequencies of constructive waves, for which acoustic waves travel across the propagation path. Arriving at the output IDT (right side), the acoustic signal is therefore converted back into electrical signal through the output feedline by piezoelectric effect (Figure 1.4).

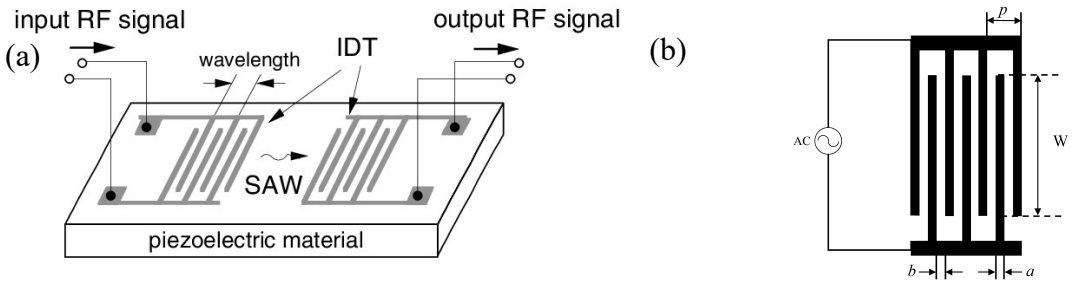

Figure 1.4 (a) Schematic diagram of conventional SAW device[32]; (b) The classic structure of IDT.

Indeed, the IDT is a typical electroacoustic conversion structure in SAW filters and other SAW devices. Its basic design is shown in the Figure 1.4 (b), with metal strips on the piezoelectric substrate intertwined and connected to the signal and the ground, alternately. These interdigitated electrodes are structurally characterized by the finger width a, interfinger distance b, acoustic aperture W, spatial periodicity p, and number of finger pairs N. When an IDT is connected to an alternating signal source, the material is deformed locally due to the converse piezoelectric effect. At the resonance frequency, the waves emitted by each pair of electrodes are constructive and the resulting SAW propagate in the two opposite directions perpendicular to the fingers. The acoustic signals reaching the second IDT are converted into electrical signals due to the piezoelectric effect. Although the two transducers are reciprocal, for simplicity, the transducer connected to the alternating signal source will be referred to as the exciting or input IDT and the transducer connected to the load will be referred to as the receiving or output IDT. The acoustic resonance frequency is expressed as:

As previously mentioned, the acoustic resonance frequency is:

$$f_0 = \frac{v_s}{p} \tag{1.1}$$

and the angular frequency:

$$\omega_0 = 2\pi \frac{v_s}{p} \tag{1.2}$$

where v_s is the velocity of surface acoustic wave, p is the period of metal strips.

For a given piezoelectric substrate, the structure of the IDTs determines the acoustic resonance frequency, as well as the overall electrical spectrum of the SAW device [22].

To characterize SAW devices, it is necessary to understand the scattering parameters of the high-frequency microwave network, the S-parameters. The above surface acoustic wave device is a typical two-port component (input and output ports). The network structure is shown in Figure 1.5. The arrows indicate the direction of the considered electrical power flow. Applying an input power a_1 to port 1 produces a transmitted signal which results in b_2 at port 2, and a reflection signal b_1. Applying an input power to port 2 has a similar effect.

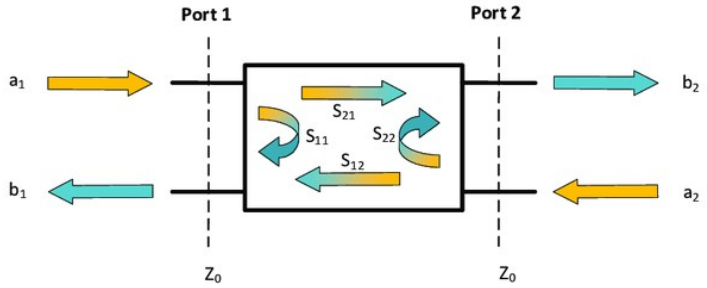

Figure 1.5 S-parameter representation of a two-port network[33].

From Figure 1.5, we can see the relationship between the output signal at Port 1 and Port 2 and the input signal at Port 1 and Port 2:

$$S_{11} = \frac{b_1}{a_1}\Big|_{a_2=0} \quad S_{21} = \frac{b_2}{a_1}\Big|_{a_2=0}$$
$$S_{22} = \frac{b_2}{a_2}\Big|_{a_1=0} \quad S_{12} = \frac{b_1}{a_2}\Big|_{a_1=0} \qquad (1.3)$$

For example, S_{21}, this parameter is the ratio between the output signal b_2 of Port 2 and the input signal a_1 of Port 1 when the impedance of Port 2 is matched, that is, when a_2 is 0.

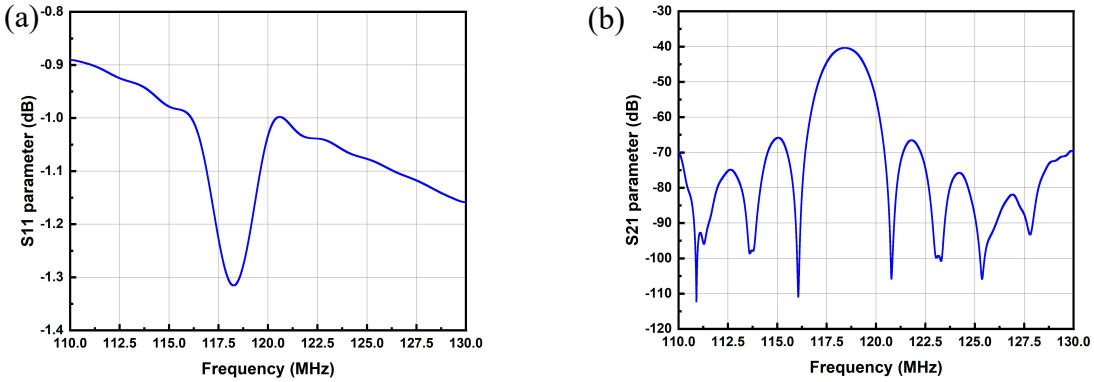

Figure 1.6 (a) S_{11} parameter; (b) S_{21} parameter of typical SAW resonator frequency response.

Figure 1.6 gives an example of characterization results of a SAW delay-line (2-port device) such as those used by Rubé. M *et al.* [34], measured with a Vector Network Analyzer (VNA) in the frequency domain. It exhibits a resonance at about 118 MHz, with a sharp dip in the reflection parameter S_{11}, which corresponds to a maximum of S_{21}, the transmission being supported by an acoustic wave between ports.

In above, we have presented the classic design of SAW devices. However, reflections on metal electrodes or other interfaces, material losses and other spurious modes, can highly influence the performances. Such effects can be reduced by an appropriate design, as described here. The first important effect is the internal reflection at the metal strips of an IDT. This is illustrated in the Figure 1.7 (a), with an electrode pitch equal to half the center-frequency wavelength ($\lambda_0/2$) resulting in an in-phase addition of the unwanted reflections at this frequency, which brings a significant impact on performances by causing ripples in the amplitude and phase. With a split-finger IDT, as shown in the Figure 1.7 (b), the electrode pitch becomes $\lambda_0/4$, so that the reflections between two adjacent electrodes cancel each other, being 180° out of phase, and the overall reflected wave get cancelled.

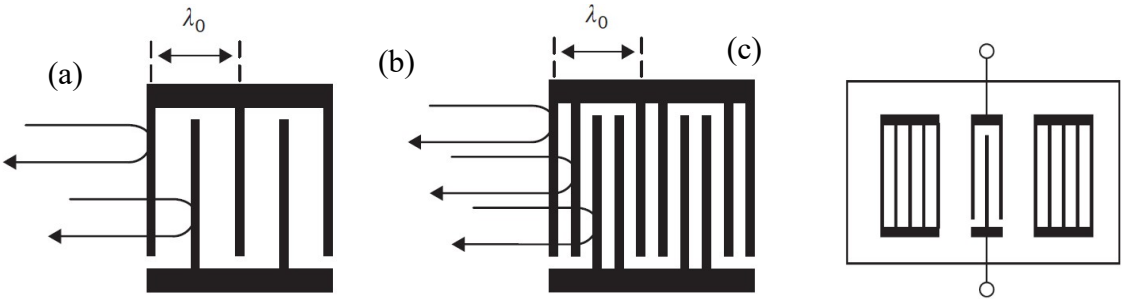

Figure 1.7 The reflection of SAW (a) Single-electrode IDT; (b) Split-finger electrode IDT; (c) One-port SAW resonator with gratings, adapted with permission from[22].

In some designs, gratings on the surface are used to improve the confinement of acoustic energy in the transducer and consequently Q value of the SAW device. In the Figure 1.7 (c), a one port resonator has two such metallic side gratings, which act as two reflectors for the acoustic energy generated by the central IDT, therefore improving the Q value. Metallic gratings can not only provide mechanical but also electrical reflection, since an electrical field can also be formed by reflected acoustic waves due to piezoelectric effect. The electrical characteristics of these reflections depend on the metal strips electrical connections, either short-circuited as in the Figure 1.7 (c), or open-circuited, or a combination of them which is named as positive and negative reflection (PNR) grating, with enhanced reflection properties. Gratings are also widely used in two-port SAW delay-line structures [35]. Another way of limiting bidirectional losses lies on specific designs enabling to control internal reflections within the generating IDT itself, such as in Single-Phase Unidirectional Transducer (SPUDT) [22].

Spurious BAW modes are also a possible source of reduced performance. Among them, so-called deep bulk acoustic waves (DBAW) can be generated by the input IDT, then propagate in the volume of piezoelectric layer, get reflected at the bottom face and propagate back to the receiving IDT. Surface skimming bulk waves (SSBW) and other leaky waves are also examples of possibly interfering (or sometimes alternating) waves [36]. Waves undergoing reflections on the device sides or bottom can be limited by sand-blasting the bottom surface of biasing the sides in order to avoid constructive reflections travelling back to the IDTs. Other interfering waves such as SSBW need for intrinsic good design, taking into account both longitudinal and shear acoustic waves. Other particular IDT structures can also be implemented during the design process in order to achieve a specific response pattern, such as apodization [37], weighted IDT transducer [38], multistrip coupler (MSC) [39], etc. All these optimizations aim to reduce the impacts of spurious modes or secondary effects, to better confine the acoustic energy and improve the Q value, therefore to improve the performances of SAW devices.

SAW devices are widely used for signal filtering in the field of telecommunication. To meet the current requirements, filters must have a large enough passband, which can be adjusted with a suitable IDTs design [40]. As for unidirectional IDTs, an appropriate design can also generate specific filter templates [22]. Much attention has also been paid to filter configurations that combine one port-SAW resonators, as impedance elements, with different topologies. A very common configuration of such low-loss coupled SAW is the ladder-type filter as shown in the Figure 1.8, which consists of cascaded multiple stages, each one based on two SAW resonators connected in series and in parallel. Coupling them by matching the resonance frequency of a serial resonator with the anti-resonance frequency of the parallel one

results in a bandpass filter centered on this frequency. Ladder-type filters exhibit a relatively flat passband with low loss and good rejection of out-of-band noise [35]. Similarly, a design coupling identical SAW resonators in double symmetric and anti-symmetric modes by inverting their electrical connections can result in a wider passband filter [35, 41]

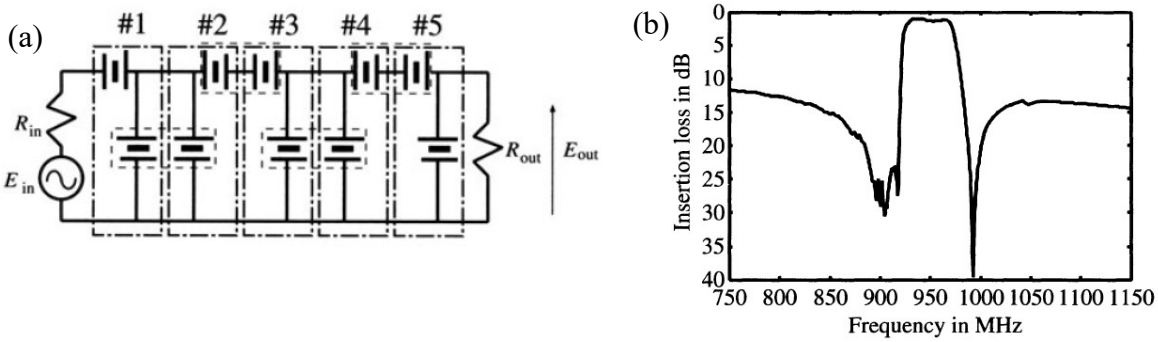

Figure 1.8 (a) Configuration of a five stages Ladder-type filter; (b) Typical frequency response of ladder-type filter[35].

There are some important properties to characterize a SAW filter:

- The minimum insertion loss (S_{21} parameter), quantifying the power dissipation caused by the device access – which depends on the input/output impedances of the device itself and of the input and output circuits (in case of unmatching, calibration tests are used to post-process the measurements results)
- The center frequency, the arithmetic average of the two cut-off frequency values, -3 dB or half-power of the specific insertion loss level at the point of minimum loss frequency
- The nominal frequency range, which is the usable bandwidth over which signal transmission is observed, defined as the range between the two cut-off frequencies.
- The out-of-band rejection, the ratio of signals inside and outside the passband, which is defined as the drop-off value between the edge of the passband and the maximum value of the stopband.
- The quality factor (Q-factor) determines the maximum intrinsic bandwidth of a filter and corresponds to the ratio of energy stored to energy dissipated, or the ratio of its centre frequency to its 3-dB bandwidth.

The demand for RF filter technology from cellular manufacturing is continuously increasing, providing new growth opportunities for the SAW filter market. From the report "Surface Acoustic Wave Filter Market" by Persistence Market Research, the global SAW filter market registered a Compound Annual Growth Rate (CAGR) of 7.5% between 2015 and 2020 and is estimated to be worth US$ 5 Bn by 2021, after which the market is expected to register a CAGR of 9% between 2021 and 2031. The top 5 vendors such as Murata Manufacturing Co, Ltd, Microchip Technologies (Vectron International), Skyworks Solutions, Inc, Qualcomm Technologies, Inc and Qorvo, Inc hold over 50% of the market share [42].

Beside the filtering application, SAW devices are also widely used as sensors, such as in viscosity, density, physical, chemical and biochemical sensing [43]. SAW resonator with delay-line is reported highly sensitive magnetic field sensor by several research teams [44-46]. For example, Meyer *et al.* [44] reported a thin-film-based SAW magnetic field sensor, whose detection of limit is 2.4 nT / $\sqrt{\text{Hz}}$ at 10 Hz and 72 pT / $\sqrt{\text{Hz}}$ at 10 kHz. This magnetic field sensor is composed by AlScN piezoelectric layer, AlCu IDTs, SiO_2 smoothing (guiding) layer and a magnetostrictive FeCoSiB film deposited on the delay-layer area. Schmalz *et al.* [46]

reported a multi-mode Love-Wave SAW magnetic field sensor, 1st and 2nd order Love-wave modes have shown sufficient sensitivity. This sensor is composed by an ST-cut quartz as piezoelectric layer, a SiO_2 layer and a magnetostrictive $(Fe_{90}Co_{10})_{78}Si_{12}B_{10}$ film on the delay line area. BAW based magnetic field sensor is less used, but some designs and simulations of BAW based magnetic field sensor are reported [47, 48].

Since nowadays bio-chemical sensing becomes a heated research topic, many SAW/BAW based bio-chemical sensors have been developed and well investigated. SAW Love-mode sensor is actually well investigated for its high sensitivity of detection especially in liquid [28]. Figure 1.9(a) and (b) show the principle of SAW sensors, based on Rayleigh and Love waves which are among the most representative. When the acoustic wave propagation is perturbed, both resonance frequency and S_{21} attenuation will change due to additional mass immobilized on the delay-line surface and possibly other mechanical parameter modifications at the surface. As shown in Figure 1.9 (c) and (d), different liquids can be distinguished by tracking S_{21} attenuation, frequency shift of S_{21} in magnitude and phase.

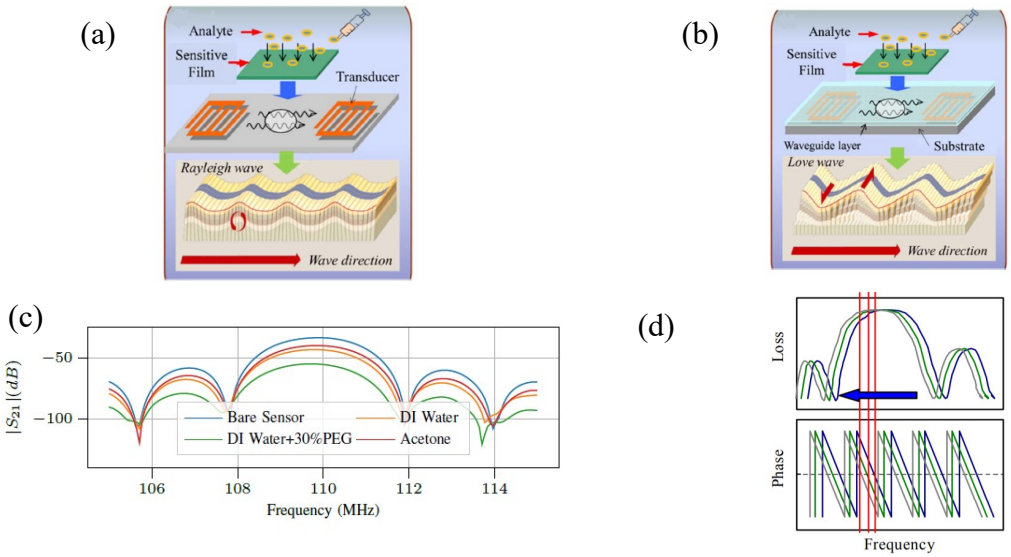

Figure 1.9 SAW sensing : Schematic of (a) Rayleigh wave and (b) shear-horizontal (SH) Love wave sensing principle[49]; (c) An example of SAW liquid detection based on S_{21} attenuation [50]; (d) Schematic illustration of the detection principle based on S_{21} magnitude and phase [51]

Indeed, in 1979, Wohltjen and Dessy [52, 53] firstly demonstrated the application and possibility of chemical/gas sensors based on SAW devices. Since then, by depositing different sensitive layers, SAW device-based gas sensors have been developed for detection of H2 [54], H2S [55, 56], NO2 [57, 58], CO2 [57], CH4 [59], SO2 [60], NH3 [61], O3 [62], O2 [63], CO [64], volatile organic compounds (VOCs) [65-67], explosives [68, 69], etc. In 2022, Singh *et al.* [70] reported a SAW-based particulate matter (PM2.5) sensor which is wearable and shows a high detection sensitivity. Another important advantage of SAW device-based sensor, is that they are passive components with the potential to be interrogated wirelessly. Indeed, by using antennas, acoustic waves can be excited and received by RF electromagnetic signal. This allows SAW based gas sensors work in high temperature, high pressure and toxic environments. Wen *et al.* [71] reported such a wireless SAW gas sensor with Teflon AF as sensitive layer for CO2 detection, they reported a sensitivity in phase shift of 1.98°/ppm. Later Lim *et al.* [57] developed a remotely controlled SAW sensor for the detection of CO2 and NO2 with simultaneous temperature measurement. The sensitive layers for CO2 and NO2

are Teflon AF and indium tin oxide and the sensitivities are 2.12°/ppm and 51.5°/ppm, respectively. Xu *et al.* [72] developed a wireless SAW sensor for organophosphorus compound detection, the sensor exhibits good linearity and repeatability, a sensitivity of 20.1°/(mg/m3).

Apart from applications in gaseous environment, SAW based-sensors are also widely used in liquid phase. In this case, they mostly involve waves horizontally polarized, as vertical components suffer from fast attenuation in liquid phase, and SAW Love-mode is actually well investigated for its high sensitivity of detection, especially in liquid [28]. Among important applications of such biosensor, is the detection of deoxyribonucleic acid (DNA). Y. Hur *et al.* [73] reported a 15-meroligonucleotide DNA sensor in liquid solutions with a sensitivity reaching 155 ng/mL/Hz. Kim *et al.* [74] reported a DNA sensor with a low detection limit of 1 ng/mL and rapid response, this sensor has the potential to be used in wireless mode. Zhang *et al.* [75] developed a DNA sensor with a sensitive layer of deoxy-nucleoside transferase in order to increase the phase shift, thus lowering the detection limit, down to 0.8 pM. Cai *et al.* [76] reported a DNA sensor with high-order harmonic acoustic mode, the sensitivity can reach 6.7×10^{-16} g/cm2 for target DNA. SAW devices are also used for protein detection. Agostini *et al.* [77] developed a biosensor targeting the Streptavidin protein and the detection limit is to sub-nanomolar, 104×10^{-12}. M. Choi *et al.* [78] developed a SAW sensor for cardiac troponin I, the detection limit is down to 24.3 pg/mL. Zhang *et al.* reported a carcinoembryonic antigen (CEA) biosensor, the sensitivity was reinforced by injecting a gold staining solution, allowing a detection limit down to 1 ng/mL. Jandas *et al.* [79] also reported a CEA sensor, the delay line area was coated with gold and immobilized Self-Assembled Monolayers (SAMs) of anti-CEA antibodies. The detection limit is down to 0.31 ng/mL. Later they improved their sensor with a nanomaterial thin film bioreceptor and the detection limit reached down to 0.084 ng/mL [80]. Apart from the detection of proteins, Brugger *et al.* [81] reported the use of SAW for monitoring the formation of neural networks. Since the pandemic of COVID-19, some SAW-based sensors for COVID virus detection are also reported [82, 83].

Bulk acoustic wave devices (BAW)

Unlike SAW resonators, Bulk Acoustic Waves (BAW) resonators use acoustic waves which propagate in the direction of the thickness of the piezoelectric material. This thickness typically equals half a wavelength (λ/2) of the fundamental resonance frequency (Figure 1.10). Though BAW resonators based on bulk piezoelectric materials are often used as so-called Quart Crystal Microbalance (QCM), the frequency is limited by the minimum thickness allowed by fabrication techniques and thin wafer robustness.

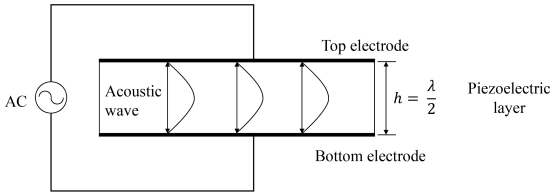

Figure 1.10 Schematic diagram of BAW resonator[84]

Though such devices are widely used based on bulk piezoelectric materials, like clock sources and Quartz Crystal Microbalances (QCM), however it highlights the need for very

thin plates for high frequency operation, not compatible with bulk materials. As a consequence, due to the limitations of the fabrication process, the performance of conventional BAW resonators remained lower compared to that of the SAW resonators. In parallel, piezoelectric layer-based devices have been investigated. In 1965, Newell first proposed a piezoelectric sandwich resonator structure using an acoustic Bragg reflector with thickness layers of λ/4 and indicated that it was likely to be used in the high-frequency range [85]. In 1967, Sliker and Roberts proposed a CdS-based acoustic resonator on a quartz wafer [86], and the theoretical model of the device is basically mature at this time. In 1980, Grudkowski *et al.* proposed the concept of a BAW resonator filter, and fabricated a ZnO-based BAW filter on a Si substrate with an operating frequency of 200~500 MHz [87]. In 1981, Lakin *et al.* clarified for the first time the application perspectives of thin-film bulk acoustic resonators (TFBAR) [88].

With the development of microfabrication processes, the advantages of BAW resonators slowly began to appear by the end of the 20th century. In 1996, Ruby prepared a BAW resonator based on a piezoelectric AlN film with a quality factor (Q value) of 2300 and an electromechanical coupling coefficient k_t^2 of 6% [89]. Q value is a dimensionless ratio of the stored energy to the energy loss within a resonant element. Then he investigated and prepared a 1900 MHz duplexer based on a film bulk acoustic waves resonators (FBAR) [90]. At this time, FBAR gradually began to be commercialized, which prompted more companies to conduct research on FBAR. In 2001, Agilent (i.e., Avago Avago) first introduced the PCS (personal communications systems) duplexer with an operation frequency of 1900 MHz for the mobile phone market [90], which was already in mass production at that time, officially initiating the commercial move of FBAR. Then the German company Infineon[91] also launched its own BAW devices. Later, Intel [92], TriQuint [93] in the United States, Philips [94] in the Netherlands, and Samsung [95] in South Korea joined the development of BAW resonators.

The current FBAR devices can be divided into two main types by their structures: front side etch or air bag type and solidly mounted type (Solidly Mounted Resonators, SMR). Both are based on the same principles; the main difference is the method of energy confinement. In FBAR, an air cavity with a length and width of 100-300 μm is etched under the bottom electrode in order to obtain a suspended piezoelectric membrane confining the acoustic energy, as illustrated in the Figure 1.11 (a) [96]. In the SMR structure, a "mirror" under the electrode reflects acoustic waves. As shown in the Figure 1.11 (b), these acoustic Bragg reflectors alternate layers of different acoustic impedances, such as W and SiO_2 (impedance ratio of about 4:1), AlN and SiO_2 (impedance ratio of about 3:1). By reflecting acoustic waves back to the piezoelectric film, they play a role in limiting energy dissipation[97]. To design the acoustic Bragg reflectors, the acoustic impedance of each material layer can be calculated as following:

$$Z_a = \rho V_L \qquad (1.4)$$

Where ρ is the volumetric mass density of the materials of each layer, V_L is the velocity of the longitudinal waves of each material if SMR works with the longitudinal acoustic mode (parallel to the wave propagation direction - perpendicular to the surface).

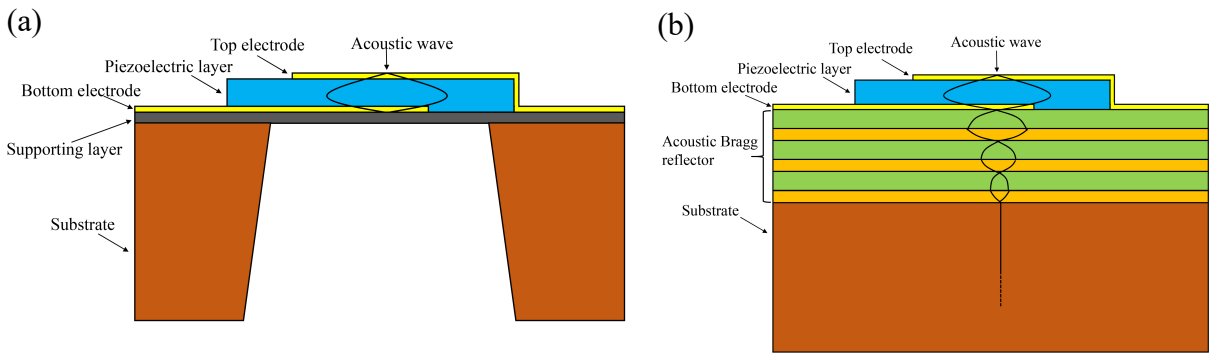

Figure 1.11 (a) Conventional FBAR structure[96]; (b) SMR type FBAR structure[97].

The difference in structure and acoustic reflection of the two resonators determines the difference in their fabrication, performance and applications. In terms of design and fabrication, the longitudinal acoustic waves are confined in the FBAR membrane, the design is flexible, and the processing is quite simple due to the smaller number of layers [23]. In the design of SMR, not only the lateral acoustic energy dissipation needs to be considered (the impact brought by the lateral acoustic modes will be presented in below), but also the design of the acoustic Bragg reflector is critical as directly impacting the energy dissipation and the performance of the resonator. To ensure the Q value, a fine control of the thickness during processing is also required [96].

As for the performance, FBAR has a higher effective electromechanical coupling coefficient ($k_{t\,eff}^2$) [23], with a larger difference in acoustic impedance at the electrode-air interface than at the junction with the Bragg reflector of the SMR structure. Furthermore, the Bragg reflector adds some new loss mechanisms that reduce its Q value. However, the SMR structure also offers some interests. Indeed, the multiple SiO_2 layers of the Bragg reflector have a negative temperature coefficient of frequency (TCF), which provides a matching effect on the TCF of the whole SMR [96]. Second, the FBAR membrane is mechanically supported at the edge of the cavity structure, which is risky during the microfabrication process, and the stress of the film must be carefully controlled to avoid mechanical cracking. On the contrary, the SMR structure does not suffer from such drawback, provided stable layers interfaces [15].

The BAW devices have a single port, they are usually characterized by measuring their reflection coefficient S_{11}. As shown in the Figure 1.12 (a), a minimum return loss is obtained near the resonance loss with a high Q value. For a BAW device with good performance, the Q value can reach several thousand [89, 98, 99]. The fundamental resonance can be expressed as follows,

$$f_r = \frac{v_L}{2h} \qquad (1.5)$$

Here v_L is the velocity of longitudinal waves in the piezoelectric medium with BAW in the longitudinal acoustic mode, h is the thickness of the piezoelectric layer. However, we must note that this formula is only valid if we assume that the electrodes are infinitely thin.

In addition to S_{11}, the electrical impedance resulting from the theory of transmission lines [100] is an important characterization property for BAW devices, which can be expressed:

$$Z = \frac{1+S_{11}}{1-S_{11}} Z_0 \qquad (1.6)$$

Where Z is the electrical impedance of the device and Z_0 is transmission line characteristic impedance, 50 Ω for a vector network analyser (VNA).

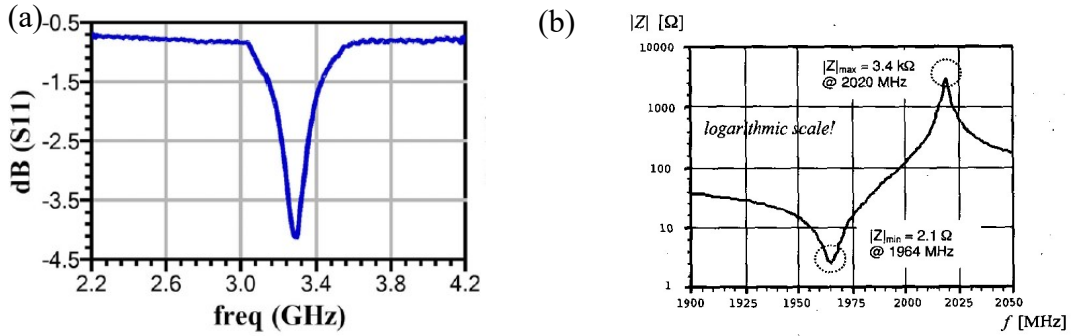

Figure 1.12 (a) S_{11} parameter of a 3.3 GHz FBAR[101]; (b) Electrical impedance of a 1.9 GHz FBAR[102].

As shown in Figure 1.12 (b), the electrical impedance Z reaches its minimum (tends to zero) at the resonance frequency f_r, which corresponds to a maximum of the mechanical deformation caused by the piezoelectric effect; at the anti-resonance frequency f_a, the electrical impedance Z reach its maximum (tends to infinity), which is associated to a minimum of the mechanical deformation.

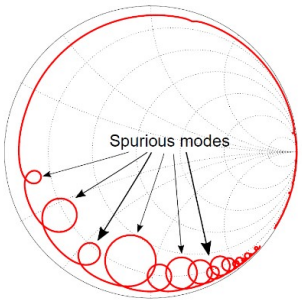

Figure 1.13 Smith Chart representation of the S_{11} parameter a FBAR resonator with several spurious modes[103]

However, longitudinal deformations are accompanied by transverse ones, so that some lateral acoustic modes also propagate in BAW devices [104]. These unwanted acoustic modes, or spurious modes, are visible in the electrical response of the resonator in the form of parasitic resonances, in addition to the main one, as in Figure 1.13. These lateral acoustic waves travel between the boundaries of the active region of the piezoelectric layer, bounce off the electrode edges, and form lateral standing waves. Since they have to share the total energy, they are responsible for the degradation of the effective electromechanical coupling coefficient and of Q value [96].

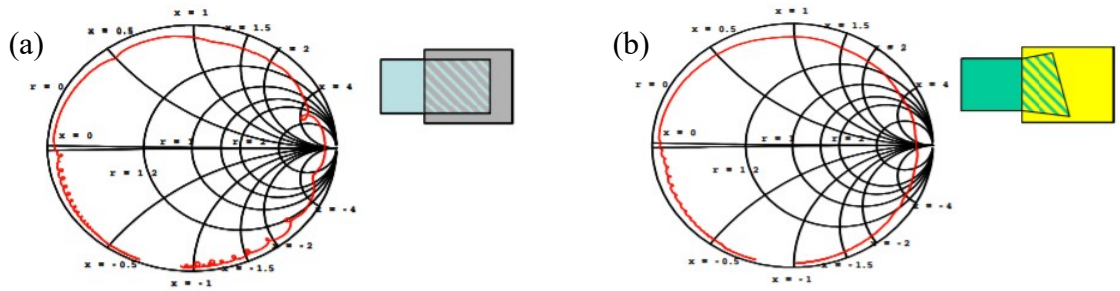

Figure 1.14 Smith Chart of S_{11} of (a) a square-shaped and (b) a quadrilateral-shaped top electrode resonator[105].

There are mainly two kinds of methods to improve this degradation caused by undesirable lateral modes. One method is called apodization. By using the asymmetrically shaped top electrode, as shown in Figure 1.14 (b), most of the standing lateral waves are

smeared out between the electrode edges and less parasitic resonances are observed in the electrical response. The most commonly used shapes of BAW top electrodes are irregular squares, pentagons and circles.

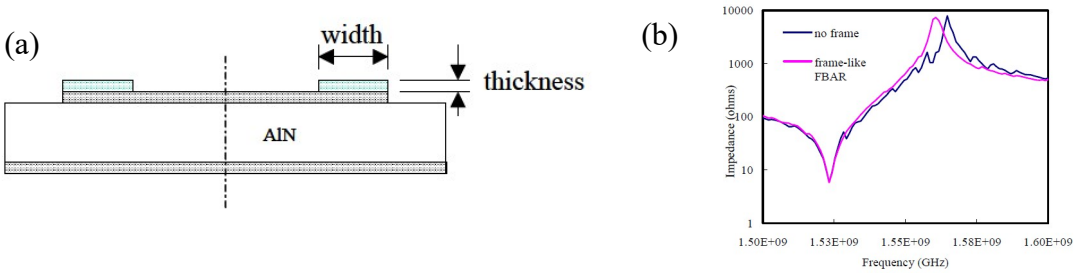

Figure 1.15 (a) Frame-like FBAR and (b) Comparison of impedance response[106].

Another method is to build a "frame" around the edge of the top electrode (as shown in Figure 1.15 (a)). By carefully designing the width and thickness of the frame, the different orders of lateral modes couple together and get vanished. This is an efficient method for suppressing unwanted modes, confining energy, obtaining a smooth electrical response and a better Q-factor [106]. The frame-type electrode has some disadvantages. One disadvantage is that it can be more difficult to manufacture compared to other types of electrodes. The wire that is used to create the frame must be precisely positioned and aligned with the edges of the piezoelectric film, which can be challenging. Another disadvantage is that the wire can create unwanted resonances in the filter, which can affect its performance. Due to the complexity of this structure and the difficulties in processing, the apodization method is commercially very successful.

Like SAW, BAW (FBAR) device is also a fundamental component for RF filters, and similarly as for the SAW components, the ladder type filters are also commonly used due to advantages such as easy design, steep filtering effect, cost, etc. Some communication systems mix ladder filters and lattice ones, in which shunt elements are diagonally-crossed, to achieve a good selectivity of frequency band with steeper filtering response [96, 107]. Like SAW filter, a good FBAR filter should have a sufficiently wide bandwidth and low insertion loss to allow lossless transmission of the signal, and a sufficient stopband is also needed to suppress transmission of the unwanted signal. Since the resonance frequency of SAW mainly depends on the spacing between interdigitated transducers (IDT), which is limited by lithography and patterning technology, it is quite difficult for SAW to operate above 2GHz[108], FBAR usually dominates the market for filters above 2.5GHz.

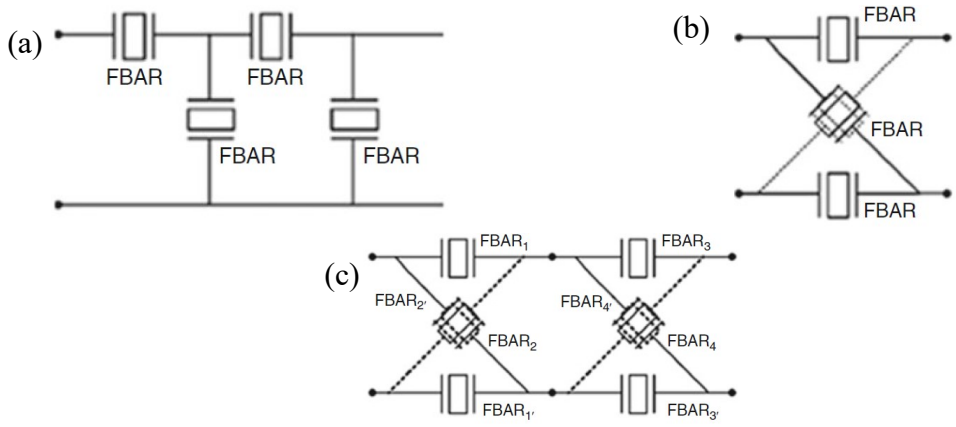

Figure 1.16 The topology of the FBAR filters, (a) ladder type (b) bridge type (c) mixture type[96]

To understand well how FBAR filters work, let us take the ladder type filters as an example. A ladder type filter consists of several series and parallel FBARs. If a filter operates at the centre frequency f_0 and the passband is Δf, the resonance and anti-resonance frequencies of the series FBARs must be f_0 and $f_0 + \frac{1}{2}\Delta f$, while the resonance and anti-resonance frequencies of the parallel FBARs must be $f_0 - \frac{1}{2}\Delta f$ and f_0, respectively. Except for these frequencies, the performances of series and parallel FBARs should be almost the same, as shown in Figure 1.17 [96]. A good FBAR filter should have a sufficiently wide bandwidth and low insertion loss to allow lossless transmission of the signal, and a sufficient stopband is also needed to suppress transmission of the unwanted signal.

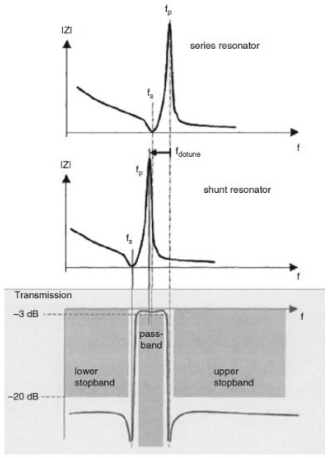

Figure 1.17 The frequency responses of the single series and parallel FBAR devices and the cascading filter[96]

There are several advantages that FBAR filters can offer:

- High-Quality Filtering: FBAR filters have high selectivity and accuracy, which makes them ideal for filtering out specific frequencies. They can filter out unwanted signals with high precision, which results in better signal quality and reduced interference.
- Wide Bandwidth: FBAR filters can operate over a wide range of frequencies, which makes them suitable for use in a variety of wireless communication systems. They can be designed to operate in a frequency range from a few megahertz to several gigahertz.
- Low Insertion Loss: FBAR filters have low insertion loss, which means that they do not significantly reduce the signal strength when filtering out unwanted frequencies. This is important in wireless communication systems where signal strength is critical.
- Small Size: FBAR filters are small in size, which makes them suitable for use in miniaturized electronic devices. They can be integrated into the circuit board of electronic devices, which reduces the overall size of the device.
- High Temperature Stability: FBAR filters are highly stable at high temperatures, which makes them suitable for use in harsh environments. They can maintain their performance even at elevated temperatures, which is important in applications where the device is exposed to high temperatures.

- Low Power Consumption: FBAR filters have low power consumption, which makes them suitable for use in battery-operated electronic devices. They consume less power than other types of filters, which helps to extend the battery life of the device.

Besides, there are also some limitations for the development of current FBAR filters:

- High Manufacturing Costs: The manufacturing process for FBAR filters is complex and involves multiple steps, which can result in high production costs. This can limit their use in applications where cost is a critical factor.
- Limited Power Handling: FBAR filters have limited power handling capability, which makes them unsuitable for high-power applications. They are typically used in low-power applications, such as in mobile phones and wireless devices.
- Limited Integration with Other Components: FBAR filters can be difficult to integrate with other components in a circuit due to their small size and complex manufacturing process. This can limit their use in applications where integration with other components is critical.

With the rapid development of 5G wireless communications, the operating frequency band will continue to expand to high frequencies, and the working bandwidth will also increase. The market for filters is expected to grow explosively. Among them, the growth of BAW filters is the fastest. Indeed, the demand for connected devices, such as vehicles, is leading to new adoption of interface standards such as Wi-Fi and BAW filters can also be used to establish a mobile connection with a network to enable a next-generation driving experience. The applications extend not only to consumer electronics and automotive, but also to aerospace, defense, environment and industry, etc. These broad industrial applications provide prospects for significant and stable growth to the BAW filter market, which is estimated at US$4.1 billion in 2020 and is expected to reach a revised size of US$13 billion by 2027, at a CAGR of 18%, as shown in Figure 1.18 [109].

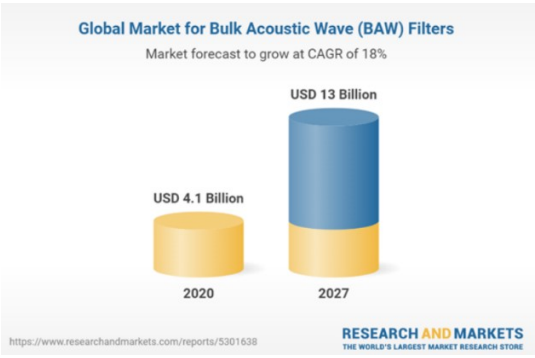

Figure 1.18 Estimated global market for BAW filters from 2020 to 2027[109]

In terms of regional analysis, according to Maximize Market Research, Asia-Pacific has the largest market share and will continue to hold it in the future. Developing economies such as China, India, South Korea and Japan are the main contributors, and China holds the most important part due to its mature semiconductor manufacturing, telecommunications, and electronics industries, as shown in Figure 1.19 [110].

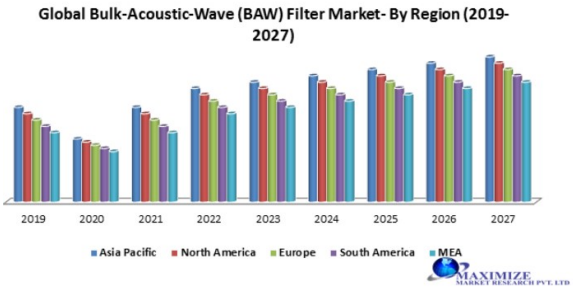

Figure 1.19 Global BAW Filters Market by Region[110]

The top 5 manufacturers in the BAW filter market are Avago Technologies (USA), Qorvo (USA), TDK (Japan), Skywork Solutions (USA), and Akoustis Technologies (USA)[110].

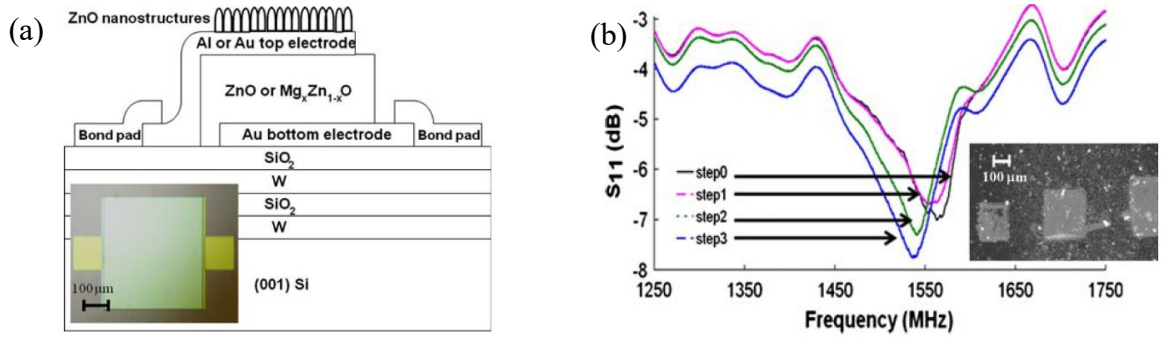

Figure 1.20 (a) Schematic diagram of a SMR for biosensing; (b) S_{11} attenuation changes and frequency shift during the detection[111]

Like SAW, BAW (FBAR) devices can also be used as sensors. The detection field includes mass pressure, gas, liquid, chemical/biosensor, etc. [112]. As shown in Figure 1.20 (a), the FBAR sensor is also a gravimetric sensor: by depositing a sensitive layer onto the top electrode of the device, the absorbed target compounds interfere with the generation and propagation of the acoustic waves. Since the vertical deformation is strongly disturbed by the deposited mass, a thickness shear mode resonator (TSM) is usually used for sensor application [113].

Since FBAR is a one-port device, detection typically consists in tracking the attenuation changes as well as the frequency or phase shift of S_{11} parameter at the resonance, as in Figure 1.20 (b). The detection is also based on mechanical effects, among them the mass loading effect. Compared to the SAW sensor, whose operating frequency is typically in the range of one hundred MHz to the GHz, the operating frequency of the FBAR sensor is usually in the range of sub-GHz to about 10 GHz thanks to the wave confinement in a very thin layer, which provides the FBAR sensor a high sensitivity. However, a high Q factor should be ensured to accurately detect small frequency shifts.

In the field of gas sensing, Lin *et al.* [114] developed a FBAR-based sensor exhibiting a high sensitivity for trinitrotoluene (TNT) and 1,3,5-trinitro-1,3,5-triazacyclohexane (RDX). The detection of hydrogen (H_2), carbon monoxide (CO) and ethanol vapors are also reported by Benetti *et al.*[115], with detection limits of 2 ppm, 40 ppm and 500 ppm, respectively. Coupling a FBAR-based sensor with a micro-preconcentrator, Yan *et al.* [116] showed a high sensitivity for dimethyl methyl phosphonate (DMMP), down to 2.64 ppm, with a fast response and a short recovery time. Zeng *et al.*[117] developed a temperature-compensated film bulk acoustic wave resonator (TC-FBAR) functionalized with a bilayer self-assembled

poly (sodium 4-styrene-sulfonate) / poly (diallyl-dimethyl-ammonium chloride) to detect and identify volatile organic compounds (VOCs), with an interesting approach based on temperature modulation as a multiparameter virtual sensor array. Gao *et al.* [118] also propose a solution for VOCs identification, based on a dual transduction using mass and resistance variation of a conductive polymer, poly (3,4-ethylenedioxy-thiophene) and poly (styrene sulfonate) (PEDOT: PSS), deposited on the top of device. The detection of 380 ppm of methanol is reported.

FBAR device is also a good candidate for sensing in liquid phase. As aging of population and disease concern have become a hot topic for many decades, not to mention the impact brought by the novel coronavirus (COVID-19), biosensing technology in liquid phase based on FBAR devices shows wide perspective. The first FBAR-based bio-sensor is reported in 2003 [119]. Clear frequency shifts show DNA attachment and protein coupling. In 2004, Gabl *et al.* [120] reported a ZnO-based FBAR biosensor with a working frequency up to 2 GHz for the detection of DNA and protein [120]. In 2006, Weber *et al.* [121] showed experimentally that in liquid phase, shear-mode FBAR has much better performances than longitudinal-mode FBAR due to higher quality factor (Q-value) and lower noise level, as expected in liquid phase. DNA sequences are also successfully detected by Zhang *et al.* [122], using a gold-top electrode FBAR and monitoring the shift of resonance frequency when DNA hybridization occurs. In 2011, Auer *et al.* reported DNA detection in a diluted serum (1%) with a resolution of 1 nM. Apart from the detection of DNA, FBAR devices have also showed their capacity to detect prostate-specific antigen (PSA), Alpha-fetoprotein (AFP) and CEA[123]. Previously in 2011, Lin *et al.* [124] reported a FBAR sensor with a detection limit of PSA of 25 ng/cm^2. Zhao *et al.* [125] reported a sensor of human prostate-specific antigen (hPSA) with a sensitivity of 1.5 ng/cm^2. Chen *et al.* [126] reported a sensor of AFP with a detection limit of 1 ng/mL. Zhang *et al.* [123] developed a sensor of CEA and the detection limit ranges from 0.2 to 1 mg/mL.

Current demands and perspectives

From the above description, both SAW and BAW can be used as RF filters. Since the resonance frequency of SAW mainly depends on the spacing between interdigitated transducers (IDT), which is limited by lithography and patterning technology, it is quite difficult for SAW to operate above 2 GHz [108]. As shown in Figure 1.21, BAW usually dominates the market for filters above 2.5 GHz. Nowadays, since a main feature of 5G New Radio (NR) systems is the use of high-frequency millimeter wave (mmWave) and sub-6 GHz bands [127], the BAW devices are becoming more and more important.

For sensing applications of acoustic devices, SAW and BAW, a high resonance frequency can bring enhanced sensitivity and lower detection limits [113], and a high Q factor is important to reduce spurious signals. Nowadays, SAW devices are often used as gas, liquid, or chemical/biochemical sensors because they have a high enough operating frequency, and they are compatible with planar collective manufacturing technologies, among other advantages. FBAR sensors with higher operating frequency have limited use due to their availability and price, as their fabrication involves less standard nanofabrication tools [113].

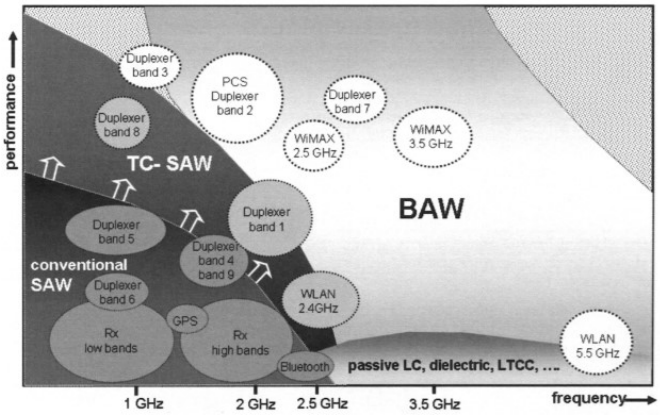

Figure 1.21 SAW and BAW application space for RF filters[108].

In order to meet the requirements of the future filtering and sensing applications, therefore, the acoustic devices should have higher operating frequency, wider bandwidth and higher Q value. Regarding BAW devices, this would mean that thinner piezoelectric layers with a high electromechanical coupling coefficient are needed, a synthesis of current acoustic devices materials and working frequency can be found in Table 1.1.

Table 1.1 Synthesis of current BAW devices materials and working frequency[128-131]

Materials	**ZnO**	**AlN**	**$LiNbO_3$**	**$LiTaO_3$**	**Units**
Density	5680	3260	4700	7460	kg/m^3
v_l	~6350	~11270	~6550	~5590	m/s
e_{33}	1.32	1.55	1.77	1.9	C/m^2
Thickness (Min)	770	120	160	700	nm
Frequency (Max)	3.38	24	12	2.5	GHz
k_t^2	8.5	6.5	23.6	17.4	%

As we mentioned previously, we search for the piezoelectric layers with high wave velocity, low thickness and high coupling coefficient, however from the synthesis, limited by the current fabrication process, the current conventional piezoelectric, we can see that current conventional piezoelectric materials cannot meet these three exigences at the same time, which limits the development of current acoustic devices.

These mentioned requirements would also lead to further enhanced miniaturization of electrical components. In addition, it could benefit flexible and wearable electrical components, which are in high demand for human-interactive and health-monitoring applications [132].

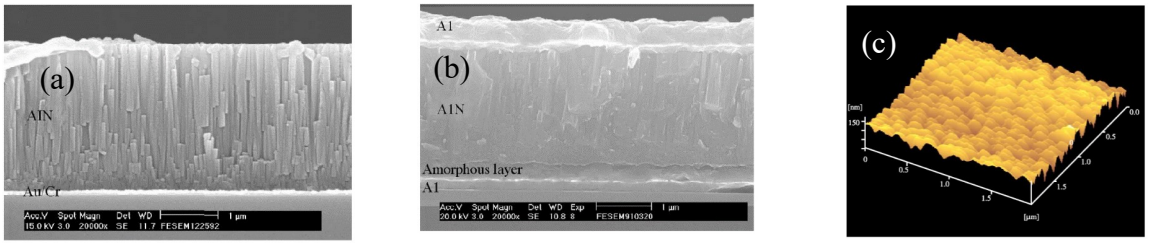

Figure 1.22 SEM Image of (a) highly and (b) randomly oriented AlN films; (c) AFM surface roughness of AlN film[133]

When it comes to the current challenge, it is quite difficult for the traditional piezoelectric materials such as AlN, ZnO or PZT to follow the current trend in acoustic

devices due to their limited coupling coefficients, elastic properties or minimum thickness. Then, the traditional fabrication process, such as metal organic chemical vapor deposition (MOCVD), sol-gel deposition, RF sputtering, or vapor deposition [134], is also a factor that limits the performance of current acoustic devices. This can be illustrated by the example on Figure 1.22[133], which shows a highly c-axis oriented thin AlN film deposited on a Au/Cr bottom electrode, but a randomly oriented one with Al electrodes, also with the formation of an amorphous intermediate layer. The randomly oriented AlN layer affects the propagation of acoustic waves and some spurious acoustic modes appear. The Q value, sensitivity, electromechanical coupling coefficient, etc. deteriorate as a result [133]. Figure 1.22 (c) shows the surface of the deposited AlN film. In general, the surface roughness increases with the film thickness, and such non-smooth surfaces can also disturb the propagation of acoustic waves [134]. The uncertainty in manufacturing acoustic devices based on conventional piezoelectric materials makes the development of the next generation of acoustic devices more urgent.

In line with the successful synthesis of two-dimensional (2D) materials which has aroused an explosion of interest for their attractive properties, several 2D semiconducting transition metal dichalcogenides (TMDs), offer some outstanding physical properties, due to their special atomic structures, such as an excellent piezoelectricity, a high flexibility, a good thermal conductivity [135-137]. What's more, since 2D materials are composed by several thin flakes, each one with a single atomic plan, it can make the piezoelectric layer very thin down to several nanometres [137]. As we described above, the resonance frequency of BAW depends on the thickness of the piezoelectric layer, so 2D piezoelectric nanomaterials can be used to realise BAW devices with very high operating frequency [138]. Furthermore, the special manufacturing process of 2D materials (this will be detailed in below) can greatly reduce the surface roughness and ensure the adequate crystal orientation, enabling the acoustic devices based on 2D piezoelectric materials to potentially exhibit very good performances.

2. Transition metal dichalcogenide (TMDs) 2-dimensional nanomaterials

Discovery and history of two-dimensional (2D) nanomaterials

The advent of low-dimensional materials has led to the development of many new areas of research. Before 2004, there were many debates about whether two-dimensional materials with a thickness of one atomic layer could exist stably at room temperature. When Andre Geim and Konstantin Novoselov succeeded in making graphite flakes (graphene) with only one layer of carbon atoms by mechanical exfoliation [139], graphene quickly attracted people's attention. Its special zero-bandgap structure and high carrier mobility made graphene shine in the application of electronic devices, due its ultrathin structure at the nanoscale, in which carriers can only move in two dimensions. Since then, two-dimensional materials were gradually developed and became a hot research topic [136]. Indeed, different 2D materials can form homo- or heterostructures by van der Waals stacking [140], so that a true "material design" can be realized, providing a rich material base for the design and practical application of new integrated devices in the future.

However, graphene has a small band gap due to edge effects, and its relatively low current on/off ratio makes it difficult to build common electrical devices such as field-effect transistors (FETs) [141]. This limited its development and application, and led researchers to investigate how to improve its properties, especially to optimise its band gap, and also to explore other routes towards 2D analogous materials [142].

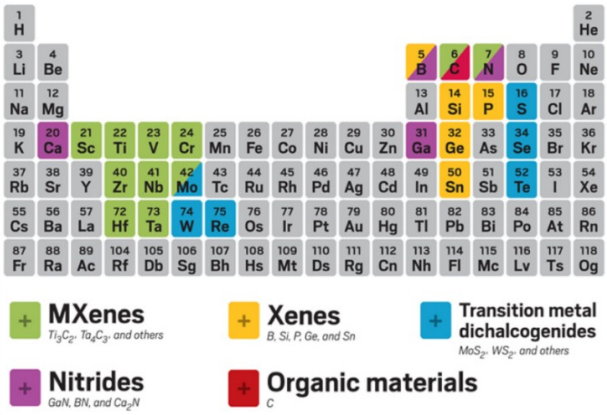

Figure 1.23 Main types of discovered 2D nanomaterials[135]

According to K. S. Novoselov *et al.* [143], the 2D materials exhibit two important characteristics :

1. the monolayers are a minority among the associated thicker flakes that make up these materials,
2. these layered materials have strong in-plane bonds and weak van der Waals-like coupling between layers.

Beyond graphene, the 2D materials can be divided into five major families: MXenes and Xenes, where M is an early transition metal and X is carbon or nitrogen, organic materials, nitrides and transition metal dichalcogenides (TMDs), as shown in Figure 1.23.

2D TMDs piezoelectric material: New candidate for high-performance acoustic devices

Compared to graphene, layered TMDs exhibit rich electronic properties, and the band structure is closely related to the number of layers, defects, and stresses [144, 145]. By introducing suitable defects, the band gap can be reduced to 0.08 eV [146]. In 2005, Andre Geim and Konstantin Novoselov succeeded in exfoliating two-dimensional MoS_2 using Scotch tape method, but they did not investigate their properties and applications in depth [143]. By 2010, single-layer MoS_2 transistors have been successfully fabricated and exhibited excellent electronic properties. This breakthrough led the optoelectronic properties of two-dimensional TMDs to attract considerable attention [147]. Furthermore, a single atomic layer of graphene has inversion symmetry because the atoms in the unit cell are identical and graphene is centrosymmetric in its three-dimensional form, but MoS_2 with a single atomic layer is predicted to be a piezoelectric material due to its strain-induced lattice distortion and associated ion charge polarization [148]. Thus MoS_2 has the potential to be considered for nanoscale acoustic devices.

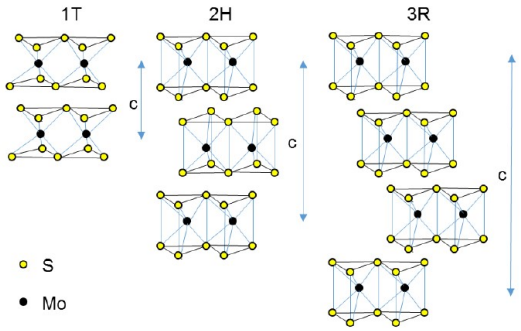

Figure 1.24 Side view schematic illustration of the 1T/2H/3R type structures of MoS_2[149]

Unlike graphene, TMDs can have different polytypes depending on the elaboration process. Indeed, depending on the stacking order and atom coordination of Mo atoms, MoS_2 can form three crystalline structures, namely 1T structure with octahedral coordination and tetragonal symmetry, 2H structure with hexagonal symmetry and 3R structure with rhombohedral symmetry. Both 2H and 3R structure have trigonal prismatic coordination as shown in Figure 1.24 [149]. 1T structure is a metastable structure, 2H and 3R structures can both occur in nature.

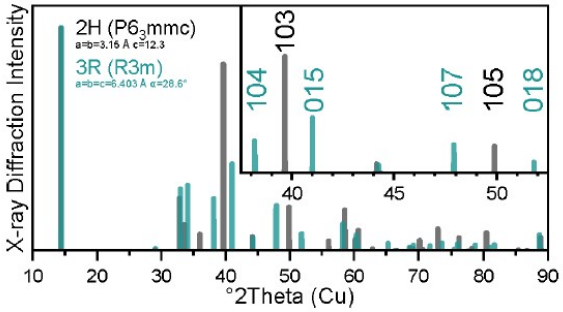

Figure 1.25 X-ray diffractograms of 2H and 3R MoS_2[137]

As shown in Figure 1.25, the powder X-ray diffractograms for 2H- and 3R- MoS_2 appear quite similar, normally the regions at ~40° and ~50° 2θ are used to differentiate the two polytypes [137]. It's reported that the scattering intensities are dominated by the heavier

Mo atoms and then the positions are slightly changed for different polytypes [150]. Since 2H-MoS_2. is the most stable and commonly used polytype, many articles and also this thesis manuscript refer to MoS_2 as 2H- MoS_2, when there is no specification.

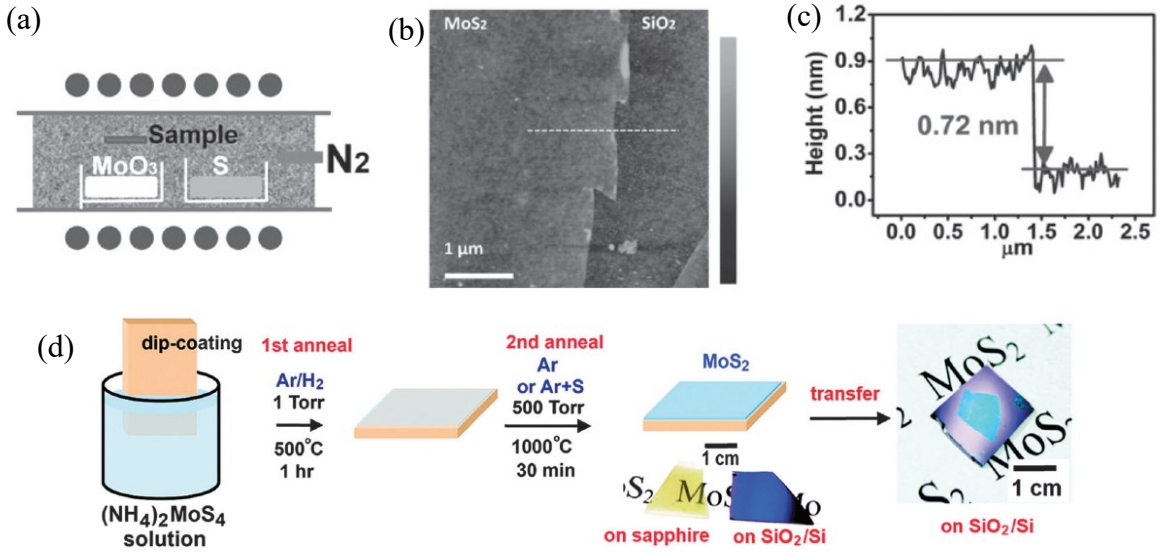

Figure 1.26 (a) the experimental set-up for CVD-growth of MoS_2[151]; (b) AFM image of a monolayer MoS_2 film on a Si/SiO_2 substrate[151]; (c) MoS_2 single layer thickness measurement by AFM[151]; (d) the two-step process for the synthesis of MoS2 thin layers on targeted substrate[152].

MoS_2 is usually synthesized by chemical vapor deposition (CVD). Yi-Hsien Lee [151] reported a direct synthesis of large area MoS_2 on Si/SiO_2 substrate by CVD. Figure 1.26 (a) shows the experimental setup. A ceramic boat of MoO_3 and a ceramic boat of S are in a reaction chamber with nitrogen environment and heated to 650 ℃. The Si/SiO_2 sample is fixed face down on the top of the boat. Before deposition, a dried aqueous solution of reduced graphene oxide (rGO), PTAS or PTCDA is spun onto the substrate. The MoO_3 powder is reduced into MoO_{3-x} by the sulfur vapor and then MoO_{3-x} diffuses onto the substrate. MoS_2 layers are formed after the reduction reaction with the sulfur vapor. Observation and thickness measurement are usually done with an atomic force microscope (AFM). Figure 1.26(b) shows the AFM topography of MoS_2 flakes deposited on Si/SiO_2 substrate and Figure 1.26(c) shows the thickness measurement of a single layer MoS_2, about 0.7-0.8 nm [151]. The current challenge in the fabrication process is the synthesis approach to obtain high quality and large area MoS_2 atomic layers. Keng-Ku Liu *et al.*[152] proposed a high temperature annealing process to fabricate large-area MoS_2 thin layers with superior electrical performance on insulating substrates. They dip-coat $(NH_4)_2MoS_4$ on Si/SiO_2 or sapphire substrate, MoS_2 are formed on the substrate after two step annealing process, then MoS_2 film can be transferred onto other substrates. The chemical reactions of Figure 1.26(d) can be given as:

$$MoO_3(s) + H_2(g) \rightarrow MoO_2(s) + H_2O(g) \qquad (1.7)$$

$$MoO_2(s) + 2S(g) \rightarrow MoS_2(s) + O_2(g) \qquad (1.8)$$

500×500 μm^2 MoS_2 is reported by CVD method, but the formation of MoS_2 films requires 1000°, it is impossible to deposit directly on device substrate [152]. Plasma assisted synthesis process has the potential to displace CVD, nevertheless, mechanical exfoliation is still the main method for fabricating MoS_2 based devices [153]. Apart from CVD method and mechanical exfoliation, other methods can be used to produce MoS_2 nanoflakes, such as

chemical exfoliation, chemical synthesis, hydrothermal synthesis, the sol-gel process, thermal decomposition, etc [153].

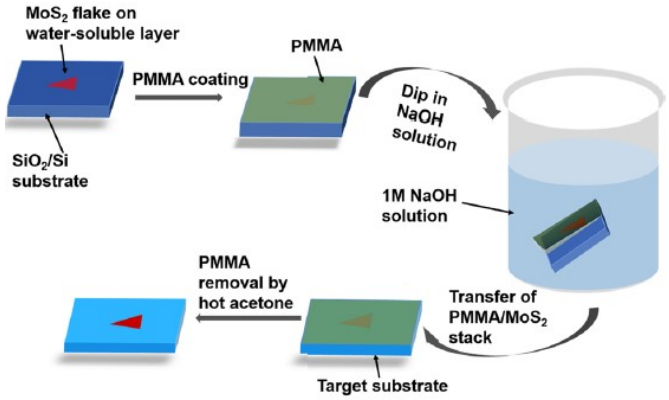

Figure 1.27 Schematic illustration of the transfer process of MoS_2 over arbitrary substrates[154].

As the MoS_2 flakes are very delicate, the transfer process of MoS_2 flakes onto target substrates is also specific. As presented by Madan Sharma *et al.* [154], shown in Figure 1.27, poly-(methyl methacrylate) (PMMA) is firstly spin-coated on the MoS_2 flake and Si/SiO_2 substrate and then the whole stack is placed into 1M NaOH solution (one edge of the MoS_2 flake should have been slightly scratched to facilitate NaOH solution penetration at the interface of MoS_2 and substrate). Then, after a rinsing step in DI water, the PMMA/ MoS_2 stack is transferred onto the target substrate. At last, the PMMA is removed after 480 sccm Ar flow for 2 h at 350 °C and dipping in hot acetone.

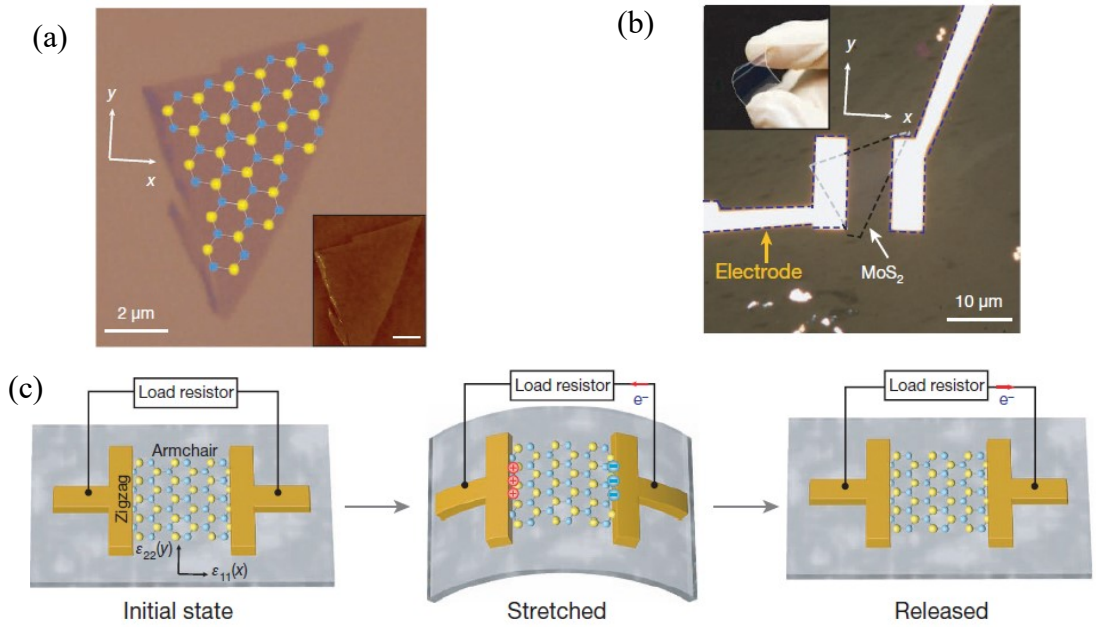

Figure 1.28 (a) Optical image of the single-atomic layer MoS_2 flake with superimposed lattice orientation; (b) A flexible device with single-layer MoS_2 flake and electrodes at its edges; (c) Operation scheme of the single-layer MoS_2 piezoelectric device to measure piezoelectric constants[155].

As discussed above, MoS_2 is expected to hold interesting piezoelectric properties, which can give it the potential to compose nanoscale acoustic devices. To measure the piezoelectric constant of MoS_2, Wenzhuo Wu *et al.* [155] proposed an experimental setup that is now widely used. Figure 1.28(a) shows an optical image of the single-atomic layer 2H-MoS_2. The crystallographic orientation is indicated, with the x-axis along the "armchair"

direction and the y-axis along the "zigzag" direction. Figure 1.28(b) shows this 2H-MoS_2 flake transferred to a flexible substrate of polyethylene terephthalate (PET). The Cr/Pd/Au electrodes were deposited with the metal-MoS_2 interface parallel to the y-axis. Figure 1.28(c) is the schematic representation of the piezoelectric constant measurement with this flexible device. When the substrate is mechanically bent, a uniaxial stress is applied to the MoS_2. The piezoelectric response is investigated by applying a periodic strain to the device connected to an external load resistor.

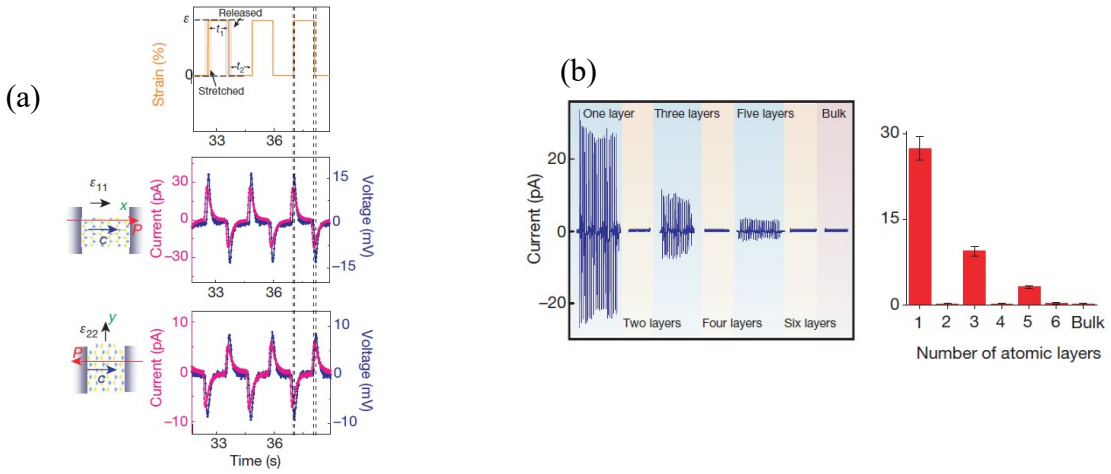

Figure 1.29 (a) Voltage and current response of a single-layer MoS_2 device under periodic strain in two different principal directions; (b) Evolution of the piezoelectric outputs with increasing number of atomic layers in MoS_2 flakes[155].

Figure 1.29 (a) shows the resulting current and voltage responses. We can see in x ("armchair"), respectively y ("zigzag"), directions that under periodic loading, positive (respectively negative) output voltage and current are observed with increasing strain and negative (respectively positive) outputs are observed with decreasing strain. This clearly shows the conversion of mechanical deformation into electrical response. Figure 1.29 (b) shows this piezoelectric signal of 2H-MoS_2 flakes as a function of the number N of atomic layers. Samples with an odd number N exhibit a piezoelectric response, decreasing with N. For an even number N, due to the opposite crystalline orientation of the alternating layers, it is assumed that flakes are centrosymmetric, cancelling the piezoelectric response [155].

Unlike 2H-MoS_2, 3R-MoS_2 is not expected to exhibit centrosymmetry regardless of the number of atomic layers, so 3R-MoS_2 should always exhibit piezoelectricity [137]. Research on the piezoelectric properties of 3R-MoS_2 is usually based on molecular dynamics simulations using first-principles density functional theory (DFT) [156, 157]. However, it should be noted that DFT calculation results vary with different methods and approximations [158]. As shown in Figure 1.30, Dan Tan *et al.* [156] present a simulated piezoelectric constant ε_{11} of 3R-MoS_2 that increases with the number of layers and starts to decrease from 5 layers; bulk 3R-MoS_2 should have a stable piezoelectric constant. This can confirm the stable existence of piezoelectricity in 3R-MoS_2.

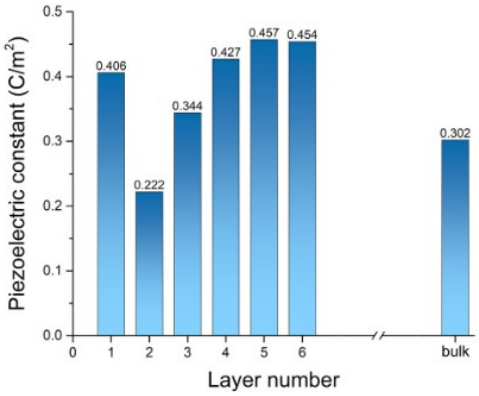

Figure 1.30 Piezoelectric constant of $3R-MoS_2$ as a function of the layer number[156]

Satoru Konabe *et al.* [157] reported a complete first-principles calculation of the material properties of 3R transition metal dichalcogenides based on DFT. The elastic and piezoelectric constants of bulk 3R- MoS_2 , $MoSe_2$, WS_2 and WSe_2 are reported. The calculation results of 3R- MoS_2 are listed in the following tables, which will be used as preliminary values for further device design. The elastic properties of 2H-MoS_2 and 3R-MoS_2 should be nearly the same due to their similar atomic stacking.

Table 1.2 Elastic constants $C_{ij}(GPa)$ for 3R- MoS_2[157]

C_{11}	C_{12}	C_{13}	C_{14}	C_{33}	C_{44}
247	67.7	32.2	-10.7	92.0	38.6

Table 1.3 Piezoelectric coefficients $e_{ij}(C/m^2)$ for 3R- MoS_2[157]

e_{22}	e_{31}	e_{33}	e_{15}	e_{16}
0.64	-0.045	-0.14	-0.079	-0.70

Table 1.4 Piezoelectric coefficients $d_{ij}(pm/V)$ for 3R- MoS_2[157]

d_{22}	d_{31}	d_{33}	d_{15}	d_{16}
3.6	-0.21	0.27	-4.1	-8.3

So far, the reported elastic constants of MoS_2 are from DFT calculations, but some measured Young's modulus (E) are also reported. Andres Castellanos-Gomez *et al.* [159] presented a method to measure Young's modulus (E) of 5 to 25 layers of suspended MoS_2 nanosheets using the tip of an atomic force microscope (AFM). As shown in Figure 1.31 (a), MoS_2 nanosheets are transferred onto the pre-patterned Si/SiO_2 substrate and the inset figure shows the thickness profile from the AFM measurement. A loading cycle is applied to the centre of the suspended region of the nanosheet by the tip (cantilever) of the AFM. The deformation of the nanosheet can be calculated from the difference between the deflection of the AFM cantilever and the displacement of the scanning piezo tube of the AFM, as imaged in Figure 1.31 (b). The resulting relationship between the applied force and the mechanical deformation of 5, 10, and 20 atomic layers MoS_2 nanosheets is represented on Figure 1.31 (c). The average Young's modulus (E) of these suspended nanosheets is found to be E = 0.33 ± 0.07 TPa, much higher than that of graphene oxide, what's more, these MoS_2 nanosheets also exhibit low pre-strain.

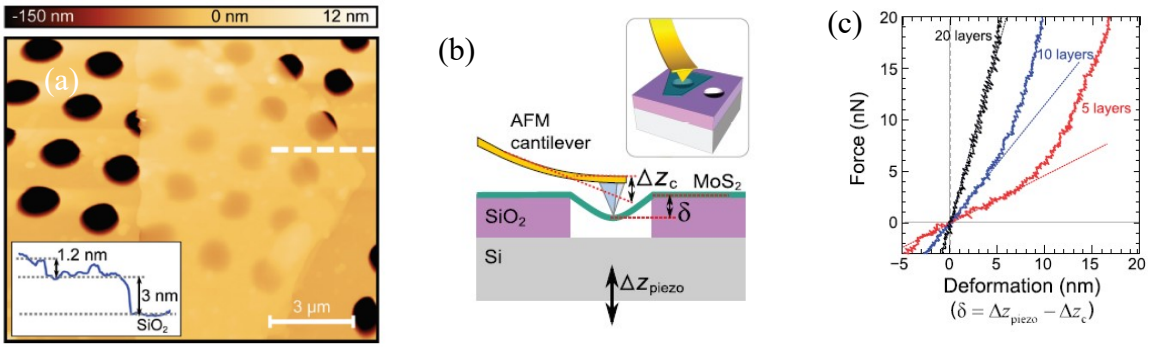

Figure 1.31 (a)AFM topography of MoS_2 flakes deposited on top of a SiO_2/Si substrate prepatterned with holes; (b)Illustration of the nanoscopic bending test experiment carried out on a suspended MoS_2 nanosheet; (c)Force versus deformation traces measured of the suspended part of MoS_2 nanosheets[159].

Similar to graphene, many 2D materials show good mechanical flexibility, combined with their outstanding electrical and optical properties, which make them materials of choice for flexible and stretchable electronics [160]. Such studies are carried out with MoS_2. For example, Jiang Pu *et al.* [161] report flexible MoS_2 electric double-layer transistors using ion gel films as gate dielectrics, a very good mechanical flexibility is showed and no obvious electrical degradation is observed during maximum bending condition, up to curvature radius of 0.75 mm.

Current applications of MoS_2

The interesting properties of MoS_2 give it potential to be applied into several fields, apart from its electrical application as transistor, MoS_2 has found applications in photoelectric, electromechanical, mechanical and biochemical fields.

Due to the altering and layered atomic structure of MoS_2, its application as a solid lubricant has been investigated for several years [162]. For example, Kalyan C. Mutyala *et al.* [163] have presented a graphene-MoS_2 ensemble as a solid lubricant to reduce friction and wear between diamond-like carbon (DLC) coatings and steel contacts. Figure 1.32(a) shows the preparation process and test method. 1 to 8 monolayers of thick graphene and MoS_2 flakes are first suspended in ethanol containing 10 $mg.L^{-1}$ graphene and 18 $mg.L^{-1}$ MoS_2, then a 50:50 graphene-MoS_2 solution is drop-casted on the steel substrate and the liquid ethanol is evaporated in dry nitrogen. For the test part, a stainless-steel ball (AISI 440C) with a diameter of 9.5 mm is fabricated and covered with a 1 mm thick generically hydrogenated diamond-like carbon layer (HDLC). The average surface roughness (R_a) is 48 nm. A pin-on-disc tribometer is used for friction and wear tests, a load of 2 N is applied, and the linear velocity was 0.1 $m.s^{-1}$ for a total distance of 500 m. Figure 1.32(b) is the schematic representation of the HDLC ball and graphene-MoS_2 coating, the average surface roughness is 38 nm. Figure 1.32 (c) and (d) show the results of the tests. The baseline tests are for the tests with uncoated steel and the HDLC-coated ball. The coefficient of friction (COF) measured for the uncoated steel is 0.292 and that of graphene-MoS_2 coated steel is 0.018, which is 16 times lower than the base friction rate. At the same time, the ball wear rate in the graphene-MoS_2 test is 29 times lower than the baseline experiments. In general, MoS_2-based solid lubricants are widely used in the aerospace industry due to their excellent performance. Conventional liquid lubricants cannot solve the problems caused by sealing, vacuum, weight, service life, etc.

Nowadays, MoS_2-based solid lubricants have a wide range of applications, not limited to the aerospace industry [162].

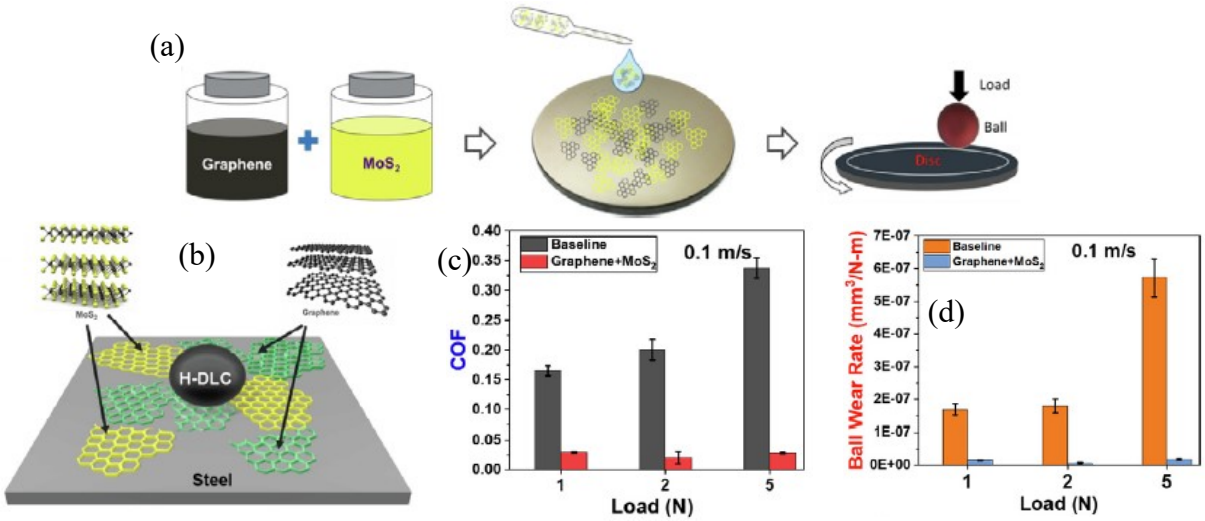

Figure 1.32 (a) Graphene + MoS_2 solid lubricant drop casting method; (b) Schematic representation of the test material pair and Graphene + MoS_2 solid lubricant; (c,d) COF and Ball wear rate behaviors at low speed (0.1 m/s) and increasing loads[163]

Among applications, one is related to gas sensing in which MoS_2 is gradually used for its interesting electric and optoelectronic properties [162]. Indeed, along with the industry development and population growth, climate change and air pollution have become a worldwide problem. As a consequence, gas sensors have become a hot topic of debate due to the necessity to detect various harmful pollutants and gases such as nitrogen oxide (NO_x), ammonia (NH_3), carbon dioxide (CO_2), hydrogen sulphide (H_2S) and sulphur dioxide (SO_2), etc. For example, Tung Pham *et al.* [164] present an MoS_2-based optoelectronic gas sensor with extremely high sensitivity down to the ppb range for the detection of NO_2. Figure 1.33(a) shows the design of this optoelectronic gas sensor. MoS_2 is placed between two Au electrodes to form a channel that allows the photocurrent to be increased. Figure 1.33(b) shows a very low current in the dark environment with a resistance of ~200 GΩ, such high resistance is the result of two Schottky diode type Au/ MoS_2 junctions. In contrast, in Figure 1.33(c), a significant increase in photocurrent of ~500 times is observed when exposed to incident power of 60.9 nW under a red LED. A pulse-like response of the photocurrent is shown in Figure 1.33(d) when the red LED irradiation is switched to "on" and "off." Figure 1.33(e) shows the response of the device to different profiles of NO_2 concentration in the dark and under illumination. R_{N2} is the resistance of the device under N_2 flux and ΔR is a resistance change caused by NO_2 exposure. Figure 1.33(f) shows the amplitude of the relative response as a function of NO_2 concentration. A sensitivity of 4.9%.ppb^{-1}, defined as the slope of this dependence, can be observed under illumination. Tung Pham *et al.* also suggest some optimizations by using Gr and Au/Gr electrodes. Figure 1.33(g,h) are the schematic diagrams illustrating the interaction of conduction band electrons in MoS_2 with NO_2 gas molecules in the dark and under red light illumination (Gr- MoS_2 -Gr device). Under illumination, electrons are excited and holes are trapped at the MoS_2/ SiO_2 interface. Due to the single-layer structure of MoS_2, the population of excited electrons on the surface of MoS_2 increases and NO_2 gas molecules are absorbed on the MoS_2 surface as electron acceptors and trap the excited electrons, increasing the photocurrent in the channel.

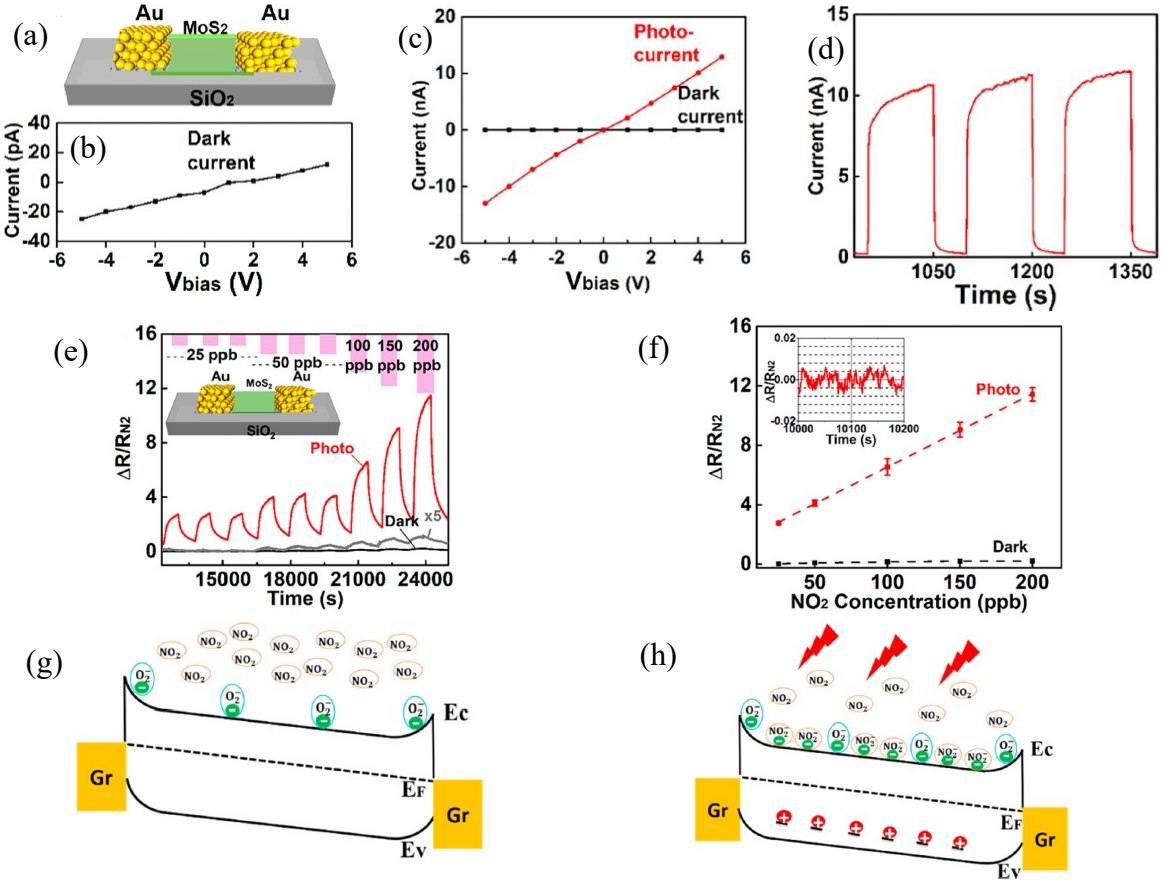

Figure 1.33 (a) Schematic of MoS_2 channel with Au electrodes; (b) in the dark and (c) under red LED illumination; (d) photocurrent pulses when "on" and "off" switching of red LED irradiation; (e) Effect of NO_2 gas exposure on normalized resistance of the Au −MoS_2 −Au device in the dark and under red LED illumination; (f) Dependence of the normalized amplitude of resistance change ΔR/RN2 on the concentration of NO_2 gas; (g, h) Schematic representation showing interaction of conduction band electrons in MoS_2 with NO_2 gas molecules in the dark and under red light illumination(Gr −MoS_2 −Gr device)[164].

In addition to gas sensing applications, MoS_2 for biosensors is also investigated, generally based on the promising semiconducting, luminescence, and electrochemical properties of MoS_2 [162]. As an example, Jingxia Liu *et al.* [165] present a monolayer MoS_2 biosensor based on field-effect transistor (FET) for detecting target DNA fragments (chromosome 21 or 13). Figure 1.34(a) is the structure diagram of the device. The monolayer MoS_2 is first placed between two metal electrodes as a channel, then gold nanoparticles (Au NPs) with optimal size and density are deposited onto the MoS_2 channel to immobilize the DNA probe, which is used to capture the target DNA. Figure 1.34(b) shows the current-voltage curve with different concentrations of chromosome 21 target DNA solutions, and Figure 1.34(c) is the response vs. concentration curve at $V_{gs} = 0.8\,V$, where the response is $(R-R_0)/R_0$, with R the channel resistance of the bare FET biosensor and R_0 after immobilization of the target DNA. The fabricated biosensor has a detection limit lower than 100 aM, and a real-time assay shows that it can detect the target DNA at concentrations as low as 1 fM. Figure 1.34(d) is a schematic representation of the energy band changes of MoS_2 after several depositions. This is a p-doping of the channel, the decrease in the number of electrons of the MoS_2 channel leads to a decrease in current accompanied by an increase in resistance.

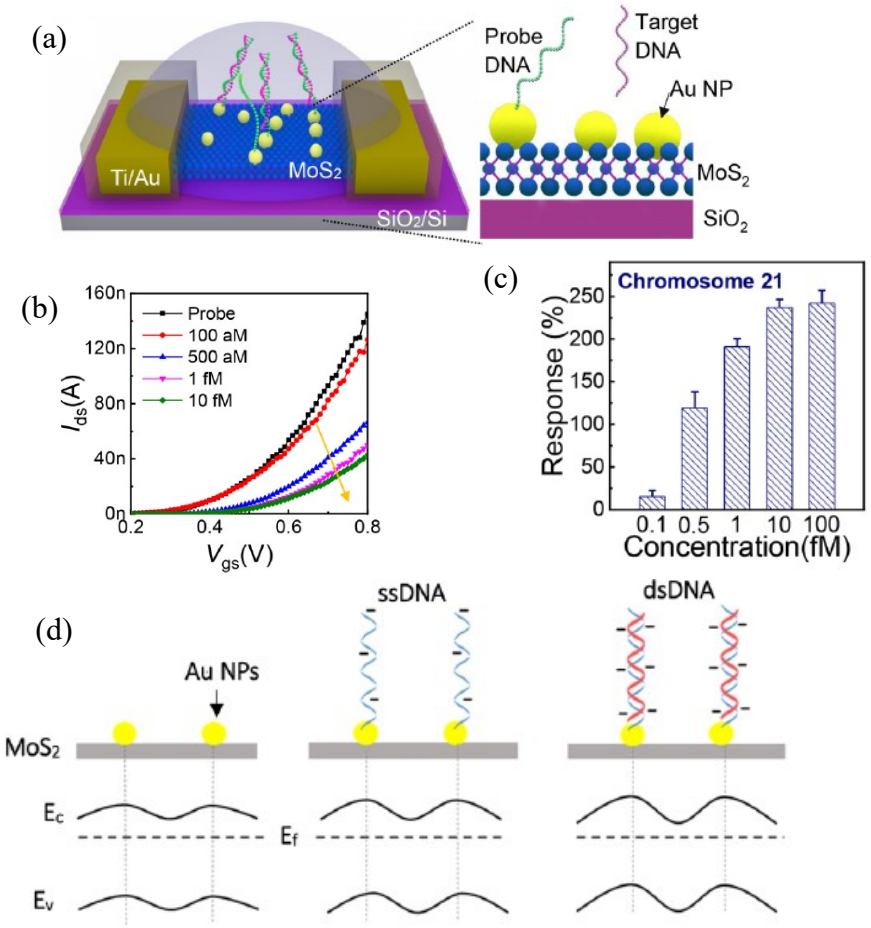

Figure 1.34 (a) The structure diagram of the MoS_2 FET-based biosensor; (b) The response curves for chromosome 21 target DNA solutions with different concentrations; (c) The response-concentration relation; (d)Schematics of energy band changes for MoS_2 after Au NP deposition, DNA probe immobilization, and target hybridization [165].

The application of MoS_2 as the electrode material of supercapacitors is also reported, the layered structure gives MoS_2 large surface area and Mo atoms can provide oxidation states to store ions, the $S-Mo-S$ stacking by van der Waals force can give enough space for efficient intercalation of ions [166]. For example, Debasish Sarkar *et al.* [167] present a MoS_2/r-GO (r-GO for reduced graphene oxide) hybrid nanoflakes-based electrode and realise a high-performance asymmetric supercapacitor (ASC) by using it. They prepare 2D hybrid nanoflakes of r-GO and MoS_2 by a one-step hydrothermal method. r-GO is reduced by thiourea (NH_2CSNH_2) and can enable improved electronic conductivity. Ammonium ions exfoliate MoS_2 in situ with an extended interlayer spacing of 0.95 nm. These spaces are sufficient for intercalating ions, for example Na+ ions, as shown in Figure 1.35(a). Figure 1.35(b) shows the cyclic voltammetry (CV) measurement for Mo foil, MoS_2 and MoS_2/r-GO electrodes (vs. saturated calomel electrode (SCE)), the scan rate is 500 mV/s. MoS_2/r-GO exhibits a nearly rectangular-shaped CV loop, which means an enhanced capacitance. Figure 1.35(c) and (d) show the structure of fabricated $MoS_2/r-GO$ and Fe_2O_3/MnO_2 ASCs and the comparison of their CV loop, respectively. $MoS_2/r-GO$ shows a better capacitance, the resulting ASC can deliver a volumetric energy density of 0.78 mWh/cm^3 at a power density of 500 mW/cm^3 and it can be charged-discharged for over 20,000 cycles in an aqueous electrolyte. Figure 1.35(e) is the schematic representation of the charge storage, the extended atomic layer distance of MoS_2 facilitates the insertion/extraction of ions.

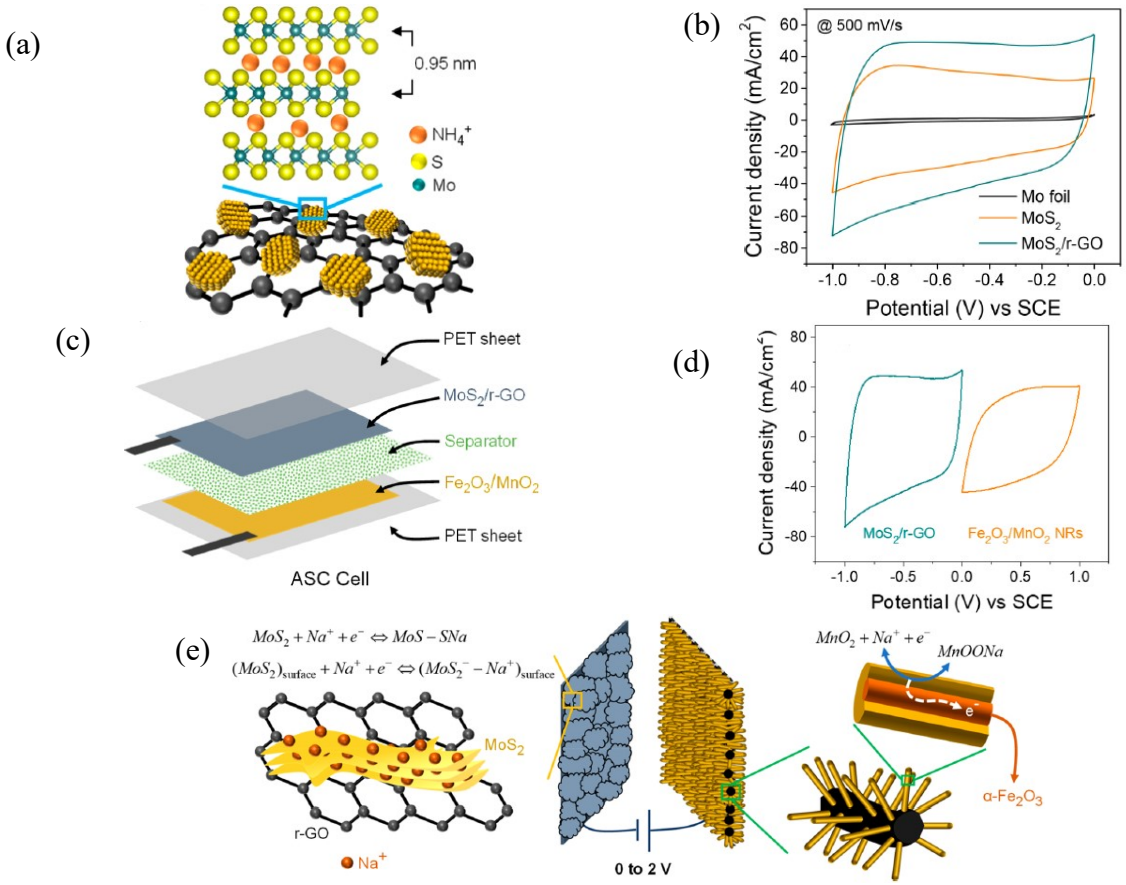

Figure 1.35 (a) Schematics of the MoS_2/r-GO showing ammonium ion intercalation into MoS_2 interlayer spacing; (b) the voltage profile for the capacitive current response; (c) schematics of the assembled ASC cell; (d) performance comparison of anode and cathode materials; (e) Schematic Charge Storage Mechanism in ASC cell[167].

In summary, MoS_2 is considered a very promising material after graphene. MoS_2-based solid lubricants have already been produced industrially, then many MoS_2-based electrical components have been developed in the laboratory, such as transistors, gas/bio-sensors, supercapacitors, etc. The current challenge is the large-scale fabrication of high-quality homogeneous MoS_2 nanoflakes. Nowadays, the interesting piezoelectricity of $3R - MoS_2$ has attracted more and more attention. However, the application in this field is rarely reported, and moreover, there are few characterization results on the properties of MoS_2, especially the elastic and piezoelectric constants.

3. Motivation and challenges

Based on the successful synthesis of 2D nanomaterials presented above, especially the piezoelectric ones, the goal of this work is to participate to the development of the next generation of acoustic devices based on 2D TMDs nanomaterials, focusing on 3R-MoS_2. Since BAW (FBAR) plays an increasingly important role in the high frequency communications and the size of transferred homogenous 3R-MoS_2 flakes currently reaches up to about 100-200 µm, we proposed to develop a 3R-MoS_2-based FBAR structure based on ultrathin 3R-MoS_2 flakes and a SMR configuration, which provides better mechanical support.

The working steps are presented as follows:

1. Based on the current fabrication conditions, especially the thickness and size of the available transferred 3R-MoS_2 flakes, a design for a 3R-MoS_2-based SMR should be established. The SMR is designed to operate in longitudinal acoustic mode and the acoustic Bragg reflector is classical with quarter wavelength alternate layers and the top electrode design should be considered to reduce the spurious modes.
2. Multiphysics FEM simulations should be performed to verify and predict the mechanical and electronic performance of the designed devices, including the top electrode.
3. To characterize the fabricated device, a RF Ground-Signal-Ground (GSG) type 50 Ω matched coplanar waveguide should be also designed, and a suitable method should be used to remove the electrical parasites of the coplanar waveguide.
4. A suitable fabrication process and associated mask design should be proposed.
5. The characterization of the fabricated devices in terms of fabrication and electrical performance, appropriate data processing and physical analysis should also be carried out.

Several challenges should be faced, the main ones are:

1. Few experimental results are found in the literature to characterise the properties of 3R-MoS_2, especially the piezoelectric constants. A deep state of art about these properties should be conducted to find probable values as a starting point for FEM simulations.
2. Since the thickness of 3R-MoS_2 is quite small, the lateral dimensions of the designed device are relatively large, thus also the number of elements of the FEM models. Therefore, appropriate methods should be carried out to improve the models and reduce the computation time.
3. Due to the complexity and uncertainty of the nanofabrication process, the set of masks should be carefully designed and also improved as the fabrication progresses.
4. When comparing simulation and characterization results, a deep understanding and appropriate physical explanation should be investigated.

Chapter 2 Basics of 2D nanomaterial-based Solidly Mounted Resonators (SMR)

1. Introduction

In the first chapter, we have reviewed the discovery, history, and origin of piezoelectricity and introduced various acoustic waves that can propagate in piezoelectric materials, as well as current acoustic devices, their applications and market shares. To meet the current demands, it is necessary to develop the next generation of acoustic devices. Encouraged by the discovery of new two-dimensional materials, we decided to develop acoustic devices based on TMDs as 2D nanomaterials. After comparing the differences between current acoustic devices and analysing the limitations in the fabrication process, we finally proposed to develop SMR-type FBARs.

Preliminary to the design, we need to perform a thorough theoretical analysis to understand the performance of the devices to be developed. In this chapter, we will take an in-depth look at the acoustic theory of FBAR/SMR. A detailed demonstration of the analytical analysis of SMR devices will be proposed, focusing on the propagation of acoustic waves in various media. Then, the electrical models of these devices will be presented, which can greatly simplify the design procedure. Finally, the finite element method (FEM) is used in the design and analysis of the performance of SMR devices: a brief introduction to FEM is given, covering the basic principle, basic analysis steps, and their applications.

2. Acoustic Theory of FBAR/SMR

As FBAR/SMR devices are basically based on bulk acoustic waves generated by and propagating in the volume of a piezoelectric thin film, it is necessary to study the wave propagation step by step. We firstly study the wave in classical FBAR devices with electrodes and finally in SMR with multilayers. The part of propagation in a non-piezoelectric layer and in a piezoelectric one is present in Annex 1 and 2.

Acoustic Wave Propagation in ideal FBAR

The ideal FBAR structure consists of one piezoelectric layer and two electrodes as shown in Figure 2.. The acoustic waves are generated by the piezoelectric effect and propagate in the piezoelectric film, here we present a simple analytical study by neglecting the influences of electrodes.

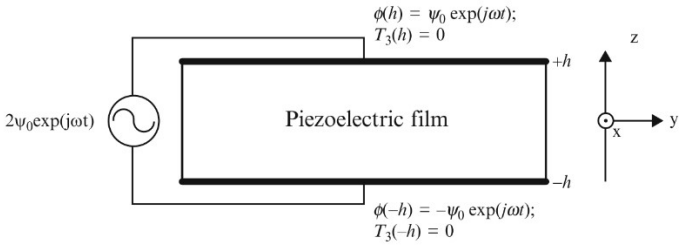

Figure 2.1 Ideal configuration of FBAR structure [96]

The thickness of the piezoelectric layer is $2h$, a bias electric field $2\Psi_0 exp(j\omega t)$ is applied between two infinitely thin electrodes in z direction. As discussed above, an acoustic longitudinal mode wave is excited by the electric field, and here we assume the piezoelectric layer is of hexagonal crystalline structure, such as ZnO, so the wave velocity is $v_l = \sqrt{\frac{c_{33}+e_{33}^2/\varepsilon_{33}}{\rho}}$, and the electric potentials of the top and bottom surfaces of the piezoelectric layer can be expressed using (A.51):

$$\phi(h) = \psi_0 exp(j\omega t) = \frac{1}{j\omega}\frac{e_{33}}{\varepsilon_{33}}[v_{z0}^{+}exp(-jkh) + v_{z0}^{-}exp(+jkh)]exp(j\omega t) + (ah + b)exp(j\omega t) \quad (2.1)$$

$$\phi(-h) = -\psi_0 exp(j\omega t) = \frac{1}{j\omega}\frac{e_{33}}{\varepsilon_{33}}[v_{z0}^{+}exp(+jkh) + v_{z0}^{-}exp(-jkh)]exp(j\omega t) + (-ah + b)exp(j\omega t) \quad (2.2)$$

Furthermore, from (A.53) and considering no stress applied on the top and bottom surfaces, we obtain:

$$T_3(h) = 0 = -\frac{c_{33}+e_{33}{}^2/\varepsilon_{33}}{v_l}[v_{z0}^{+}exp(-jkh) + v_{z0}^{-}exp(+jkh)]exp(j\omega t) + e_{z3}aexp(j\omega t) \quad (2.3)$$

$$T_3(-h) = 0 = -\frac{c_{33}+e_{33}{}^2/\varepsilon_{33}}{v_l}[v_{z0}^{+}exp(+jkh) + v_{z0}^{-}exp(-jkh)]exp(j\omega t) + e_{z3}aexp(j\omega t) \quad (2.4)$$

After solving the above equations (2.2), (2.3) and (2.4), we have:

$$a = \frac{\psi_0/h}{1-k_t^2 tan(kh)/kh} \quad (2.5)$$

$$b = 0 \quad (2.6)$$

$$v_{z0}^{+} = v_{z0}^{-} = \frac{\varepsilon_{33}}{e_{33}} \frac{k_t^2 v_l}{2cos(kh)} \frac{\psi_0/h}{1-k_t^2 tan(kh)/kh} \quad (2.7)$$

$$k_t^2 = \frac{e_{33}^2/\varepsilon_{33}}{c_{33}+e_{33}^2/\varepsilon_{33}} \quad (2.8)$$

Here k_t^2 is the electromechanical coupling coefficient of the longitudinal acoustic mode in c axis of the material.

The electric current on the surface A of the piezoelectric layer is:

$$I = -A\frac{\partial D_z}{\partial t} \quad (2.9)$$

By substituting (A.52) and (2.5), we can get:

$$I = \frac{j\omega\varepsilon_{33}A\psi_0/h}{1-1-k_t^2 tan(kh)/h} \quad (2.10)$$

The electrical impedance of FBAR can be described as:

$$Z_{in} = \frac{\phi(h)-\phi(-h)}{I} \quad (2.11)$$

By substituting (2.10) and $2\Psi_0 exp(j\omega t)$ into (2.11), we can get the expression of the electrical impedance:

$$Z_{in} = \frac{1}{j\omega C_0}[1 - k_t^2 tan(kh)/(kh)] \quad (2.12)$$

And C_0 is a static capacity:

$$C_0 = \frac{\varepsilon_{33}A}{2h} \quad (2.13)$$

Thus, the electrical characterization of an ideal FBAR can be deducted if we know the electromechanical parameters and the structure of the piezoelectric material.

Acoustic Wave Propagation in a Multi-layered FBAR

In a real FBAR structure, the top and bottom electrodes, as well as the acoustic Bragg mirror in the case of a SMR structure, have significant effects on the performance of the device. In addition, due to the miniaturization and higher frequencies, the thickness of the piezoelectric layer is ever smaller, as well as that of other layers, and the effects cannot be ignored. In a complete FBAR/SMR resonator, when an electric signal is applied to the electrodes, a bulk acoustic wave propagating along the thickness direction is excited in the functional layer "electrode/piezoelectric layer/electrode", which propagates not only in the piezoelectric layer but also in the electrodes, and Bragg reflector if any, but the propagation velocity of acoustic waves in different media is different. At this point, in order to obtain the expression for the electrical impedance of the composite structure, it is necessary to introduce the acoustic impedance:

$$Z_{mech}(z) = -\frac{T_{ij}(z)}{v_i(z)} \quad (2.14)$$

where $T_{ij}(z)$ and $v_i(z)$ are the stress and particle velocity, respectively.

These two variables generally contain components in the positive and negative directions. "+" means that the acoustic wave propagates in the positive direction, and "-" means that the acoustic wave propagates in the negative direction. The characteristic acoustic impedance is a specific acoustic property of a material, e.g. in cubic and hexagonal crystalline materials, it can be expressed as follows:

$$Z_{mech}^{c} = \sqrt{\rho c_{33}} \qquad (2.15)$$

The electrodes and each layer of the acoustic Bragg reflector can now be considered as a simplified acoustic layer. As described above, the thickness of the piezoelectric layer is $2h$, then the plane at $z = h$ corresponds to the interface between the piezoelectric film and the top electrode, and the i[th] acoustic layer on the top of the piezoelectric film is characterized by the characteristic acoustic impedance $Z_i(i = 1, 2, 3...n)$. The plane at $z = -h$ represents the interface between the piezoelectric film and the lower electrode and the characteristic acoustic impedance of the i[th] acoustic layer below the piezoelectric film is noted $Z_{bi}(i = 1, 2, 3...m)$. Figure 2.2 shows the model of a "simple" FBAR, consisting of a piezoelectric film and two equivalent acoustic layers on top and bottom.

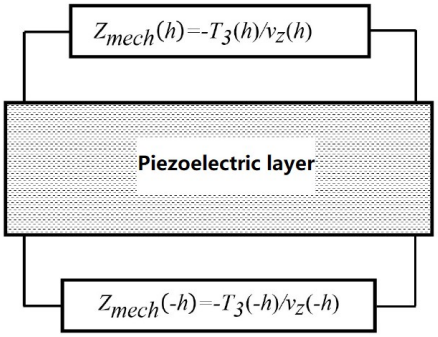

Figure 2.2 The effective acoustic impedance model of "electrode/piezoelectric layer/electrode" FBAR structure

According to acoustic transmission line theory [168, 169], the acoustic impedance at any point can be expressed as:

$$Z_{mech}(z) = Z_{mech}^{c}\left[\frac{Z_{mech}(z_r)+jZ_{mech}^{c}\tan(k_z Z)}{Z_{mech}^{c}+jZ_{mech}(z_r)\tan(k_z Z)}\right] \qquad (2.16)$$

Where $Z_{mech}(z_r)$ is the acoustic impedance of one point of reference.

When $z = h$ we have:

$$T_3(h) = \frac{c_{33} + {e_{33}}^2/\varepsilon_{33}}{v_l}[v_{z0}^{+}exp(-jkh) + v_{z0}^{-}exp(+jkh)]exp(j\omega t) + e_{z3}aexp(j\omega t)$$
$$= [v_{z0}^{+}exp(-jkh) + v_{z0}^{-}exp(+jkh)] \cdot Z_{mech}(h) \qquad (2.17)$$

When $z = -h$ we have:

$$T_3(-h) = \frac{c_{33} + {e_{33}}^2/\varepsilon_{33}}{v_l}[v_{z0}^{+}exp(+jkh) + v_{z0}^{-}exp(-jkh)]exp(j\omega t) + e_{z3}aexp(j\omega t)$$
$$= [v_{z0}^{+}exp(+jkh) + v_{z0}^{-}exp(-jkh)] \cdot Z_{mech}(-h) \qquad (2.18)$$

For the potentials, we have:

$$\phi(h) = \psi_0 exp(j\omega t) = \frac{1}{j\omega}\frac{e_{33}}{\varepsilon_{33}}[v_{z0}^{+} exp(-jkh) + v_{z0}^{-} exp(+jkh)]exp(j\omega t) + (ah + b)exp(j\omega t) \quad (2.19)$$

$$\phi(-h) = -\psi_0 exp(j\omega t) = \frac{1}{j\omega}\frac{e_{33}}{\varepsilon_{33}}[v_{z0}^{+} exp(+jkh) + v_{z0}^{-} exp(-jkh)]exp(j\omega t) + (-ah + b)exp(j\omega t) \quad (2.20)$$

Then similarly to the ideal FBAR, the electrical impedance for the "electrode / piezoelectric layer / electrode" structure can be expressed as:

$$Z_{in} = \frac{1}{j\omega C_0}\left[1 - k_t^2 \frac{\tan\theta}{\theta}\frac{(Z_T+Z_B)\cos^2\theta + j\sin 2\theta}{(Z_T+Z_B)\cos 2\theta + j(1+Z_T Z_B)\sin 2\theta}\right] \quad (2.21)$$

Where θ is the phase angle $\omega d/v_l$, Z_T and Z_B are normalized acoustic impedances on the top and bottom surfaces of piezoelectric layer, respectively:

$$Z_T = \frac{Z_{mech}(h)}{Z_p^c}, Z_B = \frac{Z_{mech}(-h)}{Z_p^c} \quad (2.22)$$

With Z_p^c the characteristic acoustic impedance for piezoelectric layer, that can be expressed for hexagonal crystalline material as:

$$Z_p^c = \sqrt{\rho\frac{c_{33}+{e_{33}}^2}{\varepsilon_{33}}} \quad (2.23)$$

For an ideal FBAR which neglects the influence of electrodes, the top and bottom surface is air-medium interface, Z_T and Z_B are zero, (2.21) comes into (2.12).

The above analysis assumes a lossless condition, but a real piezoelectric layer has elastic and viscous damping losses. It can be taken into account by considering the wavenumber as a complex number as follows:

$$k' = \frac{\omega}{v_l'} = \varepsilon\sqrt{\frac{\rho}{c_{11}'}} = k\sqrt{\frac{1}{1+j\omega\eta_{11}/c_{11}}} \quad (2.24)$$

where v_l' is the longitudinal acoustic wave velocity considering the acoustic loss, η_{11} is a coefficient of the matrix of viscosity. If the loss is low, (2.24) can be simplified as:

$$k' = k\left(1 - \frac{1}{2}\frac{j\omega\eta_{11}}{c_{11}}\right) = k - j\alpha \quad (2.25)$$

α is the attenuation coefficient and can be expressed as:

$$\alpha = \frac{1}{2}k\cdot\frac{j\omega\eta_{11}}{c_{11}} = \frac{\omega}{2}\sqrt{\frac{\rho}{c_{11}}}\cdot\frac{\omega\eta_{11}}{c_{11}} = \frac{\omega^2}{2}\cdot\frac{1}{c_{11}}\cdot\sqrt{\frac{\rho}{c_{11}}}\cdot\eta_{11} \quad (2.26)$$

Dispersion diagram of FBAR

In above, we discussed the solutions of Christoffel equation only considering the condition limit in the z direction, which means that it is an ideal infinite medium. If 2-dimensional solutions are considered (y and z directions in Figure 2.), as Feng Zhu *et al.* [170] demonstrated, the displacement and the electric potential are in form of:

$$u_y = Aexp(\bar{\zeta}z\cos\xi y)exp(i\omega t) \quad (2.27)$$

$$u_z = Bexp(\bar{\zeta} z \sin \xi y)\, exp(i\omega t) \qquad (2.28)$$

$$\phi = Cexp(\bar{\zeta} z \sin \xi y)\, exp(i\omega t) \qquad (2.29)$$

where A, B, and C are undetermined constants, ξ is the wave number.

By applying the boundary and continuity conditions, the determinant of the coefficient matrix of the equations has to vanish for nontrivial solutions, which leads to a polynomial equation of degree six for $\bar{\zeta}$. We can establish the equations between ω and ξ, because ω must be real, hence ξ should be complex. The waves with imaginary wavenumber decay along the y direction, considering the complexity of these calculations, these are done on computer.

From these wave equations in two dimensions, it can be shown that two families of acoustic waves can propagate in FBAR resonators, there are longitudinal waves and shear waves propagating in the piezoelectric layer. Shear waves here refer to the type of vertical shear waves (SV), they are polarized in the same plane as the longitudinal waves and can interact with each other, both are also reflected from the two surfaces of the plate and their coupling can generate Lamb waves [171].

(a) (b)

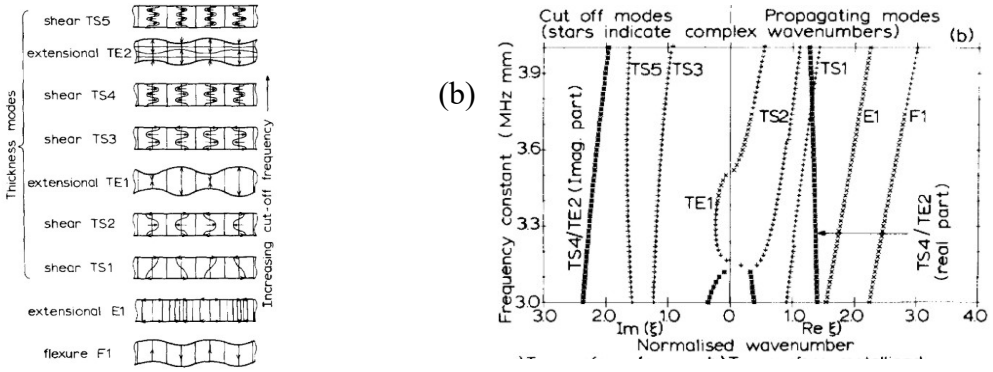

Figure 2.3 (a) The nine lowest Lamb modes of ZnO based FBAR; (b) Dispersion diagram of Lamb modes of FBAR [172].

Figure 2.3 (a) shows the nine lowest Lamb modes in FBAR resonators, the E1 and F1 exist only in the low frequency range, it describes the nature of the motion and the elastic stiffnesses that govern the velocities of propagation. They are the only modes that exist over the entire frequency spectrum. Each higher-order mode has a cut-off frequency above which it can propagate, which is so that:

$$h = \frac{n\lambda}{2} \; or \; f = \frac{nv}{2h} \qquad (2.30)$$

Where h is the thickness of the piezoelectric medium, n is any positive integer, v could be either the longitudinal or the shear bulk wave velocity, as propagating perpendicular to the plate.

Lamb waves exhibit velocity dispersion, i.e., their velocity of propagation depends on the frequency (or wavelength), the elastic constants and density of the material. Dispersion diagrams show the relationships between wave velocity, wavelength, and frequency in dispersive systems. Figure 2.3 (b) is the dispersion diagram of the nine lowest Lamb modes in FBAR. The real parts of the wavenumber correspond to propagating modes while the imaginary parts are associated to evanescent modes. FBAR are usually operated at the first-order longitudinal resonance frequency, the thickness extensional (TE1) mode. The shear vertical modes are called thickness shear (TS) modes.

In general, the velocity of the longitudinal acoustic wave is much greater than that of the shear waves. The ratio is almost 2:1 for currently used piezoelectric materials, which means that the cut-off frequency of the TE1 mode is close to the TS2 mode, as found from equation (2.30), and the TS2 mode is an undesirable mode that can severely degrade the FBAR performance. The relationship between the cut-off frequencies of these two modes is typically determined by the Poisson's ratio in a given material.

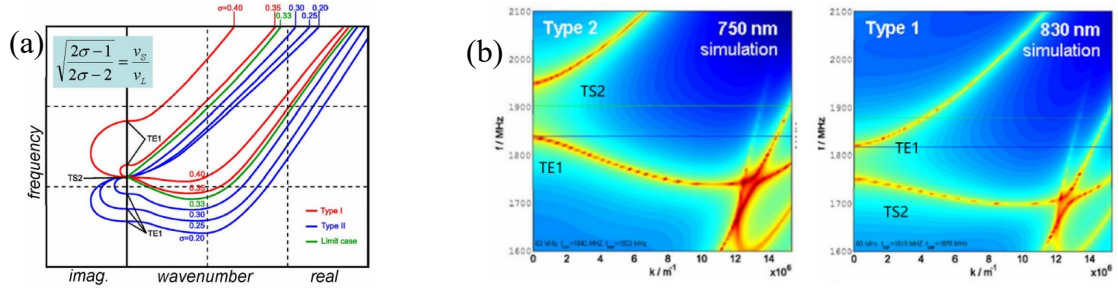

Figure 2.4 (a) Calculated dispersion diagram in function of Poisson ratio; (b) Simulated type-1 and type-2 piezoelectric materials dispersion diagram[104].

Figure 2.4 (a) shows a calculation result by varying the Poisson's ratio for an isotropic plate [104]. We can see that when the Poisson's ratio is about 0.33, corresponding to a ratio v_l/v_s=2, the longitudinal and shear resonance are at the same frequency. When the Poisson's ratio is more than 0.33, the resonance frequency of the longitudinal mode is greater than that of the shear mode, such materials are of "type-1". When the Poisson's ratio is less than 0.33, the resonance frequency of the longitudinal mode is smaller than that of the shear mode and the material is of "type-2". Figure 2.4 (b) shows the dispersion curves of AlN (left) and ZnO (right) plates simulated by finite element method [104]. It can be clearly seen that AlN is a type 2 material and ZnO is a type 1 material. The principle of the design is to keep these two cut-off frequencies far away from each other in order to avoid generating mode coupling.

Else, unlike in the ideal infinite medium, SV and longitudinal waves can reflect or refract at the free boundaries of the plate, possibly undergoing mode conversion and some additional horizontal shear (SH) waves can be generated. They can then propagate laterally between the plate boundaries, as shown in Figure 2.5 which shows the simulated dispersion curves of a FBAR with lateral boundaries, highlighting the existence of SH waves [173]. In our case, SH waves can bring some unwanted constructive wave modes, such spurious modes should thus be limited, using methods of apodization and frame-like top electrode, as shown in Chapter 1.

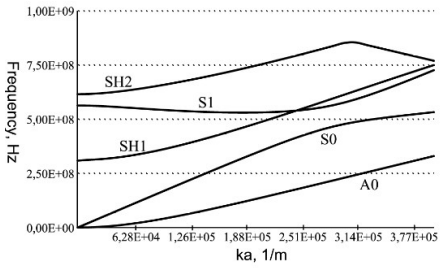

Figure 2.5 Dispersion diagram of Lamb and shear modes in the FBAR [173].

For the SMR type FBAR, the analytical analysis is even more complex, with multiple limits and continuous conditions due to the acoustic Bragg reflector. The design and simulation of SMR are usually performed by the finite element method.

3. Two equivalent circuit models of FBARs

The previous section was dedicated to an analytical solution of FBAR/SMR devices based on the acoustic theory. However, for a FBAR/SMR designer, such analytical approach does not prevent to consider equivalent circuit models to facilitate the design of a complete device integrating the resonator. These models describe FBAR/SMR devices with some lumped electrical elements.

Mason model

W.P Mason [174] proposed an equivalent electric circuit to model a multi-layered structure such as "electrode / piezoelectric layer / electrode" and further facilitate the study of a SMR integrating an acoustic Bragg mirror. We briefly present this model.

If we assume that the propagation of acoustic wave in the materials can be treated as a superposition of plane waves in positive and negative directions (incident and reflected waves), the wave velocity can be expressed as:

$$v = v_z(z) = [v_{z0}^{+}exp(-jkz) + v_{z0}^{-}exp(+jkz)]exp(j\omega t) \qquad (2.31)$$

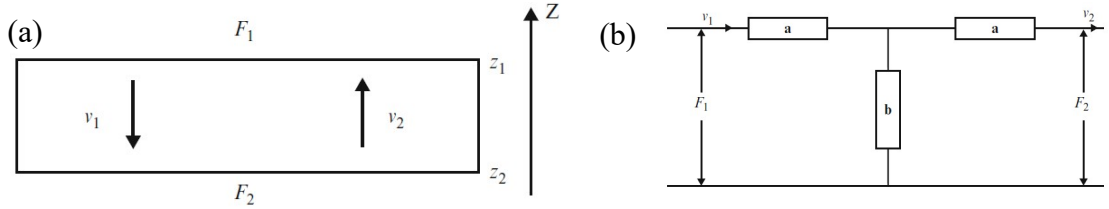

Figure 2.6 (a) The propagation of the acoustic wave in the general acoustic layer; (b) The transmission line mode of the general acoustic layer[96]

We begin with non-piezoelectric layer, for non-piezoelectric layer with the thickness d, Figure 2.6 (a) shows the propagation of an incident and a reflected longitudinal acoustic wave and we assume that $z_1 - z_2 = d$, they can be expressed as:

$$v_1 = v_z(z_1) = [v_{z0}^{+}exp(-jkz_1) + v_{z0}^{-}exp(+jkz_1)]exp(j\omega t) \qquad (2.32)$$

$$v_2 = v_z(z_2) = [v_{z0}^{+}exp(-jkz_2) + v_{z0}^{-}exp(+jkz_2)]exp(j\omega t) \qquad (2.33)$$

Then we can solve the v_{z0}^{+} and v_{z0}^{-} from (2.86) and (2.87)

$$v_{z0}^{+} = \frac{v_1 exp(jkz_2) - v_2 exp(jkz_1)}{2j\,sin\,(kd)} \qquad (2.34)$$

$$v_{z0}^{-} = \frac{v_2 exp(-jkz_1) - v_1 exp(-jkz_2)}{2j\,sin\,(kd)} \qquad (2.35)$$

The force at $z = z_1$ is

$$F_1 = AT_3(z_1) = -AZ_{mech}(z_1)v_1 = -A[v_{z0}^{+}exp(-jkz_1) + v_{z0}^{-}exp(+jkz_1)]exp(j\omega t)Z_{mech}^{A} \qquad (2.36)$$

Where A is the surface area

Substituting (2.34) and (2.35) into (2.36)

$$F_1 = \frac{Z^A_{mech}}{j\sin(kd)}(v_1 - v_2) + jZ^A_{mech}\tan\left(\frac{kd}{2}\right)v_1 \quad (2.37)$$

Where

$$Z^A_{mech} = Z^c_{mech}A \quad (2.38)$$

Similarly, we get the expression of F_2:

$$F_2 = \frac{Z^A_{mech}}{j\sin(kd)}(v_1 - v_2) - jZ^A_{mech}\tan\left(\frac{kd}{2}\right)v_2 \quad (2.39)$$

From (2.37) and (2.39), the $\boldsymbol{F_1}$ and $\boldsymbol{F_2}$ can be described as the acoustic input and output ports according to the acoustic transmission line theory [168, 169], as shown in Figure 2.6 (b). They can be expressed in form of matrix as:

$$\begin{bmatrix} F_1 \\ v_1 \end{bmatrix} = \begin{bmatrix} \frac{a+b}{b} & 2a + \frac{a^2}{b} \\ \frac{1}{b} & \frac{a+b}{b} \end{bmatrix} \begin{bmatrix} F_2 \\ v_2 \end{bmatrix} \quad (2.40)$$

Where a and b can be expressed as:

$$a = jZ^A_{mech}\tan\left(\frac{kd}{2}\right) \quad (2.41)$$

$$b = \frac{Z^A_{mech}}{j\sin(kd)} \quad (2.42)$$

When it comes to the piezoelectric layer, we will apply the same method, from the coupling piezoelectric equations, we get:

$$D_z = \varepsilon^S_{zz}E_z + e_{z3}S_z = \varepsilon^S_{zz}E_z + e_{z3}\frac{\partial u_z}{\partial t} \quad (2.43)$$

Therefore the electric field can be expressed as:

$$E_z = \frac{D_z}{\varepsilon^S_{zz}} - \frac{e_{z3}}{\varepsilon^S_{zz}}\frac{\partial u_z}{\partial t} = \frac{D_z}{\varepsilon^S_{zz}} - \frac{e_{z3}}{\varepsilon^S_{zz}}j\omega v_z \quad (2.44)$$

We can also get the electric current as:

$$I = -j\omega AD_z \quad (2.45)$$

The voltage between the surfaces of piezoelectric layer can therefore be expressed as:

$$V = \int_{z_1}^{z_2} E_z dz = \frac{d}{\varepsilon^S_{zz}}\frac{I}{jwA} + \frac{h}{j\omega A}(v_1 - v_2) \quad (2.46)$$

Where

$$h = \frac{e_{z3}}{\varepsilon^S_{zz}} \quad (2.47)$$

Finally, we can get the expression of current like:

$$I = j\omega C_0 V + hC_0(v_1 - v_2) \quad (2.48)$$

$$C_0 = \frac{\varepsilon^S_{zz}A}{d} \quad (2.49)$$

We can therefore see that the current is composed by two parts, one is through a capacitance, $j\omega C_0 V$ and the other is from the conversion of acoustic energy due to piezoelectric effect, the equivalent circuit for one piezoelectric layer can now be developed as shown in Figure 2.7.

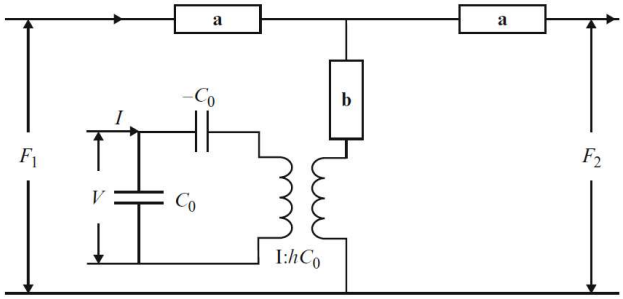

Figure 2.7 The equivalent circuit of a piezoelectric slab[96]

Based on this approach, considering the continuous propagation of the acoustic wave in the multi-layered structure "electrode/piezoelectric layer/electrode" with the output of a layer as the input of the next one, Mason proposed an equivalent model circuit of a FBAR device as represented in Figure 2.8.

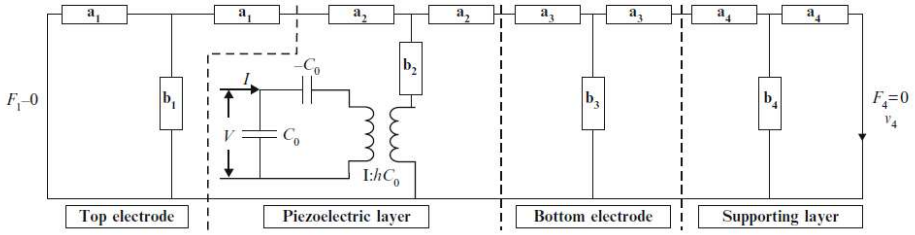

Figure 2.8 The universal Mason equivalent circuit of FBAR[96]

Butterworth Van-Dyke (BVD) model

Butterworth and Van-Dyke proposed later another equivalent model called Butterworth Van-Dyke (BVD) model with a simpler structure to simulate the electrical performance of a BAW resonator near the resonance point [175]. The BVD model is also based on lumped parameters such as resistance, capacitance and inductance. When considering the mechanical loss of the piezoelectric layer, the BVD model of the BAW resonator is shown in Figure 2.9 (a). C_0 is the static capacitance, C_m, L_m and R_m are respectively, the dynamic capacitance, static inductance and the loss related to the mechanical resonance.

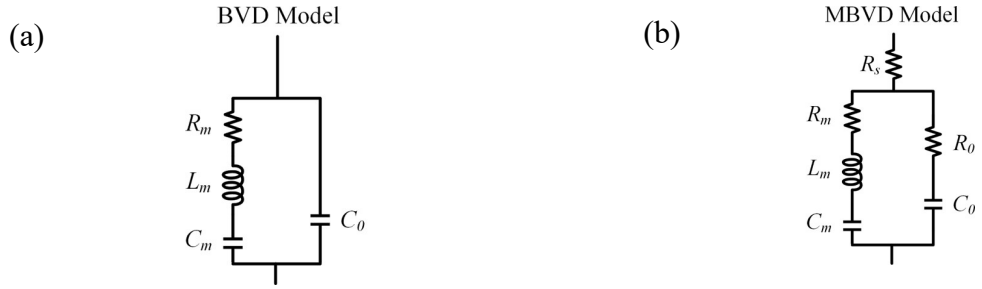

Figure 2.9 Equivalent circuit of (a) Butterworth Van-Dyke (BVD) model; (b) Modified BVD model

$$C_0 = \frac{\varepsilon_{33} A}{2h} \quad (2.50)$$

$$C_m = \frac{8}{\pi^2} k_t^2 C_0 \quad (2.51)$$

$$L_m = \frac{h^2}{2k_t^2 C_0 v_l^2} \quad (2.52)$$

$$R_m = \frac{\pi^2}{8C_0 k_t^2 \rho v_l^2} \quad (2.53)$$

From this BVD model, we can see that the electrical characteristics of a FBAR correspond to adding a resonant dipole in parallel to a capacitor. As described in Chapter 1, the resonance of an FBAR consists of a point of maximum (parallel resonance f_p) and a point of minimum (series resonance f_s) of the electrical impedance, as shown in Figure 2.10. In a non-resonance region, the device is purely capacitive and the phase is -90°(-π/2); in the resonance region, the device is purely inductive and the phase is 90°(π/2).

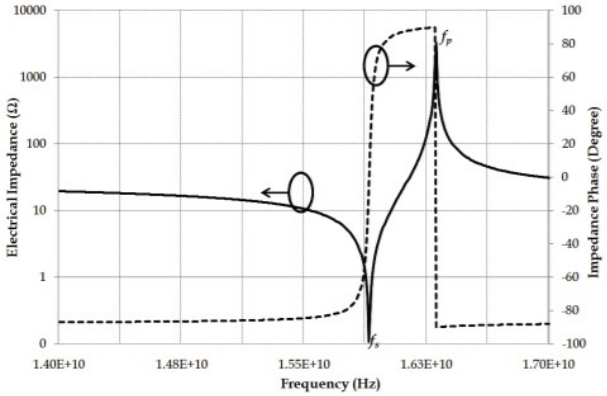

Figure 2.10 Impedance and Phase Curves of an Ideal BAW Resonator[176].

f_s is mainly determined by C_m and L_m, f_p is mainly determined by C_m, L_m and C_0:

$$f_s = \frac{1}{2\pi\sqrt{L_m C_m}} \quad (2.54)$$

$$f_p = \frac{1}{2\pi\sqrt{L_m \frac{C_m C_0}{C_m + C_0}}} \quad (2.55)$$

The BVD model only considers the mechanical loss of the piezoelectric layer of the device, but not the dielectric loss, nor the electrode and the conduction losses. Therefore, Larson *et al.* [177] proposed a modified BVD model, namely the MBVD model, by adding two elements R_0 and R_S as shown in Figure 2.9 (b). R_0 represents the dielectric loss of the piezoelectric layer and R_S represents the electrode and the conduction losses. Practically, the fabricated device is first characterized. By comparing the characterization results with the simulation results of the MBVD model, a fitting curve matching the characterization results is obtained, and by adjusting the parameters in the model, the design of the FBAR device is further optimized.

Then we can have a further study about the resonance performance, according to the expression of impedance (2.12), at parallel resonance f_p, $tan(kh)/(kh)$ should approach to infinity, leading to:

$$kh = \frac{2\pi f_p}{v_l} h = (2n+1)\frac{\pi}{2}, (n = 0,1,2\cdots) \quad (2.56)$$

Then we can have

$$f_p = \left(n + \frac{1}{2}\right)\frac{v_l}{2h} \quad (2.57)$$

When $n = 0$, we get the first order parallel resonance

$$f_p = \frac{1}{2}\frac{v_l}{2h} = \frac{v_l}{2d} \quad (2.58)$$

Where d is the thickness of piezoelectric layer.

When it comes to the series resonance f_s, the impedance in (2.12) should be zero, thus:

$$1 - \frac{k_t^2 tan(kh)}{kh} = 0 \quad (2.59)$$

So we can calculate the expression of the electromechanical coupling coefficient k_t^2

$$k_t^2 = \frac{\theta}{tan\,\theta} = \frac{2\pi f_s \frac{h}{v_l}}{tan\left(2\pi f_s \frac{h}{v_l}\right)} \quad (2.60)$$

By substituting v_l by f_p, we obtain:

$$k_t^2 = \frac{\frac{f_s}{f_p}\times\frac{\pi}{2}}{tan\left(\frac{f_s}{f_p}\times\frac{\pi}{2}\right)} \approx \frac{\pi^2}{4}\left(\frac{f_p - f_s}{f_p}\right) \quad (2.61)$$

It can be seen that k_t^2 is related to the relative interval of the series-parallel resonance frequency. The larger the relative interval $\frac{f_p - f_s}{f_p}$, the larger is k_t^2.

4. Acoustic Bragg Reflector Thickness Optimization Method

The design of a typical acoustic Bragg reflector of SMR is based on a conventional quarter wave acoustic mirror, alternating layers of thickness equal to one quarter wavelength of the longitudinal wave. Only longitudinal acoustic waves are then supposed to be reflected back to the piezoelectric layer, while shear waves, if any, would be mostly transmitted into the substrate, as it can be inferred from the transmission coefficient in such a stack at f_r illustrated in Figure 2.11 [178]. This would lead to an energy leakage due to shear modes, resulting in a decrease of the resonator quality factor (Q).

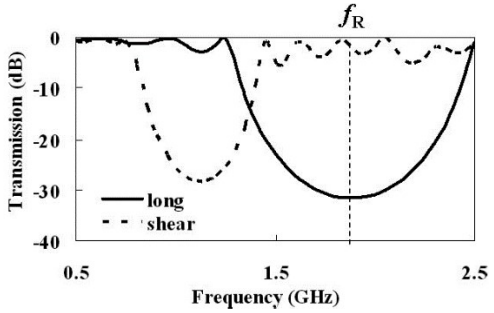

Figure 2.11 Calculated transmission curves of longitudinal and shear waves of a nine-layer Ta_2O_5/SiO_2 quarter-wave reflector stack[178].

In this context, Sumy Jose *et al.* [178] proposed two approaches to avoid this energy leakage and increase the quality factor (Q), by optimizing the acoustic Bragg reflector so that both longitudinal and shear waves can be reflected.

The first approach is named stopband theory method (STM). In this approach the average velocity ratio between longitudinal and shear waves in each layer of acoustic Bragg reflector should be close to 2 with a maximum deviation of 15%. By adjusting the thickness of layers, it is attempted to have the first-order longitudinal mode resonance and the second-order shear mode resonance at the same frequency. The thicknesses are calculated as follows:

$$t_L = \frac{3/2}{1+c+K_L+cK_H}\lambda_{L.long} \qquad (2.62)$$

$$t_H = \frac{3c/2}{1+c+K_L+cK_H}\lambda_{H.long} \qquad (2.63)$$

With:

$$K_L = v_{L.long}/v_{L.shear} \qquad (2.64)$$

$$K_H = v_{H.long}/v_{H.shear} \qquad (2.65)$$

$$c = \frac{K_L+K_H}{2} \qquad (2.66)$$

Where t is the thickness of each Bragg mirror layer, λ and v are the wavelength and the acoustic velocity in the different media, respectively; the subscripts L, H, $long$, and $shear$ are for Low impedance layer, High impedance layer, longitudinal wave mode and shear wave mode respectively. K is defined as the ratio of the longitudinal velocity to the shear one, finally, c is the mean value of K_L and K_H, these three values should be close to 2 for the STM approach.

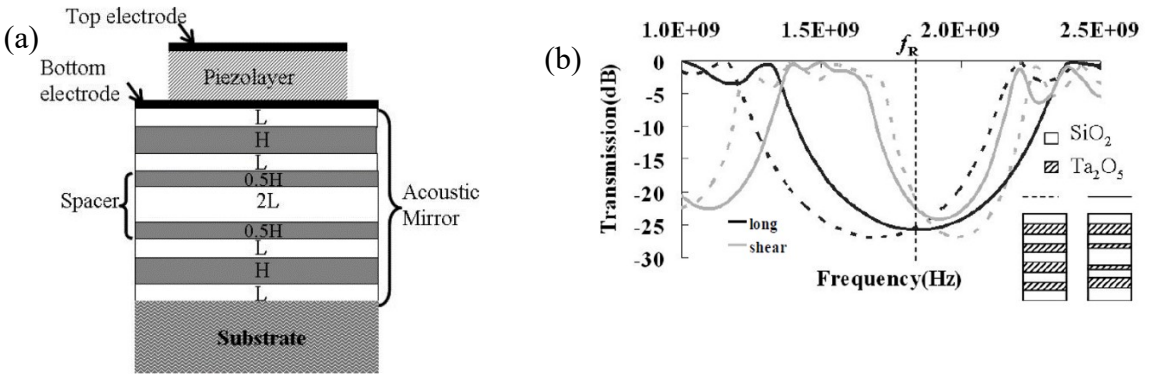

Figure 2.12 (a) The illustration of SMR with spacer layer in acoustic Bragg mirror[178]; (b)Transmission curves of a nine-layer Ta_2O_5/SiO_2 optimized reflector stack based on the new design procedure with and without the spacer layer[178].

In addition, a spacer layer can be introduced for performance improvement [179], as shown in Figure 2.12 (a), with a thicker low impedance layer at the centre of the structure, between two thinner high impedance layers, of thickness 2 L and 0.5 H respectively. This method can reduce the transmittance ripples and therefore enhance the quality factor (Q).

Figure 2.12 (b) shows the transmission curve of the optimized Bragg reflector (SiO_2/Ta_2O_5 nine-layer structure) with and without the spacer layer [178]. We can see that by using the optimized acoustic Bragg reflector, the transmission of acoustic shear wave is greatly minimized near resonance frequency (f_r) compared to the curve in Figure 2.11, especially for the spacer layer configuration, bringing the transmission bands into coincidence.

The second approach is called diffraction grating method (DGM), which shows better results when the average velocity ratio between longitudinal and shear waves deviates from 2 by 15% or more. The principle is to use the reflections of higher-order longitudinal and shear acoustic waves, this approach is more general since the material properties vary a lot from each other. As so, for a good behaviour with both the longitudinal and shear waves, the thickness should be as follows:

$$t_L = \frac{(1+2\cdot m_1)\cdot v_{L.long}}{4f_r} = \frac{(1+2\cdot m_2)\cdot v_{L.shear}}{4f_r} \qquad (2.67)$$

Here f_r is the first order resonance frequency of longitudinal acoustic wave, and the relationship between m_1 and m_2 is given as:

$$\frac{(1+2\cdot m_2)}{(1+2\cdot m_1)} = \frac{v_{L.long}}{v_{L.shear}} = K_L \qquad (2.68)$$

So, we get:

$$m_2 = K_L \cdot m_1 + \frac{(K_L-1)}{2} \qquad (2.69)$$

Theoretically m_1 and m_2 should be integers, in a practical case several integers are tested as m_1 until to find a m_2 close to be an integer, and so that the resulting layer can be technologically feasible.

Similarly, for the High impedance layer, the thickness should be as:

$$t_H = \frac{(1+2\cdot m_3)\cdot v_{H.long}}{4f_r} = \frac{(1+2\cdot m_4)\cdot v_{H.shear}}{4f_r} \qquad (2.70)$$

Thus:

$$m_4 = K_H \cdot m_3 + \frac{(K_H - 1)}{2} \qquad (2.71)$$

A pair m_3 and m_4 is chosen similarly as for m_1 and m_2.

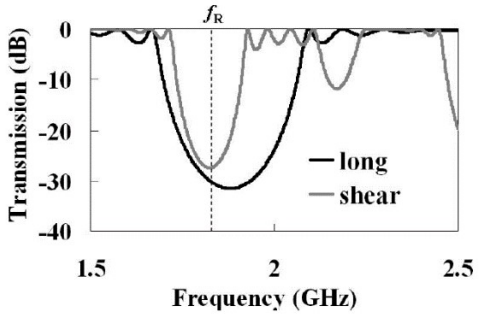

Figure 2.13 Transmission curves of a nine-layer Ta_2O_5/SiO_2 optimized reflector based on diffraction grating method [178]

Figure 2.13 shows the calculated transmission curves of a SiO_2/Ta_2O_5 nine-layer structure Bragg reflector optimized by DGM method with $m_1 = 1$, $m_2 = 1.96$, $m_3 = 1$ and $m_4 = 2.2$. Since m_4 is not an integer, the shear mode resonance frequency is not exactly the same place as that of the longitudinal mode. As a consequence, the reflection of shear and logitudinal waves will not be maximum at the same frequency, but both will remain acceptable in the close frequency region.

Both these two approaches focus on the ratio of longitudinal and shear velocities, trying to get layers of quarter wavelength thickness simultaneously for a longitudinal wave resonance and a shear wave one. As this ratio can hardly be an integer, the two approaches search a trade-off, and since diffraction grating method (DGM) looks for a reflection with higher order resonances, it leads to thicker layers of the acoustic Bragg reflector, compared to the STM approach. Both result in two resonances close to each other, and consequently an enhanced quality factor (Q), at the cost of more electric noise near the targeted longitudinal resonance frequency.

5. The Finite Element Method (FEM)

The numerical tools based on finite element method (FEM) are widely used in research and industry. In the case of FBAR, an analytical analysis as previously presented is able to handle 1D and 2D models of multi-layered structures. Nevertheless, especially in the case of SMR-type FBAR, the possible superposition of several acoustic wave modes, such as shear waves, and also the 3D geometry, play an important role in the device characteristics. FEM analysis could be a powerful tool to help understand the FBAR performances and improve the design.

The finite element method is a numerical calculation method that has developed rapidly with the advent of modern computer technology and is widely used for multiphysics simulation in science and engineering, especially when the geometry and boundary conditions are quite complex. In such case, analytical solutions require many simplifications and assumptions or are even impossible to obtain. Therefore, based on the basic principles of mechanics or any physical issues addressed in a structure, and the idea of discretization, the finite element method has been proposed to solve complex engineering problems. With the spread of finite element analysis software, simple engineers and technicians can now perform design and analysis [180].

As a consequence, this method becomes more and more popular because of its advantages, in terms of user-friendly interface and tools to facilitate modelling irregularly shaped complex structures with different materials, even non-linear, setting boundary conditions, varying the size of the elements to adjust the accuracy of calculation…

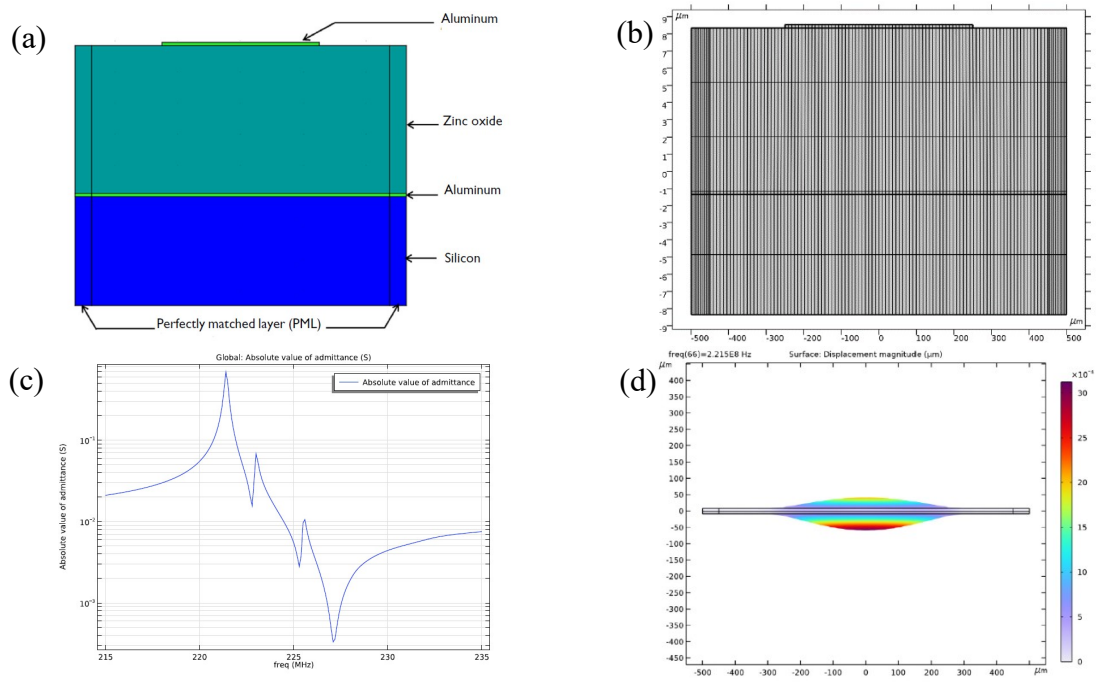

Figure 2.14 (a) 2D geometry (not drawn to scale) of FBAR tutorial model; (b) Mesh of the tutorial model; (c) Simulated absolute value of the electrical admittance vs. frequency; (d) Simulated displacement magnitude of the first order longitudinal acoustic mode in the ZnO layer [181]

COMSOL Multiphysics™ [182] is such a powerful software to perform Multiphysics FEM simulations. We will use it in the following study to design and simulate our devices – SMR type FBAR. An existing model [181] of FBAR is proposed as a reference before launching a deep analysis on our target device.

This is a ZnO-based FBAR, the structure of the model is shown in Figure 2.14 (a). The thickness of the piezoelectric ZnO layer is 9.5 μm, the top and bottom aluminum electrodes are 0.2 μm thick, and a silicon supporting layer has a thickness of 7 μm. The width of the structure is 1.7 mm with a top electrode of 500 μm. Perfectly Matched Layer (PML) domains are added to absorb elastic waves, which contribute to the damping of the structure. A 2D model and a mapped mesh as represented on Figure 2.14 (b) were chosen for this symmetric structure. In general, to obtain sufficiently accurate results, at least 5 elements per wavelength are required for a 3D problem and at least 8 elements per wavelength for a 2D problem. By applying an alternative electrical voltage of 1 V between two electrodes between 215 MHz and 235 MHz, the curve of the simulated absolute value of admittance versus frequency is shown in Figure 2.14 (c). The highest peak of admittance occurs at the first-order longitudinal acoustic resonance at 221 MHz, with a quality factor (Q) of 1326. Figure 2.14 (d) shows the mode shape or displacement magnitude of this first-order longitudinal acoustic resonance at 221 MHz. The highest/lowest displacements take place in the middle of the electrodes on vertical direction; this is the fundamental longitudinal thickness mode. After studying this model in depth, our own model of SMR type FBAR will be based on this reference.

Summary

Since the piezoelectric layer in an ideal FBAR device can be considered as a flat layer, in this chapter, the propagating wave mode in a FBAR structure was then introduced, firstly in the case of a simple structure consisting of a piezoelectric layer between two electrodes, by setting several condition limits, to get the expression of k_t^2, the electromechanical coupling constant and of Z_{in} the electric impedance. The analysis is based on the analytical analysis of the propagation of acoustic plane waves by introducing the strain-stress-displacement equation and the equation of motion of particles in a solid medium, which is detailed in Annex 1 and 2.

To tackle the SMR-type FBAR, due to its multilayer structure with an additional acoustic Bragg reflector, each layer was considered as a simplified acoustic layer with a specific acoustic impedance. We obtained the expression for of k_t^2 and Z_{in}, the electrical impedance, and considered the losses in the system.

To better understand the propagation of acoustic waves in FBAR, the acoustic dispersion diagram was also introduced, highlighting the existing acoustic modes and the frequency dispersion for a particular design.

Because of the complexity of these analytical analyses, two equivalent circuit models of FBAR, the Mason model and the Butterworth-Van Dyke (BVD) one, have been introduced. Both models consider FBAR as an electrical circuit with lumped parameters such as resistance, capacitance, and inductance, which facilitates the study of the component and its integration in a system. The BVD model is simpler but based on experimental characteristics and limited to the resonance region.

Furthermore, two ways of optimization of an acoustic Bragg mirror were presented, which may be useful for our target device, the SMR-type FBAR. Both approaches, referred to as the stopband theory method (STM) and the diffraction grating method (DGM), aim to enable the acoustic Bragg mirror to reflect both longitudinal and shear waves in order to improve the quality factor (Q), at the cost of additional noise near the longitudinal wave resonance frequency.

Lastly, a brief introduction to the powerful numerical analysis tool based on finite element method was provided, that utilises computational resources of high-performance computers. The basic theory and principle of FEM as well as a guide to the design process were presented.

In the next chapter, we will present the design of our SMR-type FBAR using these basics, propose several geometries, and perform a full simulation to understand the performances of our devices. The simulation will be divided into two parts: Butterworth Van-Dyke (BVD) equivalent circuit method and finite element method (FEM).

Chapter 3 Modelling and simulation of 2D-material based solidly mounted resonators (SMR)

Introduction

In Chapter 2, we presented the acoustic theories of FBAR/SMR including acoustic plane wave propagation in a flat plate, the wave propagation in FBAR and SMR. The acoustic dispersion diagram was also presented to better understand the propagation modes. This analytical approach was completed by two equivalent circuit models of FBAR based on lumped elements, the Mason and the Butterworth-Van Dyke (BVD) models, and two ways to improve the quality factor (Q) of the SMR, based on adding the energy of shear waves to the longitudinal ones. Finally, a brief introduction to the finite element method (FEM) as numerical analysis tool was proposed.

In this chapter, we will present the whole process of developing a SMR based on 3R-MoS_2 using the previous basics. Since 3R-MoS_2 is a newly studied piezoelectric material, we first propose a design based on the conventional piezoelectric material ZnO and perform simulations based on the FEM tool. Different geometries are introduced to reduce the spurious acoustic modes and optimisation of the acoustic Bragg reflector is also considered. After validation based on devices from the literature, the design of a SMR based on 3R-MoS_2 is carried out. An analysis with the BVD model is proposed to confirm that the propagation mode is the expected longitudinal acoustic wave. The SMR design and associated masks should be compatible with technological facilities. It should also include access lines for further electrical characterization at millimeter-wave frequency band, taking into account matching issues, based on both the integrated access lines, the classical 50 ohms impedance of a vector network analyzer and intermediate test setup.

1. Modelling and simulation of reference ZnO based SMR

As presented, in order to assess the modelling, simulation and design process, our work starts with SMRs based on the conventional piezoelectric material ZnO , whose properties are well studied and several ZnO-based SMRs are reported in the literature [123, 183, 184].

Conventional ZnO-based SMR structure

Here we choose the structure reported by Linh Mai *et al.* [184] as a reference. The thickness of the ZnO is 1.2 µm, the top and bottom electrodes are of Co and the thickness is $0.2\ \mu m$. The acoustic Bragg mirror consists of 5 alternating layers of SiO_2/W, as shown in Figure 3. (a) and (b). The results of the RF characterization show that the return loss (S_{11}) has a minimum of -30 dB at 1.85 GHz, as shown in Figure 3. (c).

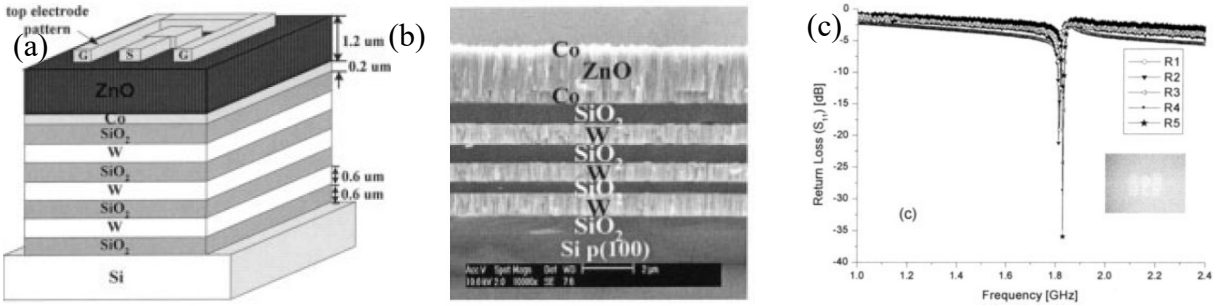

Figure 3.1 ZnO-based SMR (a) 3D schematic structure; (b) Cross-section view of a fabricated device; (c) Experimental return-loss characteristics vs. frequency of 5 devices. [184]

Our design is based on the theory detailed in Chapter 2, which should consist of a quarter-wavelength acoustic Bragg reflector and slightly differs from that in reference. To simplify the calculation, the thickness of ZnO is set to 1 µm, which will lead to a somewhat higher target resonance frequency.

The declared ZnO properties are from [185] and listed below.

The volumetric mass density (ρ): 5680 kg/m^3

The elastic constants matrix (GPa):

$$c = \begin{pmatrix} 209.71 & 121.11 & 105.36 & 0 & 0 & 0 \\ 121.11 & 209.71 & 105.36 & 0 & 0 & 0 \\ 105.36 & 105.36 & 211.19 & 0 & 0 & 0 \\ 0 & 0 & 0 & 42.37 & 0 & 0 \\ 0 & 0 & 0 & 0 & 42.37 & 0 \\ 0 & 0 & 0 & 0 & 0 & 44.25 \end{pmatrix} \qquad (3.1)$$

The dielectric constants matrix:[185]

$$\varepsilon^s = \begin{pmatrix} 9.16 & 0 & 0 \\ 0 & 9.16 & 0 \\ 0 & 0 & 12.64 \end{pmatrix} \qquad (3.2)$$

The piezoelectric constants matrix (pm/V):

$$d = \begin{pmatrix} 0 & 0 & 0 & 0 & -11.34 & 0 \\ 0 & 0 & 0 & -11.34 & 0 & 0 \\ -5.43 & -5.43 & 11.67 & 0 & 0 & 0 \end{pmatrix} \quad (3.3)$$

The piezoelectric constants matrix e $(\mathrm{C/m^2})$ can be calculated as a scalar product of piezoelectric constants matrix d and elastic constants matrix c:

$$e = d \cdot c = \begin{pmatrix} 0 & 0 & 0 & 0 & -0.480 & 0 \\ 0 & 0 & 0 & -0.480 & 0 & 0 \\ -0.567 & -0.567 & 1.320 & 0 & 0 & 0 \end{pmatrix} \quad (3.4)$$

Applying equation (A.47), we can calculate that the velocity of the longitudinal acoustic wave propagating in the piezoelectric ZnO active medium is $v_{l,ZnO} = 6097.71$ m/s and the theoretical resonance frequency $f_r = 3.05$ GHz, according to the equation (2.30) and (2.58). It refers to the first-order longitudinal acoustic resonance and contains most of the acoustic energy.

As described in Chapter 2, the acoustic Bragg mirror consists of a stack of alternating layers of low and high acoustic impedance, as defined for each material in equation (1.4). We consider an acoustic Bragg mirror of 5 alternating SiO_2/W layers, which is the most commonly described in the literature and the fabrication process is mature. Each layer has the thickness of a quarter wavelength of the longitudinal acoustic wave, based on a theoretical resonance at $f_r = 3.05$ GHz.

The SiO_2 and W are isotropic materials and their stiffness matrix can be expressed as:

$$c = \frac{E}{(1+\nu)(1-2\nu)} \begin{bmatrix} 1-\nu & \nu & \nu & 0 & 0 & 0 \\ \nu & 1-\nu & \nu & 0 & 0 & 0 \\ \nu & \nu & 1-\nu & 0 & 0 & 0 \\ 0 & 0 & 0 & \frac{(1-2\nu)}{2} & 0 & 0 \\ 0 & 0 & 0 & 0 & \frac{(1-2\nu)}{2} & 0 \\ 0 & 0 & 0 & 0 & 0 & \frac{(1-2\nu)}{2} \end{bmatrix} \quad (3.5)$$

where E is the Young's modulus and ν the Poisson's ratio.

The declared SiO_2 and W properties are from [185] and listed in Table 3.1, as well as the velocity of the longitudinal bulk acoustic wave and the acoustic impedance, calculated respectively using equation (A.26) and (3.5).

Table 3.1 Bragg mirror materials properties [185] and resulting characteristics and parameters

Property	**SiO_2**	**W**
Volumetric mass density ρ $(\mathrm{kg/m^3})$	2200	19350
Young's modulus E (GPa)	70	411
Poisson's ratio ν	0.17	0.28
Longitudinal bulk acoustic wave velocity v_l (m/s)	5848.06	5210.93
Acoustic impedance Z_a $(10^6\ \mathrm{kg \cdot m^{-2} \cdot s^{-1}})$	12.87	100.83
Wavelength λ at $f_r = 3.05$ GHz (μm)	1.917	1.709
Thickness at $\lambda/4$ (μm)	0.48	0.43

SiO_2 is the layer with the low acoustic impedance and W with the high acoustic impedance, with a ratio more than 5, indicating that they offer good acoustic reflection and can confine well acoustic energy.

From the velocity of the longitudinal bulk acoustic wave in each material and the target resonance frequency $f_r = 3.05$ GHz, the wavelength λ can be calculated, according to the equation:

$$\lambda = \frac{v_l}{f_r} \qquad (3.6)$$

The thickness of each layer of the acoustic Bragg mirror is finally calculated as a quarter-wavelength. The results for the wavelengths and the thicknesses are also presented in the Table above. Figure 3.2 (a) shows the cross-section of the designed ZnO based SMR, the top and bottom electrodes are in Aluminum (Al) and have the thickness of 0.2 µm. The width of structure is of 100 µm and 50 µm for top electrode. The substrate is made of silicon (Si).

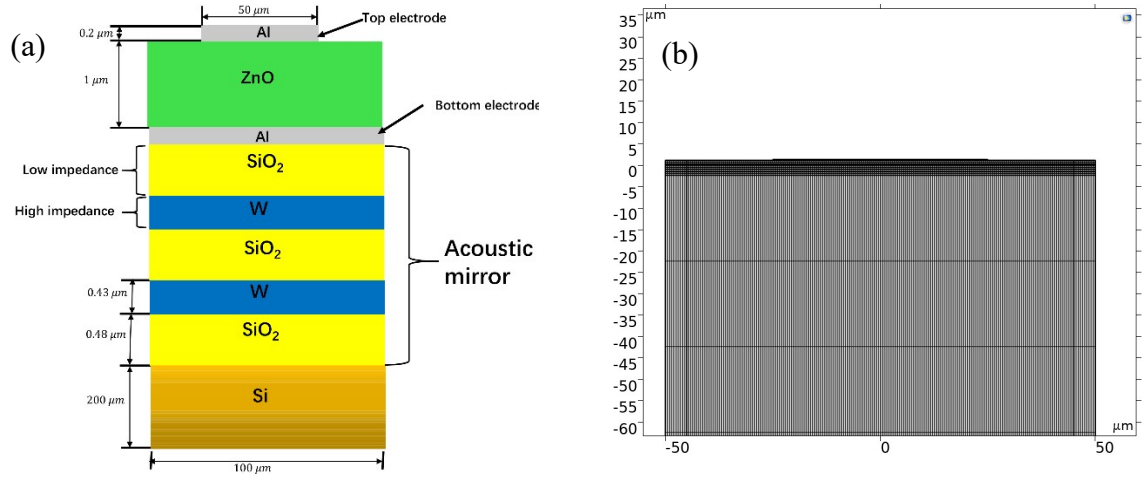

Figure 3.2 (a) Cross-section of the designed ZnO-SMR and (b) the mesh structure of its FEM model.

A finite element method (FEM) analysis was performed with the software COMSOL Multiphysics (V5.4). As described in Chapter 2, we created a 2D model in the first step, and meshed it as shown in Figure 3.2 (b), with a kind of quadrilateral elements, at least 8 per wavelength for a 2D problem to get good convergence [186], with a total number of 4511 elements, and a Perfectly Matched Layer (PML) on both sides.

The MEMS module was applied, the physics of solid mechanics and electrostatics were added. A mechanical damping of 0.001 and a dielectric loss of 0.01 were considered for the piezoelectric layer of ZnO, the effects of losses are described in Chapter 2. An electrical excitation was realized by applying an alternating potential of 1 V between the top and bottom electrodes, and adding a study of Frequency Domain in the range from 2400 to 2900 MHz, step size 0.5 MHz, which exhibited the resonance phenomenon.

Such simulation took 12 minutes and the results are illustrated in Figure 3.3 (a) shows the electrical impedance as a function of frequency. The minimum is observed at 2.63 GHz, which corresponds to the resonance frequency f_r, and the maximum at the anti-resonance frequency f_a of 2.72 GHz. The minimum and maximum of the electrical impedance are at 0.001 and 400 ohms, respectively. The behaviour agrees with the theoretical analysis described in Chapter 2.

From the resonance and anti-resonance frequencies, the electromechanical coupling coefficient k_t^2 can be calculated from the BVD equivalent circuit theory described in Chapter 2 by using equation (2.61), which leads to a k_t^2 of 7.5%. Since ZnO has a hexagonal crystal structure, its k_t^2 can also be expressed by the intrinsic material properties, as in equation (2.8), which leads to the same value, close to a reported value of 8.4% in [187].

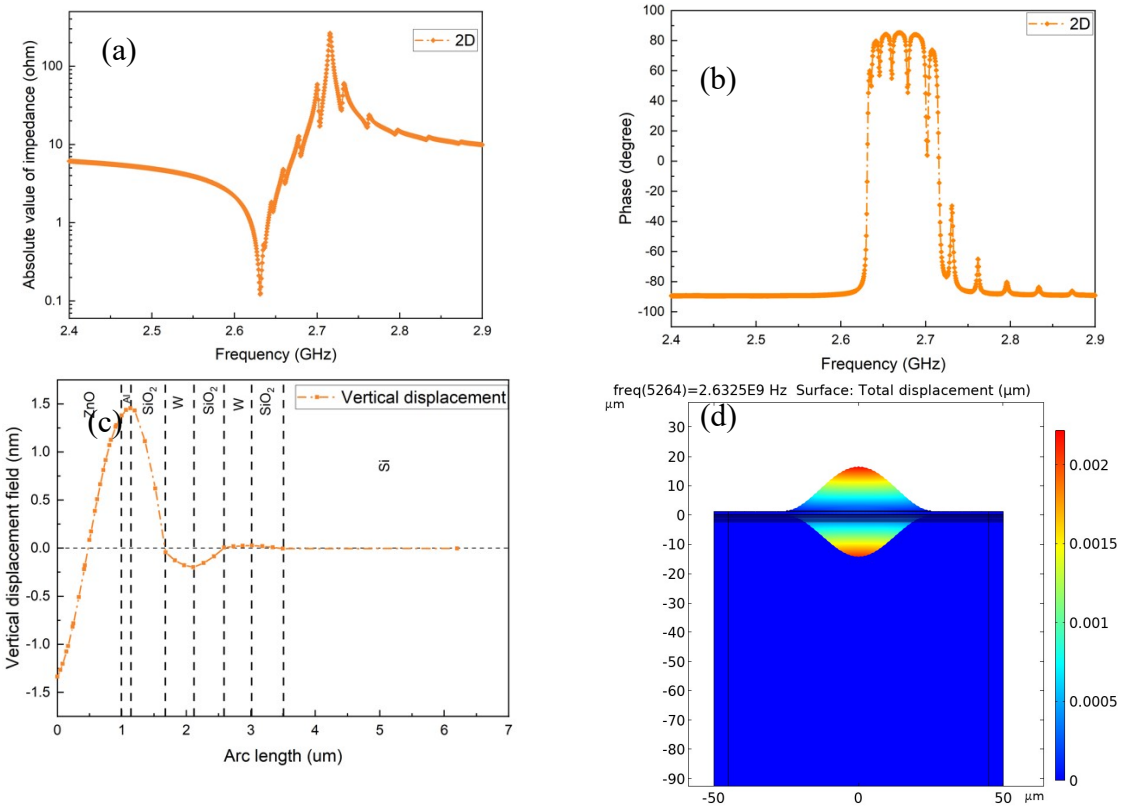

Figure 3.3 Results of the 2D model simulation: (a) Electrical impedance magnitude; (b) Impedance phase; (c) Vertical mechanical displacement and (d) mode shape at the resonance frequency f_r = 2.63 GHz.

Figure 3.3 (b) shows the phase of impedance as a function of frequency. As expected, outside the frequency range between 2.63 GHz, the resonance frequency f_r, and 2.72 GHz, the anti-resonance frequency f_a, the phase is $-90°$, typically associated to a capacitance behaviour. Within the range from f_r to f_a, the phase changes abruptly to 90°. Near the resonance frequencies, some spurious modes can also be observed. These secondary modes share the acoustic energy of the main longitudinal modes and reduce the quality factor of the whole device.

To study the mechanical performance of this device, we perform a kind of mechanical analysis by tracking the vertical displacement in the vertical direction. Figure 3.3 (c) represents the magnitude of the vertical displacement at the centre of the device, from the top surface of the ZnO layer to the Si substrate, at the frequency f_r. This analysis illustrates the longitudinal acoustic wave resonance. It can be clearly seen that half a wavelength propagates in the ZnO layer and a quarter wavelength in each layer of the mirror Bragg, with a magnitude of the displacement quickly decreasing to zero, as expected for a good acoustic Bragg mirror. On the other hand, we can also see the propagation of the acoustic wave in the bottom electrode. This can increase the effective wavelength and therefore reduces the resonance frequency, leading to a simulated resonance frequency of 2.63 GHz smaller than the frequency $f_r = 3.05$ GHz calculated from equation (A.47).

The mode shape analysis can also be seen in Figure 3.3 (d), which depicts the deformation distribution of the structure when vibrating at the resonance frequency f_r of 2.63 GHz, corresponding to the maximum deformation. This result was expected as the mechanical resonance is associated to the constructive superposition of incident and reflected acoustic waves, which amplifies the deformation of the structure. This mode shape clearly highlights the peak of the mechanical deformation at the centre of the SMR, vertically symmetric on the surface of the piezoelectric ZnO layer, suggesting that this is the desired thickness extension (longitudinal) mode and the piezoelectric layer vibrates vertically. In summary, our 2D model of the ZnO-based SMR appears in agreement with the expected result, in terms of electrical and mechanical performance.

Further studies on mechanical displacements

In order to better understand the mechanical performances of the device around its resonance, we propose to carry out a deeper analysis on mechanical displacement at and around the resonance frequency.

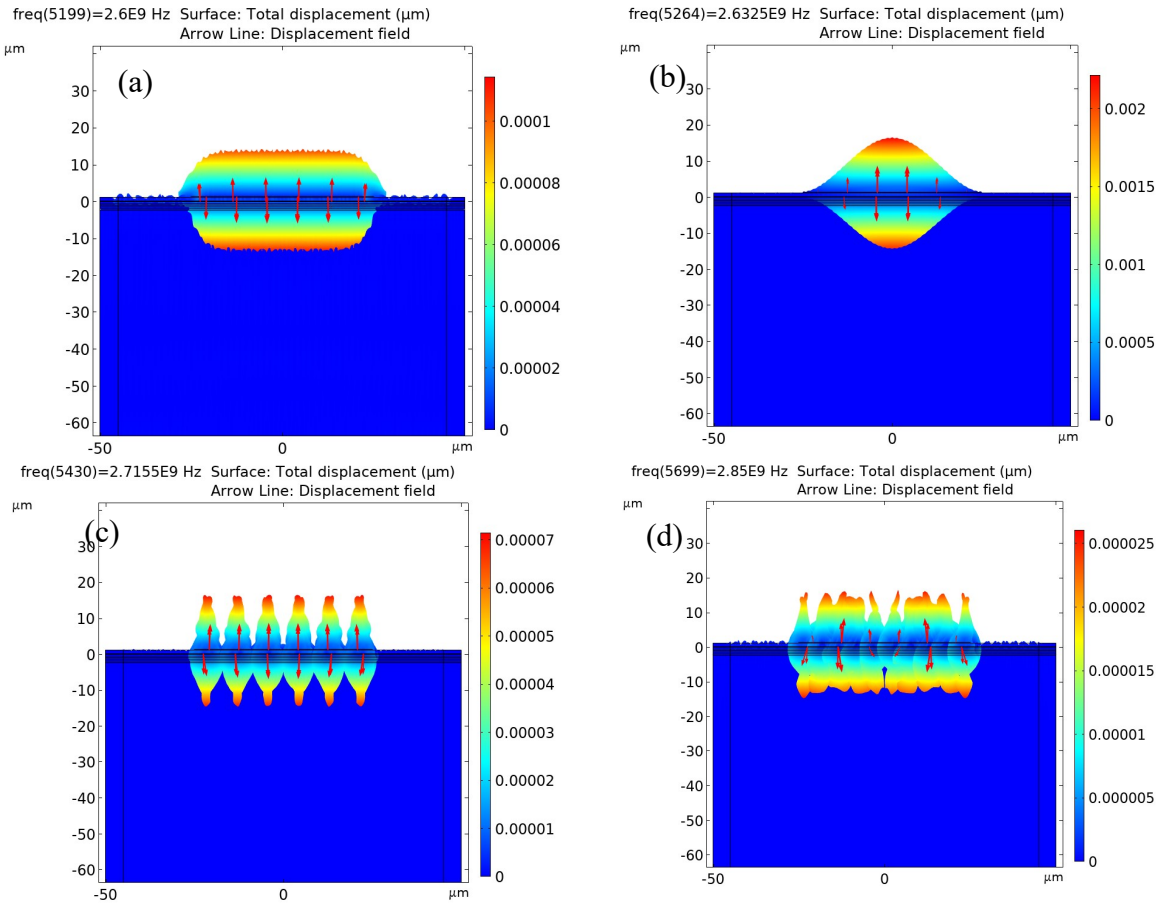

Figure 3.4 The mode shape at (a) the frequency f = 2.6000 GHz (b) the resonance frequency f_r = 2.6325 GHz; (c) the anti-resonance frequency f_a = 2.7155 GHz; (d) the frequency f = 2.8500 GHz. Red arrows indicate the direction of displacement in the vertical plane.

We focus on the mode shapes of the device at four points of frequency, as depicted in Figure 3.4. At f = 2.6000 GHz, about 30 MHz lower than the resonance frequency f_r = 2.6325 GHz, we can observe on Figure 3.4 (a) a mainly longitudinal acoustic mode with a displacement quite homogeneous and almost symmetric to the piezoelectric layer, also with

a small magnitude of maximum about 10^{-4} µm, about 20 times lower than the maximum at the resonance frequency, as depicted on Figure 3.4 (b) and Figure 3.4 (d). Red arrows slightly tilted from the vertical direction are also observed on the edges of the top electrode region. These weak lateral components are attributed to parasitic transverse acoustic modes, that also generate very small displacements out of the top electrode region. At the resonance frequency f_r = 2.6325 GHz, as in Figure 3.4 (b), the maximum displacement is achieved, with a peak of magnitude 20×10^{-6} µm at the device centre and pure longitudinal displacements as represented by vertical red arrows. When it comes to the anti-resonance frequency f_a = 2.7155 GHz, as in Figure 3.4 (c), six nodes of longitudinal acoustic modes and some lateral displacement components are observed, the mechanical displacement is down to nearly 1/30 than that of resonance frequency. At a frequency far away from anti-resonance f = 2.8500 GHz, as in Figure 3.4 (d), both lateral and longitudinal displacements become very small, the amplitude is near 1/100 than that of the resonance frequency f_r = 2.6325 GHz.

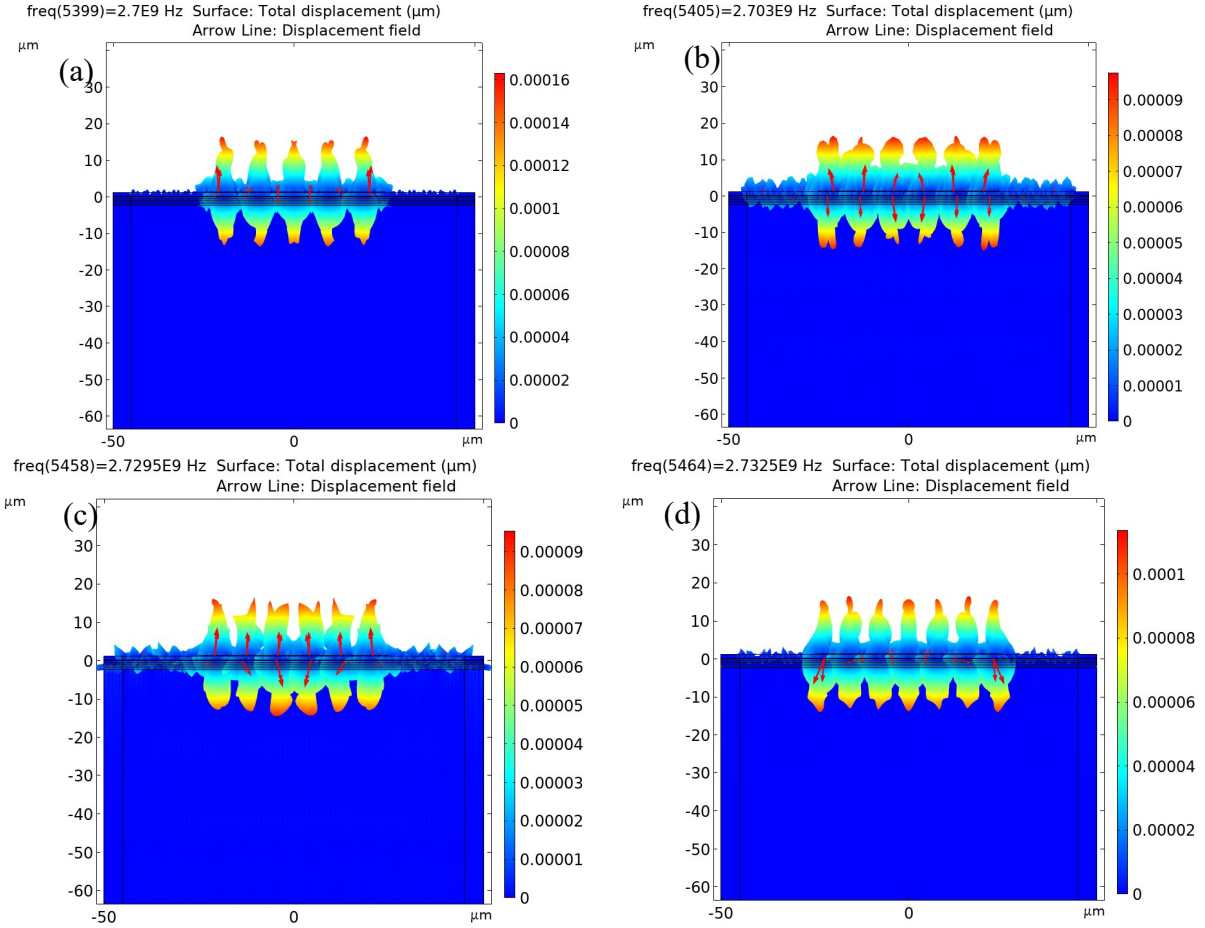

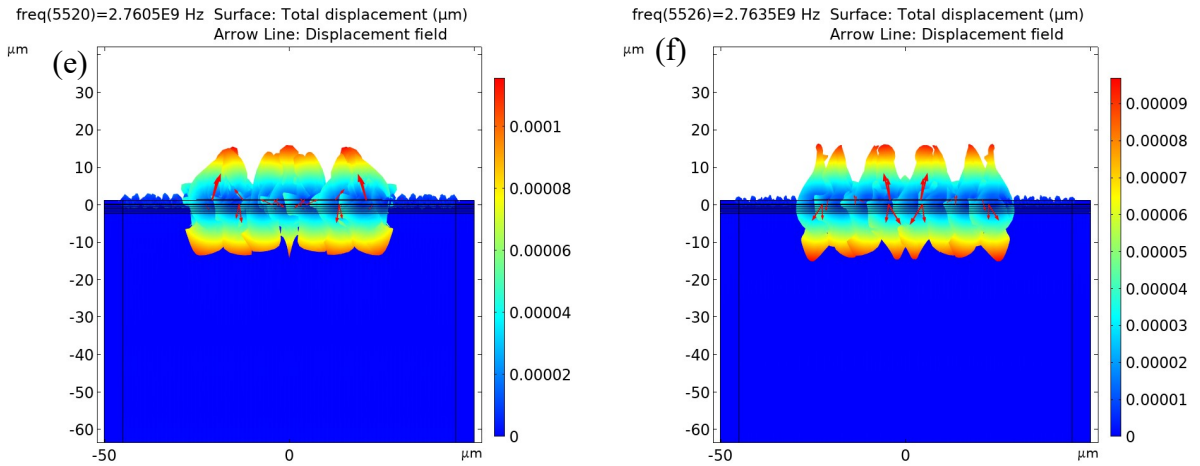

Figure 3.5 The mode shape at the frequency f of (a) 2.7000 GHz; (b) 2.7030 GHz; (c) 2.7295 GHz; (d) 2.7325 GHz; (e) 2.7605 GHz; (f) 2.7635 GHz.

As shown in Figure 3.3(a), several undesirable spurious modes are observed at and near the principal resonance, that will certainly affect the performance of devices. In this context, we perform a further analysis on such spurious modes by mode shape. As shown in Figure 3.5, 3 frequency pairs are chosen, each of them has a maximum and minimum peak: 2.7000 GHz and 2.7030 GHz; 2.7295 GHz and 2.7325 GHz; 2.7605 G Hz and 2.7635 GHz; 2.8320 GHz and 2.8350 GHz. For 2.7000 GHz and 2.7030 GHz, as shown in Figure 3.5(a) and (b), we can see some lateral components of displacement accompanying the principal longitudinal one. The maximum displacement magnitude is about 10^{-4} μm, again somewhat 20 times lower than the maximum at the resonance frequency. Some more lateral displacements are found outside the active electrode area at 2.7030 GHz. For the higher frequency spurious modes depicted on Figure 3.5(c) to (f), it can be observed more lateral components and very weak longitudinal ones, as well as small acoustic perturbation outside the active electrode area. Such behaviour could be expected from the piezoelectric structure as well as from the boundaries between active and non-active region. From this analysis, we can verify that these spurious are lateral acoustic modes.

What's more, we also performed an FEM simulation analysis to evaluate the behaviour of the acoustic Bragg mirror, the reflection and transmission coefficients as functions of the frequency are displayed on Figure 3.6.

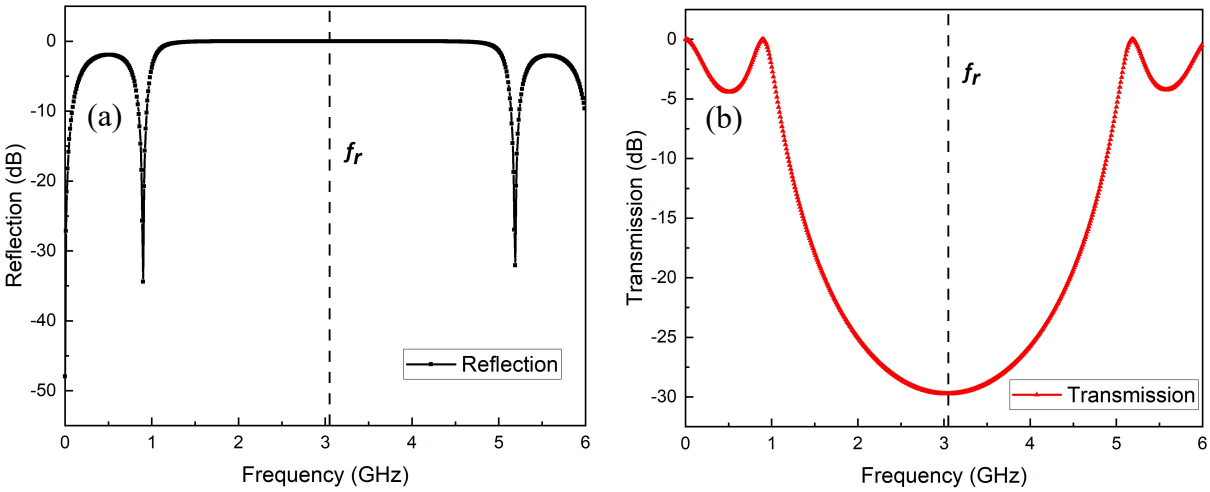

Figure 3.6 (a) Reflection and (b) Transmission coefficient of acoustic Bragg mirror in function of frequemcy.

We can see that the designed acoustic Bragg mirror exhibits good reflection properties a very good reflection from 1.3 to 4.7 GHz, as shown in Figure 3.6 (a), and the central frequency is around 3.05 GHz, the resonance frequency; for transmission coefficient, the curve shows a minimum of near -30 dB at 3.05 GHz, these two reflection and transmission coefficient curves correspond to those from the literature [188]. It is noted that the resonance frequency of 3.05 GHz differs from the same resonance frequency of 2.635 GHz resulting from the simulation of the whole device, as the initial design did not take the wave coupling in the electrodes into account, as previously explained.

Optimization of electrode shape

In Chapter 1, we presented a top electrode design with an irregular shape to blur the constructive lateral acoustic waves and reduce the effects of the spurious modes. To confirm this design, the current 2D models are no longer sufficient and we developed 3D models to perform this analysis.

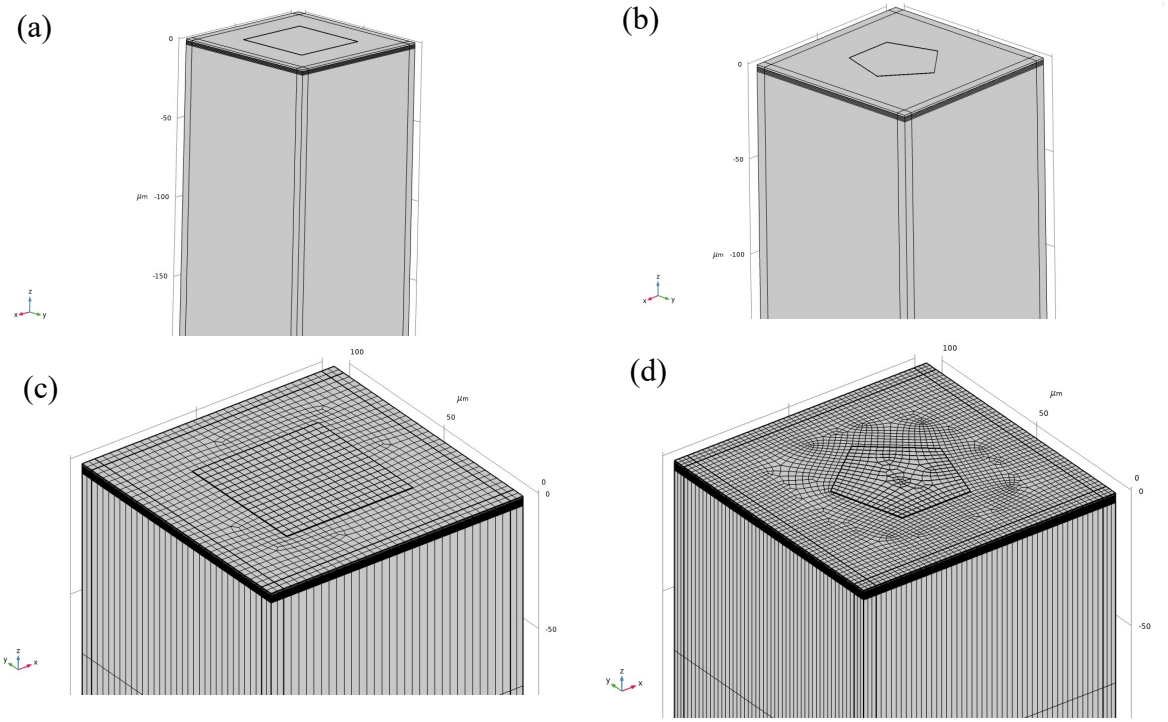

Figure 3.7 Illustration of the 3D model with (a) square top electrode and (b) pentagonal top electrode; (c, d) Respective mesh structures.

The dedicated 3-dimensional (3D) models of the SMR are described in Figure 3.7 (a) with a square top electrode and Figure 3.7 (b) with a pentagonal one. The dimensions are the same as the previous 2D model with conventional quarter-wavelength Bragg mirror. The width of each square and pentagonal top electrode is 50 µm, the Perfectly Matched Layer (PML) is added around all the boundaries of these two models.

The corresponding mesh structures of these two models are shown in Figure 3.7 (c) and (d), respectively. For the square top electrode model, which is regular and symmetric, quadrilateral elements are applied on the surfaces, hexahedral elements in the volume. For a 3D model, at least 5 elements per wavelength are required [186]. However, to save the computational effort, enough elements are applied only in the vertical direction. For example,

for the thickness of the piezoelectric ZnO layer, 3 elements are added, and for each layer of the Bragg mirror, 2 elements are added; in the lateral directions and also in the substrate, a compromise is made between the calculation time and the number of elements. The total number of elements is 30747, much more than that of the 2D model. For the pentagonal top electrode model, triangular and irregular quadrangular elements are applied especially at the surface of the top electrode and its near-by region. A similar compromise is made between the computing time and the number of elements, and because of the lower symmetry, a higher number of elements of 66978 is obtained.

The module MEMS is applied. The physics of solid mechanics and electrostatics is added, an alternating potential of 1 V is applied between the top and bottom electrodes surface, instead of the representative lines of the 2D model. The frequency ranges from 2400 to 2900 MHz, the step size is 0.5 MHz. For 3D models, the calculation time is longer, 85 h 30 min for the square top electrode model and 69 h 10 min for the pentagonal one, because the number of elements is much larger than for the 2D model and the interactions between the 3D elements are also more complex.

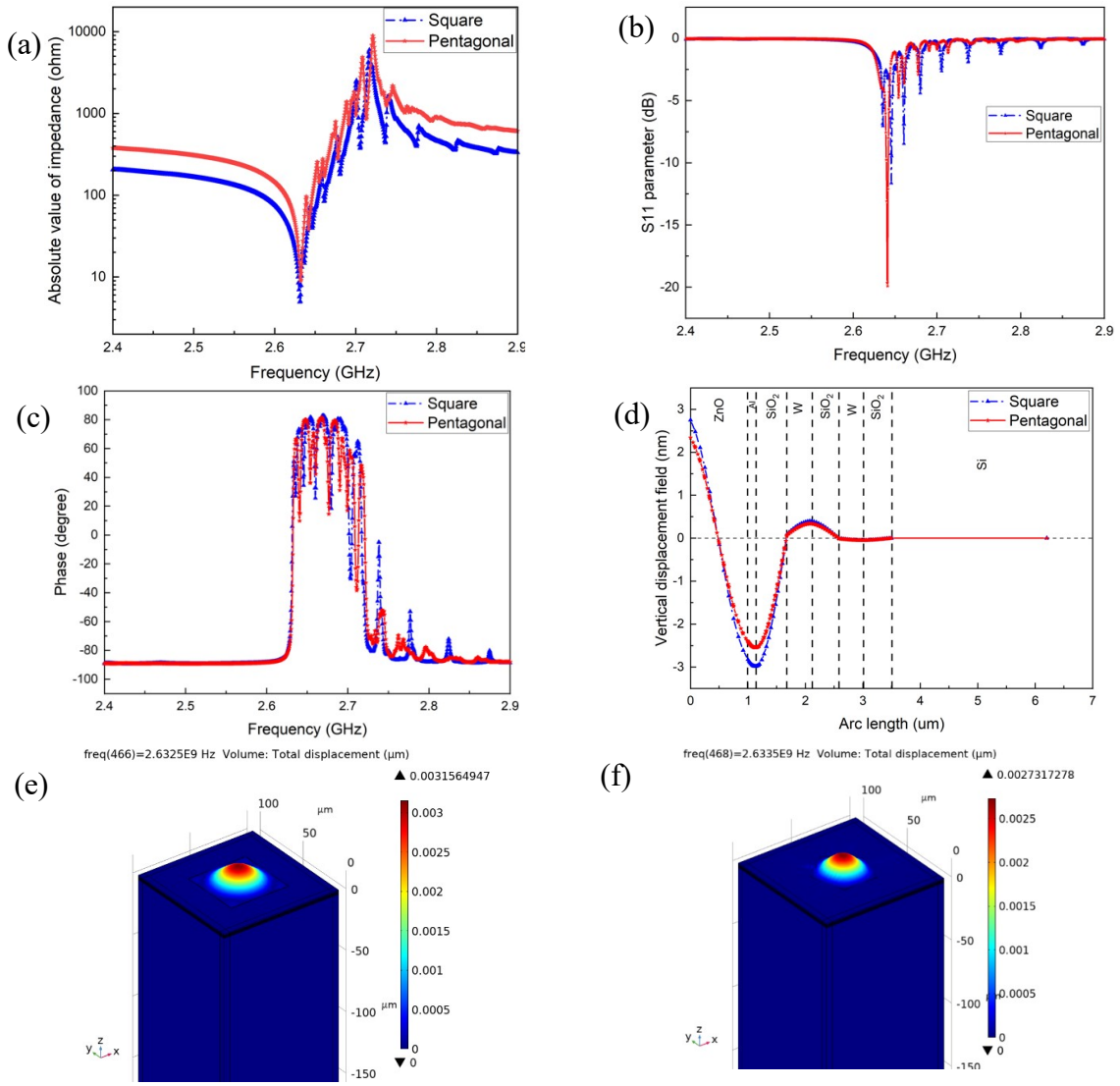

Figure 3.8 Simulated results with the 3D models, square and pentagonal top electrodes: (a) Electrical impedance magnitude; (b) Scattering parameter S11 (Reflection coefficient); (c) Impedance phase; (d) Vertical mechanical displacement at the resonance frequency f_r; Mode shape with the (e) square and (f) pentagonal top electrode at f_r.

The results of the simulation are shown in Figure 3.8. Figure 3.8(a) displays the electrical impedance curve as a function of frequency for these two models. For the square top electrode model, the minimum and maximum electrical impedances are at 2.64 GHz, resonance frequency f_r, and 2.72 GHz, anti-resonance frequency f_a, respectively. Very similar values are obtained for the model with pentagonal top electrode, 2.64 GHz and 2.73 GHz, respectively. They are in good agreement with that of the 2D model. Regarding the electrical impedance, the minimum values of both models are in the range of a few ohms and the maximum values, around 10000 ohms. They are found to be much higher than that of the 2D model, which appears to be closer to the ideal case than the 3D model in terms of electrical impedance. Finally, according to the calculation, the electromechanical coupling coefficient k_t^2 is also 7.5% for both models.

Figure 3.8 (b) illustrates the reflection parameter S_{11}. For the model with pentagonal top electrode, a main peak of -21 dB is found at 2.64 GHz, for which the matched 50 Ω impedance value is observed too, indicating a good coupling of energy to the piezoelectric device at its resonance frequency. Other peaks are far less important, indicating more reflected electrical signal, as compared to the reflection at f_r. For the square top electrode model, several peaks can be observed near the resonance with matched impedance, the major one at 2.65 GHz with a magnitude of -12.5 dB. The greater values of all these minima, close but not at f_r, compared to the pentagonal top electrode model, denote more reflected signal, but they may cause perturbations to the fundamental longitudinal acoustic mode. Based on these simulated results, the pentagonal top electrode design shows better performance with reduced spurious modes.

The circuit performance of these two models is confirmed by the impedance phase curve, as shown in Figure 3.8 (c). Though, as the spurious modes are more visible with the square top electrode at frequencies higher than the anti-resonance f_a, they appear similar for both models near the resonance f_r, and the improvement due to the design of the pentagonal shape is not very remarkable here.

The analysis of mechanical performance for these two models is shown in Figure 3.8 (d). For both models, at the resonance frequency f_r, half a wavelength propagates in the ZnO layer and a quarter wavelength in each mirror Bragg layer, and the amplitude of the displacement goes down to zero quickly. By the way, the maximum displacement for the pentagonal top electrode model is slightly smaller than that of the square one.

The mode shape of these two models are illustrated in Figure 3.8(e) and (f). A very regular arch of displacement is shown for the square top electrode model, still associated to the longitudinal acoustic resonance. A similar arch of displacement can also be observed for the pentagonal top electrode model.

In summary, the performances of 3D models of SMR show a good coherence with those of the 2D model. Furthermore, the pentagonal top electrode seems to result in better performance than the square one. This improvement in performance is attributed to a minimization of the acoustic modes generated with an irregular electrode, by reducing the horizontal standing waves.

Optimization of electrode shape with reduced 3D model

Though the previous results are interesting, it appeared that the simulation with such full 3D models is very computationally intensive. Thus, it would be of interest to use the FEM software by applying a periodic condition and then reduce the size of the model. We propose a one-fourth model for the square top electrode SMR and a one-fifth model for the pentagonal top electrode SMR.

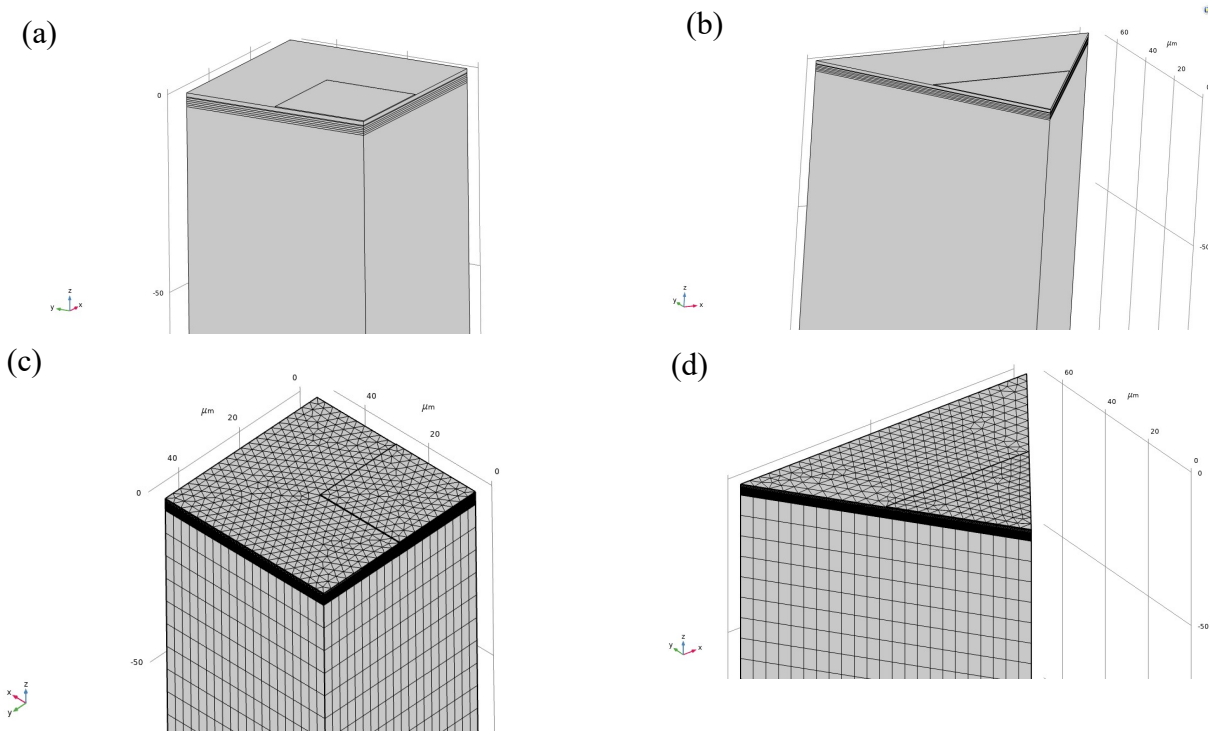

Figure 3.9 The illustration of reduced 3D model with (a) square and (b) pentagonal top electrode. The mesh structure of (c) square and (d) pentagonal top electrode model.

The created reduced 3-dimensional (3D) models are shown in Figure 3.9. In Figure 3.9 (a) and (b), the reduced models of SMR with square and pentagonal top electrode are illustrated, respectively. They are based on the previously described models, and a kind of periodic condition is applied. The periodic condition means that the model is repeated four and five times, respectively. For the one-fifth model with pentagonal top electrode, we assume that the shape of the substrate and the acoustic Bragg mirror do not affect the performance of the device.

The mesh structures of these two models are indicated in Figure 3.9 (c) and (d). Compared to the previous ones, since the model is reduced, the size of elements is set to smaller dimensions, both square and pentagonal top electrode models have triangular and irregular quadrangular elements applied on the surface, and smaller quadrilateral elements are applied on the surface of the substrate. In the vertical direction, as for the previous model, 3 elements are added in the thickness of the piezoelectric ZnO layer, and 2 elements for each layer of the Bragg mirror. Since the size of elements is smaller, the mesh resolution is enhanced in the lateral direction. The total number of elements is 66978 and 52512 for the square and pentagonal top electrode models, respectively.

The condition limits are the same as the for 3D complete models except that the periodic condition is applied, as previously introduced. The frequency still ranges from 2400

to 2900 MHz and the step size is 0.5 MHz. The computation time is 36 h 11 min for the square top electrode model and 16 h 35 min for the pentagonal one.

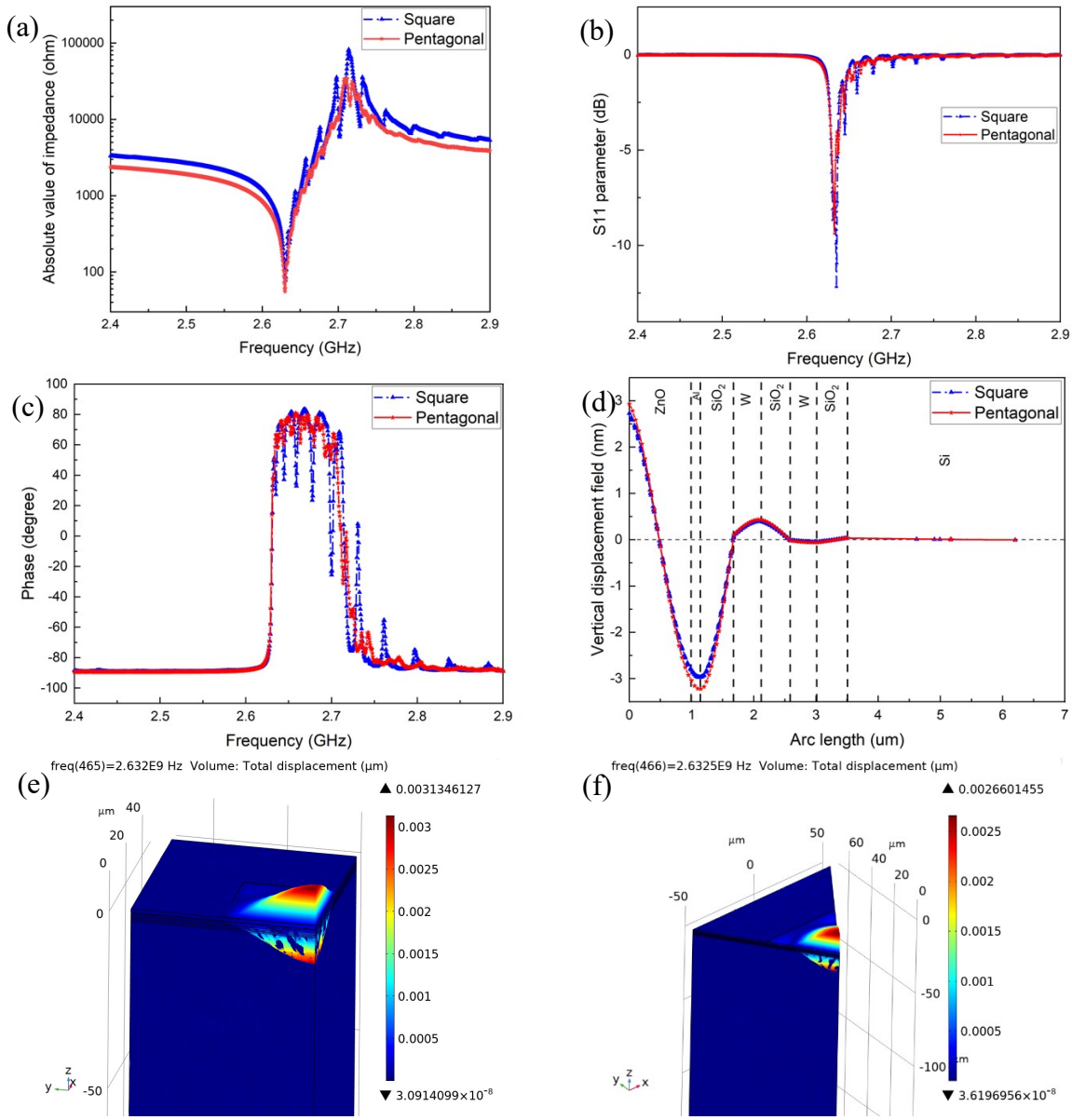

Figure 3.10 Simulated behavior of the reduced 3D models: (a) Electrical impedance; (b) Scattering parameter: Reflection coefficient S11; (c) Impedance phase; (d) Mechanical vertical displacement at the resonance frequency f_r ; Mode shape with a (e) square and (f) pentagonal top electrode at f_r.

The results of the simulation are shown in Figure 3.10. Compared to the previous complete models, the same resonance and anti-resonance frequencies are obtained. The minimum values of the electrical impedance of these two models are both in the range of a few tens of ohms at f_r (2.64 GHz) and the maximum values, a few tens of kiloohms at f_a (2.72 and 2.73 GHz for the square and pentagonal electrodes, respectively). The electromechanical coupling coefficient k_t^2 is also 7.5% for both models.

Figure 3.10 (b) shows the reflection parameter S_{11}. For the model with pentagonal top electrode, a major peak of -10 dB is found at 2.64 GHz, for which the impedance magnitude is close to the matched one of 50 Ω as it can be seen on Figure 3.10 (c), and other peaks are far less important. For the square top electrode model, a peak of -15 dB is found at 2.65 GHz, also close to the matched impedance point. Compared to the previous full models, the

reflection parameter S_{11} shows improvement for both models, and the pentagonal top electrode design still shows less spurious modes and better performance. This can result from the finer meshing in the lateral direction.

According to the impedance phase curve, as shown in Figure 3.10 (c), far less spurious modes can be also observed with the pentagonal top electrode model, with a smoother simulated curve.

The analysis of mechanical performance at the resonance frequency f_r for these two models is shown in Figure 3.10 (d). The results are close to the full model ones, with half a wavelength propagating in the ZnO layer and a quarter wavelength in each mirror Bragg layer, and similar displacements rapidly decreasing down to zero.

The mode shape of both models is illustrated in Figure 3.10 (e) and (f). It can be pointed out the whole displacement field on the vertical symmetry planes, with two 3D arch shapes in opposite direction, perpendicular to the surface of the piezoelectric ZnO layer, validating the longitudinal acoustic mode.

So far, we validate the whole design of ZnO based SMR with 2D, 3D and 3D reduced models with a very good coherence. Furthermore, we demonstrated that the pentagonal top electrode provides better performance than the square one. What's more, the applied periodic condition reduces the size of model, allowing better resolution along with greatly reduced computation time.

Modelling and simulation of $3R - MoS_2$ based SMR

Following the previous descriptions, the reference model of ZnO based SMR has been validated in a FEM environment. On this basis, the next step is to complete the design and simulation of our targeted $3R - MoS_2$ based SMR.

As discussed in Chapter 1, $3R - MoS_2$ is a novel 2D nanomaterial whose electrical and mechanical property have not been deeply explored yet. The existing studies are mainly based on density functional theory simulations (DFT), and few experimental results are reported.

We will follow the same steps as above for ZnO based SMR to complete our design of $3R - MoS_2$ based SMR and explore few references and our collaboration with NTU-CINTRA Singapore to update the mechanical and electrical properties of this study.

The declared $3R - MoS_2$ properties are synthesized below, from data in the literature.

The volumetric mass density (ρ): 5060 kg/m^3 [189]

The elastic constants matrix (GPa) [157] as following:

$$c = \begin{pmatrix} 247 & 67.7 & 32.2 & -10.7 & 0 & 0 \\ 67.7 & 247 & 32.2 & 10.7 & 0 & 0 \\ 32.2 & 32.2 & 92 & 0 & 0 & 0 \\ -10.7 & 10.7 & 0 & 38.6 & 0 & 0 \\ 0 & 0 & 0 & 0 & 38.6 & -10.7 \\ 0 & 0 & 0 & 0 & -10.7 & 89.65 \end{pmatrix} \qquad (3.7)$$

The dielectric constant matrix:[157]

$$\varepsilon^S = \begin{pmatrix} 16.3 & 0 & 0 \\ 0 & 16.3 & 0 \\ 0 & 0 & 2.6 \end{pmatrix} \quad (3.8)$$

The piezoelectric constants (pm/V):[157]

$$d = \begin{pmatrix} 0 & 0 & 0 & 0 & -4.1 & -3.6 \\ -3.6 & 3.6 & 0 & -4.1 & 0 & 0 \\ -0.21 & -0.21 & 3 & 0 & 0 & 0 \end{pmatrix} \quad (3.9)$$

The piezoelectric constants matrix e ($\mathrm{C/m^2}$):

$$e = d \cdot c = \begin{pmatrix} 0 & 0 & 0 & 0 & -0.119 & -0.278 \\ -0.601 & -0.601 & 0 & -0.081 & 0 & 0 \\ 1.670 & 1.670 & 0.598 & 0 & 0 & 0 \end{pmatrix} \quad (3.10)$$

Based on these data, we can calculate the velocity of the longitudinal "bulk" acoustic wave in $3\mathrm{R}-\mathrm{MoS_2}$ which is $v_{l,3\mathrm{R}-\mathrm{MoS_2}} = 4264.1\ \mathrm{m/s}$. The acoustic Bragg mirror is still composed of 5 alternating layers of $\mathrm{SiO_2/W}$. As described in Chapter 1, the $3\mathrm{R}-\mathrm{MoS_2}$ flakes are mechanically exfoliated from bulk on adhesive and then transferred to the target substrate. This fabrication process makes the thickness control difficult. Therefore, we perform the design with two thicknesses of 100 nm and 200 nm, which prove to be realistic in terms of large area flake (50*50 μm^2) transferred from this material, as from feedback by NTU-CINTRA Singapore team in charge of fabrication. For the 100 nm thick $3\mathrm{R}-\mathrm{MoS_2}$, the theoretical corresponding thickness of $\mathrm{SiO_2}$ and W is $t_{\mathrm{SiO_2}} = 73.6$ nm, $t_{\mathrm{W}} = 65.6$ nm, and for 200 nm thick $3\mathrm{R}-\mathrm{MoS_2}$, $t_{\mathrm{SiO_2}} = 147.2$ nm, $t_{\mathrm{W}} = 131.2$ nm, adapted to an expected frequency about 10 GHz.

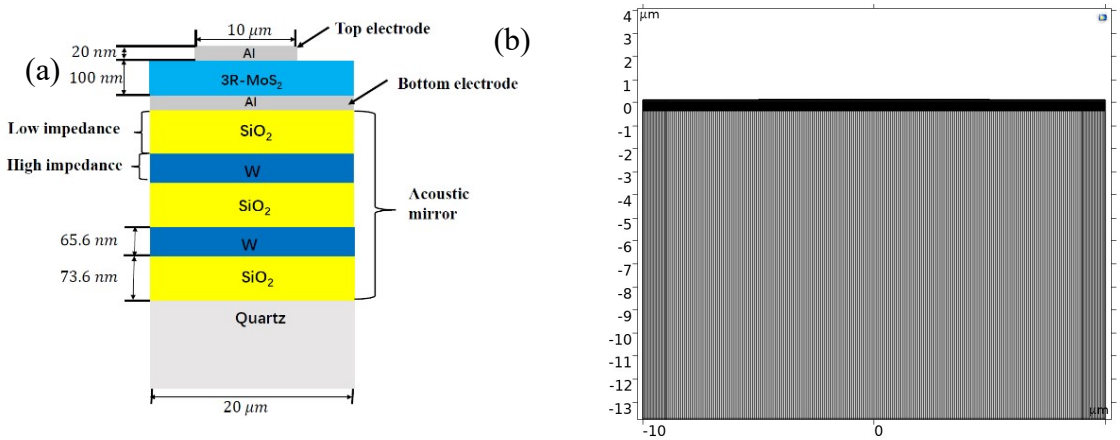

Figure 3.11 (a) Cross-section of the designed 100 nm thick 3R- MoS_2-SMR with classic acoustic Bragg mirror; (b) Mesh structure of the 2D FEM model.

For 100 nm thick $3\mathrm{R}-\mathrm{MoS_2}$ SMR, the constructed model is shown in Figure 3.11 (a). Since the transferred $3\mathrm{R}-\mathrm{MoS_2}$ flakes hardly have a large surface area, the length of the substrate is set to 20 μm and the length of the top electrode side is set to 10 μm. The substrate is made of fused quartz, which is transparent and simplifies the fabrication process at NTU Singapore. The thickness of the acoustic Bragg mirror layers is one quarter wavelength. The mesh structure is shown in Figure 3.11 (b). It is similar to the mesh of the 2D ZnO model, regular and symmetric, so that the elements are quadrangular. Since the thicknesses of the

$3R-MoS_2$ flakes are much smaller than that of the ZnO model, the resonance frequency is much higher, resulting in a much finer mesh structure. The total number of elements is 6840, and a Perfectly Matched Layer (PML) is also used. The condition limits are similar to that of 2D ZnO model, MEMS module is used, the physics of solid mechanics and electrostatics are added. A mechanical damping of 0.001 and a dielectric loss of 0.01 are added to the piezoelectric layer $3R-MoS_2$. The alternating potential of 1 V is applied between the top and bottom electrodes. The frequency ranges from 15000 to 25000 MHz, the step size is 1 MHz. The simulation takes 2 h 58 minutes.

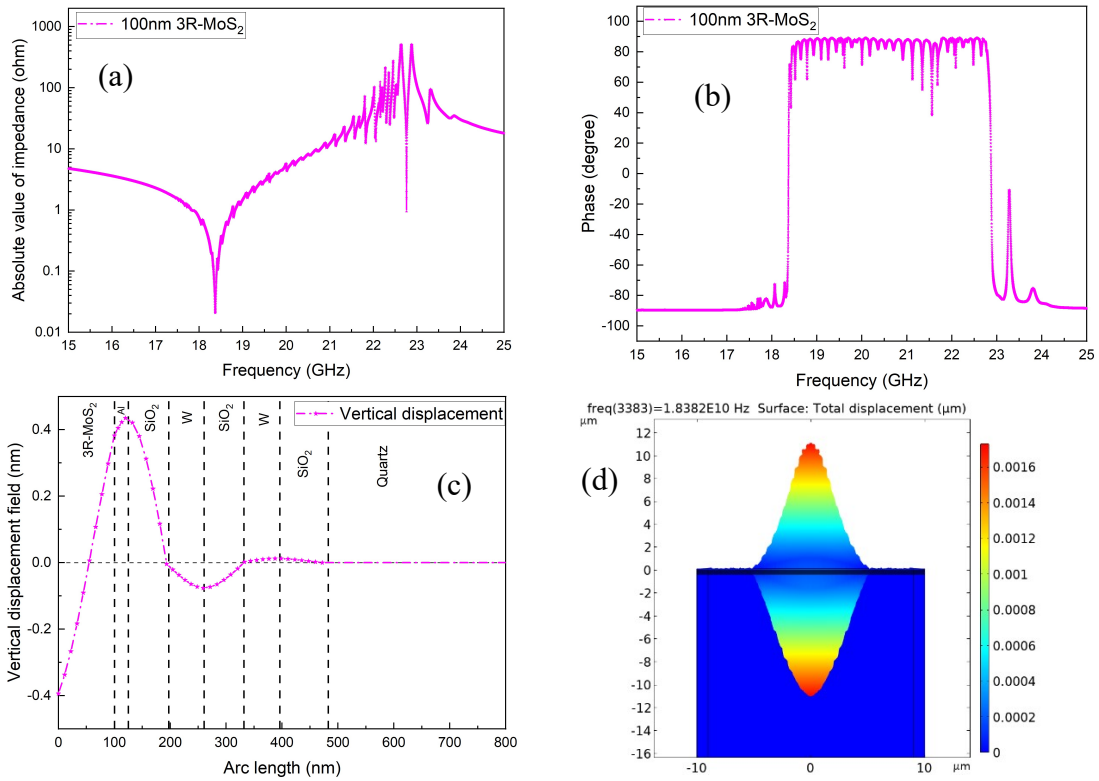

Figure 3.12 Simulated results of the 100 nm thick $3R-MoS_2$ based SMR structure with acoustic Bragg mirror (a) Electrical impedance response; (b) Phase; (c) Mechanical vertical displacement at f_r; (d) Mode shape at f_r.

The results of the simulation are shown in Figure 3.12. Figure 3.12 (a) shows the curve of the electrical impedance magnitude as a function of frequency. The minimum is observed at 18.3 GHz, resonance frequency f_r, and the maximum at 22.7 GHz, anti-resonance frequency f_a. The minimum and maximum of the electrical impedance are at 0.02 and 500 ohms, respectively. Compared to the results of the 2D ZnO model, much more spurious modes are observed and the curve is highly uneven, especially near the anti-resonance frequency f_a. The electromechanical coupling coefficient k_t^2 is calculated to be 47.8%, it suggests that $3R-MoS_2$ has a very high electromechanical coupling and thus the resonance has a large passband.

Figure 3.12 (b) shows the phase of impedance as a function of frequency. Like previously, the phase is $-90°$ out of the frequency band between the resonance frequency f_r and the anti-resonance frequency f_a, as expected from a typical capacitor made of two parallel electrodes separated by a dielectric material. From 18.3 GHz to 22.7 GHz, the phase changes to 90°, as expected from a typical BAW device. Many spurious and sharp modes are found near this frequency range. Some of them look like similar to the ones observed in the ZnO, quite regularly spaced in frequency and which have been found to correspond to higher

order longitudinal modes. However, a lot of other peaks are superimposed here, especially near f_r and f_a, which are very close to each other and sharp, making it difficult to calculate and analyze the quality factor (Q value).

The analysis of mechanical performance is also performed. The displacement field at the resonance frequency is shown in Figure 3.12 (c), which indicates the propagation of longitudinal acoustic wave in each layer. However, the displacement magnitude in the piezoelectric layer is lower compared to the results with ZnO, which may be at least partly attributed to a lower top electrode surface. Furthermore, it is not any more symmetric on both faces of this layer, as the absolute value at the interface with the bottom electrode is smaller than at the top electrode. Finally, the displacement reduces to zero along with the multi-layered Bragg mirror structure, like in previous models.

By studying the mode shape shown in Figure 3.12 (d), we can see that two main peaks of the mechanical deformation are observed at the centre of the SMR, that are vertically symmetric on the surface of the piezoelectric layer, corresponding to the desired thickness extension (longitudinal) mode. However, the overall shape of the displacement is less homogenous than in the ZnO model. This, in addition to the previous observation of many spurious modes near the resonance frequency, may suggest a mixture of longitudinal and shear modes that could explain these electrical and mechanical results. These spurious modes mainly depend on the elastic and piezoelectric properties of $3R - MoS_2$.

What's more, we also performed an analysis to evaluate the behaviour of acoustic Bragg mirror, we traced the reflection and transmission coefficient in function of frequency, as shown in Figure 3.13.

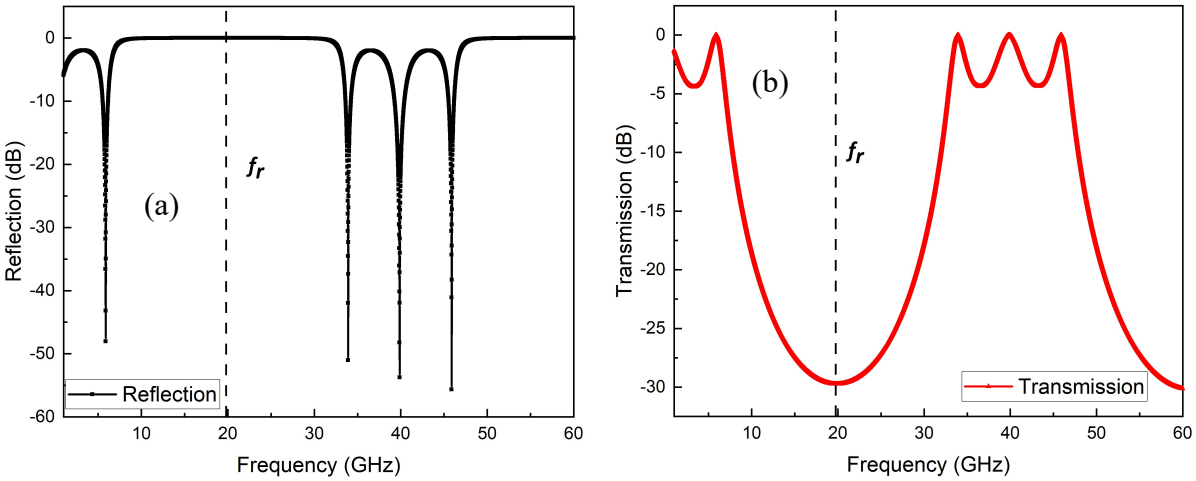

Figure 3.13 (a) Reflection and (b) Transmission coefficient of acoustic Bragg mirror in function of frequemcy.

We can see our designed acoustic Bragg mirror has a very good reflection from 5.8 – 33.9 GHz, as shown in Figure 3.13 (a), and the central frequency is around 19.9 GHz, the resonance frequency; for transmission coefficient, the curve shows a minimum of near -30 dB at 19.9 GHz, as shown in Figure 3.13 (b).

The created 2D model of the 200 nm thick $3R - MoS_2$ based SMR is shown in Figure 3.14 (a). Again, the thickness of each layer of acoustic Bragg mirror is adjusted to one-quarter wavelength, but the thickness of electrodes remains 20 nm. The mesh structure of this model is shown in Figure 3.14 (b), the same quadrangular elements are applied, the total number of elements is 6840. A Perfectly Matched Layer (PML) is also used. The condition limits are the

same as for the other 2D models, the physics of solid mechanics and electrostatics are added. The same mechanical damping of 0.001 and dielectric loss of 0.01 are also added to the piezoelectric layer of $3R-MoS_2$. The frequency ranges from 5000 to 15000 MHz, the step size is 1 MHz, the calculation time is 2 h 19 minutes.

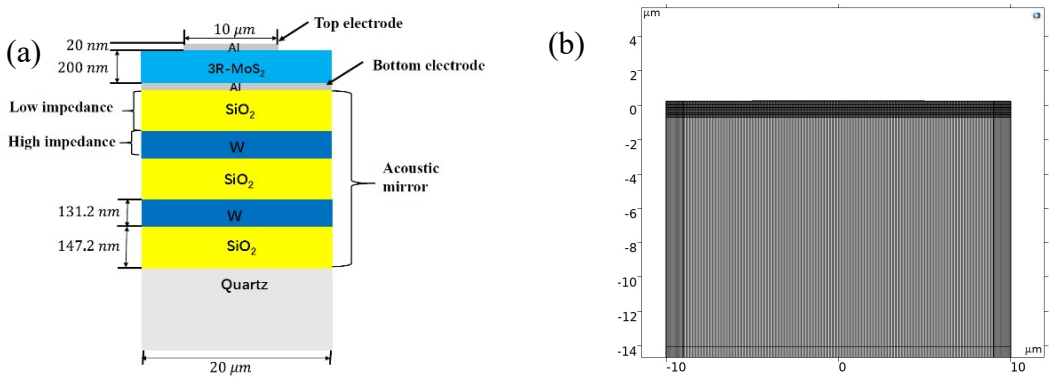

Figure 3.14 (a) Cross-section of the 300 nm $3R-MoS_2$ SMR with non-conventional acoustic Bragg mirror; (b) Mesh structure of the 2D FEM model.

The results of the simulation are shown in Figure 3.15. From the Figure 3.15 (a) with the curve of the electrical impedance as a function of frequency, the minimum of the electrical impedance is observed at 9.9 GHz, resonance frequency f_r, and the maximum at 12.3 GHz, anti-resonance frequency f_a. The minimum and maximum of the electrical impedance are at 0.085 and 1400 ohms, respectively. As for the 100 nm thick $3R-MoS_2$ model, the curve is uneven and many spurious modes are observed. The electromechanical coupling coefficient k_t^2 is calculated to be 48.1%.

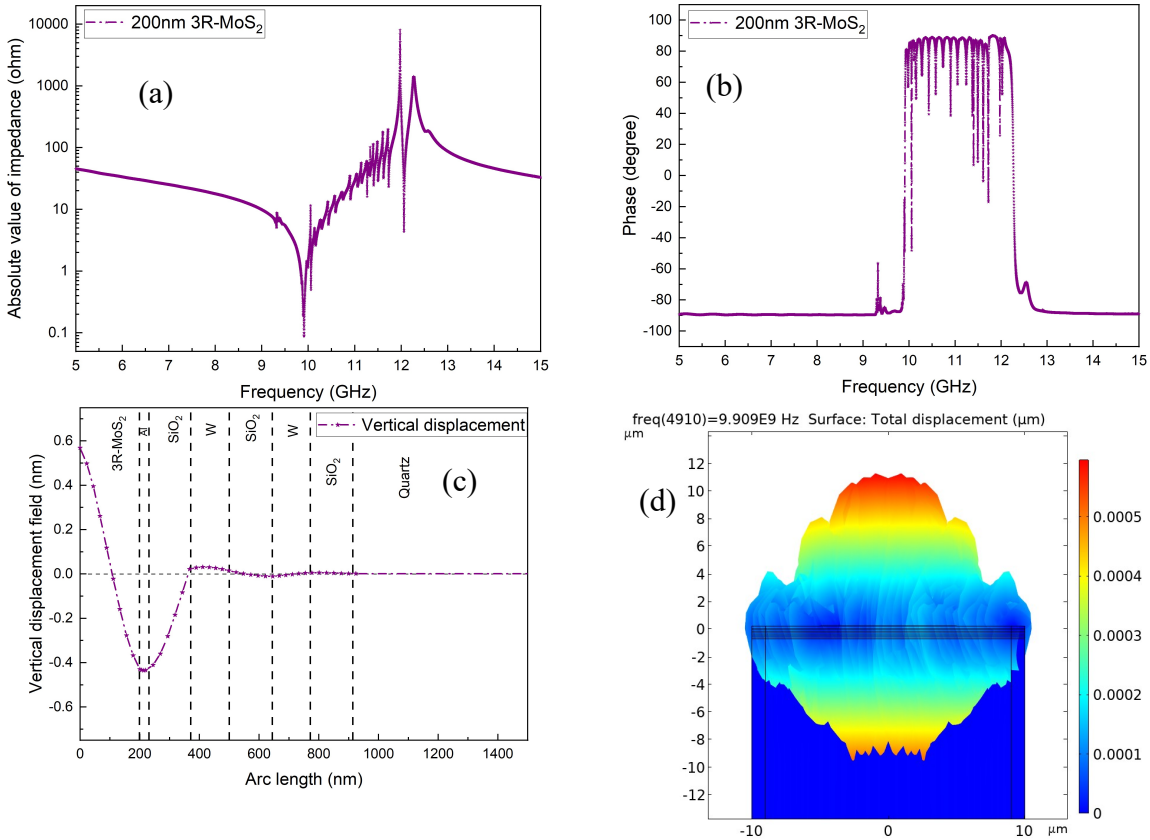

Figure 3.15 Simulated results of the 200 nm thick 3R- MoS_2-based SMR structure with acoustic Bragg mirror (a) Electrical impedance; (b) Impedance phase; (c) Mechanical vertical displacement at f_r; (d) Mode shape at f_r.

Figure 3.15 (b) shows the phase of impedance as a function of frequency. Again, the curve exhibits many spurious modes, even more remarkable than that of the 100 nm thick $3R - MoS_2$ model.

The same analysis of mechanical performance is performed. From the displacement field analysis, as shown in Figure 3.15 (c), the propagation of longitudinal waves can be clearly observed in each layer, and is less symmetric on both faces of the piezoelectric layer, compared to the 100 nm thick $3R - MoS_2$ model. From the mode shape, shown in Figure 3.15 (d), the two vertically symmetric peaks confirm the existence of thickness extension (longitudinal) acoustic mode, but spurious modes are still visible and cannot be neglected.

We also performed an analysis to evaluate the behaviour of acoustic Bragg mirror, we traced the reflection and transmission coefficient in function of frequency, as shown in Figure 3.16.

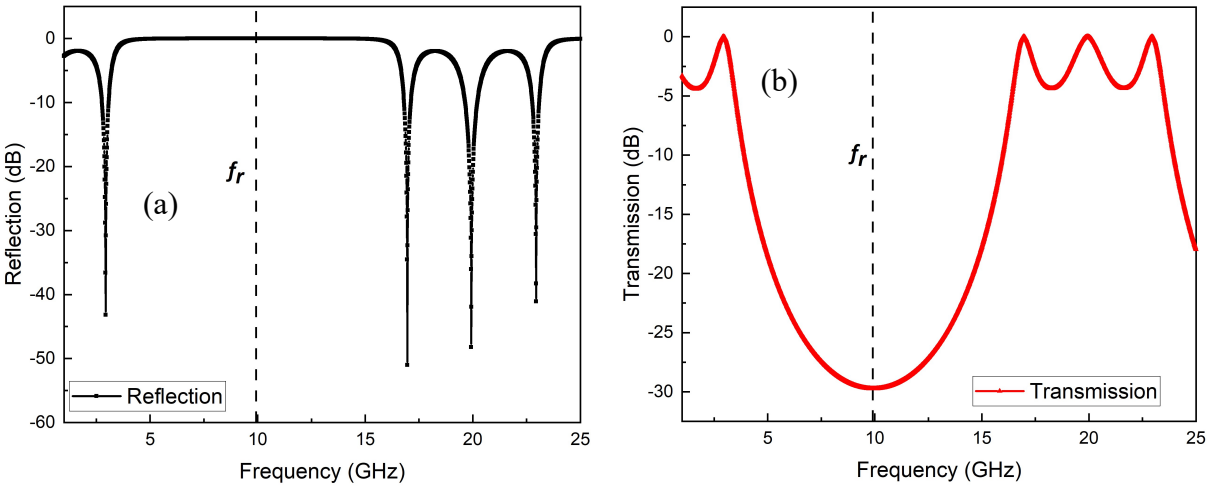

Figure 3.16 (a) Reflection and (b) Transmission coefficient of acoustic Bragg mirror in function of frequemcy.

We can see our designed acoustic Bragg mirror has a very good reflection from 2.9 – 16.9 GHz, as shown in Figure 3.16 (a), and the central frequency is around 9.9 GHz, the resonance frequency; for transmission coefficient, the curve shows a minimum of near -30 dB at 9.9 GHz, as shown in Figure 3.16 (b).

2. Dispersion Curve

Apart from the previous simulation and as presented in Chapter 2, the dispersion curve is also a powerful tool to study the propagating acoustic modes. The condition limits are the same as for the other 2D models, the physics of solid mechanics and electrostatics are added. The frequency ranges from 1 to 4000 MHz, the step size is 1 MHz, the calculation time is about 3 h.

The simulation results are illustrated in Figure 3.15. Several acoustic modes are visible. As described in the Chapter 2, ZnO is a type-2 piezoelectric material, and the cut-off frequency, at which the acoustic modes start, of the thickness extensional (TE1) mode is higher than the thickness shear (TS2) mode. We can observe for this model the one cut-off frequency at near 2.63 GHz, which is the resonance frequency of longitudinal acoustic mode described. Another cut-off frequency is observed at near 2.15 GHz, it should to be the second-

order thickness shear (TS2) mode, according to shear wave velocity of ZnO, but the identification of acoustic mode should be performed. And then another cut-off frequency with much smaller intensity is observed near 1.25 GHz, which is supposed to be the first order thickness shear (TS1) mode. Beside these dominant acoustic modes, other ones with small intensity can also be observed, which refers to the spurious modes discussed before.

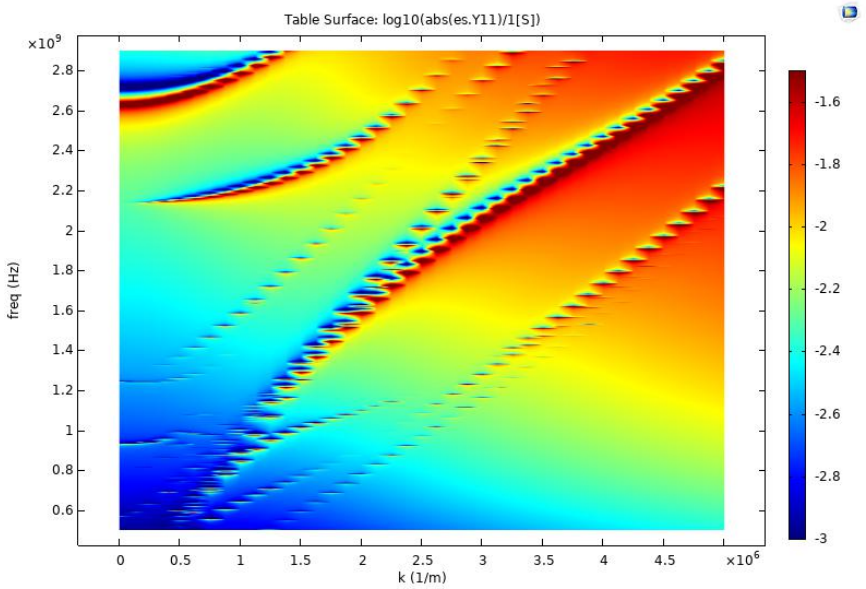

Figure 3.17 Dispersion curve of the ZnO based SMR.

This analysis shows the possibility of performing the dispersion curve analysis of our designed SMR. The longitudinal acoustic mode is approved by this analysis, the appearing spurious modes are also confirmed, however the calculation time remains long.

While this analysis could be used to better analyze the various modes, it has been difficult to perform on the $3R - MoS_2$ thin flakes model, probably due to the great number of parasitic modes, and it has not been carried out at this point.

3. Butterworth-Van Dyke (BVD) model

As pointed out in Chapter 2, in addition to analytical solutions and FEM simulation, the Butterworth-Van Dyke (BVD) equivalent circuit model is also a common method to perform FBAR design and simulation. Such model has been investigated for the ZnO and the $3R-MoS_2$ based structures as defined above. The resonance of the longitudinal acoustic mode has been introduced, as well as the ohmic losses caused by the electrodes. However, the BVD model cannot describe the effects of the acoustic Bragg mirror and of spurious modes.

BVD model of the ZnO-based structure

We first perform the BVD model of the ZnO based structure, based on the equations (2.50), (2.51), (2.52) and (2.53). The needed parameters are listed in Table 3.2. The k_t^2 coefficient results from the FEM simulation presented above.

Table 3.2 Main parameters to calculate the lumped elements of the BVD equivalent circuit model of the ZnO based FBAR

Material parameters (ZnO)	Values
h	0.5 µm
ε_r	12.64
A	400 μm^2
k_t^2	7.5%
ρ	5680 kg/m^3
v_l	6097.1 m/s

The resulting values of lumped elements are listed in Table 3.3. The simulations are performed by using ADS (Agilent Advanced Design System) and is shown in Figure 3.18. Two models are designed, without and with the electrode losses. The circuit shown in Figure 3.18 represents the model without electrode losses ($R_s = R_0 = 0\ \Omega$). For the model with electrode losses, the losses are set to be 5 Ω ($R_s = R_0 = 5\ \Omega$). The frequency ranges from 1 to 5 GHz, the step size is 0.5 MHz, the simulation takes around 30 s.

Table 3.3 Lumped elements of the BVD model for the ZnO-based FBAR

Elements	Values
C_0	0.2798 pF
C_m	17.236 fF
L_m	158.1 nH
R_m	0.874 Ω

The simulation results are illustrated in Figure 3.19. Figure 3.19 (a) shows S_{11} parameter of two models, with a resonance near 3.05 GHz, similar without and with electrode losses. This value is almost the same as calculated from equation (2.58), which is the ideal value without taking into account the wave propagation in the electrodes. The return loss is of about – 0.34 dB and – 2.1 dB without and with the parasite resistance, respectively. Furthermore, the parasite resistance causes losses over the full frequency range. For example, the return loss reaches – 0.55 dB at 5 GHz in this case for a resistance of 5 Ω. These return losses calculated with the BVD model are not the same as those from the FEM simulation.

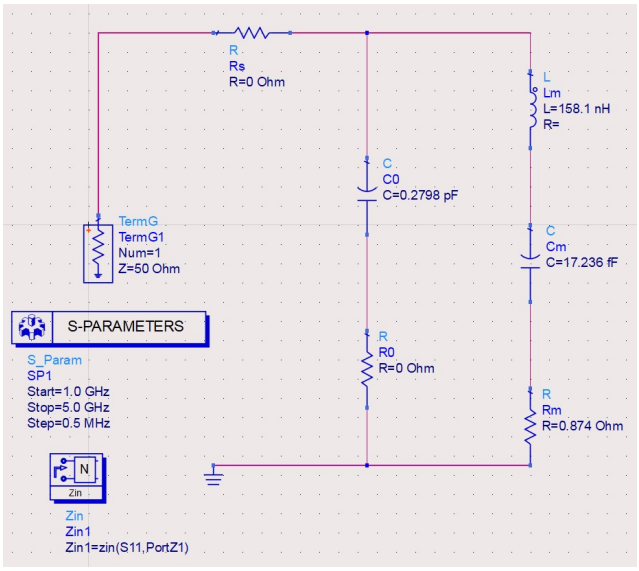

Figure 3.18 Circuit Structure of ZnO FBAR model in ADS software

Figure 3.19 (b) shows electrical impedance of two models, with a resonance near 3.05 GHz, similar without and with electrode losses. For both two models, we can see that a minimum of impedance occurs at resonance frequency near 3.05 GHz, and a maximum occurs at anti-resonance frequency near 3.14 GHz. For the model without parasite resistances, the minimum is around 0.9 ohms and the maximum is around 36000 ohms. For the model with parasite resistances, the minimum is around 6 ohms and the maximum is around 5600 ohms.

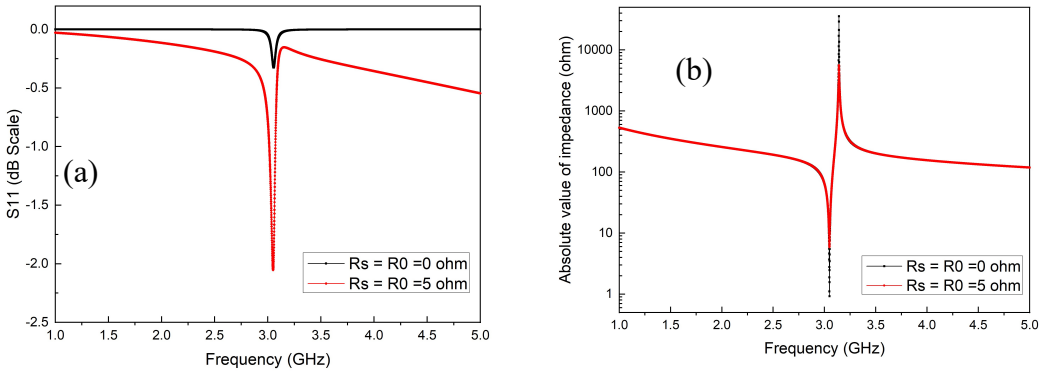

Figure 3.19 Simulation results of the BVD model of the ZnO-based FBAR from ADS without and with parasite resistances (a) S_{11} parameter; (b) Electrical Impedance.

BVD model of the 3R − MoS_2 -based structure

The same approach has been applied to perform the analysis for 3R − MoS_2 based models. The parameters are listed in Table 3.4, the k_t^2 results from the FEM simulation.

Table 3.4 Main parameters to calculate the lumped elements of BVD model of the 3R − MoS_2 based FBARs

Material parameters (3R − MoS_2)	Values
h_1	50 nm
h_2	100 nm
ε_r	2.6
A	100 µm^2
k_t^2	48%

ρ	5060 kg/m^3
v_l	4264.1 m/s

By the way, we calculate values of the lumped elements of the equivalent circuits for 210 and 300 nm thick (respectively 2*h_1 and 2*h_2) $3R-MoS_2$ based models, these values (respectively (1) and (2)) are shown in Table 3.5.

Table 3.5 Lumped elements of BVD model for the $3R-MoS_2$ based FBARs

Elements	Values (1), $2h_1 = 100\ nm$	Values (2), $2h_1 = 200\ nm$
C_0	0.02302 pF	0.01151 pF
C_m	8.9566 fF	4.4783 fF
L_m	6.2215 nH	49.773 nH
R_m	12.1352 Ω	24.271 Ω

The proposed circuit is shown in Figure 3.20 (a) and (b). Two types of models are designed, without and one with the electrode losses, by setting respectively $R_s = R_0 = 0\ \Omega$ as represented on Figure 3.20, and $R_s = R_0 = 5\ \Omega$, with which the simulation shows the similar phenomena as ZnO model.

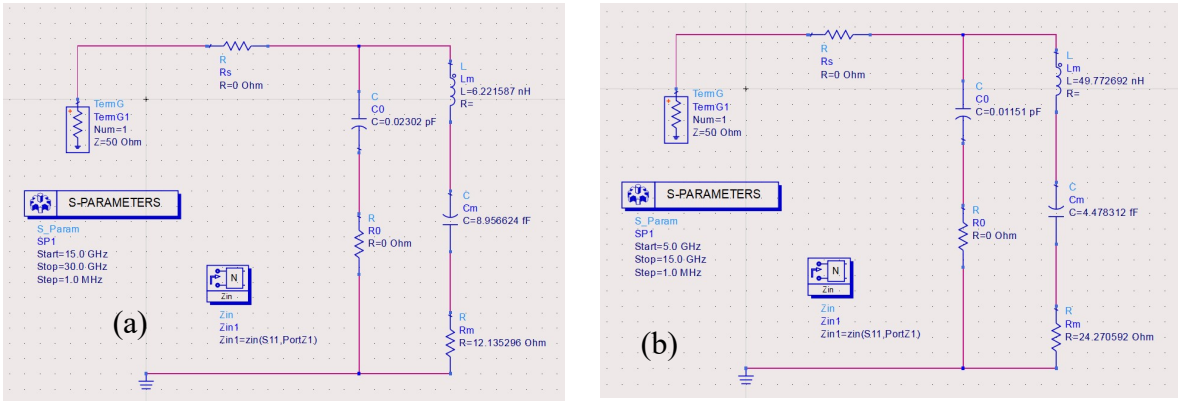

Figure 3.20 Circuit Structure of (a) 100 nm and (b) 200 nm thick $3R-MoS_2$ FBAR model in ADS software without parasite resistances ($R_s = R_0 = 0\ \Omega$).

The simulation results are presented in Figure 3.21. Figure 3.21 (a) and (b) show S_{11} parameter of these two thicknesses $3R-MoS_2$ based FBAR. For the 100 nm thick $3R-MoS_2$ based FBAR model with and without parasite resistances, we can observe a resonance at near 21.4 GHz with a return loss of -4.45 dB for no parasite resistance structure. For the model with parasite resistances, the resonance occurs nearly at the same frequency and the return loss is around -6.3 dB. The added parasite resistances also induce more losses, the return loss reaches -0.14 dB at 30 GHz. For the 200 nm thick $3R-MoS_2$ based model, the simulated results show a resonance at near 10.6 GHz with a return loss of -9.22 dB for no parasite resistance structure. With parasite resistances, the return loss is around -11.7 dB at the same frequency and the return loss reaches -0.015 dB at 15 GHz.

Figure 3.21 (c) and (d) show electrical impedance of these two thicknesses $3R-MoS_2$ based FBAR. For the 100 nm thick $3R-MoS_2$ based FBAR model with and without parasite resistances, we can observe that a minimum of impedance occurs at resonance frequency near 21.4 GHz, and a maximum occurs at anti-resonance frequency near 25.1 GHz. For the model without parasite resistances, the minimum is around 12 ohms and the maximum is around 6500 ohms. For the model with parasite resistances, the minimum is around 17 ohms and the maximum is around 4400 ohms. For the 200 nm thick $3R-MoS_2$ based FBAR model with

and without parasite resistances, we can observe that a minimum of impedance occurs at resonance frequency near 10.6 GHz, and a maximum occurs at anti-resonance frequency near 12.5 GHz. For the model without parasite resistances, the minimum is around 74 ohms and the maximum is around 50000 ohms. For the model with parasite resistances, the minimum is around 79 ohms and the maximum is around 41400 ohms.

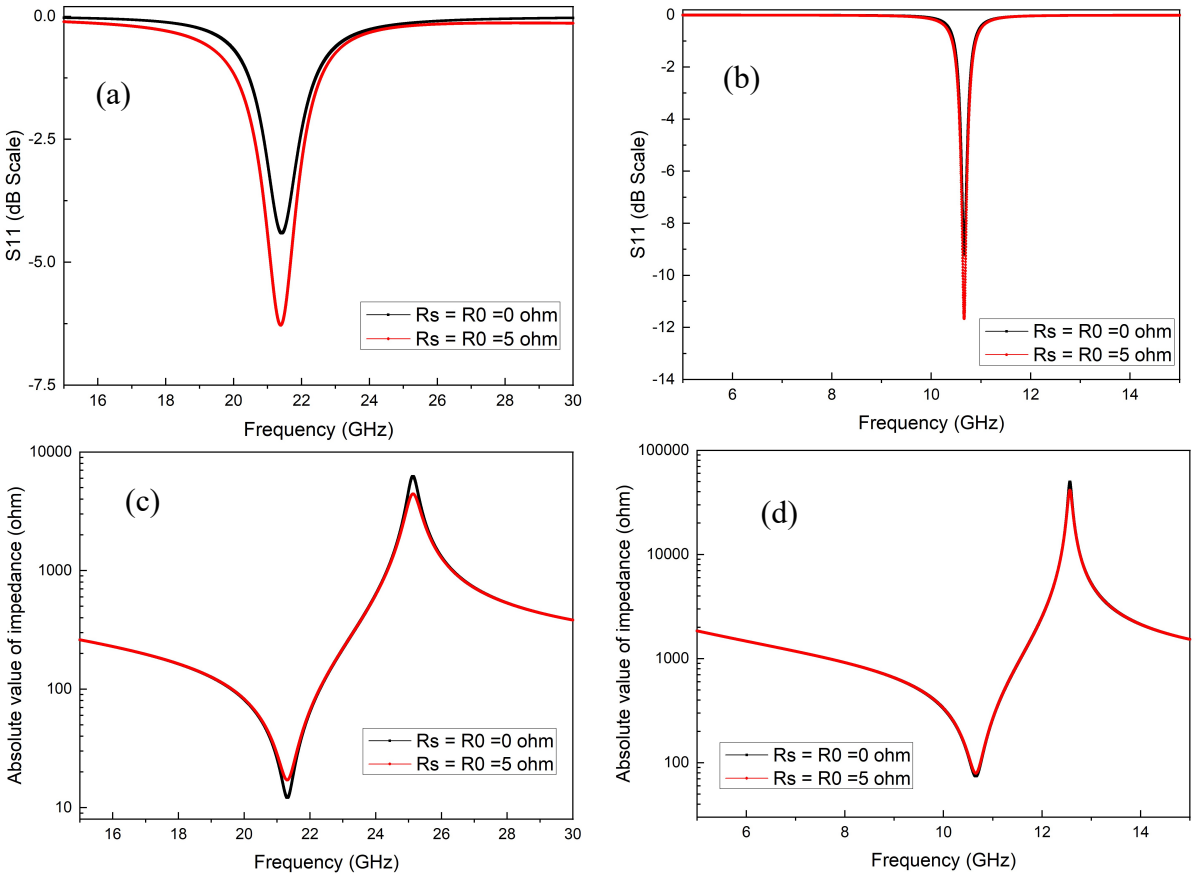

Figure 3.21 Simulation results of the BVD models of the (a) 100 nm and (b) 200 nm thick $3R-MoS_2$ FBAR S_{11} parameter; (c) and (d) Electrical Impedance.

In summary, the BVD model analysis shows some differences with FEM simulation results, especially for the resonance frequency. A further study on this behaviour will be given in Chapter 4. The BVD model simulation has a very important advantage in the efficiency of simulation, the impacts brought by the losses of electrodes can be easily simulated. However, the BVD model can only realise the simulation of the fundamental longitudinal acoustic wave mode, the other spurious modes are not visible by this simple model. To better understand the propagation of acoustic wave in such structure, FEM analysis is still more powerful A further study based on the characterization of $3R-MoS_2$ based prototypes will be given in Chapter 4.

4. The design of RF characterization set-up

Previously, we have proposed a design of the core of the FBAR/SMR device, 100 nm thick 3R − MoS_2 flakes based SMR device is the target one for the following process, which shows good simulation results. The target frequency of RF characterization set-up is 20 GHz, and the acoustic Bragg mirror is SiO_2 and W is t_{SiO_2} = 73.6 nm, t_W = 65.6 nm, the substrate is 500 μm fused quartz.

However, electrical characterization needs to consider suitable electrical connections within the whole design. This consists of matched access to 50 Ω for operation at GHz frequencies, also with pads compatible with commercial ground-signal-ground (GSG) probes. Considering the size of our device, a probe of 150 μm pitch size is chosen, the design is completed by using ADS LineCalc, with coplanar waveguide (CPW) planar transmission lines.

The CPW port is designed to be deposited on a fused quartz substrate with a relative permittivity ε_r of 3.78 [190] and a thickness h of 500 μm. The metal of the CPW transmission lines is the same as the electrodes of the SMR, Aluminum, with a thickness of 1 μm. This transmission line was designed to get an impedance matching of 50 Ω. An impedance of 55 Ω at 20 GHz could be obtained with a width of the signal access line of 125 μm, a spacing of 20 μm with the ground plan and a length of transmission line set to 200 μm, as shown in Figure 3.22 (a). The final design of the device with the CPW port is shown on Figure 3.22 (b).

By using the circuit on Figure 3.22 (c) in ADS software and a matched environment with two impedances of 50 Ω, we performed two-port simulation of the S parameters of the proposed CPW line over the frequency range from 1 to 70 GHz with a step size of 0.5 GHz.

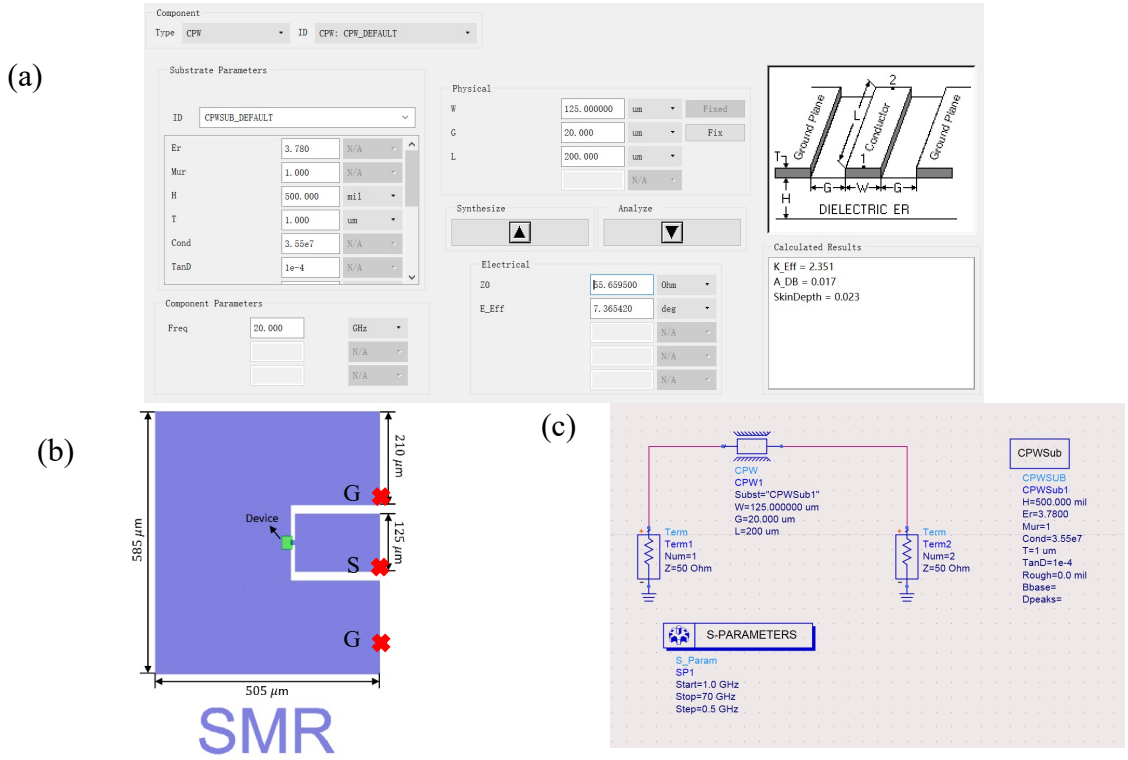

Figure 3.22 (a) Parameters of the CPW-type access lines and the calculated impedance (ADS LineCalc screen); (b) Mask structure of the SMR device with CPW access; (c) Circuit for simulation in ADS of the access lines impedance.

The simulation results are illustrated in Figure 3.23. The reflection parameter S_{11} of this transmission line, shown in Figure 3.23 (a), exhibits a low value near -60 dB at 1 GHz, which means that only 0.0001% of the electrical energy is reflected, the major part being transmitted as confirmed by the S_{21} parameter near 0 dB (transmission almost 100 %) on Figure 3.23 (b). Then, the S_{11} parameter increases slowly and at 70 GHz, a value near -27.5 dB is obtained, corresponding to about 0.18 % of electrical energy reflected, while the S_{21} parameter decreases near -0.05 dB (99 % electrical energy transmitted).

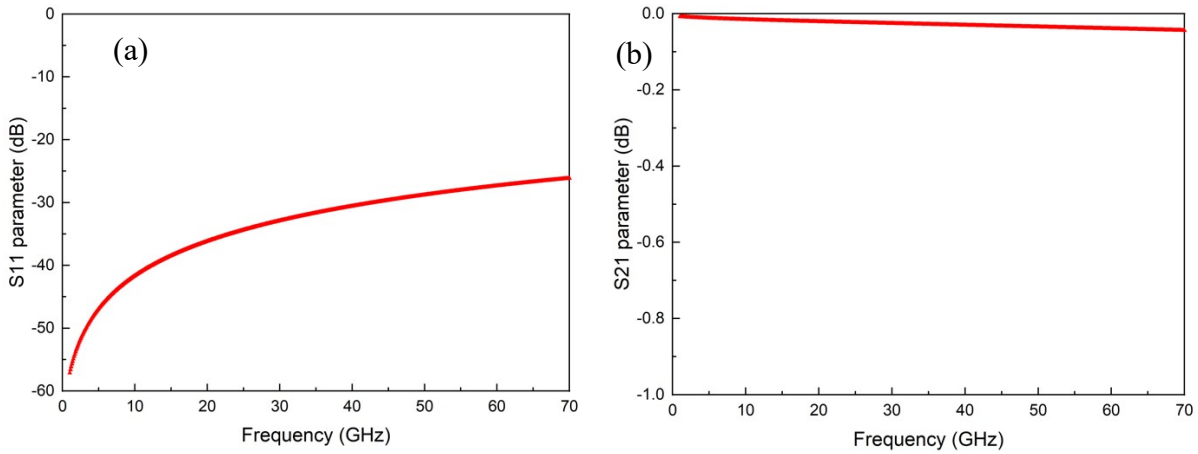

Figure 3.23 Simulation results of the S parameter of the CPW access lines with ADS (a) Reflection parameter S_{11}, (b) Transmission parameter S_{21} parameter.

At 20 GHz, near the operating frequency of our designed SMR, S_{11} and S_{21} parameters of near -36 dB and -0.02 dB are obtained, respectively, which means that near 0.025 % electrical energy is reflected and over 99 % of electrical energy is transmitted by the CPW line, in matched conditions.

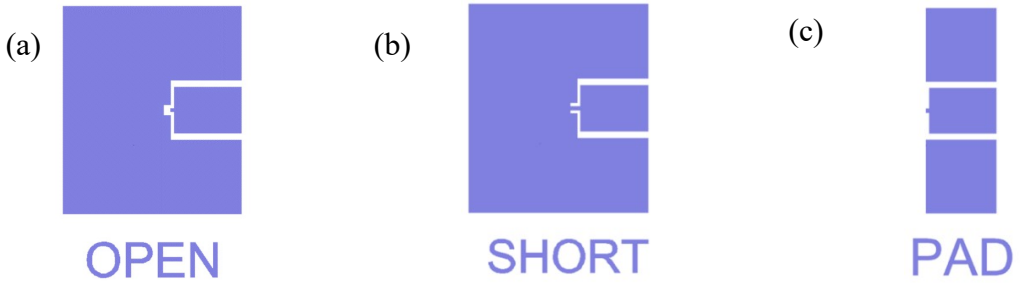

Figure 3.24 De-embedding structure composed of (a) Open, (b) Short and (c) Pad calibration circuits.

Though good performance of the designed CPW port characterization, we cannot neglect the parasite capacitors, inductors and ohmic losses created between the signal and ground plan, especially at frequencies over 10 GHz. To remove these parasite electrical modes and ensure a calibration at the nearest of the SMR device itself, a kind of "Open-Short" de-embedding process is proposed [191], another "Pad" structure is added to verifier "Open", which should show a higher capacitance. In this perspective, three additional Open, Short and Pad patterns have been designed, based on the same CPW structure, as shown in Figure 3.24. A De-embedding process will be performed on the whole device using the measurements with these three individual characterization structures to extract the electrical characteristics of the bare SMR device. A homemade Python program is proposed to perform this numerical processing.

5. Mask design

After validation of the geometry of the coplanar accesses, the next step consists in carrying out the design of the mask, in close collaboration with the NTU-CINTRA team to launch the fabrication of the SMR on a 5-inch fused quartz wafer as substrate.

A representative part of the mask design is shown in Figure 3.25. It contains the different fabrication step layers and 9 devices for each pattern. The final manufacturing process and thus mask design, was obtained after 7 iterations on the geometry of the SMRs and access ports.

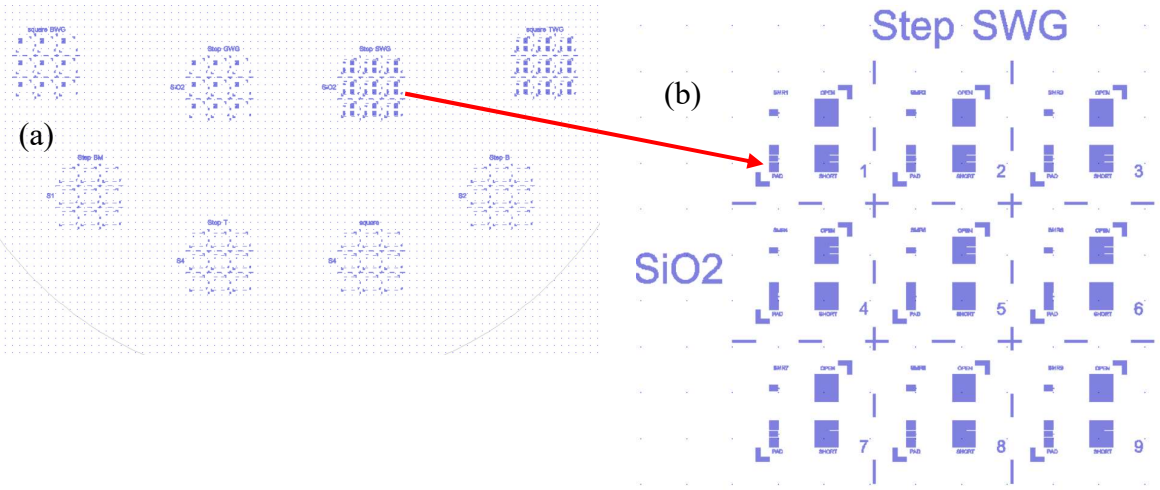

Figure 3.25 (a) General half-view of the designed mask, and (b) a zoom of one bloc

In the next chapter, we will discuss the fabrication and the characterization details.

Summary

In this chapter, we proposed the whole process of SMR development based on the theories developed in Chapter 2. Before performing the design of our target $3R-MoS_2$ based SMR, we first proposed the design of a ZnO -based SMR as a reference to validate the design and the theories. So, we first designed a SMR based on a 1µm thick ZnO film with conventional quarter wavelength and optimized acoustic Bragg mirror. By starting the simulation in a FEM environment with a 2D model, we validated the design of the ZnO -based SMR, which exhibited similar resonance performance as described in the literature.

The simulation of irregularly shaped top electrodes led to propose 3D models. Square and pentagonal top electrodes could then be considered. The improvement with the pentagonal top electrode is significant, less spurious modes are observed. However, the computational time is very important. To limit it, we proposed reduced-size models by applying a kind of periodic condition and decomposing the model for the square and pentagonal top electrode models into a quarter and a fifth, respectively. The saved computational effort enables a finer mesh structure and thus more precise results.

The same approach was then applied to perform out the design of the target $3R-MoS_2$ -based SMR. However, since the thickness of $3R-MoS_2$ flakes is only a few hundred nanometers, the size of the elements should be set much smaller than that of the reference model, leading to a too large number of elements for 3D models compared to the current computational capacity. Thus, the simulation of $3R-MoS_2$ based SMR was carried out with the 2D model. The simulation results show a resonance near 20 GHz for different thicknesses of $3R-MoS_2$, the longitudinal acoustic mode is confirmed.

An analysis based on a Butterworth-Van Dyke (BVD) equivalent circuit model was also performed on ZnO and $3R-MoS_2$ models. A quite good coherence with FEM simulations is shown. What's more, the BVD model can show the impact brought by the mechanical and electrical losses of electrodes, which is not applicable in FEM simulation.

At last, we target the device with 100 nm thick 3R- MoS_2 flakes, resonance frequency around 20 GHz, with acoustic Bragg mirror of 73.6 nm SiO_2 and 65.6 nm W. The design of a RF characterization set-up is proposed, a ground-signal-ground (GSG) coplanar transmission line is designed to get 50 ohms impedance matching. To remove the electric parasite modes of GSG and ensure an appropriate calibration at the nearest to the SMR chip, an Open-Pad-Short kit and associated de-embedding process is also proposed. After intense exchanges with our collaborator at NTU Singapore, who is in charge of the device fabrication, the mask design is done. The fabrication and characterization results are shown in the next chapter.

Chapter 4 Fabrication and characterization of $3R-MoS_2$ based solidly mounted resonators (SMR)

Introduction

In the previous Chapter, we presented the whole SMR design process, firstly based on a reference model consisting of a ZnO -based SMR, with both conventional quarter wavelength and optimized acoustic Bragg mirror. The performances were investigated by 2D FEM simulations, then 3D FEM simulations allowed the study of irregularly shaped top electrode, pointing out the interest of pentagonal top electrode to reduce spurious modes. A four- or five-fold reduction of the FEM models thanks to structural symmetries of the top electrode (square or pentagonal) enabled a gain in computational time, though a finer meshing and thus better resolution. The same approach was then carried out to design the target $3R-MoS_2$ based SMR, highlighting a longitudinal acoustic mode at very high resonance frequencies, though also more spurious modes. A preliminary study based on a modified Butterworth-Van Dyke (MBVD) equivalent circuit was also proposed for both structures, which can greatly simplify some investigations in terms of resonance frequency as well as electrode losses impact. At last, the design of a RF characterization set-up was proposed, including matched coplanar waveguides access and de-embedding process based on a specific calibration kit, and the design of the mask was done in strong collaboration with our collaborator from NTU Singapore to take into account the technological constraints.

In this Chapter, we will present some characterization results of $3R-MoS_2$ flakes, which are used for our devices, including the thickness and piezoelectric constant measurement as well as the surface roughness imaging. The device fabrication process is then also briefly described, as developed by our collaborator. The core of our own experimental work focused on the RF characterizations, they are presented and compared with FEM simulation results, leading to a discussion about the propagation of acoustic wave in $3R-MoS_2$. A fitted BVD equivalent circuit is also proposed, based on the characterization results.

1. Characterization of $3R - MoS_2$ flakes

The characterization of $3R - MoS_2$ flakes by the Singaporean team, as used for the SMR, was crucial for the design steps, especially the thickness and piezoelectric constant C_{33}, since these two factors play an important role on the device performances.

Thickness characterization

$3R - MoS_2$ ultrathin flakes are exfoliated from a $3R - MoS_2$ crystal, using the scotch-tape micromechanical cleavage technique method. The thickness of MoS_2 flakes is measured by Asylum Research Cypher Atomic Force Microscope (AFM).

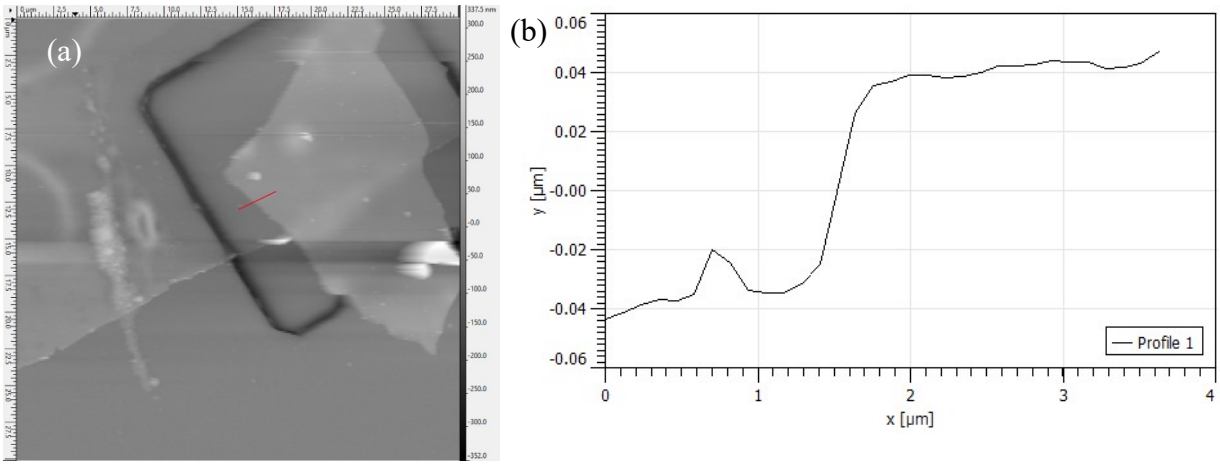

Figure 4.1 (a) AFM imaging of $3R - MoS_2$ flakes (irregular shape) transferred on the electrode (square shape) with red trace for profilometry; (b) Thickness profile on red trace of (a).

Figure 4. (a) shows the AFM imaging of $3R - MoS_2$ flakes transferred on the bottom electrode. The details of AFM profile can be analyzed by using the software GWYDDION [192]. The top and left scales show the dimensions of the AFM image (full-scale 30×30 µm^2), the right-side colour bar shows the altitude (full-scale near 690 nm). The flake thickness can be estimated from the profilometry measurement at the edge of the $3R - MoS_2$ flake on the electrode (red line on Figure 4. (a)). The profile is shown in Figure 4. (b), the thickness of this $3R - MoS_2$ flake is near 80 nm.

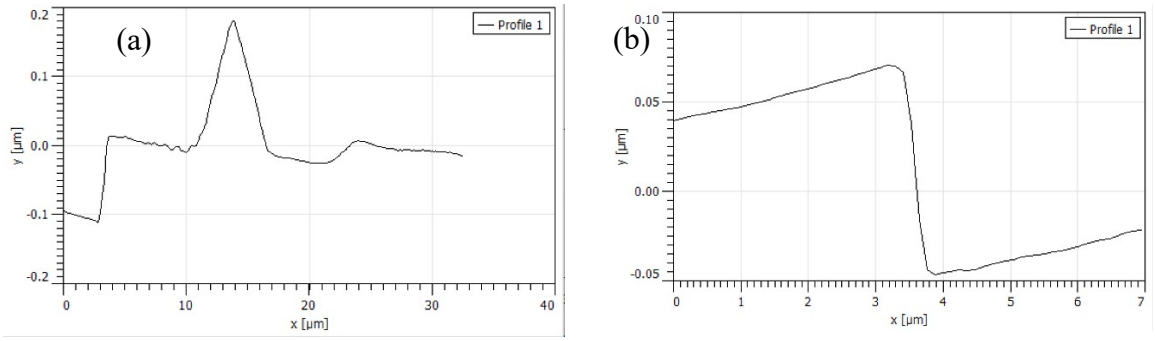

Figure 4.2 Thickness profiles of measured $3R - MoS_2$ flakes.

As on Figure 4. (b), two other examples of profiles at the edge of transferred $3R - MoS_2$ flakes on Figure 4.2 highlight a low roughness on flakes of thickness about 100 nm.

Rare defaults are also observed such as on Figure 4.2 (a) with a protrusion of almost 200 nm, width about 7 nm.

Five such devices could be successfully fabricated with transferred $3R-MoS_2$ flakes of thickness 210 nm, 220 nm, 235 nm, 240 nm and 290 nm, respectively, even though our targeted thickness is 100 nm. As of now, we should note that, since the acoustic Bragg reflector is fabricated at first for a target wavelength, some mismatch depending on the $3R-MoS_2$ flakes thickness will influence the overall performances of the prototypes.

Piezoelectricity characterization

The piezoelectric characteristics of the $3R-MoS_2$ flakes have been also measured by our collaborator, using the Asylum Research Cypher piezo-response force microscopy (PFM). We focus on the measurement of the d_{33} piezoelectric constant, which plays an important role on the electromechanical coupling coefficient (k_t^2) of the longitudinal acoustic wave.

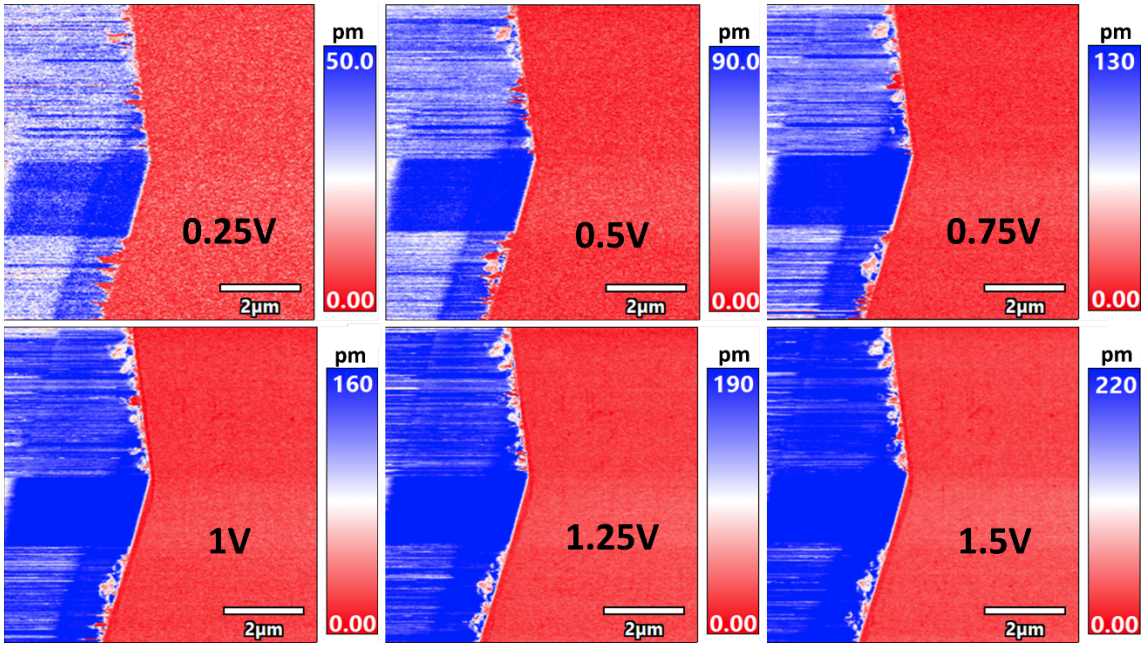

Figure 4.3 PFM images of a $3R-MoS_2$ flake on metal substrate with a bias voltage from 0.25 to 1.5 V between the PFM tip and the substrate. (provided by collaborating NTU-Singapore research team)

The c-axis oriented $3R-MoS_2$ flakes are placed on a metal stage first and the PFM conductive tip, charged by an alternating current (AC), is brought into contact with the surface of the $3R-MoS_2$ flake to measure the mechanical displacements. The d_{33} piezoelectric constant can be calculated by the equation (4.1).

$$d_{33} = \frac{\triangle Amplitude}{\triangle V_{ac} \times Q} \qquad (4.1)$$

Where $\triangle Amplitude$ is the difference between the maximum and minimum of the tip mechanical displacement, $\triangle V_{ac}$ is the applied AC voltage and Q is the sensitivity of the cantilever, which usually ranges from 40 to 50 and is given by the instrument software of PFM for each measurement.

Figure 4.3 shows results of PFM images obtained with a bias voltage from 0.25 to 1.5 V. The blue zone refers to the $3R-MoS_2$ flake, exhibiting different mechanical displacements under different potentials, the red zone is the metal stage used as a ground plan. We can observe that the mechanical displacement increases with the bias voltage, and then some places show high displacements but some places show no displacement, it highly depends on the quality of $3R-MoS_2$ flakes, so for our measurements, we try to find the $3R-MoS_2$ flakes of good flatness and uniformity.

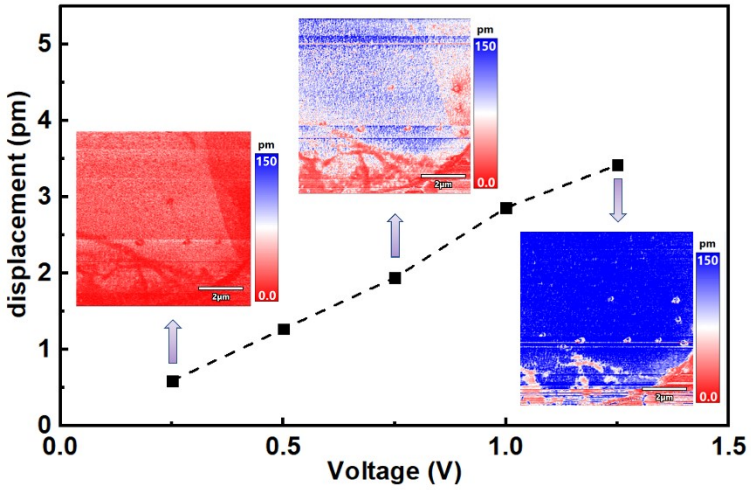

Figure 4.4 PFM measurement of a 200nm thick 3R-MoS2 flake. The displacement on Y axis takes into account the division by the sensitivity Q of the cantilever. Insets: the PFM images of a 3R-MoS2 flake under a biased voltage of 0.25, 0.75 and 1.25 V, respectively. (provided by collaborating NTU-Singapore research team)

Figure 4.4 shows the results of PFM measurement of a 200 nm thick 3R-MoS_2 flake, similar to those of our SMR devices. The displacements are already divided by the sensitivity Q of the cantilever. The results show a good linearity and the d_{33} value calculated by the equation (4.1) led to a value of 2.5-3.5 pm/V, which is greater than the previously reported value of 0.9 pm/V by H. Hallil *et al.* [193].

2. The fabrication of $3R-MoS_2$ based SMR

After characterization of the $3R-MoS_2$ flakes, this part describes the whole fabrication process, based on the mask designed as presented in Chapter 3.

Fabrication process

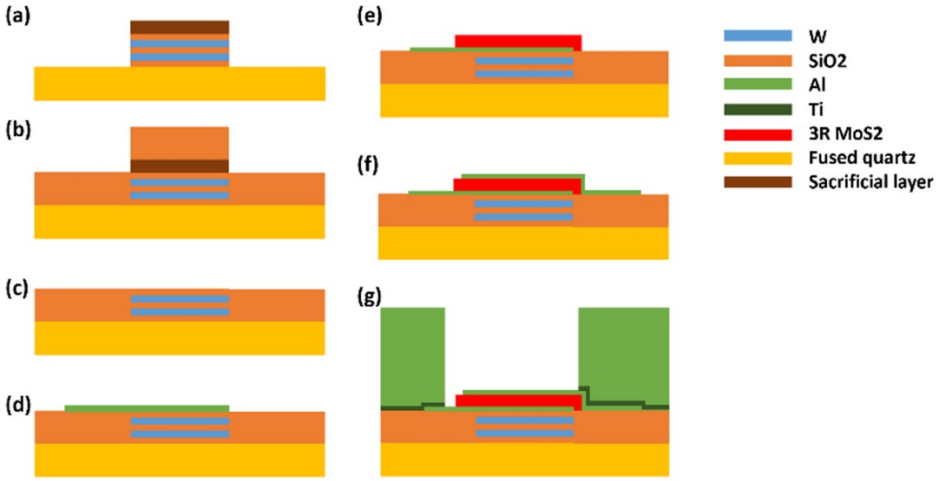

Figure 4.5 Schematic diagram of the fabrication process for $3R-MoS_2$ based SMRs. (provided by collaborating NTU-Singapore research team)

Figure 4.5 illustrates the main steps of the fabrication process. The first one is the deposition of the acoustic Bragg mirror, as shown in Figure 4.5 (a). It consists of low acoustic impedance SiO_2 layers with a thickness of 65-75 nm and high acoustic impedance W layers of 60-70 nm, alternately deposited on double-polished fused quartz using Elite sputtering system. This stack of 5 layers (3 SiO_2 layers + 2 W layers) is completed by a sacrificial layer of Al on the top, followed by a SiO_2 passivation layer with the same thickness as the Bragg mirror (Figure 4.5 (b)), also with the Elite sputtering system. After dissolution of the sacrificial layer and of the above SiO_2 by HCl, the remaining SiO_2 around the acoustic Bragg mirror prevents any connection and crosstalk between the CPW waveguide and the W layers, as shown in Figure 4.5 (c). A 35×60 µm Al layer with thickness around 20 nm is then sputtered to form the bottom electrode, as shown in Figure 4.5 (d).

The next step is to transfer piezoelectric $3R-MoS_2$ flakes, as shown in Figure 4.5 (e). The multilayers $3R-MoS_2$ flakes were exfoliated from bulk $3R-MoS_2$, firstly transferred to a PDMS film and then aligned onto the Al bottom electrode under microscope using a two-dimensional material transfer stage. After alignment, a 10-minutes anneal at 200 °C is performed and the PDMS is slowly lifted. Due to the adhesion force difference of 3R-MoS_2 between PDMS and Al at 100°C, the $3R-MoS_2$ flakes are attached on the Al bottom electrode. By the way, the temperature of stage should be limited to avoid phase change of 3R-MoS_2 [194].

This crucial step is ended by the sputter deposition of a 20 nm thick pentagonal Al top electrode with area around 150 μm^2 on the $3R-MoS_2$ Figure 4.5 (f)), and a 1µm thick Ti-Al coplanar waveguide to provide signal and ground plan using sputter system (Figure 4.5 (g)).

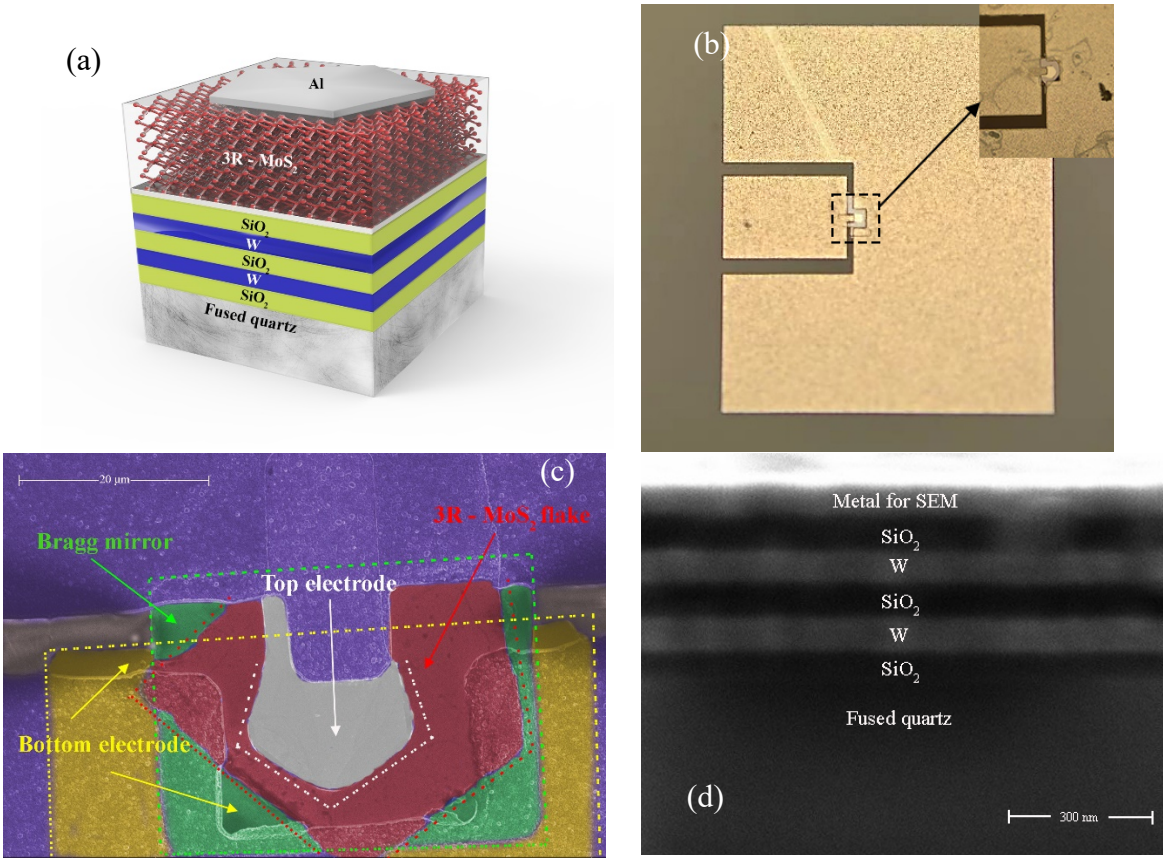

Figure 4.6 (a) 3D illustration of the $3R - MoS_2$ based SMR; (b) Top view and (c) SEM image with coloured material areas of a $3R - MoS_2$ SMR prototype; (d) SEM image of a cross-section of the acoustic Bragg Mirror.

Figure 4.6 (a) is a 3D illustration of the $3R - MoS_2$ based SMR on top of the acoustic Bragg mirror designed to reflect the longitudinal acoustic wave at 20 GHz. The thickness of $3R - MoS_2$ flakes is designed to be 100 nm, however, because of its special transfer process, the effective thickness cannot yet be controlled with a high precision and the final are as previously presented, between 210 and 290 nm.

Figure 4.6 (b) is the optical image of the top view of a whole device, the large area of signal and ground zones can guarantee the connectivity and minimize the ohmic losses on the transmission line. Furthermore, the deposited Al waveguide shows a good homogeneity.

Figure 4.6 (c) is the SEM image of the device, focused on the SMR part, we can see clearly that the transferred 3R-MoS_2 flake has an irregular shape but the layered structure and the mechanical exfoliation ensure a flat surface as it can be observed, which is important for a good propagation of the acoustic wave. The pentagonal top electrode is also clearly visible, as well as a good alignment of the signal and ground zones.

To analyse the deposition of the acoustic Bragg mirror, a SEM characterization is performed on the cross section, as shown in Figure 4.6 (d). Low acoustic impedance silicon dioxide (SiO_2) layers with a thickness of 65-75 nm and high acoustic impedance Tungsten (W) layers with a thickness of 60-70 nm were alternately deposited on a double-polished fused quartz substrate using a magnetron sputtering system, forming a 5 layers acoustic Bragg reflector (3 SiO_2 layers + 2 W layers). We can clearly see that SiO_2 and W layers are alternately deposited on the substrate, the thickness control is good and each kind of layers has nearly the same thickness.

Fabrication issues

As the fabrication process had to be developed dynamically along with the device design, in a mutual optimization cycle and with a total of 7 steps with some critical ones, several types of defaults have been encountered. The main ones, which caused the device failures, are presented in Figure 4.7.

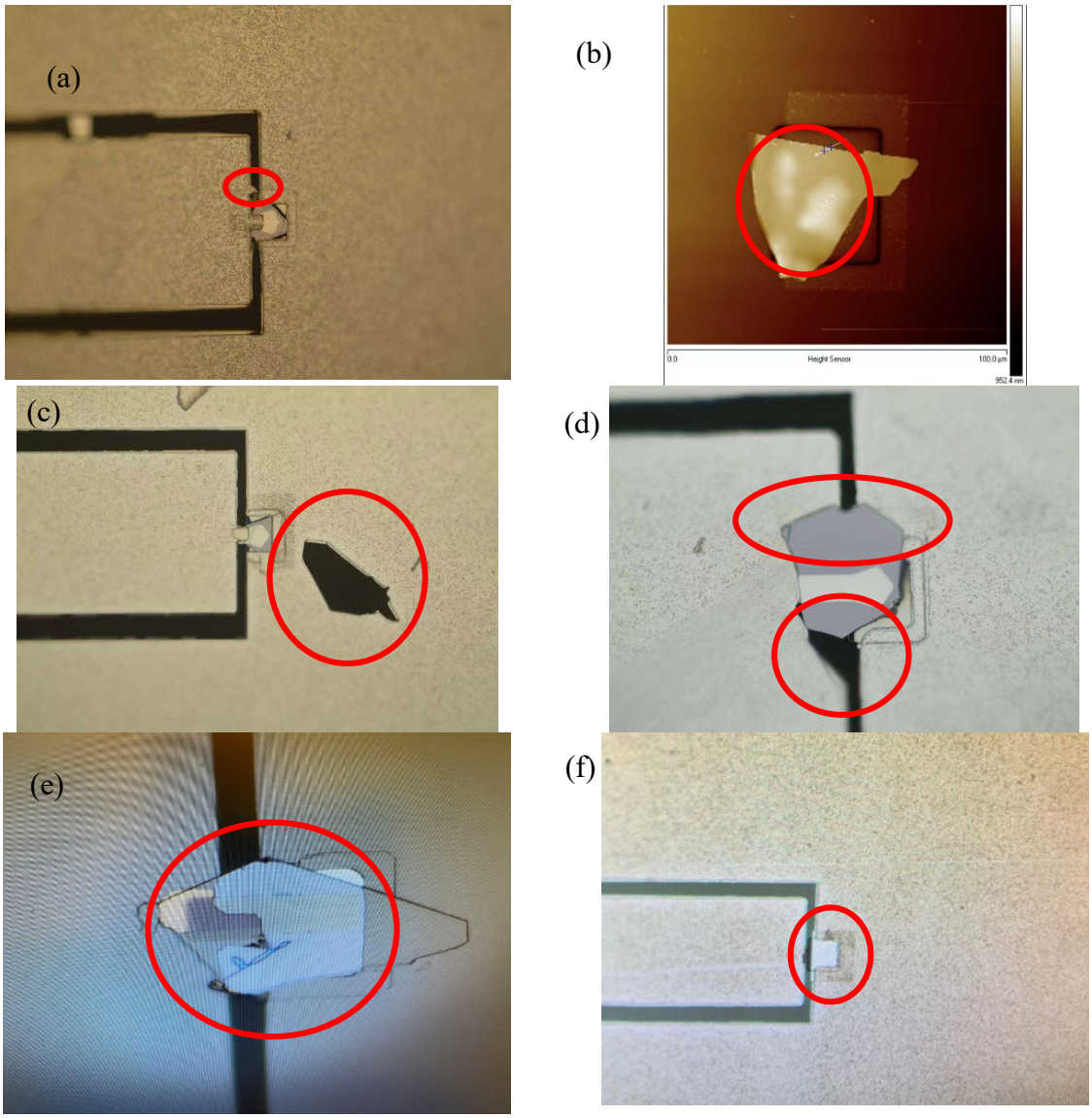

Figure 4.7 Defaults encountered during devices fabrication: (a) Short circuit; (b) Bubbles and contaminations; (c) and (d) Broken patterns; (e) and (f) Broken and missing 3R-MoS2 flakes. (provided by collaborating NTU-Singapore team)

1. On Figure 4.7 (a), a default in metal deposition causes a short circuit between signal and ground due to the short distance.
2. On Figure 4.7 (b), bubbles and contaminations of $3R - MoS_2$ flakes are visible as white areas on the flake region. Such defaults can be generated during the transfer process. Indeed, the manipulation of finding a flat, uniform flake with proper thickness, and transferring it onto the target zone with proper alignment and perfect adhesion over the flake surface needs very good skills. This issue has been limited with an annealing process helpful in enhancing adhesion.

3. Metal shortage areas have been found in pictures of Figure 4.7 (c) and (d). This kind of defaults are usually caused by the repetitive manipulation of the mask (a single one with all layer patterns), which can induce the uncomplete metal deposition. Those defaults can influence the device performance.
4. Figure 4.7 (e) and (f) illustrate examples of chips with broken and missing $3R-MoS_2$ flakes, respectively. Indeed, the deposition of Al coplanar waveguide after flakes transfer brings internal constraints that can break the $3R-MoS_2$ flakes. Furthermore, the lift off process of photoresist before the deposition of top electrode, can sometimes peel off the $3R-MoS_2$ flakes.
5. Another difficulty is associated to the 5-times mask alignment. This requires a very good grasp of multiple alignments at the micrometric scale.

3. The characterization of $3R - MoS_2$ based SMR

After successful fabrication of several samples, their RF characterization was carried out. It was implemented using a Keysight N5244A 10 MHz to 43.5 GHz PNA-X network analyser with a 150 µm-pitch ground-signal-ground (GSG) Formfactor Infinity Probe. Open-Short-Load (OSL) calibration was made before the measurements. Besides the SMR devices, the Open and Short specifically designed structures (detailed in the Chapter 3) were also characterised similarly in order to carry out the de-embedding process. In this part, we detail the de-embedding process based on measurements with a first sample prototype, then characterization results of a set of five devices are presented.

De-embedding process and preliminary results

The first characterization results are shown in Figure 4.8. The characterization was performed over a frequency range from 1 to 40 GHz. The magnitude of the scattering parameter S_{11} is shown in Figure 4.8 (a), the first sample exhibits a minimum peak at -3 dB near 25 GHz and shows a very wide passband. Indeed, S_{11} starts from 0 dB at low frequency, begins to decrease from 10 GHz and decreases more sharply from 15 GHz. At about 25 GHz, it starts to increase again, slowly, still not back to 0 at 40 GHz. The quality factor (Q value) is less than 10. Open and Short structures don't show any resonance, but there are still some off-sets, especially the Short structure shows an increasing loss, reaching 0.5 dB at 40 GHz.

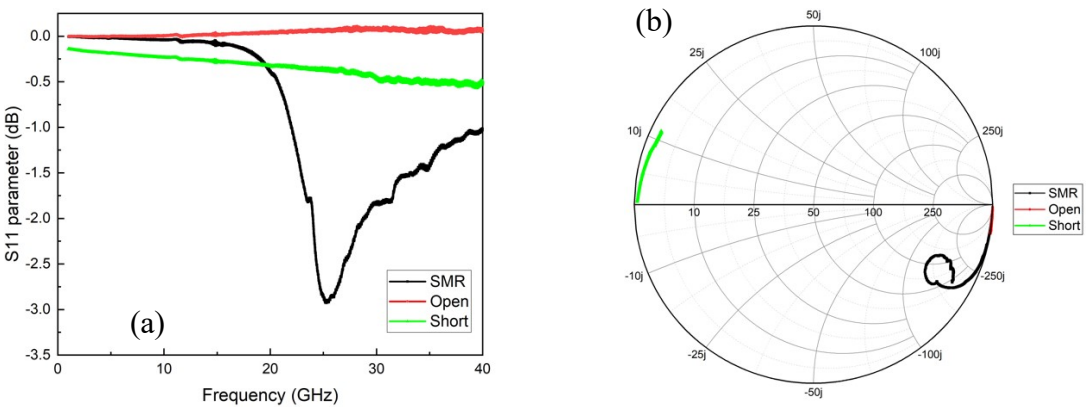

Figure 4.8 (a) S11 parameter in magnitude vs. frequency of Open, Short and SMR samples without de-embedding process; (b) Corresponding Smith chart.

Fig 4.8 (a) and (b) show the magnitude of the reflection parameter and the Smith chart, respectively, of these three structures, without de-embedding step. The curve of the Open structure starts from the open circuit point (infinite Z) on the Smith chart at low frequency, and travels slightly into the capacitive zone, still close to the external circle (reflection coefficient magnitude of 0 dB). The curve of the Short structure starts from the short circuit point (impedance zero) at low frequency and remains on the left side of the chart, which means a small value of impedance. It also travels slightly into the inductive zone and away from the outer circle, which explains the drift in S_{11} magnitude at higher frequencies, reaching about -0.6 dB at 40 GHz. The curve of the SMR structure on the Smith chart starts as the Open circuit, from the right edge at low frequency and travelling into the capacitive zone, where it exhibits a loop, almost but not entirely closed and corresponding to the resonance which is observed on the S_{11} magnitude curve. However, this loop stays in the capacitive zone, far from the matched impedance at the chart centre and, most of all, without phase transition

that is expected in this case at the resonance. The de-embedding process will remove the electrical influence of CPW RF characterization access from this SMR device response, especially the capacitance which is in parallel and so added to that of the SMR.

Before performing the de-embedding process, it is noted that there are four kinds of process: remove open parasites only (Open), remove short parasites only (Short), remove open parasites followed by short parasites (Open-Short) and remove short parasites followed by open parasites (Short-Open). Open-Short process is a commonly used de-embedding method for on-wafer applications. To compare these four different methods, we apply each of them on our first sample.

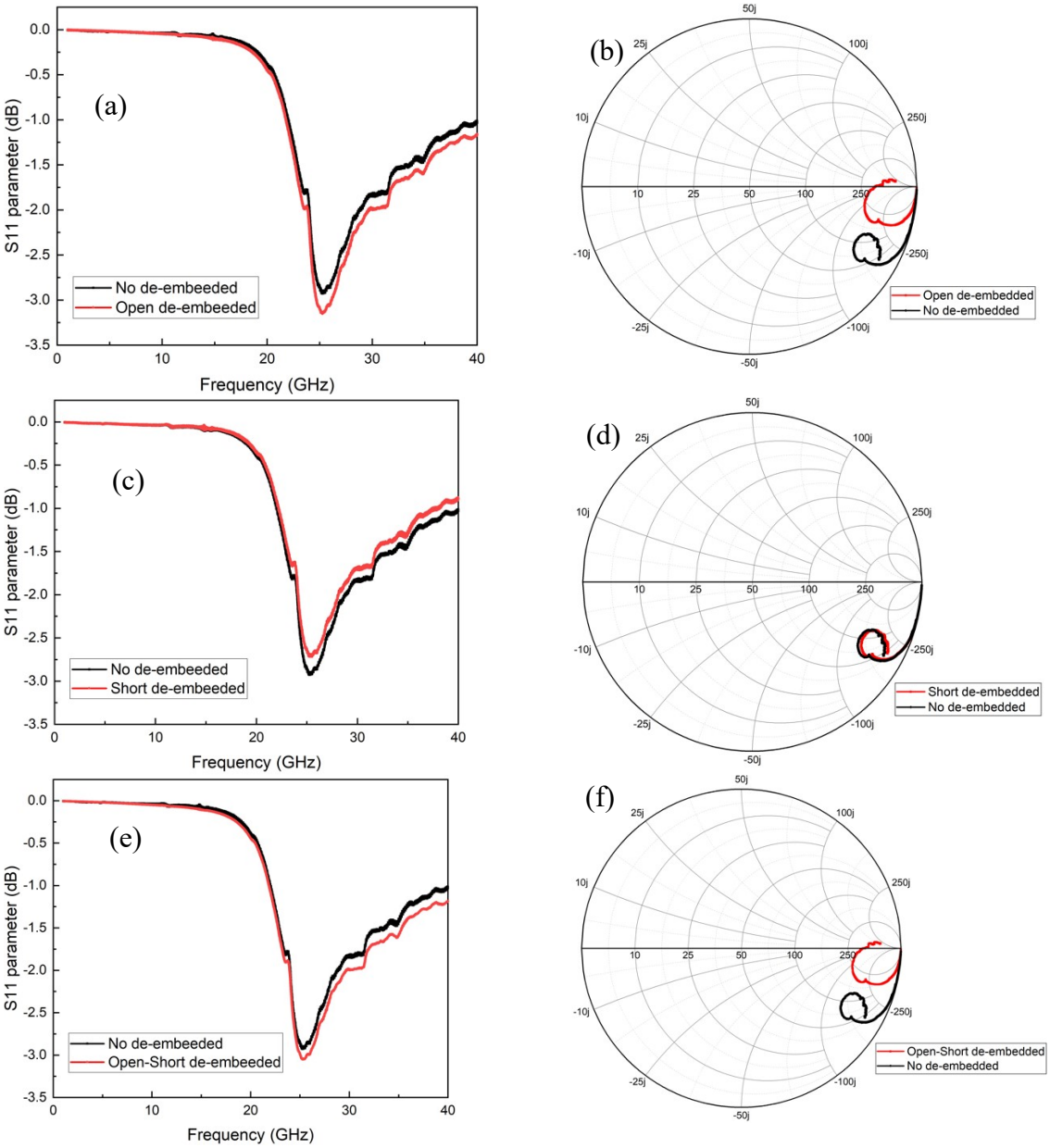

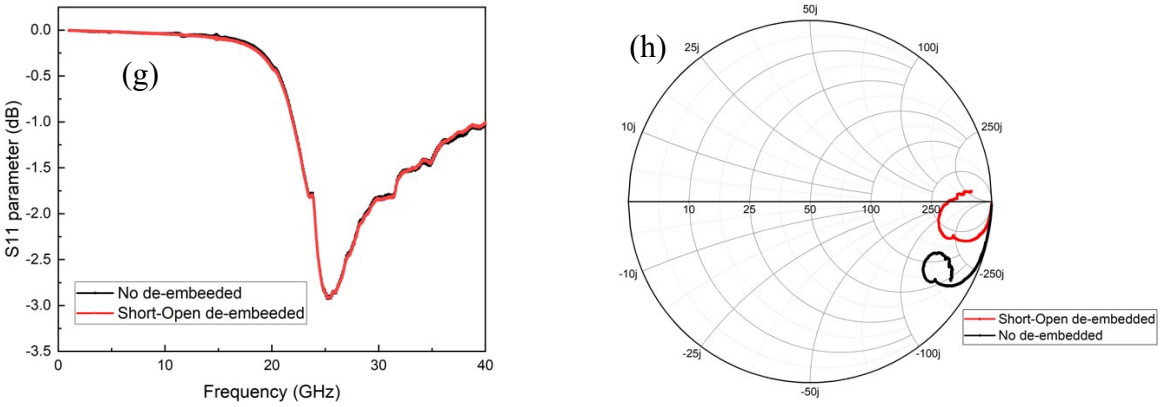

Figure 4.9 (a,c,e,g) S_{11} parameter in magnitude vs. frequency and (b,d,f,h) corresponding Smith chart, with and without (a,b) Open, (c,d) Short, (e,f) Open-Short, (g,h) Short-Open de-embedding process

Figure 4.9 (a) to (h) show the S_{11} parameter in XY graphs as well as Smith charts after each one of the four de-embedding processes: Open, Short, Open-Short, Short-Open. It can be observed similar results for all ones, except the only "Short" de-embedding process, for which both curves are very close, especially on the Smith chart. This suggests that, as expected, the influence of the capacitance of the out structure with CPW RF lines, characterized by measuring the Open structure, is the most significant on the full response. On the three other de-embedding processes, all including the Open structure measurement, the loop on the Smith chart is clearly modified, still starting from the open circuit point and travelling into the capacitive zone, but also slightly entering into the inductive zone. This agrees with the expected resonance with a phase transition of the SMR device. Again, the loop is not closed but it exhibits a downturn, though not travelling back to the capacitive half-circle.

Based on these results, and considering that the Open-Short de-embedding process is commonly used for on-wafer applications, we will choose it for our further post-treatments.

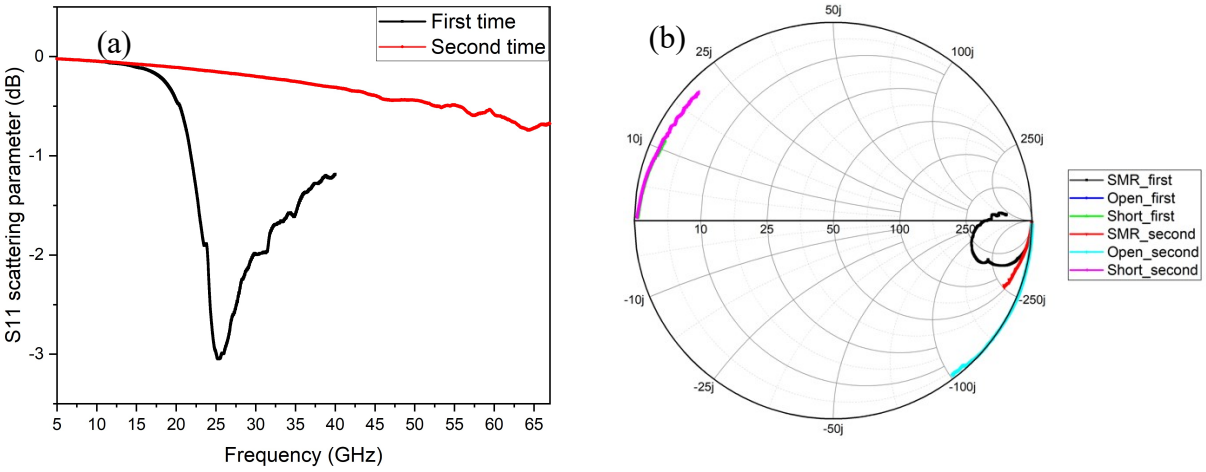

Figure 4.10 (a) Reflection scattering parameter S_{11} and (b) corresponding Smith chart of those prototype samples before and after one-week air exposure.

By the way, these prototypes exhibited a high fragility. Indeed, Figure 4.10 (a) and (b) show the characterization results after air exposure for one week. The resonance peak is no more visible on Figure 4.10 (a), even over a frequency sweep enlarged from 1 to 67 GHz. On the Smith chart, the de-embedded SMR curve after one-week air exposure exhibits no resonance loop and always stays in the capacitive zone. The curves for the Open and Short structures are not different after exposure, which is not so surprising as made of thicker metal only. The default may be attributed to an oxidation of the $3R - MoS_2$ flakes after one week of

air exposure, or of the very thin electrodes, which is still to be confirmed. A failure analysis is further planned on this first sample for a better understanding on our device and of material properties, especially the $3R - MoS_2$.

Characterization results of the fabricated devices

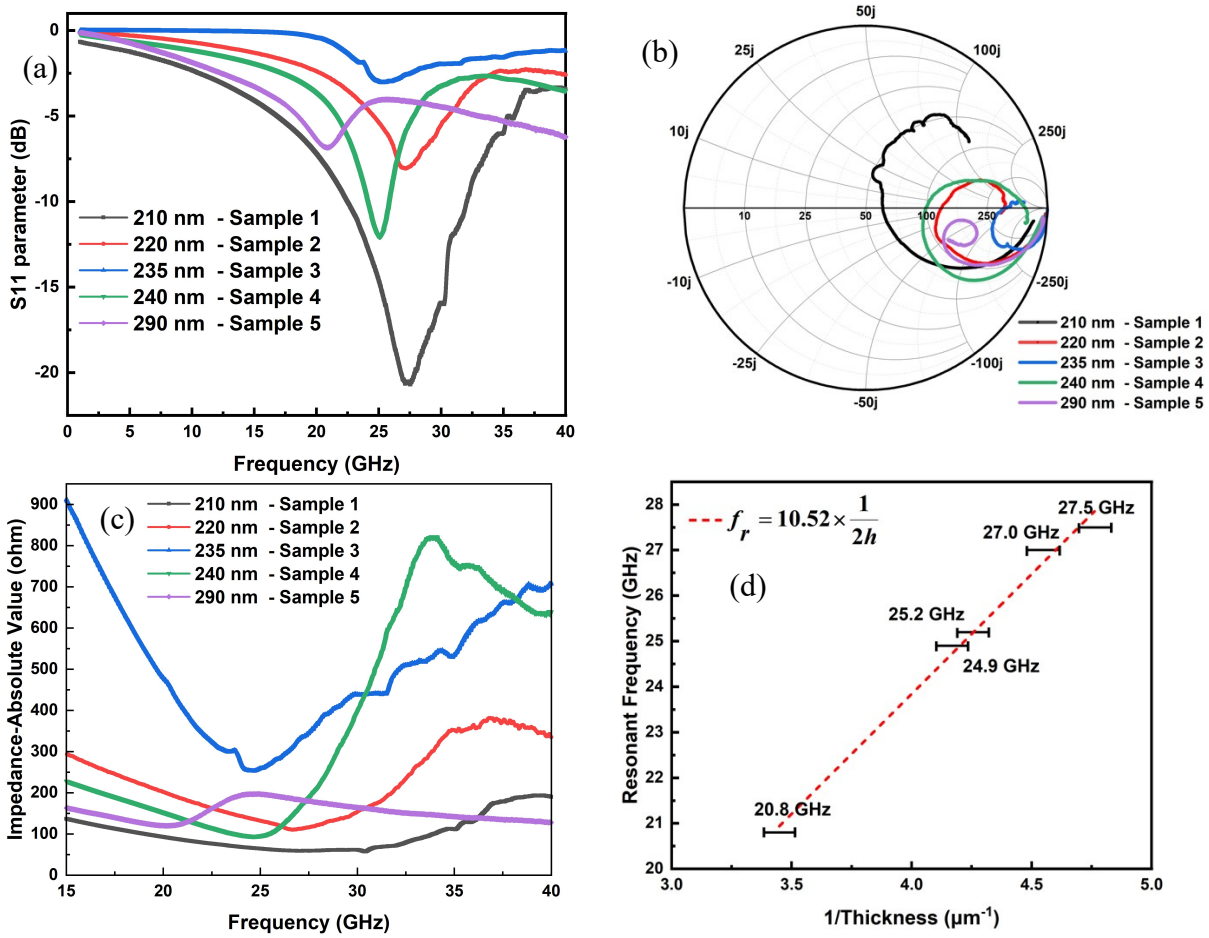

Figure 4.11 Characterization results of 5 SMR samples with different thicknesses of $3R - MoS_2$ flakes: (a) Reflection scattering parameter S_{11} in magnitude; (b) Smith chart; (c) Impedance modulus near the resonance frequency; (d) Resonance frequency vs. 1/thickness

At last, a set of samples was successfully fabricated, we consider here 5 samples with different thickness of 3R-MoS_2 flakes, from 210 nm to 290 nm. Their RF characterization was performed similarly, by using a Keysight N5244A 10 MHz to 43.5 GHz PNA-X network analyser, over the frequency range from 0.5 to 40 GHz. The synthesis of the characterization results, after de-embedding as previously presented, is presented in Figure 4.11.

Figure 4.11 (a) shows the measured scattering parameter S_{11} of those 5 samples. The resonance frequencies and the insertion losses differ with the thicknesses of the layers of 3R-MoS_2 of 210 nm, 220 nm, 235 nm, 240 nm and 290 nm, they are respectively 27.5 GHz and -22.5 dB, 27 GHz and -8 dB, 25.2 GHz and -3 dB, 24.9 GHz and -12.5 dB, and 20.8 GHz and -8 dB, the resulting values are gathered in the Table 4.1. We can see an improvement of the fabrication process compared to the first prototype, with a lower minimum value of S_{11} at the resonance for the whole set. The quality factor (Q value) remains low, less than 10 for all 5

samples, however as presented in Chapter 1, a commercial FBAR/SMR often has a quite high Q value ranging from a few hundred to several thousands.

Table 4.1 Brief synthesis of characterization results

Thickness (nm)	f_r (nm)	S_{11} (dB)
210	27.5	-22.5
220	27	-8
235	25.2	-3
240	24.9	-12.5
290	20.8	-8

Figure 4.11 (b) shows the 5 samples response on Smith chart. All of them exhibit a resonance loop, not closed as for the prototype and accordingly with the uncomplete recovery of the S_{11} baseline at high frequency, but entering from the capacitive into the inductive half-circle, except the sample 5 with greater film thickness of 290 nm. The S_{11} minimum values can be seen from the closeness of the curves to the Smith chart centre, they are in a good agreement with Figure 4.11 (a). As for the first prototype too, material losses, acoustic Bragg mirror mismatching, as well as the RF test setup including the chip access and impedance mismatching, participate to the observed response. Furthermore, these 5 samples were quite different, due to the sample preparation details.

Figure 4.11 (c) shows the electrical impedance curve of these 5 different samples, with a minimum at the resonance frequency, followed by a maximum. Minimum values are of a few dizains of ohms, about 50 to 150, except the sample 3 for which the minimum impedance is about 300 Ω and the maximum is not reached at 40 GHz. We chose the sample 4, which exhibits a strong resonance on the impedance curve and a regular S_{11} curve, to perform a deeper analysis. For this sample, the electrical impedance minimum is observed at f_r with nearly 50 ohms and the maximum at f_a with 900 ohms. The electromechanical coupling coefficient (k_t^2) is 47.6%, calculated from the equation (2.61).

Finally, on Figure 4.11 (d) are represented the resonance frequencies versus thickness. The result puts to evidence that the resonance frequency is almost inversely proportional to the thickness of the 3R-MoS_2 flakes, in agreement with the theoretical analysis. From the equation (2.58), the slope of these curve corresponds to half the longitudinal acoustic wave velocity in 3R-MoS_2 flakes. This leads to a wave velocity of 10526.4 m/s. However, it should be noted that this neglects the electrodes thickness, though a continuity of the wave displacement as it can be seen on the simulation results. As a consequence, the effective wave velocity should be larger.

When compared to the simulation results in Chapter 3, with a velocity supposed to be 4264.1 m/s, the value calculated from the characterization results is twice or even threefold. From the description in Chapter 2, the acoustic wave velocity depends on density, elastic constant, permittivity and piezoelectric constants. Among them, the density and the elastic constant play a dominant role. It suggests that the effective material parameters differ significantly from the expected ones, which is probably due to the layered structure of the 2D material compared to a bulk one. In this context, we try to perform a kind of retro-simulation to have a deeper understanding on 3R-MoS_2 properties.

4. The retro-simulation of $3R-MoS_2$ based SMR

From the above characterization results, all the fabricated devices show resonance frequencies over 20 GHz. However, the FEM simulation results presented in Chapter 3, for example for a SMR with 100 nm thickness 3R-MoS_2, led to a resonance at only 18.3 GHz. Our experimental results for this thickness, as shown in Fig 4.11 (d), suggest a longitudinal acoustic wave velocity of $10526.4\ \mathrm{m/s}$. In this part, we present two approaches based on some FEM retro-simulation to gain a better understanding of the behaviour and the material properties, based on the characterization results.

Simulation based on an ultra-high elastic constant C_{33}

We firstly perform a retro-simulation to fit the resonance frequency of 25 GHz of the sample 4, which has a 240 nm thick $3R-MoS_2$ flake. As described in the Chapter 2, and considering that the density and thickness could be measured with a reasonable precision, the effective velocity of the longitudinal acoustic wave is finally mainly determined by the elastic constant C_{33}. This would lead to consider a fitted value of C_{33} as high as 900 GPa.

The declared $3R-MoS_2$ properties are synthesized below, from data in the literature.

The volumetric mass density (ρ): 5060 $\mathrm{kg/m^3}$ [189]

The elastic constants matrix (GPa) [157] as following:

$$c=\begin{pmatrix} 247 & 67.7 & 32.2 & -10.7 & 0 & 0 \\ 67.7 & 247 & 32.2 & 10.7 & 0 & 0 \\ 32.2 & 32.2 & 900 & 0 & 0 & 0 \\ -10.7 & 10.7 & 0 & 38.6 & 0 & 0 \\ 0 & 0 & 0 & 0 & 38.6 & -10.7 \\ 0 & 0 & 0 & 0 & -10.7 & 89.65 \end{pmatrix} \qquad (4.2)$$

The dielectric constant matrix:[157]

$$\varepsilon^s=\begin{pmatrix} 16.3 & 0 & 0 \\ 0 & 16.3 & 0 \\ 0 & 0 & 2.6 \end{pmatrix} \qquad (4.3)$$

The piezoelectric constants (pm/V):[157]

$$d=\begin{pmatrix} 0 & 0 & 0 & 0 & -4.1 & -3.6 \\ -3.6 & 3.6 & 0 & -4.1 & 0 & 0 \\ -0.21 & -0.21 & 3.5 & 0 & 0 & 0 \end{pmatrix} \qquad (4.4)$$

The piezoelectric constants matrix e ($\mathrm{C/m^2}$):

$$e=d\cdot c=\begin{pmatrix} 0 & 0 & 0 & 0 & -0.119 & -0.278 \\ -0.601 & -0.601 & 0 & -0.081 & 0 & 0 \\ 0.046 & 0.046 & 3.136 & 0 & 0 & 0 \end{pmatrix} \qquad (4.5)$$

The d_{33} with the value of 3.5 is issued from the final PFM characterization from NTU Singapore team and d_{31} with the value of -0.21 is from the reported DFT calculation value [157], since we cannot measure this value by using current technology.

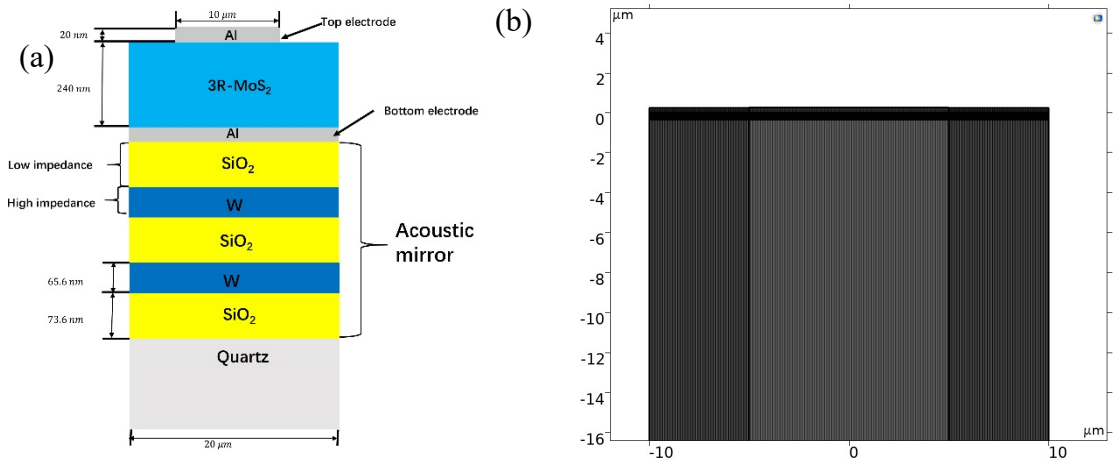

Figure 4.12 (a) The cross-section of 3R- MoS_2-SMR for retro-simulation; (b) The mesh structure of FEM model.

The 2D model of SMR with a 240 nm thick 3R-MoS_2 flake is shown on Figure 4.12 (a). The mesh structure is on Figure 4.12 (b), the same quadrangular elements are applied, the total number of elements is 11200. a Perfectly Matched Layer (PML) is also used. The condition limits are still the same as for the other 2D models, the physics of solid mechanics and electrostatics are added. A mechanical damping of 0.001 and a dielectric loss of 0.01 are also added to the piezoelectric layer $3R-MoS_2$. The frequency ranges from 23000 to 32000 MHz, the step size is 1 MHz, the calculation time is 3 h 33 minutes.

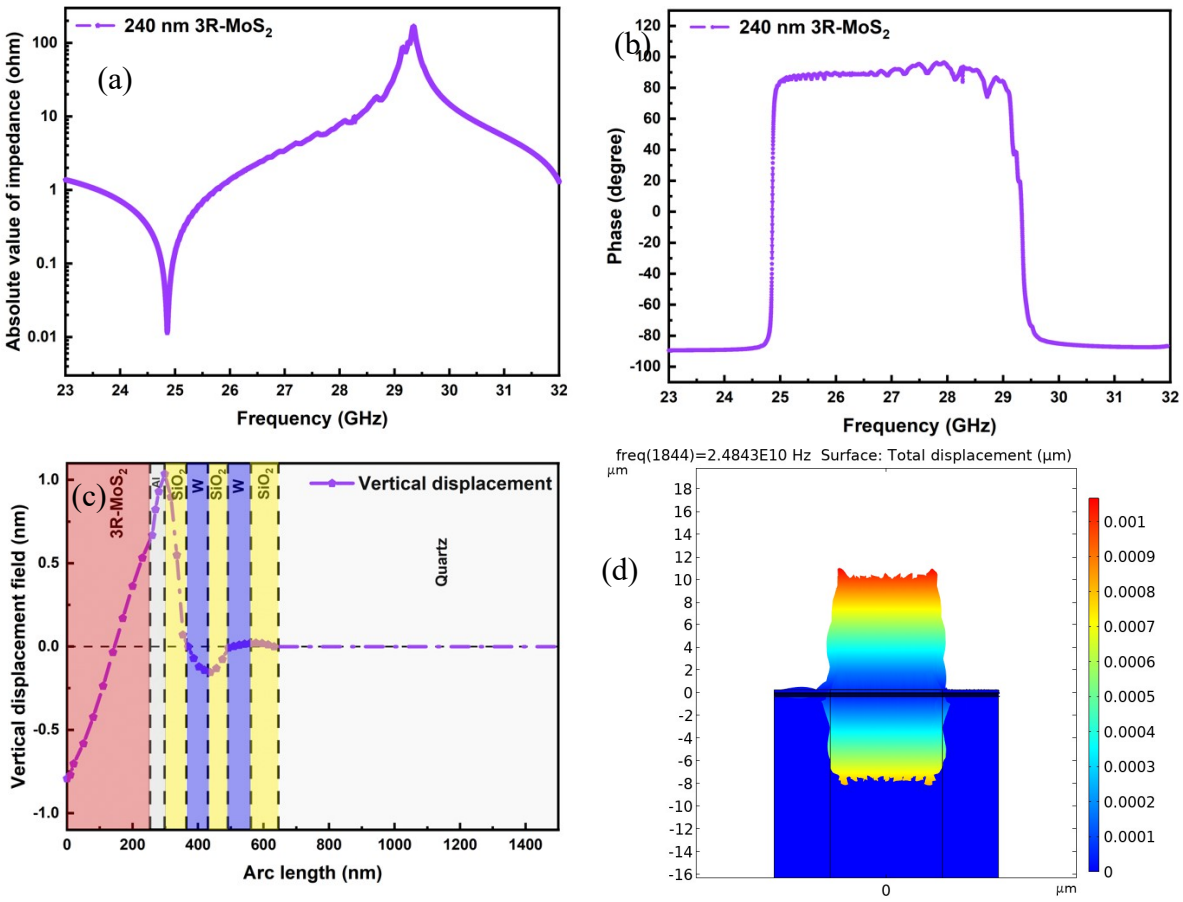

Figure 4.13 2D model simulation results: (a) Electrical impedance spectrum in magnitude; (b) Impedance phase; (c) Vertical mechanical displacement and (d) mode shape at the resonance frequency f_r .

The results of the simulation are shown in Figure 4.13. From the curve of the electrical impedance as a function of frequency in Figure 4.13 (a), the minimum is observed at the

resonance frequency f_r of 24.856 GHz, and the maximum at the anti-resonance frequency f_a of 29.35 GHz, with values of 0.01 and 130 ohms, respectively. The phase curve on Figure 4.13 (b) put to evidence a typical result with a value near 90° in the range between the resonance and anti-resonance frequencies, and -90° out of this range. A few spurious modes can be seen on both curves, though less than that of simulation results in Chapter 3. The electromechanical coupling coefficient k_t^2 is calculated to be 37.5%, which is not far from that of our characterization results.

The same analysis of mechanical performance is performed. From the displacement field analysis, as shown in Figure 4.13 (c), the propagation of longitudinal waves can be clearly observed in each layer.

From the mode shape, shown in Figure 4.13 (d), the two vertical quite symmetric peaks also confirm the existence of thickness extension (longitudinal) acoustic mode, the uneven edges suggest other modes which share a part of the total energy.

Thus, since then we got several simulation and characterization results of 3R-MoS based SMR, we draw a synthesis of all FEM simulation and characterization results with different introduced parameters in Table 4.2 in order to get a whole comparison and understanding of these obtained results, k_t^2 can be calculated by using equation (2.61):

Table 4.2 Synthesis of FEM simulation and characterization results

Method	Thickness (nm)	f_r (GHz)	c_{33} (GPa)	d_{33} (pm/v)	d_{31} (pm/v)	k_t^2 (%)
FEM Simulation	100	18.3	92	3	5	47.8
	200	9.9	92	3	5	48.1
	240	24.9	900	3.5	-0.21	37.5
Characterization results	210	27.5	-	-	-	49.8
	220	27				45.5
	235	25.2				-
	240	24.9				47.6
	290	20.8				34.1

From this table, we can observe some differences between simulation and characterization results, these differences come from the material properties that we put into FEM simulation, since the thickness of 3R-MoS_2 cannot be controlled with high precision due to its special transfer process, and the material properties are not yet well known, this fact leads to the mismatching of acoustic Bragg mirror, and then influence the analysis of device performances and material properties. In this context, it leads to consider fabricate air cavity type FBAR, which will not need to consider the problems brought from the mismatching of acoustic Bragg mirror.

In this context, we performed the simulation based on air cavity type FBAR, without acoustic Bragg mirror, this simulation is based on the FEM model for retro-simulation and with the fitted material parameters. The results of simulation can be observed on Figure 4.14.

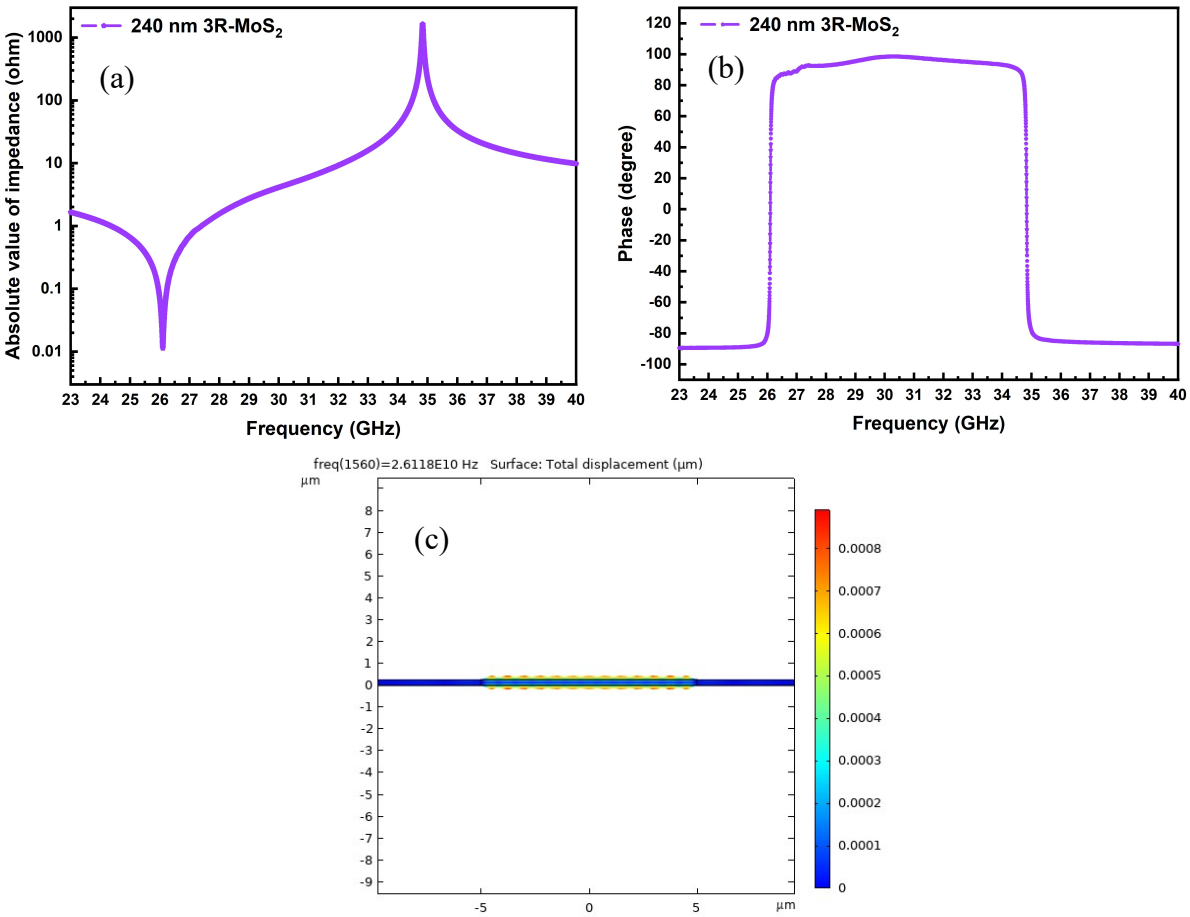

Figure 4.14 2D model simulation results of air cavity type FBAR: (a) Electrical impedance spectrum in magnitude; (b) Impedance phase; (c) mode shape at the resonance frequency f_r .

From the curve of electrical impedance as a function of frequency in Figure 4.14 (a), the minimum is observed at the resonance frequency f_r of 26.1 GHz, and the maximum at the anti-resonance frequency f_a of 34.84 GHz, with values of 0.01 and 1630 ohms, respectively. The phase curve on Figure 4.14 (b) put to evidence a typical result with a value near 90° in the range between the resonance and anti-resonance frequencies, and -90° out of this range. We do not see the spurious modes as in the retro-simulation with acoustic Bragg mirror. The electromechanical coupling coefficient k_t^2 is calculated to be 48.92%, which is closer to our characterization results. From the mode shape, shown in Figure 4.14 (c), the two vertical quite symmetric peaks also confirm the existence of thickness extension (longitudinal) acoustic mode, several nodes of resonance can be observed. Compared to the retro-simulation results with acoustic Bragg mirror, we can see some differences, it is therefore proved that the mismatching acoustic Bragg mirror will affect the performance of the whole device, making the development of air cavity type FBAR demanding, especially when we can not control the thickness of 3R-MoS_2 flakes with high precision.

Discussion on the 3R-MoS_2 multi-layered structure

From these results, it appears that the 3R-MoS_2 behaves as if it has a huge effective elastic constant C_{33}, as fitted at the resonance, about 10 times that of the reported value of 92 GPa [157], not far from the Young's modulus of diamond, 1143 GPa [195]. As discussed above, the layered-structure of 3R-MoS_2 is not expected to be highly compact, but rather

flexible though still stiff and with a quite low density, which impacts a lot the propagation of acoustic waves.

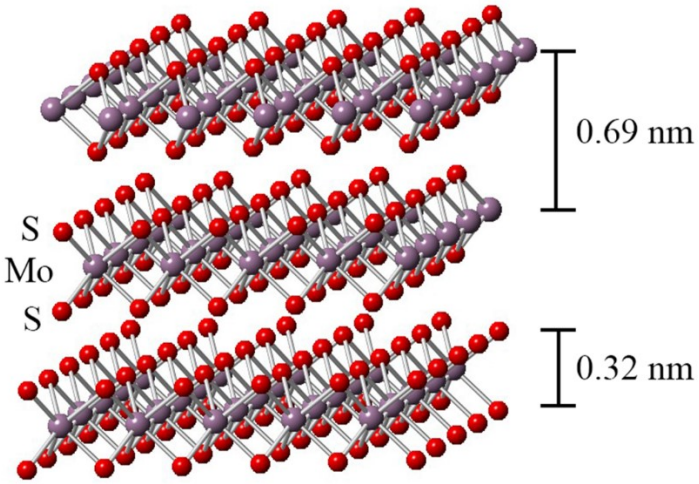

Figure 4.15 3D view of the atomic structure of 3R MoS_2

Indeed, whereas piezoelectric materials like ZnO or AlN can be considered as bulk materials even as thin films, the structure of 3R-MoS_2, as shown in Figure 4.15, exhibits atomic layers with interlayers and an overall bond based on Van der Waals forces. The layer-to-layer distance is around 0.69 nm [196], each atomic layer has a thickness of 0.3241 nm [197], which induces an interlayer gap of 0.3659 nm. This would mean about 340 atomic layers in a 240 nm 3R-MoS_2 flake, with an effective "physical" propagation path nearly a half the overall thickness and the other half-part being interlayer space. This suggests enhanced elasticity for acoustic waves propagation, but also possible multiple reflections at each interface of single layers and even mode conversion, which may induce spurious waves in case of coherent superposition and may also reduce the quality factor (Q value) of the whole device.

In the simulation presented in Chapter 3, we considered the vertical elastic constant C_{33} of 3R-MoS_2 calculated by S. Konabe *et al.* [157], 92 GPa, which is a quite low vertical elastic constant. Inversely, the value of 900 GPa resulting from the previous fit seems very high. But, this C_{33} parameter can hardly be measured for a multi-layered thin film such as the flakes embedded in the device, and reported measurements only address C_{11}. Indeed, measured values of Young modules of MoS_2 ultrathin layers of 330 ± 70 GPa and 270 ± 100 GPa have been reported by Andres Castellanos-Gomez *et al.*[159], and Simone Bertolazzi *et al.*[198], respectively. What' more, they suggest that the elastic properties vary when suffering certain constraints, and Young modules get an important increase under stress. As we discussed above, the existence of interlayer Van Der Waals force provides a very weak interlayer connection and then therefore decrease the elastic constant C_{33} of the bulk 3R-MoS_2. Inversely, under stress, the interlayer distance gets compressed which increases the C_{33} of monolayers, so the C_{33} of 3R-MoS_2 is highly influenced by the applied stress[199].

For our case, at the resonance, the longitudinal acoustic waves form the constructive waves, and then 3R-MoS_2 flakes get their maximum mechanical displacements, which induces internal stress. Furthermore, during the fabrication process, the 3R-MoS_2 flakes are placed on the bottom Al electrode by a transfer method, and they are fixed under the thick

waveguide sputtered afterwards, this generates stress related to the pretension of 3R-MoS_2 flakes.

In this context, the previous FEM simulations based on 92 GPa of C_{33} seems not convincible, but the fitted C_{33} of 900 GPa seems a high value even for an "effective" 3R-MoS_2 film, we perform a preliminary simulation on a "compact" 3R-MoS_2 structure, which is presented in Annex Chapter 4.

Discussion on the behaviour of the 3R-MoS_2 layered structure supporting thickness extensional acoustic mode

From the above results of a retro-simulation based on a kind of effective acoustic wave path theory, we can see that there is still a difference between the simulated and characterised results. We try here to discuss the approximation made, and to further analyse it by considering the underlying physics of interaction between atomic layers of the 2D nanomaterial.

We already introduced the Van der Waals force existing between two atomic layers of 3R-MoS_2. The total force of Van der Waals interaction can be approximated by the Lennard-Jones expression [200]:

$$F_{rep} = 4\varepsilon\left(\left[\frac{\sigma}{r}\right]^{12} - \left[\frac{\sigma}{r}\right]^{6}\right) \qquad (4.6)$$

Where F_{rep} is the repulsive force between two particles, ε is an energy parameter, r is the distance between the centres of two particles, σ is the distance at which the particle-particle force is zero.

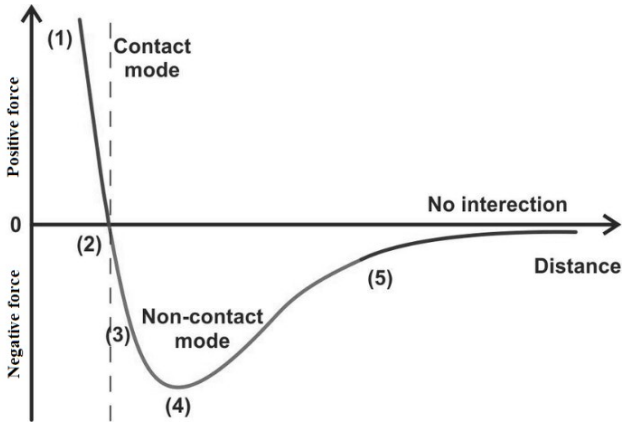

Figure 4.16 Typical curve of the Van der Waals interaction divided into three distinct regions [201].

From the typical curve of the Van der Waals interaction on Figure 4.16, 5 kinds of particle behaviours are highlighted:

1. The particles are in "contact" mode, the repulsive force is positive and increases as they are closer.
2. The repulsive force is zero, the particles are in an equilibrium state, σ is often referred to as "size of the particle", more precisely, it is the length of the chemical bond between them.

3. When the distance increases, the particles attract each other, they are in “non-contact” mode but expected to go back to the equilibrium state.
4. The attractive force reaches its maximum.
5. When the distance r is large enough, the interaction force tends to zero, the chemical bond is broken.

For our case, when the acoustic resonance occurs, the longitudinal acoustic waves compress and stretch the 3R-MoS_2 layers, which leads to changes of their interaction distance r , thus the Van der Waals forces will also experience changes between repulsive and attracting forces. From the macroscopic view, the stress on 3R-MoS_2 flakes varies during the resonance. For 240 nm thickness 3R-MoS_2 flakes, with 340 3R-MoS_2 atomic layers and 340 Van der Waals forces interfaced air gaps, it becomes an acoustic question of multilayer system, with a non-homogenous excitation as the bias potential is applied on the top and bottom of the flake.

Y. Q. GUO *et al.* [202] presented a theoretical analysis of the acoustic wave propagation in multi-layered piezoelectric structures, which may be partly similar to our case. The N-layered piezoelectric laminate section view is shown in Figure 4.17 (a). At each interface between two different piezoelectric materials, the acoustic waves undergo reflections and diffractions, it can result in 2 or 3 more kinds of waves for each acoustic mode, as shown in Figure 4.17 (b). By using a general formulation of the method of the reverberation-ray matrix (MRRM) in function of the material properties and the thickness of each layer, the dispersion curve of the multi-layered piezoelectric structure can be then obtained by using a numerical tool, as shown in Figure 4.17 (c). Various modes are obtained, that will share the total acoustic energy with the expected fundamental mode, and decrease the Q factor.

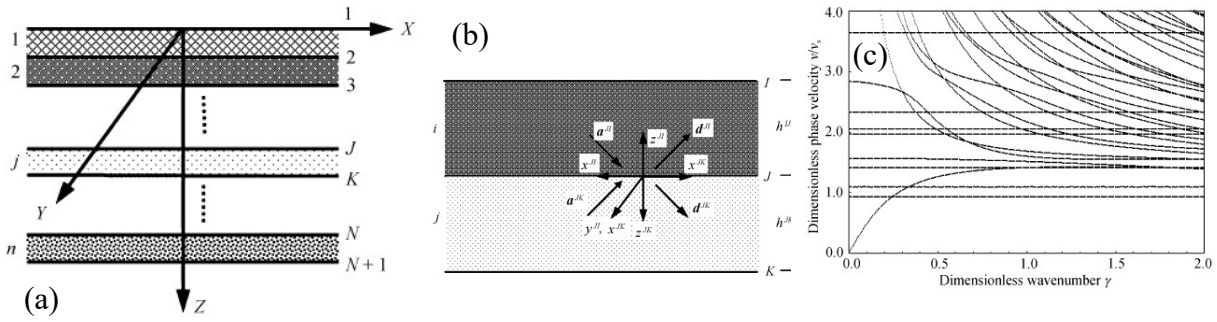

Figure 4.17 (a) N-layered piezoelectric laminate; (b) Interface in the multilayered structure; (c) Dispersion curve of the ten-layered piezoelectric structure [202].

For our case, a system of alternating 340 3R-MoS_2 monolayers and 340 Van der Waals forces interfaced air gaps, such a quantitative analytical analysis seems difficult to perform. Indeed, when the resonance occurs, the interaction distance between each layer (particles) and Van der Waals forces keeps changing, which is not a homeostatic state and then makes the condition limits in the analytical analysis unfixed. More powerful numerical and computational skills and resources are needed to perform this kind of analytical analysis. From a qualitative analysis, there will be much more existing modes in this complex structure than that of the ten-layered structure shown in Figure 4.17 (c), which decrease the Q factor, less than 10.

However, since the acoustic impedance between 3R-MoS2 and air gap is quite huge, the acoustic waves will mostly undergo reflections and the acoustic energy will mainly stays in 3R-MoS2 layers, which means the acoustic waves will mostly propagate in the 3R-MoS2 layers. This is the reason why we proposed to ignore the interlayer force field, and considered the system as a uniform 3R-MoS2 layer, by the way neglecting reflection and diffraction of acoustic waves at the interface, resulting in the effective acoustic path approach presented above. Furthermore, the thickness of each 3R-MoS2 monolayer and air gap is less than 1 nm, which is very low compared to the propagating wave wavelength of hundreds of nanometres and reinforces the possibility to consider the 3R-MoS2 layer as a homogeneous medium in a first approximation. However, it is a first-step and estimating approach, an advanced method is urgently needed to consider the propagation of acoustic wave in such nanometric scale multilayers. It is also a very promising field to investigate, since many nanomaterials show some very interesting properties. Some preliminary simulations about this hypothesis can be found in Annex Chapter 4.

5. BVD model after characterization

Finally, as analysed in the Chapter 3, here we also perform a BVD equivalent circuit analysis based on the characterization results. We still choose the sample 4 and the main material parameters are listed in Table 4.3

Table 4.3 Main parameters to calculate the lumped elements of the BVD model

Material parameters	Values
h	120 nm
ε_r	2.6
A	160 μm^2
k_t^2	47.6%
ρ	5060 kg/m^3
v_l	13336.63 m/s

The acoustic velocity here is taken from the first FEM retro-simulation results, with a C_{33} of 900 GPa, leading to a v_l of 13336.63 m/s. The k_t^2 results from the characterization of the sample 4. The values of the lumped elements as calculated based on the equations (2.50), (2.51), (2.52) and (2.53), are listed in Table 4.4.

Table 4.4 The values for lumped elements of the BVD model with a 240 nm thick $3R-MoS_2$ flake

Elements	Values
C_0	0.015347 pF
C_m	5.921324 fF
L_m	5.541301 nH
R_m	1.876456 Ω

The simulations are performed by using ADS (Agilent Advanced Design System), the structure of the circuit is shown in Figure 4.18. Two models are designed, without and with the electrode losses. The circuit shown in Figure 4.18 represents the model without electrode losses ($R_s = R_0 = 0\ \Omega$). For the model with electrode losses, the losses are set to be 5 Ω ($R_s = R_0 = 5\ \Omega$). The frequency ranges from 15 to 40 GHz, the step size is 1 MHz, the simulation takes around 30 s.

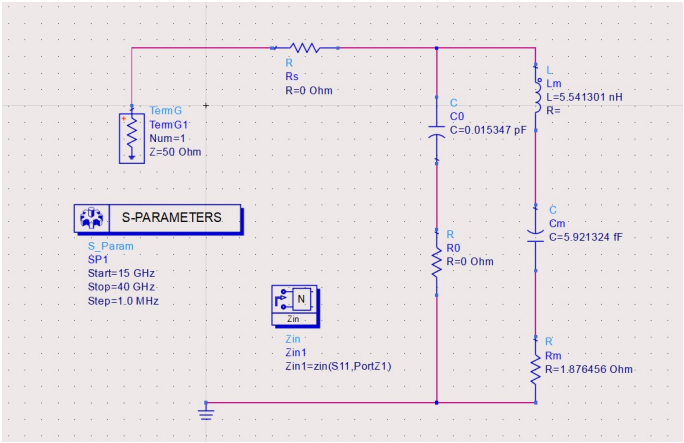

Figure 4.18 Circuit Structure of the 240 nm thick $3R-MoS_2$ based FBAR after characterization in ADS software.

The simulation results are shown in Figure 4.19. Figure 4.19 (a) shows S_{11} parameter of two models, they show a resonance near 27.8 GHz with a return loss of – 0.67 dB and – 2.42 dB without and with parasite resistances, respectively. We can see a very slight impact brought by the added parasite resistances, which brings a - 0.1 dB loss at 40 GHz.

Figure 4.19 (b) shows electrical impedance of two models, with a resonance near 27.8 GHz, similar without and with electrode losses. For both two models, we can see that a minimum of impedance occurs at resonance frequency near 27.8 GHz, and a maximum occurs at anti-resonance frequency near 32.7 GHz. For the model without parasite resistances, the minimum is around 1.9 ohms and the maximum is around 54000 ohms. For the model with parasite resistances, the minimum is around 7 ohms and the maximum is around 14650 ohms.

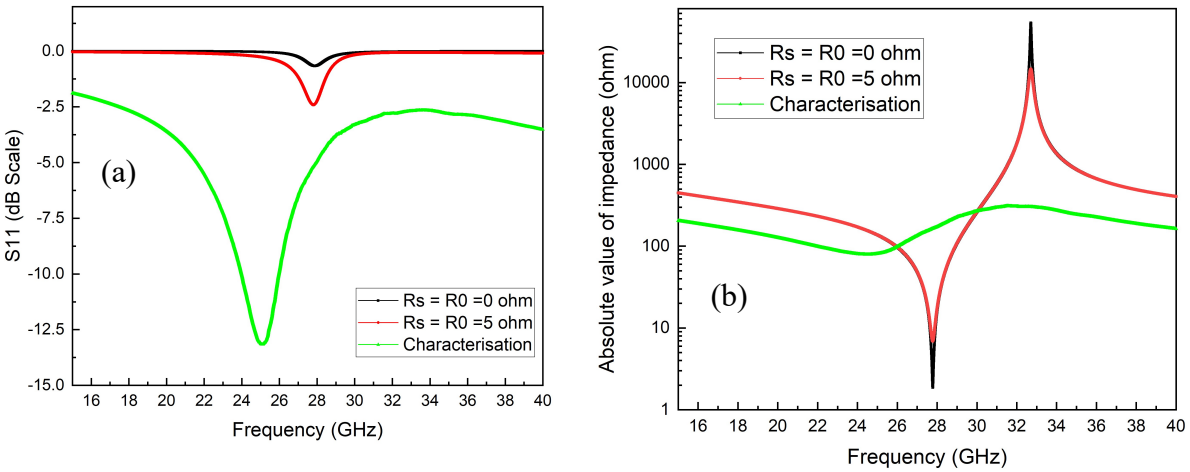

Figure 4.19 Simulation results of the BVD model of 240 nm thick $3R-MoS_2$ based FBAR from ADS without and with parasite resistances (a) S_{11} parameter; (b) Electrical Impedance.

These results based on simplified analytical calculations are quite different from the characterization results, which led us to use the Tuning function in ADS to search the fitted equivalent circuit [203]. We first proposed a circuit based on the same BVD model with C_0, C_m, L_m, R_m, R_s and R_0, then and tuned the lumped element values to fit the curves of S_{11} and electrical impedance as well as possible. Figure 4.20 and Table 4.5 show the optimized circuit and resulting parameters.

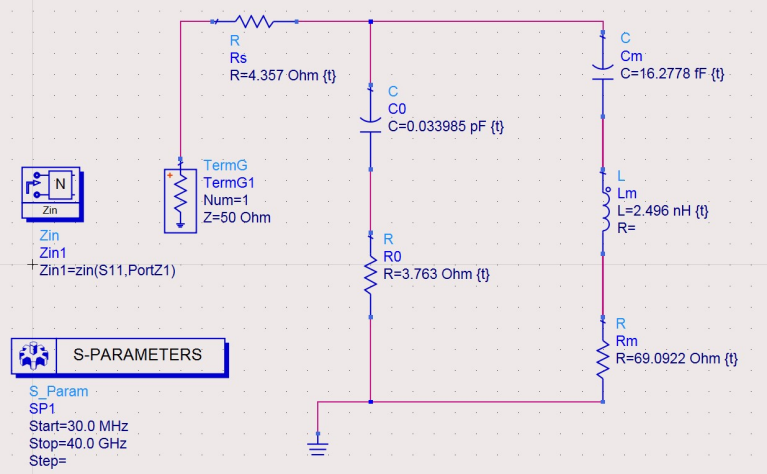

Figure 4.20 The circuit and the configuration of the performed optimization.

Figure 4.21 shows S_{11} parameters and electrical impedance issued from the initial characterization and simulated from the optimised circuit. We can see a good coherence between these two results especially in the resonance zone, some differences can be observed, but these differences are acceptable.

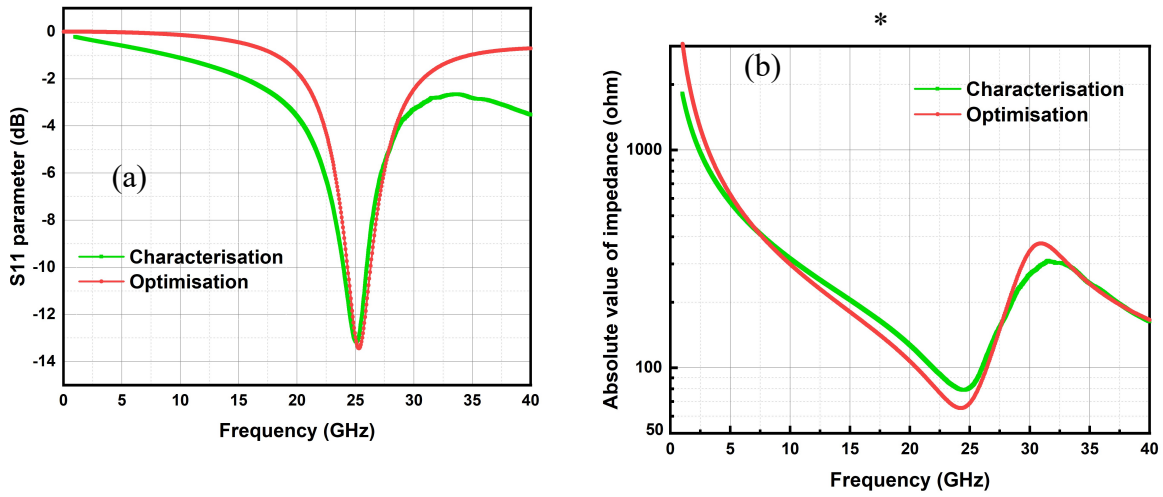

Figure 4.21 (a)Reflection parameter S_{11} and (b) Electrical impedance issued from the characterization and from the optimized model.

When comparing the values of lumped elements obtained from the optimization as listed in Table 4.5, to those from the analytical calculations, in Table 4.4, we can see that the capacitances C_0 and C_m iare about 2 and 2.5 times larger, respectively, L_m is nearly 1/2. Furthermore, this optimization process gives values of R_m, R_s and R_0, for the materials losses associated to the electrodes, the piezoelectric layer and the acoustic viscosity[204], which can hardly be determined by the theoretical calculations.

Table 4.5 Values of the lumped elements of the BVD model after the optimization process

Elements	Values
C_0	0.033985 pF
C_m	16.2779 fF
L_m	2.496 nH
R_m	69.0922 Ω
R_0	3.763 Ω
R_s	4.357 Ω

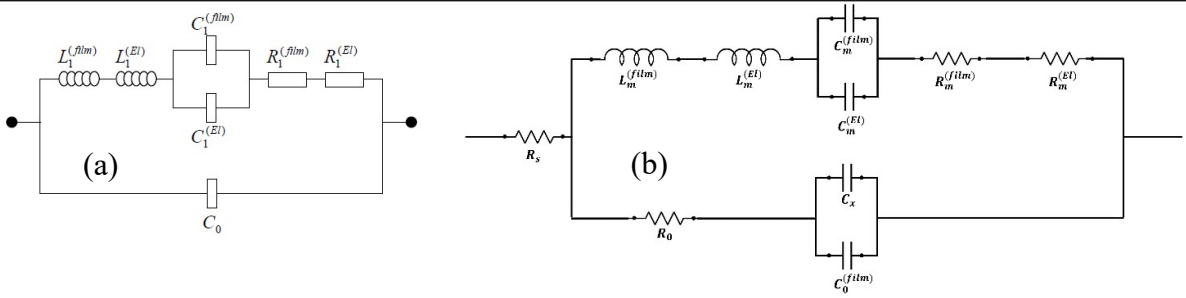

Figure 4.22 (a) Modified BVD model with thin electrodes[205]; (b)Proposed equivalent circuit.

Min-Chiang Chao *et al.* [205] proposed an equivalent circuit considering the impact of the top/bottom electrodes with the same thickness. This model adds the lumped elements $L_m^{(El)}$, $C_m^{(El)}$ *and* $R_m^{(El)}$ to describe wave propagation in electrodes, as shown in Figure 4.22 (a). For our case, as described in above, the static capacitance C_0 is nearly 2 times larger than that of the calculated value and the wave propagation in electrodes can usually not affect the static dielectric properties of the piezoelectric layer, thus we propose another capacitor C_x in parallel with the static capacitance of $3R-MoS_2$ layer to form a new C_0, the circuit is shown in Figure 4.22 (b), in this circuit, we also consider the material losses of electrodes and

piezoelectric layer by adding R_s and R_0. By using the calculated value in Table 4.4, we can therefore obtain the capacitance of C_x with 0.018638 pF, the origin of C_x is still under investigation. Then we can re-calculate all the values of these lumped values of electrodes and $3\mathrm{R}-\mathrm{MoS}_2$ layer by using equation (2.51) and (2.52) and combining with the circuit in Figure 4.22 (b), all these values are listed in Table 4.6.

Table 4.6 The values for lumped elements of proposed equivalent circuit

Elements	Values
C_x	0.018638 pF
$L_m^{(film)}$	2.496 nH
$L_m^{(El)}$	$-$
$C_m^{(film)}$	13.1124 fF
$C_m^{(El)}$	3.1655 fF
$R_m^{(film)}$	$0.84907\ \Omega$
$R_m^{(El)}$	$68.2431\ \Omega$

Since the material properties of $3\mathrm{R}-\mathrm{MoS}_2$ are still in investigation, we assume that the origin of capacitance of C_x may come from a higher dynamic permittivity of $3\mathrm{R}-\mathrm{MoS}_2$ during acoustic resonance, or, like we discussed above, the multi-layered structure of $3\mathrm{R}-\mathrm{MoS}_2$ is not compact, acoustic resonance may bring a shorten effective thickness of $3\mathrm{R}-\mathrm{MoS}_2$ layer, which may increase the effective capacitance of static C_0. These assumptions should be verified with further studies on $3\mathrm{R}-\mathrm{MoS}_2$ material properties. Besides, the electrodes are very thin and a phenomenon of oxidation of Al may occur, which could increase the resulting mechanical resistance and explain an estimated value of $R_m^{(El)}$ that appears to be quite large

Finally, this analysis points out a method to re-build the equivalent circuit, since the classic BVD model does not take the electrodes into account, and for the circuit in Figure 4.22 (a), we cannot calculate easily the values of the lumped elements of electrodes. By combining the characterization and calculation results, we can therefore re-build and complete the BVD model, though leaving the need for further physical explanation. Furthermore, such study should be applied to a set of reproducible devices in order to better validate the model and the physical origin of parameters.

Summary

In this Chapter, we presented first the characterization results of the 3R-MoS_2 flakes which were used for our devices. The characterization results include the measurements of thickness and piezoelectric constant. We focused the presentation of results for devices with five flakes thicknesses of 210, 220, 235, 240 and 290 nm, which exhibited visible resonance properties. These flakes have good flatness and uniformity. The characterization of piezoelectricity showed a d_{33} value of 2.5-3.5 pm/V.

Then the details of the seven-step fabrication process are presented, which requires well-controlled alignment. A few samples were found to be defective. The main problems in the fabrication process include non-uniform thickness of each acoustic Bragg mirror layer, the falling-off of the transferred 3R-MoS_2 after the deposition of the Al top electrode and the short circuit between signal and ground plans induced by alignment errors.

The RF characterizations are assisted by a homemade de-embedding program. After comparing the results of 4 different configurations, we chose the Open-Short profile, which removes at first the capacitive and then the inductive parasites.

A first prototype exhibited a resonance peak at 25 GHz with a 210 nm thick 3R-MoS_2 flake. Then, a set of five samples with different flake thicknesses all showed very high operating frequencies, more than 20 GHz. These devices showed a good inversely proportional relation between the resonance frequency and the 3R-MoS_2 flake thickness, and then the electromechanical coupling coefficient (k_t^2) is calculated to be 47.6%, which is much larger than that of common piezoelectric materials. What's more, the fabrication process went more and more mature, enhancing the devices electrical response, with a S_{11} parameter varying from -3 to -21 dB.

However, when comparing the characterization results with the simulation results presented in Chapter 3, the obtained resonance frequencies are more than twice. It means the real velocity of the longitudinal wave propagation is larger than that considered in the simulation, knowing that it is supposed to be mainly determined by the density and the elastic constant C_{33}. Considering that the density could be measured, it led us to consider a very high value of C_{33} of 900 GPa instead of that issued from DFT calculations.

Besides, we considered the atomic structure of $3R-MoS_2$ flakes, different from common dense piezoelectric materials, but rather composed by alternating $3R-MoS_2$ atomic layers and air gaps with Van der Waals interaction. Furthermore, we should consider that the thickness of the air gap and Van der Waals interaction force keep changing during the piezoelectric resonance, which makes the classic analytical solutions for an acoustic multilayer unsuitable to well model and understand the behaviour, a more powerful computation tool is needed. In this context, we proposed to consider an effective acoustic path method as a first attempt, by neglecting the interlayer air gaps and associated interfaces, and then treating this system as a uniform $3R-MoS_2$ layer with reduced thickness. By also increasing the initial C_{33} by an arbitrary value of 30% to consider the mechanical constraints, the retro-simulation also shows quite good results though still not exactly the same as characterization.

Finally, more studies should be performed to better understand the effective properties of $3R-MoS_2$, as very thin layer integrated in such a microstructure.

Chapter 5 Conclusions and prospects

Conclusions

The past few decades have witnessed the fast development of wireless telecommunication systems, such as mobile communication systems, global positioning systems, data transmission systems, etc. In these applications, RF acoustic devices play an important role. FBAR is a kind of acoustic resonator consisting of a piezoelectric thin film sandwiched by two electrodes[206]. The SMR is a particular configuration that integrates an acoustic Bragg reflector composed of alternating layers with high and low acoustic impedance to allow the mechanical resonance of the piezoelectric film at the surface while providing a robust mechanical structure[207]. FBARs are widely use as RF filters[208], oscillator[209] or sensors[210]. Nowadays, current FBARs cannot meet the requirements of high operating frequencies, as a key for increased sensor sensitivity, also with wide bandwidth and high quality coefficient (Q) of 5G telecommunication[211, 212]. Unfortunately, scaling down the thickness of conventional piezoelectric materials like AlN and ZnO to sub 1 µm while maintaining good piezoelectricity, which could allow higher frequencies, faces significant problems. Indeed, the inconsistency of orientation, the large number of defects near the surface and the surface roughness induced by the conventional deposition process lead to the degradation of piezoelectricity and disturb the propagation of acoustic waves[133, 134, 213].

MoS_2, as a type of 2D TMDs nanomaterial, is gaining more and more attention for its interesting electrical and mechanical properties. MoS_2 has three polytypes, 1T, 2H and 3R. Both 2H and 3R type MoS_2 can exist stably and 1T is a metastable state. Strong piezoelectricity was found in thin $2H-MoS_2$ flakes stacked with an even number of layers. However, piezoelectricity disappears with $2H-MoS_2$ with an odd number of layers because of reverse polarization directions of the bilayers. Recently, the asymmetric lattice structure of $3R-MoS_2$ has attracted much attention[137]. Indeed, its non-centrosymmetric trigonal crystalline structure with the space group of 3m, allows piezoelectricity for any number of layers. To design a resonator based on thin piezoelectric films operating at hyper frequencies, the coefficient d_{33} is one of the most important piezoelectric parameters. The d_{33} values of $3R-MoS_2$ flakes varies with their thickness and flatness [193].

In this thesis, we present the first theoretical and experimental study of the proof of concept of using ultrathin piezoelectric $3R-MoS_2$ flakes to fabricate FBAR (SMR type) with ultrahigh operation frequency.

We proposed at first a state-of-art of TMDs materials and of the current acoustic devices, highlighting that the material properties of $3R-MoS_2$ have not yet been explored. Most of the reported properties are issued from first-principle density-functional theory (DFT) calculation, however, many factors are not considered which can greatly influence the properties of $3R-MoS_2$. Due to the delicate fabrication process of SMR and also the special transfer process of $3R-MoS_2$ flakes, the mask and technological process should also be carefully designed. Along with basic analytical calculations, we performed finite element method (FEM) simulations to better understand the influence of the material properties and the wave propagation in 2D layered-structure materials.

Thus, based on the acoustic theories detailed in Chapter 2, we firstly developed and validated a reference model by considering a ZnO-based SMR. We performed successfully

the simulation in the FEM environment with 2D and 3D models, also a reduced 3D model, which allowed saving computational time by applying a kind of periodic condition. We could also highlight a way to smear spurious modes by applying a special design of the top electrode. Then we performed the design of a target $3R-MoS_2$ based SMR, limited to a 2D model because with a thickness of $3R-MoS_2$ flakes around a few hundred nanometres, the number of elements is important and thus the computational effort also. Taking into account material parameters of the literature, the simulation resulted in ultrahigh resonance frequency around 20 GHz.

A Butterworth-Van Dyke (BVD) equivalent circuit was also proposed for the ZnO and $3R-MoS_2$ based structures. After validating the SMR general design, the fabrication process was discussed and a mask was designed, with the SMR itself, as well as a coplanar waveguide (CPW) RF characterization access with a 50 Ω impedance matching. Furthermore, we considered an Open-Short de-embedding process to limit the electrical influence of this CPW access on the characterization results.

A set of samples was successfully fabricated with 5 different thicknesses of $3R-MoS_2$ flakes, 210, 220, 235, 240 and 290 nm. The characterization results of piezoelectricity measurements showed that a piezoelectric constant d_{33} of $3R-MoS_2$ flakes in the range from 2.5 to 3.5 pm/V. The main issues in the fabrication process include non-uniform thickness of each acoustic Bragg mirror layer, the falling-off of the transferred $3R-MoS_2$ after the deposition of the Al top electrode and the short circuit between signal and ground plans caused by alignment errors.

For these samples, the RF characterization showed very interesting results, with resonance frequencies over 20 GHz, inversely proportional to the $3R-MoS_2$ flake thickness. The electromechanical coupling coefficient (k_t^2) was calculated to be around 50%, which is a very impressive value compared to the other piezoelectric materials, less than 20%. This k_t^2 permits large passband when considering filter application. Furthermore, is has be noted an enhancement of the characteristics after each new sample, attesting an improved control of the technological process, with S_{11} parameter decreased from -3 down to -21 dB. By comparing with the simulation results, the difference especially in resonance frequency led us to propose two assumptions. First, the elastic constant C_{33} of $3R-MoS_2$ is much larger than that issued from the DFT calculation in the literature. A retro-simulation with C_{33} of 900 GPa showed a good coherence with the characterization results.

Secondly, we noticed the special atomic structure of $3R-MoS_2$ flakes, composed by alternating $3R-MoS_2$ atomic plan and air gap with Van der Waals interaction force changing during the resonance. The classic elastic acoustic theory seems invalid in this case. Therefore, we proposed a simplified effective acoustic path method to treat this problem, by considering the thickness of a "compacted" $3R-MoS_2$ as the effective acoustic path and the C_{33} can then be reduced to around 250 GPa. It is a first-step attempt to understand the mechanical resonance of $3R-MoS_2$. Both approaches provide results closer to the experimental ones, though still with discrepancies in both cases, thus further studies are expected.

Finally, based on the characterization results, we also proposed a BVD equivalent circuit, which shows a quite good fit with the characterization and should facilitate the integration of such SMR in further circuits design.

Prospects

The $3R-MoS_2$ based SMRs, as designed and fabricated, show very interesting performances and good potential for further applications. Meanwhile, at least four areas would need further investigation.

1. A better understanding of the material properties of $3R-MoS_2$. As pointed out in Chapters 3 and 4, the differences between the simulation and characterization results are mainly due to the material parameters considered for the simulations, especially the elastic and piezoelectric constants. Most of the material properties in the literature are from the DFT calculations, few experimental results are reported with contradictions between them. In the DFT calculation, many factors are not considered, such as impurities, internal constraints, temperature variations, etc. In addition, the first device became not functional (no resonance) after one week in air, leading to suspect an oxidation of the $3R-MoS_2$ flakes, that should still be more investigated. Therefore, the material properties of $3R-MoS_2$ should be better understood for better design and application, and structures integrating such films may be a way.
2. A better understanding of acoustic wave propagation in 2D nanomaterials with layered structure. As we have shown in Chapter 4, the fabricated devices exhibit much higher resonance frequencies, which highlights the peculiarity of wave propagation in 2D nanomaterials with layered structure in contrast to conventional piezoelectric materials that have a compact structure. Indeed, the layered structure of 2D nanomaterials consists of atomic layers and Van der Waals interactions. When acoustic resonance occurs, the Van der Waals force between the layers no longer remains at equilibrium and then begins to interact with the force caused by the piezoelectric effect, thus affecting the wave propagation. An analytical analysis based on the classical elastic theory was carried out for a unit structure "$3R-MoS_2$ atomic layer - Van der Waals interaction - $3R-MoS_2$ atomic layer", but structures in this study are made of hundreds of such monolayers, which makes it impossible to solve in this way. In this context, a deeper analysis should be performed to understand the electrical performances of the devices, especially in terms of Q factor.
3. A better understanding of acoustic wave propagation in the multilayer SMR structure. We have performed an analytical analysis of the FBAR structure without electrodes. The multilayer SMR structure with acoustic Bragg mirror can be modeled by using equivalent acoustic impedances, considering a thickness extensional mode (longitudinal wave perpendicular to the surface). However, when considering the dispersion curves of a ZnO-based SMR, there seems to be a superposition of propagating modes in the piezoelectric layer and also in the acoustic Bragg mirror. How these propagating acoustic modes affect the performance of the device should be studied in depth if one wants to improve the SMR performance.
4. An idea that is being investigated by our Singaporean partner, is the fabrication of FBAR with suspended membrane, in order to avoid the frequency bandwidth limitation due to acoustic Bragg mirror. Though leading to more fragile devices, it may facilitate getting a better knowledge of the piezoelectric material properties, before going back to the SMR structure for increased robustness.
5. As FBAR/SMR have huge applications in RF filtering and sensing, it is very promising to develop $3R-MoS_2$ based high working frequency FBAR/SMR RF filters and high sensitivity sensors.

Reference

1. Wells, J.C., *Longman pronunciation dictionary*. New ed. ed. 2000, Harlow: Longamn.
2. Skoog, D.A., F.J. Holler, and S.R. Crouch, *Principles of instrumental analysis*. 6th ed. / Douglas A. Skoog, F. James Holler, Stanley R. Crouch. ed. 2007, Belmont, CA ; United Kingdom: Thomson Brooks/Cole.
3. Curie, J. and P. Curie, *Développement par compression de l'électricité polaire dans les cristaux hémièdres à faces inclinées.* Bulletin de minéralogie, 1880. **3**(4): p. 90-93.
4. Curie, J. and P. Curie, *Contractions and expansions produced by voltages in hemihedral crystals with inclined faces.* Comptes Rendus, 1881. **93**: p. 1137-1140.
5. Manbachi, A. and R.S. Cobbold, *Development and application of piezoelectric materials for ultrasound generation and detection.* Ultrasound, 2011. **19**(4): p. 187-196.
6. Safari, A. and E.K. Akdogan, *Piezoelectric and acoustic materials for transducer applications*. 2008: Springer Science & Business Media.
7. Casini, M., *Smart buildings: Advanced materials and nanotechnology to improve energy-efficiency and environmental performance*. 2016: Woodhead Publishing.
8. Mishra, S., et al., *Advances in piezoelectric polymer composites for energy harvesting applications: a systematic review.* Macromolecular Materials and Engineering, 2019. **304**(1): p. 1800463.
9. Arnau, A., *Piezoelectric transducers and applications*. Vol. 2004. 2004: Springer.
10. Wang, Z.L. and W. Wu, *Piezotronics and piezo-phototronics: fundamentals and applications.* National Science Review, 2014. **1**(1): p. 62-90.
11. Newnham, R.E., *Properties of materials: anisotropy, symmetry, structure*. 2005: Oxford University Press on Demand.
12. Wang, Z.L., *Piezopotential gated nanowire devices: Piezotronics and piezo-phototronics.* Nano Today, 2010. **5**(6): p. 540-552.
13. Wu, M., et al., *Acoustofluidic separation of cells and particles.* Microsystems & nanoengineering, 2019. **5**(1): p. 1-18.
14. Ruppel, C.C., *Acoustic wave filter technology–a review.* IEEE transactions on ultrasonics, ferroelectrics, and frequency control, 2017. **64**(9): p. 1390-1400.
15. Lakin, K.M. *Thin film resonator technology*. in *IEEE International Frequency Control Symposium and PDA Exhibition Jointly with the 17th European Frequency and Time Forum, 2003. Proceedings of the 2003*. 2003. IEEE.
16. Wright, P. *A review of SAW resonator filter technology*. in *IEEE 1992 Ultrasonics Symposium Proceedings*. 1992. IEEE.
17. Makkonen, T., et al., *Estimating materials parameters in thin-film BAW resonators using measured dispersion curves.* ieee transactions on ultrasonics, ferroelectrics, and frequency control, 2004. **51**(1): p. 42-51.
18. Campbell, C., *Surface acoustic wave devices and their signal processing applications*. 2012: Elsevier.
19. Weigel, R., et al., *Microwave acoustic materials, devices, and applications.* IEEE Transactions on microwave theory and techniques, 2002. **50**(3): p. 738-749.
20. Tirado, J.A.V., *Bulk acoustic wave resonators and their application to microwave devices*. 2010, Universitat Autònoma de Barcelona.
21. Tummala, R.R., *System on package: miniaturization of the entire system*. 2008: McGraw-Hill Education.
22. Morgan, D., *Surface acoustic wave filters: With applications to electronic communications and signal processing*. 2010: Academic Press.
23. Hashimoto, K.-y., *RF bulk acoustic wave filters for communications*. 2009: Artech House.
24. Voinova, M.V., *On mass loading and dissipation measured with acoustic wave sensors: A review.* Journal of Sensors, 2009. **2009**.

25. Binder, A. and R. Fachberger, *Wireless SAW temperature sensor system for high-speed high-voltage motors.* IEEE Sensors Journal, 2010. **11**(4): p. 966-970.
26. Jakoby, B., H. Eisenschmid, and F. Herrmann, *The potential of microacoustic SAW-and BAW-based sensors for automotive applications-a review.* IEEE Sensors Journal, 2002. **2**(5): p. 443-452.
27. Nomura, T., A. Saitoh, and Y. Horikoshi, *Measurement of acoustic properties of liquid using liquid flow SH-SAW sensor system.* Sensors and Actuators B: Chemical, 2001. **76**(1-3): p. 69-73.
28. Länge, K., B.E. Rapp, and M. Rapp, *Surface acoustic wave biosensors: a review.* Analytical and bioanalytical chemistry, 2008. **391**(5): p. 1509-1519.
29. Viktorov, I.A., *Rayleigh and Lamb waves: physical theory and applications*. 1967: Plenum Press.
30. Love, A.E.H., *Some Problems of Geodynamics: Being an Essay to which the Adams Prize in the University of Cambridge was Adjudged in 1911*. Vol. 911. 1911: University Press.
31. White, R.M. and F.W. Voltmer, *Direct piezoelectric coupling to surface elastic waves.* Applied physics letters, 1965. **7**(12): p. 314-316.
32. Nakahata, H., et al., *Diamond-based surface acoustic wave devices.* Semiconductor science and technology, 2003. **18**(3): p. S96.
33. Nyikayaramba, G. and B. Murmann, *S-Parameter-Based Defect Localization for Ultrasonic Guided Wave SHM.* Aerospace, 2020. **7**(3): p. 33.
34. Rube, M., et al., *Unconventional protocol for SAW sensor: multi-physic response enrichment in liquid medium.* IEEE Sensors Journal, 2021. **22**(12): p. 11345-11354.
35. Hashimoto, K.-y. and K.-Y. Hashimoto, *Surface acoustic wave devices in telecommunications*. Vol. 116. 2000: Springer.
36. Koskela, J., et al., *Acoustic loss mechanisms in leaky SAW resonators on lithium tantalate.* ieee transactions on ultrasonics, ferroelectrics, and frequency control, 2001. **48**(6): p. 1517-1526.
37. Giovannini, M., et al. *Spurious mode suppression via apodization for 1 GHz AlN contour-mode resonators*. in *2012 IEEE International Frequency Control Symposium Proceedings*. 2012. IEEE.
38. Bausk, E.V., *Optimization of broadband withdrawal weighted interdigital transducers for high selective SAW filters.* IEEE transactions on ultrasonics, ferroelectrics, and frequency control, 1999. **46**(5): p. 1276-1282.
39. Marshall, F.G., C. Newton, and E. Paige, *Theory and design of the surface acoustic wave multistrip coupler.* IEEE Transactions on Microwave Theory and Techniques, 1973. **21**(4): p. 206-215.
40. World, R.W. *Difference between SAW filters types | IIDT, DMS, Ladder type*. 2012; Available from: https://www.rfwireless-world.com/Terminology/Difference-between-SAW-filter-types-IIDT-DMS-and-Ladder.html.
41. Morita, T., et al. *Wideband low loss double mode SAW filters*. in *IEEE 1992 Ultrasonics Symposium Proceedings*. 1992. IEEE.
42. PersistenceMarketResearch. *Surface Acoustic Wave Filter Market* 2020; Available from: https://www.persistencemarketresearch.com/market-research/surface-acoustic-wave-filter-market.asp.
43. Pohl, A., *A review of wireless SAW sensors.* IEEE transactions on ultrasonics, ferroelectrics, and frequency control, 2000. **47**(2): p. 317-332.
44. Meyer, J.M., et al., *Thin-Film-Based SAW Magnetic Field Sensors.* Sensors, 2021. **21**(24): p. 8166.
45. Durdaut, P., et al., *Phase Noise of SAW Delay Line Magnetic Field Sensors.* Sensors, 2021. **21**(16): p. 5631.
46. Schmalz, J., et al., *Multi-mode love-wave SAW magnetic-field sensors.* Sensors, 2020. **20**(12): p. 3421.
47. Ren, W., et al., *Design and Optimization of a BAW Magnetic Sensor Based on Magnetoelectric Coupling.* Micromachines, 2022. **13**(2): p. 206.
48. Chen, S., et al. *Modeling of magnetic sensor based on BAW magnetoelectric coupling micro-heterostructure*. in *2021 IEEE 16th International Conference on Nano/Micro Engineered and Molecular Systems (NEMS)*. 2021. IEEE.

49. Xu, Z. and Y.J. Yuan, *Implementation of guiding layers of surface acoustic wave devices: A review.* Biosensors and Bioelectronics, 2018. **99**: p. 500-512.
50. Rube, M., et al. *A Dual Love wave and Impedance-based Sensor: Response Enrichment*. in *2020 IEEE SENSORS*. 2020. IEEE.
51. Kondoh, J., et al. *Development of SH-SAW Sensing System for Liquids*. in *2007 IEEE International Frequency Control Symposium Joint with the 21st European Frequency and Time Forum*. 2007. IEEE.
52. Wohltjen, H. and R. Dessy, *Surface acoustic wave probe for chemical analysis. I. Introduction and instrument description.* Analytical chemistry, 1979. **51**(9): p. 1458-1464.
53. Wohltjen, H. and R. Dessy, *Surface acoustic wave probes for chemical analysis. II. Gas chromatography detector.* Analytical Chemistry, 1979. **51**(9): p. 1465-1470.
54. Sil, D., et al., *Palladium nanoparticle-based surface acoustic wave hydrogen sensor.* ACS applied materials & interfaces, 2015. **7**(10): p. 5709-5714.
55. Luo, W., et al., *A surface acoustic wave H2S gas sensor employing nanocrystalline SnO2 thin film.* Sensors and Actuators B: Chemical, 2013. **176**: p. 746-752.
56. Asad, M. and M.H. Sheikhi, *Surface acoustic wave based H2S gas sensors incorporating sensitive layers of single wall carbon nanotubes decorated with Cu nanoparticles.* Sensors and Actuators B: Chemical, 2014. **198**: p. 134-141.
57. Lim, C., et al., *Development of SAW-based multi-gas sensor for simultaneous detection of CO2 and NO2.* Sensors and Actuators B: Chemical, 2011. **154**(1): p. 9-16.
58. Thomas, S., et al., *Graphene-coated Rayleigh SAW resonators for NO2 detection.* Procedia Engineering, 2014. **87**: p. 999-1002.
59. Wang, W., et al., *Development of a room temperature SAW methane gas sensor incorporating a supramolecular cryptophane a coating.* Sensors, 2016. **16**(1): p. 73.
60. Lee, Y., et al., *Development of a SAW gas sensor for monitoring SO2 gas.* Sensors and Actuators A: Physical, 1998. **64**(2): p. 173-178.
61. Tang, Y.-L., et al., *Ammonia gas sensors based on ZnO/SiO2 bi-layer nanofilms on ST-cut quartz surface acoustic wave devices.* Sensors and Actuators B: Chemical, 2014. **201**: p. 114-121.
62. Westafer, R.S., et al., *Detection of ppb ozone using a dispersive surface acoustic wave reflective delay line with integrated reference signal.* Sensors and Actuators B: Chemical, 2014. **192**: p. 406-413.
63. Zheng, P., et al., *High-temperature langasite SAW oxygen sensor.* IEEE transactions on ultrasonics, ferroelectrics, and frequency control, 2011. **58**(8): p. 1538-1540.
64. Sadek, A., et al., *A layered surface acoustic wave gas sensor based on a polyaniline/In2O3 nanofibre composite.* Nanotechnology, 2006. **17**(17): p. 4488.
65. Reichert, J., W. Coerdt, and H. Ache, *Development of a surface acoustic wave sensor array for the detection of methanol in fuel vapours.* Sensors and Actuators B: Chemical, 1993. **13**(1-3): p. 293-296.
66. Tang, K.-T., C.-H. Li, and S.-W. Chiu, *An electronic-nose sensor node based on a polymer-coated surface acoustic wave array for wireless sensor network applications.* Sensors, 2011. **11**: p. 4609-4621.
67. Wang, Y., et al., *Real-time detection of styrene using SAW sensors based on hexafluoroisopropanol group functionalized hydrogen-bond acidic polymers.* Sensors and Actuators B: Chemical, 2015. **206**: p. 252-257.
68. Houser, E.J., et al., *Rational materials design of sorbent coatings for explosives: applications with chemical sensors.* Talanta, 2001. **54**(3): p. 469-485.
69. Kannan, G., et al., *Adsorption studies of carbowax coated surface acoustic wave (SAW) sensor for 2, 4-dinitro toluene (DNT) vapour detection.* Sensors and Actuators B: Chemical, 2004. **101**(3): p. 328-334.
70. Singh, G., S. Kim, and K. Lee, *Development of a highly sensitive and portable particulate matter SAW sensor and interface electronics.* Sensors and Actuators A: Physical, 2022: p. 113641.

71. Wang, W., et al., *A novel wireless, passive CO2 sensor incorporating a surface acoustic wave reflective delay line.* Smart Materials and Structures, 2007. **16**(4): p. 1382.
72. Xu, F.-Q., et al., *Development of a wireless and passive SAW-based chemical sensor for organophosphorous compound detection.* Sensors, 2015. **15**(12): p. 30187-30198.
73. Hur, Y., et al., *Development of an SH-SAW sensor for the detection of DNA hybridization.* Sensors and Actuators A: Physical, 2005. **120**(2): p. 462-467.
74. Kim, S.-G., et al., *A highly sensitive and label free biosensing platform for wireless sensor node system.* Biosensors and Bioelectronics, 2013. **50**: p. 362-367.
75. Zhang, Y., et al., *A surface acoustic wave biosensor synergizing DNA-mediated in situ silver nanoparticle growth for a highly specific and signal-amplified nucleic acid assay.* Analyst, 2017. **142**(18): p. 3468-3476.
76. Cai, H.-L., et al., *A third-order mode high frequency biosensor with atomic resolution.* Biosensors and Bioelectronics, 2015. **71**: p. 261-268.
77. Agostini, M., G. Greco, and M. Cecchini, *A Rayleigh surface acoustic wave (R-SAW) resonator biosensor based on positive and negative reflectors with sub-nanomolar limit of detection.* Sensors and Actuators B: Chemical, 2018. **254**: p. 1-7.
78. Choi, Y.-S., et al., *Increase in detection sensitivity of surface acoustic wave biosensor using triple transit echo wave.* Applied Physics Letters, 2018. **113**(8): p. 083702.
79. Jandas, P., et al., *Highly selective and label-free Love-mode surface acoustic wave biosensor for carcinoembryonic antigen detection using a self-assembled monolayer bioreceptor.* Applied Surface Science, 2020. **518**: p. 146061.
80. Jandas, P., et al., *Highly stable, love-mode surface acoustic wave biosensor using Au nanoparticle-MoS2-rGO nano-cluster doped polyimide nanocomposite for the selective detection of carcinoembryonic antigen.* Materials Chemistry and Physics, 2020. **246**: p. 122800.
81. Brugger, M.S., et al., *Orchestrating cells on a chip: Employing surface acoustic waves towards the formation of neural networks.* Physical Review E, 2018. **98**(1): p. 012411.
82. Peng, Y.-C., et al., *A novel rapid test to detect Anti-SARS-CoV-2 N protein IgG based on shear horizontal surface acoustic wave (SH-SAW).* Diagnostics, 2021. **11**(10): p. 1838.
83. Kumar, M. and D. Bhadu, *Design performance and frequency response analysis of SAW-based sensor for dichloromethane gas sensing amidst the COVID-19.* Journal of Vibration Engineering & Technologies, 2021. **9**(5): p. 725-732.
84. Bi, F. and B.P. Barber, *Bulk acoustic wave RF technology.* IEEE Microwave Magazine, 2008. **9**.
85. Newell, W., *Face-mounted piezoelectric resonators.* Proceedings of the IEEE, 1965. **53**(6): p. 575-581.
86. Sliker, T. and D. Roberts, *A thin-film CdS-quartz composite resonator.* Journal of Applied Physics, 1967. **38**(5): p. 2350-2358.
87. Grudkowski, T., et al., *Fundamental-mode VHF/UHF minature acoustic resonators and filters on silicon.* Applied Physics Letters, 1980. **37**(11): p. 993-995.
88. Lakin, K. and J. Wang, *Acoustic bulk wave composite resonators.* Applied Physics Letters, 1981. **38**(3): p. 125-127.
89. Ruby, R. *Micromachined cellular filters*. in *1996 IEEE MTT-S International Microwave Symposium Digest*. 1996. IEEE.
90. Ruby, R., et al., *PCS 1900 MHz duplexer using thin film bulk acoustic resonators (FBARs).* Electronics letters, 1999. **35**(10): p. 794-795.
91. Aigner, R., *MEMS in RF filter applications: Thin-film bulk acoustic wave technology.* Sensors Update, 2003. **12**(1): p. 175-210.
92. Wang, L.-P., et al. *Method of fabricating multiple-frequency film bulk acoustic resonators in a single chip*. in *2006 IEEE International Frequency Control Symposium and Exposition*. 2006. IEEE.
93. Fattinger, G.G. *BAW resonator design considerations-an overview*. in *2008 IEEE International Frequency Control Symposium*. 2008. IEEE.

94. Loebl, H., et al., *Piezoelectric thin AlN films for bulk acoustic wave (BAW) resonators.* Materials Chemistry and Physics, 2003. **79**(2-3): p. 143-146.
95. Kim, E.K., et al., *Air gap type thin film bulk acoustic resonator fabrication using simplified process.* Thin Solid Films, 2006. **496**(2): p. 653-657.
96. Zhang, Y. and D. Chen, *Multilayer integrated film bulk acoustic resonators*. 2012: Springer Science & Business Media.
97. Villa-López, F.H., et al., *Design and modelling of solidly mounted resonators for low-cost particle sensing.* Measurement Science and Technology, 2015. **27**(2): p. 025101.
98. Yokoyama, T., et al. *New electrode material for low-loss and high-Q FBAR filters*. in *IEEE Ultrasonics Symposium, 2004*. 2004. IEEE.
99. Pang, W., et al. *High Q film bulk acoustic resonator from 2.4 to 5.1 GHz*. in *17th IEEE International Conference on Micro Electro Mechanical Systems. Maastricht MEMS 2004 Technical Digest*. 2004. IEEE.
100. Caspers, F., *RF engineering basic concepts: S-parameters.* arXiv preprint arXiv:1201.2346, 2012.
101. Bai, X., et al., *The thin film bulk acoustic wave resonator based on single-crystalline 4 3 ○ Y-cut lithium niobate thin films.* Aip Advances, 2020. **10**(7): p. 075002.
102. Aigner, R., et al. *RF-filters in mobile phone applications*. in *TRANSDUCERS'03. 12th International Conference on Solid-State Sensors, Actuators and Microsystems. Digest of Technical Papers (Cat. No. 03TH8664)*. 2003. IEEE.
103. Nguyen, N.T.B., *High-Q bulk acoustic wave resonators for RF filter applications.* 2019.
104. Fattinger, G., et al. *Optimization of acoustic dispersion for high performance thin film BAW resonators*. in *IEEE Ultrasonics Symposium, 2005.* 2005. IEEE.
105. Ruby, R., et al. *The effect of perimeter geometry on FBAR resonator electrical performance*. in *IEEE MTT-S International Microwave Symposium Digest, 2005.* 2005. IEEE.
106. Lee, J.-H., et al. *Optimization of frame-like film bulk acoustic resonators for suppression of spurious lateral modes using finite element method*. in *IEEE Ultrasonics Symposium, 2004*. 2004. IEEE.
107. Chatras, M., et al., *Modeling and Design of BAW Resonators and Filters for Integration in a UMTS Transmitter*, in *Modeling and Measurement Methods for Acoustic Waves and for Acoustic Microdevices*. 2013, InTech Rijeka. p. 323-354.
108. Aigner, R. *SAW and BAW technologies for RF filter applications: A review of the relative strengths and weaknesses*. in *2008 IEEE Ultrasonics Symposium*. 2008. IEEE.
109. researchandmarkets. *Bulk Acoustic Wave (BAW) Filters - Global Market Trajectory & Analytics*. 2021; Available from: https://www.researchandmarkets.com/reports/5301638/bulk-acoustic-wave-baw-filters-global-market.
110. Research, M.M. *Global Bulk-Acoustic-Wave (BAW) Filters Market – Industry Analysis and Forecast (2019-2027) – By Type, Application, and Region.* 2021; Available from: https://www.maximizemarketresearch.com/market-report/global-bulk-acoustic-wave-baw-filters-market/69367/.
111. Chen, Y., et al., *Multifunctional ZnO-based thin-film bulk acoustic resonator for biosensors.* Journal of electronic materials, 2009. **38**(8): p. 1605-1611.
112. Zhang, Y., et al., *Film bulk acoustic resonators (FBARs) as biosensors: A review.* Biosensors and Bioelectronics, 2018. **116**: p. 1-15.
113. Mujahid, A., A. Afzal, and F.L. Dickert, *An overview of high frequency acoustic sensors—QCMs, SAWs and FBARs—chemical and biochemical applications.* Sensors, 2019. **19**(20): p. 4395.
114. Lin, A., et al. *Explosive trace detection with FBAR-based sensor*. in *2008 IEEE 21st International Conference on Micro Electro Mechanical Systems*. 2008. IEEE.
115. Benetti, M., et al., *Microbalance chemical sensor based on thin-film bulk acoustic wave resonators.* Applied Physics Letters, 2005. **87**(17): p. 173504.
116. Yan, X., et al., *A prototype portable instrument employing micro-preconcentrator and FBAR sensor for the detection of chemical warfare agents.* Nanotechnology and Precision Engineering, 2022. **5**(1): p. 013005.

117. Zeng, G., et al., *Detection and discrimination of volatile organic compounds using a single film bulk acoustic wave resonator with temperature modulation as a multiparameter virtual sensor array.* ACS sensors, 2019. **4**(6): p. 1524-1533.
118. Gao, F., et al., *Dual transduction on a single sensor for gas identification.* Sensors and Actuators B: Chemical, 2019. **278**: p. 21-27.
119. Gabl, R., et al. *Novel integrated FBAR sensors: a universal technology platform for bio-and gas-detection*. in *SENSORS, 2003 IEEE*. 2003. IEEE.
120. Gabl, R., et al., *First results on label-free detection of DNA and protein molecules using a novel integrated sensor technology based on gravimetric detection principles.* Biosensors and Bioelectronics, 2004. **19**(6): p. 615-620.
121. Weber, J., et al., *Shear mode FBARs as highly sensitive liquid biosensors.* Sensors and Actuators A: Physical, 2006. **128**(1): p. 84-88.
122. Zhang, H., et al., *Sequence specific label-free DNA sensing using film-bulk-acoustic-resonators.* IEEE Sensors Journal, 2007. **7**(12): p. 1587-1588.
123. Zheng, D., et al., *Streptavidin modified ZnO film bulk acoustic resonator for detection of tumor marker mucin 1.* Nanoscale Research Letters, 2016. **11**(1): p. 1-8.
124. Lin, A., et al. *Label-free detection of prostate-specific antigen with FBAR-based sensor with oriented antibody immobilization*. in *2011 IEEE International Ultrasonics Symposium*. 2011. IEEE.
125. Zhao, X., et al., *Label-free detection of human prostate-specific antigen (hPSA) using film bulk acoustic resonators (FBARs).* Sensors and Actuators B: Chemical, 2014. **190**: p. 946-953.
126. Chen, D., et al., *Film bulk acoustic resonator based biosensor for detection of cancer serological marker.* Electronics letters, 2011. **47**(21): p. 1169-1170.
127. Li, Y.-N.R., et al., *Beam management in millimeter-wave communications for 5G and beyond.* IEEE Access, 2020. **8**: p. 13282-13293.
128. Hara, M., et al., *Super-high-frequency band filters configured with air-gap-type thin-film bulk acoustic resonators.* Japanese journal of applied physics, 2010. **49**(7S): p. 07HD13.
129. Link, S., et al. *An A1 Mode Resonator at 12 GHz using 160nm Lithium Niobate Suspended Thin Film*. in *2021 IEEE International Ultrasonics Symposium (IUS)*. 2021. IEEE.
130. Chang, Y.-C., et al., *Effects of thermal annealing on the characteristics of high frequency fbar devices.* Coatings, 2021. **11**(4): p. 397.
131. Kadota, M., F. Yamashita, and S. Tanaka, *4 and 7 GHz solidly mounted thickness extension mode bulk acoustic wave resonators using 36ºY LiNbO3.* Japanese Journal of Applied Physics, 2023.
132. Takei, K., et al., *Toward flexible and wearable human‐interactive health‐monitoring devices.* Advanced healthcare materials, 2015. **4**(4): p. 487-500.
133. Huang, C.-L., K.-W. Tay, and L. Wu, *Fabrication and performance analysis of film bulk acoustic wave resonators.* Materials Letters, 2005. **59**(8-9): p. 1012-1016.
134. Larson, J., S.R. Gilbert, and B. Xu. *PZT material properties at UHF and microwave frequencies derived from FBAR measurements*. in *IEEE Ultrasonics Symposium, 2004*. 2004. IEEE.
135. Jacoby, M. *2-D materials go beyond graphene*. 2017; Available from: https://cen.acs.org/articles/95/i22/2-D-materials-beyond-graphene.html.
136. Gupta, A., T. Sakthivel, and S. Seal, *Recent development in 2D materials beyond graphene.* Progress in Materials Science, 2015. **73**: p. 44-126.
137. Strachan, J., A.F. Masters, and T. Maschmeyer, *3R-MoS2 in Review: History, Status, and Outlook.* ACS Applied Energy Materials, 2021. **4**(8): p. 7405-7418.
138. Huang, X., Z. Zeng, and H. Zhang, *Metal dichalcogenide nanosheets: preparation, properties and applications.* Chemical Society Reviews, 2013. **42**(5): p. 1934-1946.
139. Novoselov, K.S., et al., *Electric field effect in atomically thin carbon films.* science, 2004. **306**(5696): p. 666-669.
140. Novoselov, K., et al., *2D materials and van der Waals heterostructures.* Science, 2016. **353**(6298).
141. Lin, M.-W., et al., *Room-temperature high on/off ratio in suspended graphene nanoribbon field-effect transistors.* Nanotechnology, 2011. **22**(26): p. 265201.

142. Bhimanapati, G.R., et al., *Recent advances in two-dimensional materials beyond graphene.* ACS nano, 2015. **9**(12): p. 11509-11539.
143. Novoselov, K.S., et al., *Two-dimensional atomic crystals.* Proceedings of the National Academy of Sciences, 2005. **102**(30): p. 10451-10453.
144. Xu, H., et al., *Observation of gap opening in 1T′ phase MoS2 nanocrystals.* Nano letters, 2018. **18**(8): p. 5085-5090.
145. Tian, H., et al., *Optoelectronic devices based on two-dimensional transition metal dichalcogenides.* Nano Research, 2016. **9**(6): p. 1543-1560.
146. Wang, S., et al., *Broadband few‐layer MoS2 saturable absorbers.* Advanced materials, 2014. **26**(21): p. 3538-3544.
147. Radisavljevic, B., et al., *Single-layer MoS 2 transistors.* Nature nanotechnology, 2011. **6**(3): p. 147-150.
148. Duerloo, K.-A.N., M.T. Ong, and E.J. Reed, *Intrinsic piezoelectricity in two-dimensional materials.* The Journal of Physical Chemistry Letters, 2012. **3**(19): p. 2871-2876.
149. Ye, M., et al. *Recent advancement on the optical properties of two-dimensional molybdenum disulfide (MoS2) thin films*. in *Photonics*. 2015. Multidisciplinary Digital Publishing Institute.
150. Houben, L., et al., *Diffraction from disordered stacking sequences in MoS2 and WS2 fullerenes and nanotubes.* The Journal of Physical Chemistry C, 2012. **116**(45): p. 24350-24357.
151. Lee, Y.H., et al., *Synthesis of large‐area MoS2 atomic layers with chemical vapor deposition.* Advanced materials, 2012. **24**(17): p. 2320-2325.
152. Liu, K.-K., et al., *Growth of large-area and highly crystalline MoS2 thin layers on insulating substrates.* Nano letters, 2012. **12**(3): p. 1538-1544.
153. Krishnan, U., et al., *A synoptic review of MoS2: Synthesis to applications.* Superlattices and Microstructures, 2019. **128**: p. 274-297.
154. Sharma, M., A. Singh, and R. Singh, *Monolayer MoS2 Transferred on Arbitrary Substrates for Potential Use in Flexible Electronics.* ACS Applied Nano Materials, 2020. **3**(5): p. 4445-4453.
155. Wu, W., et al., *Piezoelectricity of single-atomic-layer MoS 2 for energy conversion and piezotronics.* Nature, 2014. **514**(7523): p. 470-474.
156. Tan, D., M. Willatzen, and Z.L. Wang, *Prediction of strong piezoelectricity in 3R-MoS2 multilayer structures.* Nano Energy, 2019. **56**: p. 512-515.
157. Konabe, S. and T. Yamamoto, *Piezoelectric coefficients of bulk 3R transition metal dichalcogenides.* Japanese Journal of Applied Physics, 2017. **56**(9): p. 098002.
158. Makkar, P. and N.N. Ghosh, *A review on the use of DFT for the prediction of the properties of nanomaterials.* RSC Advances, 2021. **11**(45): p. 27897-27924.
159. Castellanos‐Gomez, A., et al., *Elastic properties of freely suspended MoS2 nanosheets.* Advanced materials, 2012. **24**(6): p. 772-775.
160. Kim, S.J., et al., *Materials for flexible, stretchable electronics: graphene and 2D materials.* Annual Review of Materials Research, 2015. **45**: p. 63-84.
161. Pu, J., et al., *Highly flexible MoS2 thin-film transistors with ion gel dielectrics.* Nano letters, 2012. **12**(8): p. 4013-4017.
162. Gupta, D., V. Chauhan, and R. Kumar, *A comprehensive review on synthesis and applications of molybdenum disulfide (MoS2) material: Past and recent developments.* Inorg. Chem. Commun, 2020. **121**: p. 108200.
163. Mutyala, K.C., et al., *Graphene-MoS2 ensembles to reduce friction and wear in DLC-Steel contacts.* Carbon, 2019. **146**: p. 524-527.
164. Pham, T., et al., *MoS2-based optoelectronic gas sensor with sub-parts-per-billion limit of NO2 gas detection.* ACS nano, 2019. **13**(3): p. 3196-3205.
165. Liu, J., et al., *Ultrasensitive monolayer MoS2 field-effect transistor based DNA sensors for screening of down syndrome.* Nano letters, 2019. **19**(3): p. 1437-1444.

166. Joseph, N., P.M. Shafi, and A.C. Bose, *Recent advances in 2D-MoS2 and its composite nanostructures for supercapacitor electrode application.* Energy & Fuels, 2020. **34**(6): p. 6558-6597.
167. Sarkar, D., et al., *Expanding interlayer spacing in MoS2 for realizing an advanced supercapacitor.* ACS Energy Letters, 2019. **4**(7): p. 1602-1609.
168. Pollard, H., *Resonant behaviour of an acoustical transmission line.* Australian Journal of Physics, 1962. **15**(4): p. 513-526.
169. Bongard, F., H. Lissek, and J.R. Mosig, *Acoustic transmission line metamaterial with negative/zero/positive refractive index.* physical Review B, 2010. **82**(9): p. 094306.
170. Zhu, F., Z.-h. Qian, and B. Wang, *Wave propagation in piezoelectric layered structures of film bulk acoustic resonators.* Ultrasonics, 2016. **67**: p. 105-111.
171. Achenbach, J., *Wave propagation in elastic solids*. 2012: Elsevier.
172. Murray, S.L., et al. *Effect of mesa-shaping on spurious modes in ZnO/Si bulk-wave composite resonators*. 1983. Institute of Electrical and Electronics Engineers.
173. Gaydazhiev, D.G., *Acoustic Dispersion Analysis of the Resonant Modes in FBAR.*
174. Mason, W.P., *Electromechanical Transducers and Wave Filters*. 1948: D. Van Nostrand Company.
175. Rosenbaum, J.F., *Bulk Acoustic Wave Theory and Devices*. 1988: Artech House.
176. Nor, N., et al. *The influence of design parameters on the performance of FBAR in 15–19 GHz*. in *AIP conference proceedings*. 2018. AIP Publishing LLC.
177. Larson, J.D., et al. *Modified Butterworth-Van Dyke circuit for FBAR resonators and automated measurement system*. in *2000 IEEE ultrasonics symposium. proceedings. an international symposium (Cat. No. 00CH37121)*. 2000. IEEE.
178. Jose, S., et al., *Optimized reflector stacks for solidly mounted bulk acoustic wave resonators.* IEEE transactions on ultrasonics, ferroelectrics, and frequency control, 2010. **57**(12): p. 2753-2763.
179. Gu, P.-f. and Z.-r. Zheng, *Design of non-polarizing thin film edge filters.* Journal of Zhejiang University-SCIENCE A, 2006. **7**(6): p. 1037-1040.
180. Logan, D.L., *A first course in the finite element method*. 2016: Cengage Learning.
181. *COMSOL Tutorial <<Thin-Film BAW Composite Resonator>>.* 2021; Available from: https://www.comsol.fr/model/thin-film-baw-composite-resonator-5784.
182. *Introduction to COMSOL Multiphysics*. Available from: https://www.comsol.fr/comsol-multiphysics.
183. Mai, L., et al., *Design and fabrication of ZnO-based FBAR microwave devices for mobile WiMAX applications.* IEEE microwave and wireless components letters, 2007. **17**(12): p. 867-869.
184. Mai, L., et al., *A comprehensive investigation of thermal treatment effects on resonance characteristics in FBAR devices.* Microwave and optical technology letters, 2005. **47**(5): p. 459-462.
185. Multiphysics, C. *Comsol Multiphysics material database, version 5.4, 2018*. 2018; Available from: www.comsol.com.
186. COMSOL. *How to Implement a Mesh Refinement Study*. 2013; Available from: https://www.comsol.fr/blogs/how-to-implement-mesh-refinement-study?wtime=%7Bseek_to_second_number%7D%3Fwtime%3Fwtime&setlang=1.
187. Sano, K.-h., R. Karasawa, and T. Yanagitani. *High electromechanical coefficient k t 2= 19% thick ScAlN piezoelectric films for ultrasonic transducer in low frequency of 80 MHz*. in *2017 IEEE International Ultrasonics Symposium (IUS)*. 2017. IEEE.
188. Jose, S., A. Jansman, and R.J.E. Hueting. *A design procedure for an acoustic mirror providing dual reflection of longitudinal and shear waves in Solidly Mounted BAW Resonators (SMRs)*. in *2009 IEEE International Ultrasonics Symposium*. 2009. IEEE.
189. Worsley, M.A., et al., *Ultralow density, monolithic WS2, MoS2, and MoS2/graphene aerogels.* ACS nano, 2015. **9**(5): p. 4698-4705.
190. Serway, R.A.H.J.V.C., *College physics*. 2015.

191. Tiemeijer, L.F., et al., *Comparison of the" pad-open-short" and" open-short-load" deembedding techniques for accurate on-wafer RF characterization of high-quality passives.* IEEE Transactions on Microwave Theory and Techniques, 2005. **53**(2): p. 723-729.
192. Smirnov, W. *The tutorial for GWYDDION*. 2012; Available from: http://gwyddion.net/presentations/tutorials.php.
193. Hallil, H., et al., *Strong Piezoelectricity in 3R-MoS2 Flakes.* Advanced Electronic Materials, 2022: p. 2101131.
194. Wang, S., et al., *Sulfur-catalyzed phase transition in MoS2 under high pressure and temperature.* Journal of Physics and Chemistry of Solids, 2014. **75**(1): p. 100-104.
195. Klein, C.A. and G.F. Cardinale, *Young's modulus and Poisson's ratio of CVD diamond.* Diamond and Related Materials, 1993. **2**(5-7): p. 918-923.
196. Hwang, H., H. Kim, and J. Cho, *MoS2 nanoplates consisting of disordered graphene-like layers for high rate lithium battery anode materials.* Nano letters, 2011. **11**(11): p. 4826-4830.
197. Sun, J., et al., *Synthesis methods of two-dimensional MoS2: A brief review.* Crystals, 2017. **7**(7): p. 198.
198. Bertolazzi, S., J. Brivio, and A. Kis, *Stretching and breaking of ultrathin MoS2.* ACS nano, 2011. **5**(12): p. 9703-9709.
199. Peelaers, H. and C. Van de Walle, *Elastic constants and pressure-induced effects in MoS2.* The Journal of Physical Chemistry C, 2014. **118**(22): p. 12073-12076.
200. Singh, A.K., *Engineered nanoparticles: structure, properties and mechanisms of toxicity*. 2015: Academic Press.
201. Oliveira, F., *Raman Spectroscopy Studies of Sn x Ge and ZnO: Mn Semiconductor Solid Solutions.* 2018.
202. Guo, Y., W. Chen, and Y. Zhang, *Guided wave propagation in multilayered piezoelectric structures.* Science in China Series G: Physics, Mechanics and Astronomy, 2009. **52**(7): p. 1094-1104.
203. Keysight, *Chapter 2 : Tuning and Optimization PathWave Advanced Design System (ADS)*. 2009.
204. Uzunov, I.S., et al. *Extraction of modified butterworth—Van Dyke model of FBAR based on FEM analysis*. in *2017 XXVI international scientific conference electronics (ET)*. 2017. IEEE.
205. Chao, M.-C., et al. *Modified BVD-equivalent circuit of FBAR by taking electrodes into account*. in *2002 IEEE Ultrasonics Symposium, 2002. Proceedings.* 2002. IEEE.
206. Krishnaswamy, S., et al. *Film bulk acoustic wave resonator technology*. in *IEEE Symposium on Ultrasonics*. 1990. IEEE.
207. Lakin, K., K. McCarron, and R. Rose. *Solidly mounted resonators and filters*. in *1995 IEEE Ultrasonics Symposium. Proceedings. An International Symposium*. 1995. IEEE.
208. Ruby, R.C., et al. *Thin film bulk wave acoustic resonators (FBAR) for wireless applications*. in *2001 IEEE Ultrasonics Symposium. Proceedings. An International Symposium (Cat. No. 01CH37263)*. 2001. IEEE.
209. Nelson, A., et al. *A 22μw, 2.0 GHz fbar oscillator*. in *2011 IEEE Radio Frequency Integrated Circuits Symposium*. 2011. IEEE.
210. Mastromatteo, U. and F. Villa, *High sensitivity acoustic wave AlN/Si mass detectors arrays for artificial olfactory and biosensing applications: A review.* Sensors and actuators B: Chemical, 2013. **179**: p. 319-327.
211. Islam, S., M. Zada, and H. Yoo, *Low-pass filter based integrated 5G smartphone antenna for sub-6-GHz and mm-wave bands.* IEEE Transactions on Antennas and Propagation, 2021. **69**(9): p. 5424-5436.
212. Mateu, J., et al., *Acoustic Wave Transversal Filter for 5G N77 Band.* IEEE Transactions on Microwave Theory and Techniques, 2021. **69**(10): p. 4476-4488.
213. Park, S.-H., et al., *Film bulk acoustic resonator fabrication for radio frequency filter applications.* Japanese Journal of Applied Physics, 2000. **39**(7R): p. 4115.

Annex Chapter 1

Market share of SAW RF filters by companies

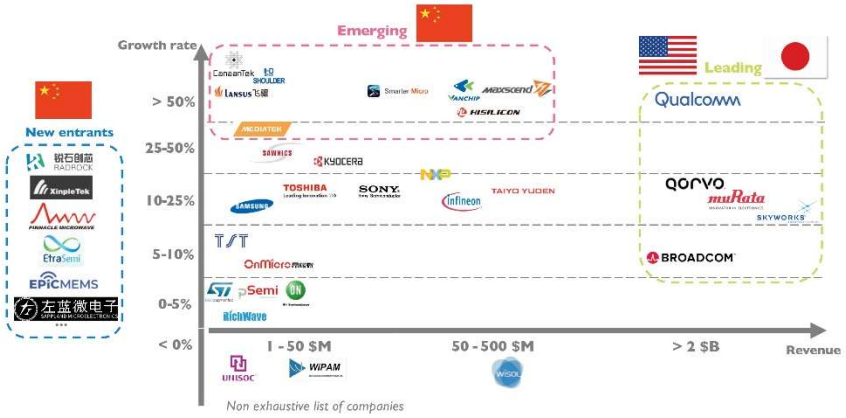

Figure A.1 RF front-end modules market – 2020 market share by companies[1]

Some more examples of SAW devices for sensing applications

SAW devices are also the good candidate for pressure and temperature sensor [2-5]. Rodríguez-Madrid et al. [5] reported a SAW based pressure sensor with a sensibility of 0.33 MHz / bar. It is a one port resonator with AlN as piezoelectric layer and is deposited on a free-standing nanocrystalline diamond (NCD) layer. Müller et al. [4] reported a SAW based temperature sensor with sensitivities higher than 300 kHz/°C. It is GaN based SAW sensor, the detection of temperature is realized by tracking resonance frequency changes in function of temperature. For BAW based temperature sensor, there are also many research teams which reported some BAW based sonsors of high temperatire or with high sensitivity [6-8].

What's more, SAW based mechanical sensors are widely used in automotive industry, such as acceleration, tire-road friction sensor, etc [9, 10]. Wen et al. [11] reported a SAW acceleration sensor with a sensitivity of 29.7 kHz/ g. It is a two-port SAW and a very good temperature compensation is achieved by using a metal package base. SAW sensors are also used for tire-road friction in car and truck tires [12]. A continuous monitoring of tire pressure is achieved to estimate the riding conditions (braking maneuvers, over a curbstone, etc.).

SAW devices are also well investigated as gyroscope since several decades [13]. For example, a standing wave type SAW gyroscope is proposed by Kurosawa et al [14]. This design was then confirmed by Varadan et al. [15] with experimental results. Then, a two delay lines SAW micro rate gyroscope is proposed by Lee et al. [16]. Another progressive waves type SAW gyroscope was proposed by Oh et al. [17, 18].

Besides the physical sensor applications listed above, SAW devices can also serve as motors and actuators [19]. For example, Kurosawa et al. [20, 21] proposed a Rayleigh type SAW based motor with a resonance frequency near 10 MHz. It is a two-port SAW resonator with delay line, a pre-loaded slider is placed on the wave propagation path and is driven by the frictional force. Besides, SAW devices are also widely used in microfluidic actuation and micro-object manipulation [22]. The travelling or standing SAW between two sets of IDTs.

Usually, leaky type travelling waves are usually used for actuation and manipulation, Lamb type standing waves are used for micro actuators.

Annex Chapter 2

Propagation of Acoustic Plane Wave in a non-piezoelectric material

When a force is applied to a solid object, that force is immediately transmitted to the constitutive particles, causing a mechanical displacement. In an elastic object, this force causes a deformation as the particles leave their state of equilibrium, resulting in a vibration when submitted to an alternate force. This is the origin of an acoustic wave in solids. Similarly, as the electromagnetic wave, which is described by Maxwell's equations, the acoustic wave can be described by the strain-stress-displacement equation and the equation of motion of the particles. In Cartesian coordinates, the relationship between the displacement and the strain is given by

$$S = \nabla u \qquad (A.\ 1)$$

and

$$\nabla \cdot T = \rho \frac{\partial^2 u}{\partial t^2} \qquad (A.\ 2)$$

Where u (m) is the displacement, S the strains, T (N/m^2) the stresses, ρ (kg/m^3) the mass density and t (s) the time.

The $\nabla \cdot$ and ∇ operator are described as:

$$\nabla \cdot \rightarrow \nabla_{iK} = \begin{bmatrix} \frac{\partial}{\partial x} & 0 & 0 & 0 & \frac{\partial}{\partial z} & \frac{\partial}{\partial y} \\ 0 & \frac{\partial}{\partial y} & 0 & \frac{\partial}{\partial z} & 0 & \frac{\partial}{\partial x} \\ 0 & 0 & \frac{\partial}{\partial z} & \frac{\partial}{\partial y} & \frac{\partial}{\partial x} & 0 \end{bmatrix} \qquad (A.\ 3)$$

$$\nabla \rightarrow \nabla_{iK} = \begin{bmatrix} \frac{\partial}{\partial x} & 0 & 0 \\ 0 & \frac{\partial}{\partial y} & 0 \\ 0 & 0 & \frac{\partial}{\partial z} \\ 0 & \frac{\partial}{\partial z} & \frac{\partial}{\partial y} \\ \frac{\partial}{\partial z} & 0 & \frac{\partial}{\partial x} \\ \frac{\partial}{\partial y} & \frac{\partial}{\partial x} & 0 \end{bmatrix} \qquad (A.\ 4)$$

S and T are described as symmetric tensors in a crystal:

$$S = \begin{pmatrix} S_{xx} & S_{xy} & S_{xz} \\ S_{xy} & S_{yy} & S_{yz} \\ S_{xz} & S_{yz} & S_{zz} \end{pmatrix} = \begin{pmatrix} S_1 & \frac{1}{2}S_6 & \frac{1}{2}S_5 \\ \frac{1}{2}S_6 & S_2 & \frac{1}{2}S_4 \\ \frac{1}{2}S_5 & \frac{1}{2}S_4 & S_3 \end{pmatrix} \rightarrow \begin{bmatrix} S_1 \\ S_2 \\ S_3 \\ S_4 \\ S_5 \\ S_6 \end{bmatrix} \quad (A.5)$$

$$T = \begin{pmatrix} T_{xx} & T_{xy} & T_{xz} \\ T_{xy} & T_{yy} & T_{yz} \\ T_{xz} & T_{yz} & T_{zz} \end{pmatrix} = \begin{pmatrix} T_1 & T_6 & T_5 \\ T_6 & T_2 & T_4 \\ T_5 & T_4 & T_3 \end{pmatrix} \rightarrow \begin{bmatrix} T_1 \\ T_2 \\ T_3 \\ T_4 \\ T_5 \\ T_6 \end{bmatrix} \quad (A.6)$$

The velocity v of the particle in the material can be described as:

$$\nabla v = \frac{\partial u}{\partial t} \quad (A.7)$$

When applying Hooke law, the stress is:

$$T = c : S \quad (A.8)$$

Where c is the elastic stiffness matrix and described as:

$$c_{ijkl} \Longrightarrow c_{\alpha\beta} = c = \begin{bmatrix} c_{11} & c_{12} & c_{13} & c_{14} & c_{15} & c_{16} \\ c_{12} & c_{22} & c_{23} & c_{24} & c_{25} & c_{26} \\ c_{13} & c_{23} & c_{33} & c_{34} & c_{35} & c_{36} \\ c_{14} & c_{24} & c_{34} & c_{44} & c_{45} & c_{46} \\ c_{15} & c_{25} & c_{35} & c_{45} & c_{55} & c_{56} \\ c_{16} & c_{26} & c_{36} & c_{46} & c_{56} & c_{66} \end{bmatrix} \quad (A.9)$$

By substituting (A.7) and (A.8) into (A.2), we get:

$$\nabla \cdot c : \frac{\partial S}{\partial t} = \rho \frac{\partial^2 v}{\partial t^2} \quad (A.10)$$

Since we have (A.1), then we get:

$$\nabla \cdot c : \nabla v = \rho \frac{\partial^2 v}{\partial t^2} \quad (A.11)$$

We rewrite the equation (A.11) in the form of elements of matrix:

$$\nabla_{iK} c_{KL} \nabla_{Lj} v_j = \rho \frac{\partial^2 v_i}{\partial t^2} \quad (A.12)$$

Then we define that a plane wave propagating in a direction $l = l_x x + l_y y + l_z z$, and we assume that the particle displacements have time-dependant harmonic forms $\exp[j(\omega t - kl \cdot r)]$, where ω is the angular frequency, $k = 2\pi/\lambda$ the wavenumber and r the position vector:

$$r = \hat{x} l_x + \hat{y} l_y + \hat{z} l_z \quad (A.13)$$

So, the particle velocity has the form as:

$$v = A_i exp\{j[\omega t - k(l_x x + l_y y + l_z z)]\} \quad (A.14)$$

In this case, we can rewrite operators ∇_{iK} and ∇_{Lj} to operators $-jkl_{iK}$ and $-jkl_{Lj}$, which are defined as:

$$-jkl_{iK} \rightarrow -jk\begin{bmatrix} l_x & 0 & 0 & 0 & l_z & l_y \\ 0 & l_y & 0 & l_z & 0 & l_x \\ 0 & 0 & l_z & l_y & l_x & 0 \end{bmatrix} \quad (A.\ 15)$$

$$-jkl_{Lj} \rightarrow -jk\begin{bmatrix} l_x & 0 & 0 \\ 0 & l_y & 0 \\ 0 & 0 & l_z \\ 0 & l_z & l_y \\ l_z & 0 & l_x \\ l_y & l_x & 0 \end{bmatrix} \quad (A.\ 16)$$

And then the equation (A.12) can be developed as:

$$k^2\left(l_{iK}c_{KL}l_{Lj}\right)v_j = k^2\Gamma_{ij}v_j = \rho\omega^2 v_i \quad (A.\ 17)$$

This equation is called Christoffel Equation and:

$$\Gamma_{ij} = l_{iK}c_{KL}l_{Lj} \quad (A.\ 18)$$

We rewrite the equation (A.18) in the form of element of matrix:

$$\begin{bmatrix} \Gamma_{11} & \Gamma_{12} & \Gamma_{13} \\ \Gamma_{21} & \Gamma_{22} & \Gamma_{23} \\ \Gamma_{31} & \Gamma_{32} & \Gamma_{33} \end{bmatrix} = \begin{bmatrix} l_x & 0 & 0 & 0 & l_z & l_y \\ 0 & l_y & 0 & l_z & 0 & l_x \\ 0 & 0 & l_z & l_y & l_x & 0 \end{bmatrix} \begin{bmatrix} c_{11} & c_{12} & c_{13} & c_{14} & c_{15} & c_{16} \\ c_{12} & c_{22} & c_{23} & c_{24} & c_{25} & c_{26} \\ c_{13} & c_{23} & c_{33} & c_{34} & c_{35} & c_{36} \\ c_{14} & c_{24} & c_{34} & c_{44} & c_{45} & c_{46} \\ c_{15} & c_{25} & c_{35} & c_{45} & c_{55} & c_{56} \\ c_{16} & c_{26} & c_{36} & c_{46} & c_{56} & c_{66} \end{bmatrix} \begin{bmatrix} l_x & 0 & 0 \\ 0 & l_y & 0 \\ 0 & 0 & l_z \\ 0 & l_z & l_y \\ l_z & 0 & l_x \\ l_y & l_x & 0 \end{bmatrix} ($$

A. 19)

The Christoffel Equation can be written in the form of matrix:

$$k^2\left[\begin{pmatrix} \Gamma_{11} & \Gamma_{12} & \Gamma_{13} \\ \Gamma_{21} & \Gamma_{22} & \Gamma_{23} \\ \Gamma_{31} & \Gamma_{32} & \Gamma_{33} \end{pmatrix}\right]\begin{bmatrix} v_x \\ v_y \\ v_z \end{bmatrix} = \rho\omega^2\begin{bmatrix} v_x \\ v_y \\ v_z \end{bmatrix} \quad (A.\ 20)$$

We take the example of an isotropic medium, its stiffness constant matrix is:

$$c = \begin{bmatrix} c_{11} & c_{12} & c_{12} & 0 & 0 & 0 \\ c_{12} & c_{11} & c_{12} & 0 & 0 & 0 \\ c_{12} & c_{12} & c_{11} & 0 & 0 & 0 \\ 0 & 0 & 0 & c_{44} & 0 & 0 \\ 0 & 0 & 0 & 0 & c_{44} & 0 \\ 0 & 0 & 0 & 0 & 0 & c_{44} \end{bmatrix} \quad (A.\ 21)$$

$$c_{44} = \frac{1}{2}(c_{11} - c_{12}) \quad (A.\ 22)$$

And now we consider an acoustic wave propagating in z direction ($l_x = 0$, $l_y = 0$, $l_z = 1$), and we can develop (A.19) as:

$$k^2 \begin{bmatrix} c_{44} & 0 & 0 \\ 0 & c_{44} & 0 \\ 0 & 0 & c_{11} \end{bmatrix} \begin{bmatrix} v_x \\ v_y \\ v_z \end{bmatrix} = \rho\omega^2 \begin{bmatrix} v_x \\ v_y \\ v_z \end{bmatrix} \quad (A.\ 23)$$

To have the nontrivial solution, the determinant of the matrix should be zero, leading to three eigenvalues c_{44}, c_{44} and c_{11} corresponding to three eigenvectors $[1 \quad 0 \quad 0]^T$, $[0 \quad 1 \quad 0]^T$ and $[0 \quad 0 \quad 1]^T$, which means that three kinds of acoustic waves can propagate in z direction, with a phase velocity equal to ω/k, one is a shear mode polarized along the x direction and the velocity is:

$$v_{s1} = \sqrt{\frac{c_{44}}{\rho}} \quad (A.\ 24)$$

The second one is a shear mode polarized along the y direction and the velocity is:

$$v_{s2} = \sqrt{\frac{c_{44}}{\rho}} \quad (A.\ 25)$$

The third one is a longitudinal mode polarized along the z direction and the velocity is:

$$v_l = \sqrt{\frac{c_{11}}{\rho}} \quad (A.\ 26)$$

Acoustic Plane Wave Propagation in a Piezoelectric Crystal

Since the piezoelectric effect is a reversible effect, the material generates an electrical displacement when a mechanical stress is present, and it also undergoes a deformation under an electric field. In this case, an analysis based on the Christoffel equation is not sufficient and must be coupled with Maxwell's equation to describe both the strain and the electric charge density displacement:

$$S = d \cdot E + s^E : T \quad (A.\ 27)$$

$$D = \varepsilon^T \cdot E + d : T \quad (A.\ 28)$$

And similarly, for the stress:

$$T = c^E : S - e \cdot E \quad (A.\ 29)$$

$$D = e : S + \varepsilon^S \cdot E \quad (A.\ 30)$$

Where ε^T is dielectric coefficient matrix at constant stress, d the piezoelectric strain coefficient matrix, s^E the elastic compliance coefficient matrix, c^E the elastic stiffness coefficient matrix at constant electric field, ε^S the dielectric coefficient matrix at constant strain, e the piezoelectric stress coefficient matrix.

The electric-field intensity can be written as the function of the gradient of electric potential:

$$E = -\nabla\phi \quad (A.\ 31)$$

By using (A.2), (A.7) and (A.31), (A.29) can be rewritten into:

$$\nabla \cdot c^E : S + \nabla \cdot e \cdot \nabla\phi = \rho \frac{\partial v}{\partial t} \qquad (A.32)$$

After differentiating (A.32) with respect to t, we obtain:

$$\nabla \cdot c^E : \frac{\partial S}{\partial t} + \nabla \cdot e \cdot \frac{\partial \phi}{\partial t} = \rho \frac{\partial^2 v}{\partial t^2} \qquad (A.33)$$

Since we have (A.7), (A.33) can be rewritten into:

$$\nabla \cdot c^E : \nabla v + \nabla \cdot e \cdot \frac{\partial \phi}{\partial t} = \rho \frac{\partial^2 v}{\partial t^2} \qquad (A.34)$$

And as the dielectric has no free charge, $\nabla \cdot D = 0$, after differentiating (A.30) with respect to t, we obtain:

$$\nabla \cdot \varepsilon^S \cdot \nabla \frac{\partial \phi}{\partial t} = \nabla \cdot e \cdot \frac{\partial S}{\partial t} \qquad (A.35)$$

These two equations (A.34) and (A.35) are called the coupled equation and they can also be reformulated in matrix form as:

$$\nabla_{iK} c^E_{KL} \nabla_{Lj} v_j + \nabla_i e_{iL} \nabla_{Lj} v_j = \rho \frac{\partial^2 v_i}{\partial t^2} \qquad (A.36)$$

$$\nabla_i e_{iL} \nabla_{Lj} v_j = \nabla_i \varepsilon^S_{ij} \nabla_j \frac{\partial \phi}{\partial t} \qquad (A.37)$$

We consider that the waves propagation has time-dependant harmonic forms, and simplify operators ∇_{iK}, ∇_{Lj}, ∇_i and ∇_j as $-jkl_{iK}$, $-jkl_{Lj}$, $-jkl_i$ and $-jkl_j$, the equations (A.36) and (A.37) can be written as:

$$k^2\left(l_{iK} c^E_{KL} l_{Lj}\right) v_j + j\omega q^2 \left(l_{iK} e_{Kj} l_j\right) \phi = \rho\omega^2 v_i \qquad (A.38)$$

$$j\omega\left(l_i \varepsilon^S_{ij} l_j\right) \phi = \left(l_i e_{iL} l_{Lj}\right) v_j \qquad (A.39)$$

Here l_i and l_j are $[l_x \quad l_y \quad l_z]$ and $[l_x \quad l_y \quad l_z]^T$, then (A.39) can be simplified as:

$$\phi = \frac{l_i e_{iL} l_{Lj}}{j\omega\left(l_i \varepsilon^S_{ij} l_j\right)} v_j \qquad (A.40)$$

By substituting (A.40) into (A.38), we get:

$$k^2 \left(l_{iK} \left\{ c^E_{KL} + \frac{[e_{Kj} l_j][l_i e_{iL}]}{l_i \varepsilon^S_{ij} l_j} \right\} l_{Lj} \right) v_j = \rho\omega^2 v_i \qquad (A.41)$$

This is the Christoffel equation for a piezoelectric material and:

$$\Gamma_{ij} = l_{iK} \left\{ c^E_{KL} + \frac{[e_{Kj} l_j][l_i e_{iL}]}{l_i \varepsilon^S_{ij} l_j} \right\} l_{Lj} \qquad (A.42)$$

Considering $c^E_{KL} + \frac{[e_{Kj} l_j][l_i e_{iL}]}{l_i \varepsilon^S_{ij} l_j}$ as the effective elastic stiffness constant in a piezoelectric material, the analysis described above can be applied in this case.

For a current piezoelectric material such as ZnO, with a hexagonal crystalline structure, the matrices of the elastic stiffness, piezoelectric and dielectric constants can be expressed respectively as:

$$c^E = \begin{bmatrix} c_{11} & c_{12} & c_{13} & 0 & 0 & 0 \\ c_{12} & c_{11} & c_{13} & 0 & 0 & 0 \\ c_{13} & c_{13} & c_{33} & 0 & 0 & 0 \\ 0 & 0 & 0 & c_{44} & 0 & 0 \\ 0 & 0 & 0 & 0 & c_{44} & 0 \\ 0 & 0 & 0 & 0 & 0 & (c_{11} - c_{12})/2 \end{bmatrix} \quad (A.43)$$

$$e = \begin{bmatrix} 0 & 0 & 0 & 0 & e_{15} & 0 \\ 0 & 0 & 0 & e_{15} & 0 & 0 \\ e_{31} & e_{31} & e_{33} & 0 & 0 & 0 \end{bmatrix} \quad (A.44)$$

$$\varepsilon^S = \begin{bmatrix} \varepsilon_{11} & 0 & 0 \\ 0 & \varepsilon_{11} & 0 \\ 0 & 0 & \varepsilon_{33} \end{bmatrix} \quad (A.45)$$

Then by substituting (A.43) (A.44) (A.45) into (A.41), and assuming propagation in the z direction ($l_x = 0, l_y = 0, l_z = 1$), with similar process as for solving (A.43), the determinant of the matrix should be zero, we get the equation:

$$\left[\left(\frac{k}{\omega}\right)^2 \left(c_{33} + \frac{e_{33}^2}{\varepsilon_{33}}\right) - \rho\right]\left[\left(\frac{k}{\omega}\right)^2 c_{44} - \rho\right]^2 = 0 \quad (A.46)$$

after solving the equations, we get the velocities of three propagating modes:

1. Longitudinal mode wave:

$$v_l = \sqrt{\frac{c_{33} + e_{33}^2/\varepsilon_{33}}{\rho}} \quad (A.47)$$

2. Shear mode wave 1:

$$v_{s1} = \sqrt{\frac{c_{44}}{\rho}} \quad (A.48)$$

3. Shear mode wave 2:

$$v_{s2} = \sqrt{\frac{c_{44}}{\rho}} \quad (A.49)$$

Similar to that of non-piezoelectric medium, in the c axis of the hexagonal crystal, three kinds of acoustic waves can propagate, v_l is the longitudinal acoustic wave generated by piezoelectric effect and depends on the piezoelectric and dielectric properties of materials, and two shear modes are independent on the piezoelectric properties, which result from the existence of Poisson's ratio of materials.

For a further study, we assume that the velocity of the particles of longitudinal mode wave can be written as:

$$v = v_z z = \{v_{z0}^+ exp[j(\omega t - kz)] + v_{z0}^- exp[j(\omega t - kz)]\}z \quad (A.50)$$

where v_{z0}^+ and v_{z0}^- are the amplitudes of the waves in positive and negative directions.

Φ can be developed from (A.40) and E can be developed from (A.31):

$$\phi = \frac{1}{j\omega}\frac{e_{33}}{\varepsilon_{33}}\{v_{z0}^{+}exp[j(\omega t - kz)] + v_{z0}^{-}exp[j(\omega t - kz)]\} + (az + b)exp(j\omega t) \quad (A.\ 51)$$

$$E = E_z z = \frac{1}{v_l}\frac{e_{33}}{\varepsilon_{33}}\{v_{z0}^{+}exp[j(\omega t - kz)] + v_{z0}^{-}exp[j(\omega t - kz)]\}z - aexp(j\omega t)z \quad (A.\ 52)$$

Then the strain can be developed as:

$$T \rightarrow \begin{cases} T_1 = -\frac{c_{13}+e_{31}e_{33}/\varepsilon_{33}}{v_l}\{v_{z0}^{+}exp[j(\omega t - kz)] + v_{z0}^{-}exp[j(\omega t - kz)]\} + e_{31}aexp(j\omega t) \\ T_2 = -\frac{c_{13}+e_{31}e_{33}/\varepsilon_{33}}{v_l}\{v_{z0}^{+}exp[j(\omega t - kz)] + v_{z0}^{-}exp[j(\omega t - kz)]\} + e_{31}aexp(j\omega t) \\ T_3 = -\frac{c_{33}+{e_{33}}^2/\varepsilon_{33}}{v_l}\{v_{z0}^{+}exp[j(\omega t - kz)] + v_{z0}^{-}exp[j(\omega t - kz)]\} + e_{33}aexp(j\omega t) \end{cases} (A.\ 53)$$

Where T_1, T_2 and T_3 are the strains in x, y and z directions respectively.

Some basic theories about FEM method

In the finite element method, an attempt is made to obtain a system of simultaneous algebraic equations. By subdividing the object under study into a system of smaller parts or units (finite elements), the FEM method is intended to get the approximate values of the unknowns at a discrete number of points in the continuum. The process that divides the object into finite elements is called discretization. The elements are connected by common points (nodal points or nodes) and/or boundary lines and/or surfaces. Rather than solving the equations for the entire object, the FEM method attempts to formulate the equations for each finite element and to combine them in specific ways, taking into account boundary conditions, to obtain numerical solutions for the entire object [23].

To simplify the formulation of the element equations in the FEM method, a matrix method is used. Matrix notation is simple and user-friendly for writing and solving sets of simultaneous algebraic equations, provided the used of high-performance computers. Here we take a purely mechanical problem as an example.

The force components $(F_{1x}, F_{1y}, F_{1z}, F_{2x}, F_{2y}, F_{2z} \cdots F_{nx}, F_{ny}, F_{nz})$ at different nodes or points $(1,2 \cdots n)$ and the corresponding set of nodal displacements $(d_{1x}, d_{1y}, d_{1z}, d_{2x}d_{2y}, d_{2z} \cdots d_{nx}, d_{ny}, d_{nz})$ can be expressed as below in form of matrices :

$$\{F\} = \underline{F} = \begin{Bmatrix} F_{1x} \\ F_{1y} \\ F_{1z} \\ F_{2x} \\ F_{2y} \\ F_{2z} \\ \vdots \\ F_{nx} \\ F_{ny} \\ F_{nz} \end{Bmatrix} \quad \{d\} = \underline{d} = \begin{Bmatrix} d_{1x} \\ d_{1y} \\ d_{1z} \\ d_{2x} \\ d_{2y} \\ d_{2z} \\ \vdots \\ d_{nx} \\ d_{ny} \\ d_{nz} \end{Bmatrix} \quad (A.\ 54)$$

We know that for a purely mechanical problem, the relationship between force and displacement can be expressed by the Hooke's Law, which has here to be extended to the full set of nodes by using the so-called stiffness influence coefficients $\underline{K}$:

$$\underline{F} = \underline{K}\,\underline{d} \qquad (A.55)$$

Or:

$$\begin{Bmatrix} F_{1x} \\ F_{1y} \\ \vdots \\ F_{nz} \end{Bmatrix} = \begin{bmatrix} K_{11} & K_{12} & \cdots & K_{1n} \\ K_{21} & K_{22} & & K_{2n} \\ & \vdots & \ddots & \vdots \\ K_{n1} & K_{n2} & \cdots & K_{nn} \end{bmatrix} \begin{Bmatrix} d_{1x} \\ d_{1y} \\ \vdots \\ d_{nz} \end{Bmatrix} \qquad (A.56)$$

If we assume that the structure displacement is $d_{1x} = 1, d_{1y} = d_{1z} = \cdots d_{nz} = 0$ and according to the equation (A.56), it comes:

$$F_{1x} = K_{11} \qquad F_{1y} = K_{21}, \ldots, F_{nz} = K_{n1} \qquad (A.57)$$

With the equation (A.57), we can see that all elements in the first column of $\underline{K}$ represent the forces for the full set of nodal forces with a displacement at node 1 in x direction. Similarly, all elements in the second column of $\underline{K}$ represent the values of forces associated to a displacement node 1 in y direction, and other nodal displacements at zero. This is the physical understanding of the stiffness influence coefficients $\underline{K}$, to be distinguished with the stiffness constants matrix. The use of matrix concept in solving complicated systems and multiphysics investigations is a crucial issue for digital computers calculation, and high-performance computers solve those problems by associating a large number of simultaneous equations [23]. Many programs or softwares are developed for such specific or general purpose, like Abaqus, Ansys, COMSOL which are developed for applying FEM method in several physical themes [23].

Before starting a FEM analysis, the model should be defined at first, the input data include the position of the element nodal coordinates, the way these elements are connected, the material properties, the boundary conditions, the physics to be used, etc [23]. We describe now the general steps for FEM analysis. Based on the structure, the first step is the discretization and the selection of the element types. This "meshing" step is a matter of dividing the object into an equivalent set of finite elements, choosing the most appropriate element type, and defining the nodes between them. The size and total number of elements is a very important factor determining the performance of the simulation. Indeed, the elements should be small enough to provide appropriate information about the model and obtain accurate simulation results. At the same time, they should be large enough to limit the computational resources (material and computation time). If the results of the simulation converge, there is no longer need to have smaller elements. Generally, the commercial software suggests a discretized body or mesh to the user according to the underlying applied physics, but sometimes the user still needs to optimise it, by defining smarter ways of meshing or even by further reducing the model for example based on symmetry properties, especially for a complex geometry with a large number of elements [23].

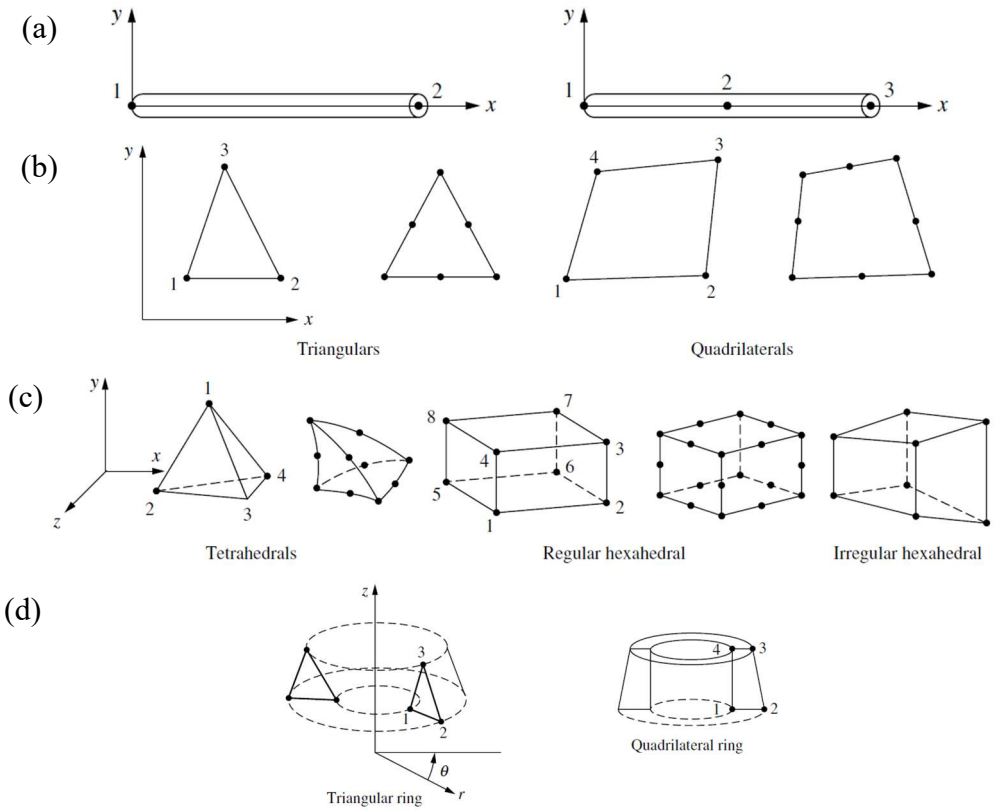

Figure A.2 (a) Simple two-noded line element and the higher-order line element; (b) Simple two-dimensional elements with corner nodes and higher-order two-dimensional elements; (c) Simple three-dimensional elements and higher-order three-dimensional elements; (d) Simple axisymmetric triangular and quadrilateral elements [23]

Figure A.2 shows some typical types of elements most commonly used. Figure A.2 (a) shows the primary line elements. These basic elements in FEM analysis consist of bar and beam elements, represented by line segments. They are usually used to model trusses and frame structures. The simplest line elements have two nodes, higher order ones can have three or even more nodes. Figure A.2 (b) shows the basic two-dimensional elements, triangles and quadrilateral. The simplest ones consist of first-order line elements with only corner nodes and straight sides or boundaries; higher-order 2D elements have also nodes on their boundaries. Such 2D elements are commonly used as basic building blocks for the mesh of 2D models or the surfaces of 3D models. Figure A.2 (c) shows the most common three-dimensional elements, tetrahedra and hexahedra, used as basic building blocks for performing a 3D analysis. The first order 3D elements have only corner nodes with straight sides, higher order ones have side or face nodes, possibly with curved surfaces. Figure A.2 (d) shows some examples of axisymmetric elements, here triangles and quadrilaterals rotated about a fixed axis. Identifying such symmetries in the geometry or the applied load is a way to greatly reduce the computation time [23].

Figure A.3 shows two examples of discretization. Figure A.3 (a) is an example of the hydraulic cylinder rod end. It is a 2D model with 120 nodes and 297 plane strain triangular elements. A condition of symmetry is applied and only a half of the whole rod end is modelled in order to save the calculation efforts. Figure A.3 (b) shows a 3D model of a swing casting for a backhoe frame and 3D hexahedral elements are used since the model is irregularly shaped. 2D models can often be used to handle highly symmetric models, for complex and irregularly shaped structures, the solutions of 2D models are no longer accurate [23].

(a) (b)

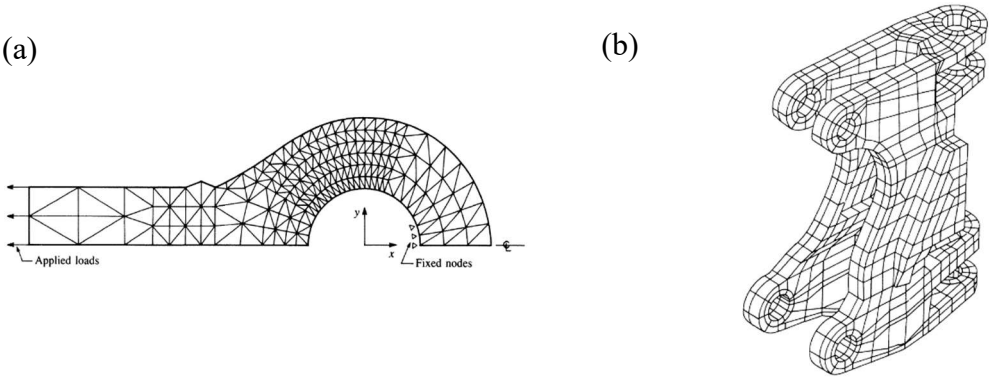

Figure A.3 (a) Two-dimensional analysis of a hydraulic cylinder rod end (120 nodes, 297 plane strain triangular elements); (b) Three-dimensional solid element model of a swing casting for a backhoe frame[23].

Step 2 of a FEM analysis is to choose the function between elements. Linear, quadratic and cubic polynomials are the commonly defined functions using the nodal values of the element. For a 2D element, the displacement function is described as a function of the coordinates in its plane and expressed by the unknown nodal values. The displacement function is used repeatedly for each element and the FEM tool must solve a set of piecewise continuous functions defined in each finite element [23].

The next step for a FEM-based mechanical analysis is to define the relationships between strain/displacement and stress/strain, an important step for deriving the equations. For a purely structural problem, the relationships are based on Hooke's law as shown in the equation (A.8).

Step 4 is to derive the element stiffness matrix and equations as presented earlier. Because of the differences in types of elements, several methods are applied to get a better calculation like direct equilibrium method, work or energy methods, methods of weighted residuals [23].

Then, the nodal equilibrium equations of each element should be assembled into the global nodal equilibrium system, and some boundary conditions are introduced, which depend on the real case to be simulated [23].

As shown in equation (A.54), the next step is to find the *n* that relates to the unknown degrees of freedom.

Finally, after solving the full system to find solutions for the various output quantities, here typically the elements strains and stresses, comes the interpretation of the results. Nowadays, with the help of high-performance computers and well-developed softwares, the procedures of the FEM methods are ever user-friendly and easy to learn, though it is still crucial to have a good understanding of the physics and software tools underlying the simulation.

Classical areas of FEM analysis in the structural domain include stress analysis, vibration analysis, etc. In the non-structural areas, FEM analysis can also address heat transfer, fluid flow, electric or magnetic potential distribution, among others, as well as multiphysics issues coupling different physical fields. This gives us a powerful tool to design and simulate acoustic devices, since piezoelectricity is a typical multiphysics problem.

Annex Chapter 3

Non-Conventional ZnO-based SMR structure

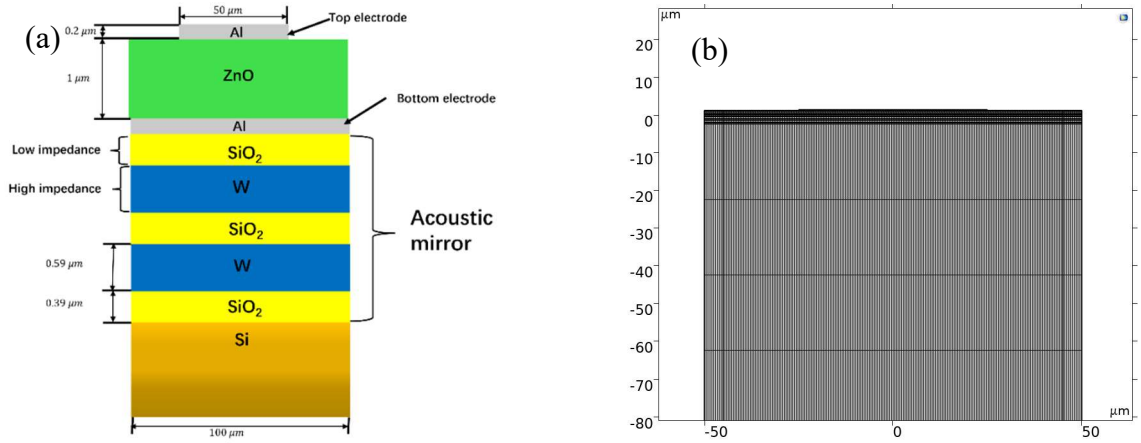

Figure A.4 (a) The cross-section of designed ZnO-SMR with non-conventional acoustic Bragg mirror; (b) The mesh structure of FEM model.

After validating our model of the ZnO-based SMR, an analysis of the Acoustic Bragg Reflector Thickness Optimization Method (detailed in Chapter 2) is also performed. The stopband theory method (STM) is chosen, which makes the calculations easier to perform. The velocity of the acoustic shear waves of SiO_2 and W can be calculated using equation (A.25), and we obtain $v_{s,SiO2} = 3687.48\, m/s$ and $v_{s,W} = 2880.45\, m/s$. Combining this with the velocity of the longitudinal waves, we get the value of (2.64), (2.65) and (2.66), $K_{SiO_2} = 1.59$, $K_W = 1.80$ and $c = 1.70$. So, if we put all these values into (2.62) and (2.63), we get the new thicknesses of SiO_2 and W, $t_{SiO_2} = 0.39\ \mu m$ and $t_W = 0.59\ \mu m$.

The cross-section of the new structure is shown in Figure A.4 (a). Compared to the conventional structure, the W layer is thicker and the SiO_2 layer is thinner. The other dimensions remain the same. The created FEM model and the mesh structure are shown in Figure A.4 (b). As in the conventional structure, the mesh is regular and symmetrical and consists of a kind of quadrilateral elements. The total number of elements is 4511 and a Perfectly Matched Layer (PML) is used.

The configurations of the simulations are also the same as the previous model. MEMS Module is applied, solid mechanics and electrostatics are added. The frequency range is also between 2400 and 2900 MHz and the calculation takes 12 minutes.

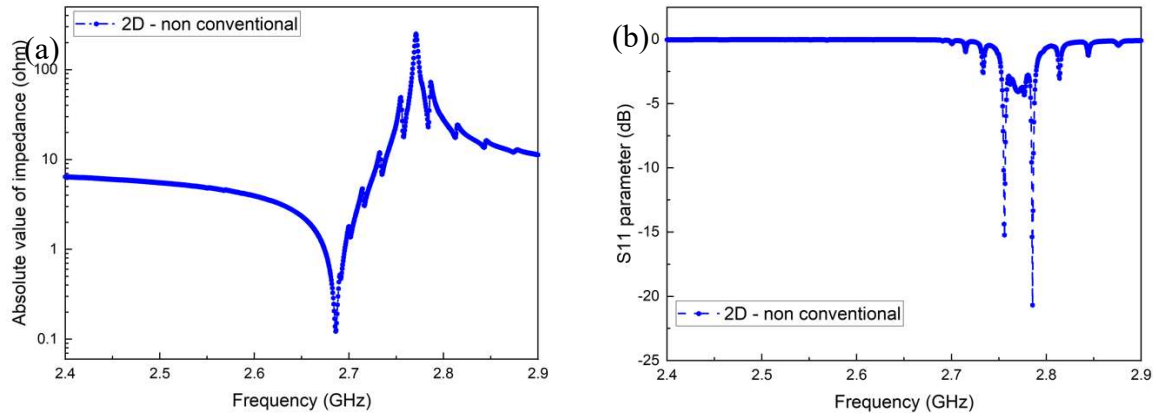

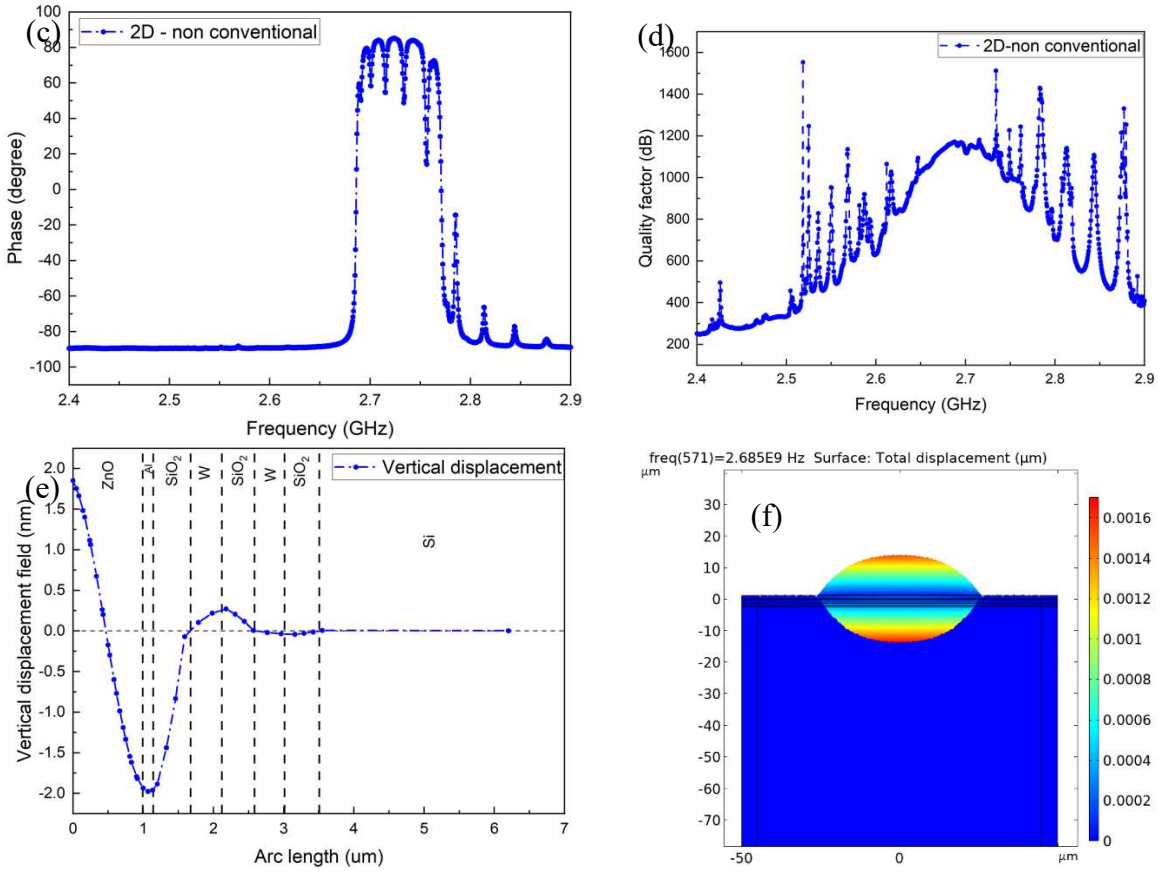

Figure A.5 (a) The Electrical impedance response of non-conventional SMR; (b) Scattering parameters: Reflection coefficient S11 of non-conventional SMR; (c) Phase of non-conventional SMR; (d) The mechanical vertical displacement of non-conventional SMR; (e) The mode shape of non-conventional SMR.

The results of the simulation are shown in Figure A.5. The SMR with non-conventional Bragg mirror has a resonance frequency f_r at 2.69 GHz and an anti-resonance frequency f_a at 2.77 GHz. According to Figure A.5 (a), the maximum and minimum of the electrical impedance have the same magnitude as in the previous model. However, the presence of the non-conventional Bragg mirror leads to a shift of f_r and f_a, by 50 MHz. The same calculation of the electromechanical coupling coefficient k_t^2 is performed, a k_t^2 of 7.6% is found, which correspond well to the previous model.

Figure A.5 (b) shows the reflection parameter S_{11}. A minimum of -22.5 dB is observed at 2.79 GHz and another peak of -17 dB is found at 2.75 GHz. Like the previous model, many superimposed dispersion modes are found.

The change of open-short-load-open circuit is confirmed by the phase curve, as shown in Figure A.5 (c), and the spurious modes are also observed during or near the resonance frequencies. Besides, as shown in Figure A.5 (d) the quality factor (Q value) of 1185 at 2.69 GHz, the resonance frequency f_r, is slightly higher than that of the model with conventional Bragg mirror. However, the impacts brought the spurious modes are more important than conventional Bragg mirror. The aim of this optimisation of the Bragg mirror is to reflect not only the longitudinal waves but also the shear waves, as described in Chapter 2, so that the spurious modes can share more energy and have more impact.

The analysis of the mechanical performances is shown in Figure A.5 (e) at the resonance frequency 2.69 GHz. As in the previous model, half a wavelength propagates in the ZnO layer

and a quarter wavelength in each mirror Bragg layer, then the amplitude of the displacement reduces to zero, and we can see that the peak in bottom Al electrode does not occur at the Al/ SiO_2 interface, but shifts slightly into the Al layer, which can explain why the resonance frequency f_r is slightly higher than the previous model, thinner SiO_2 can reduce the effective wavelength. Then, the thickness extension (longitudinal) acoustic mode at f_r is confirmed by the mode shape, as shown in Figure A.5 (f).

Influence of a mechanical stress

In parallel, we performed an analysis on the influence of mechanical stress on SMR devices. This can be of interest, as during the fabrication process, especially the deposition of metallic electrodes, the induced stresses are not evitable. For this study, we use the reduced model with a pentagonal top electrode. We consider 5 different loads, 0.1, 0.5, 1.0, 1.5 and 2.0 mN, corresponding to mechanical stresses of 0.8, 4.0, 8.0, 12.0 and 16.0 bar (1 bar = 100 kPa), respectively.

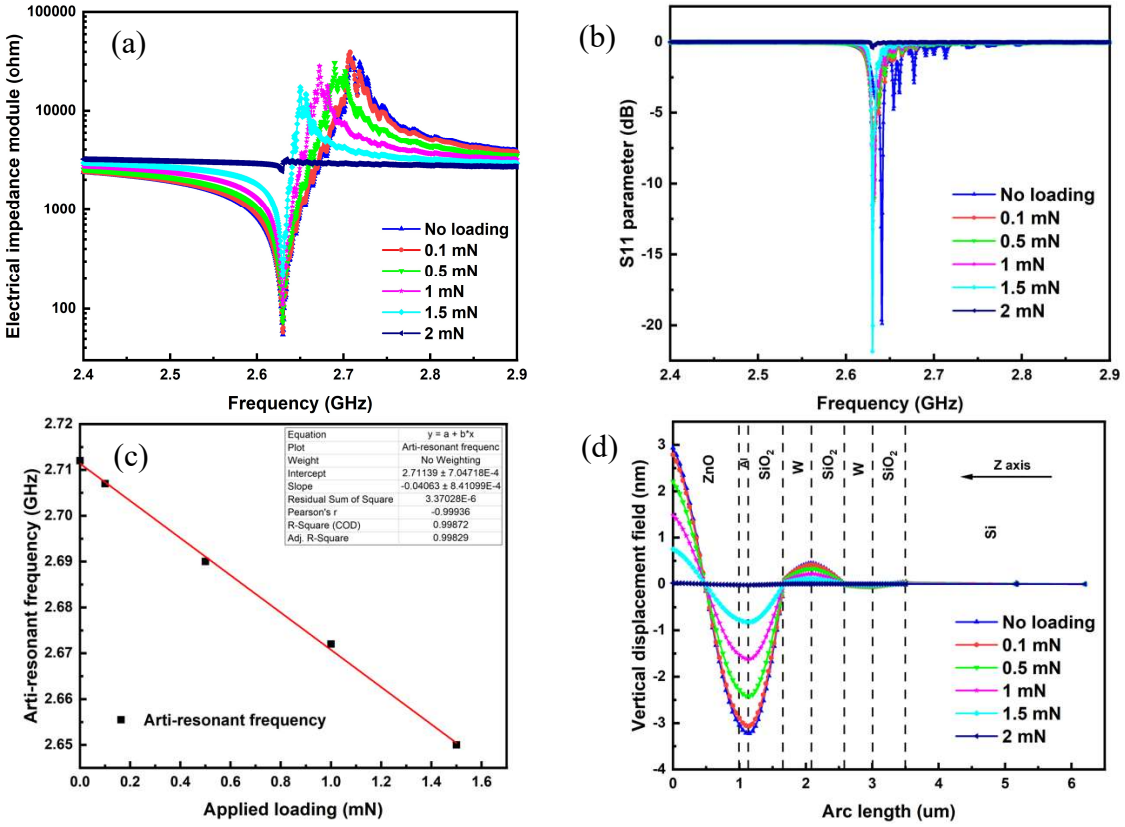

Figure A.6 Simulated results of the 3D reduced model with a pentagonal top electrode under different mass loadings (a) Electrical impedance spectrum; (b) Reflection coefficient S_{11}; (c) Anti-resonance frequency vs applied loading; (d) Mechanical vertical displacement at the resonance frequency f_r.

The simulation setup is based on the 3D reduced models and the results are presented in Figure A.6. Figure A.6 (a) illustrates that the anti-resonance frequency f_a varies from 2.71 down to 2.65 GHz when the applied stress increases, whereas the resonance frequency f_r remains unchanged. As previously observed in the model without load effect, a few spurious modes are still visible on the loaded resonators, that are slightly lowered by the added load. The calculated electromechanical coupling coefficient k_t^2 varies from 7.0 % down to 1.8 %, and when the load increases to 2 mN, the resonance is strongly damped.

The reflection parameter S_{11} is shown in Figure A.6 (b). The calculated magnitude of S_{11} increases with the increased applied stress up to 1.5 mN and ranges from -8 to -22.5 dB, thus avoiding sharing acoustic energy. When the transducer is loaded by 2 mN, the RF signal vanishes.

Furthermore, we performed a simulation study of the relationship between the anti-resonance frequency f_a and the applied stress, as shown in Figure A.6 (c). From the red curve-fitting we can observe a linear behavior. The sensitivity of this designed transducer is estimated to 40 MHz/mN.

A similar analysis of the mass loading effects on the transducer mechanical performance was also performed, as shown in Figure A.6 (d). The wave vertical component profile in the loaded models, like in the non-loaded one, is a half wavelength in the ZnO layer and a quarter wavelength in each Bragg mirror layer, the maximum of displacement decreases with the increased loading

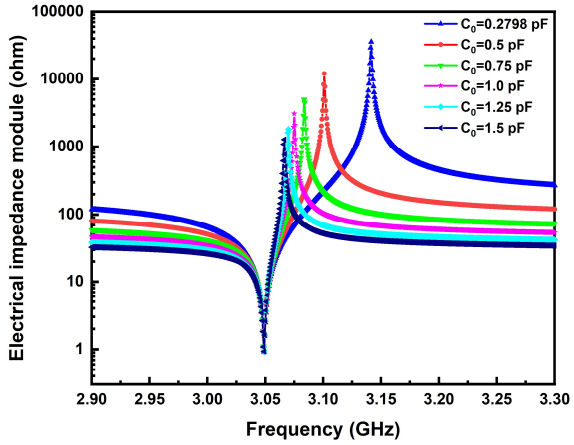

Figure A.7 Electrical impedance module for different C_0

Based on that, we also performed an analysis on the tunability of the anti-resonance under mass loadings. From the FEM simulation results, only anti-resonance frequency f_a changes with increasing loading. By combining with the BVD model, we can observe that f_s (f_r) should be stable, which depends mainly on C_m and L_m from the Equation (2.54), but $f_p(f_a)$ keeps changing and depends on C_0, C_m and L_m from the Equation (2.55). This supports our proposition to model mechanical loads as different C_0 values in the BVD model. For the BVD equivalent circuit simulation, the tunability is modelled by varying the value of the static capacitance C_0. A set of values has been proposed, from 0.28 pF (initial value) up to 1.5 pF. The simulation set-ups are the same than that of the ZnO based model.

The simulation results are shown in Figure A.7. All curves show a resonance frequency f_r at 3.05 GHz, which is the same value as from equation (2.47), as the BVD model does not consider the wave propagation inside the bottom electrode. The anti-resonance frequency f_a is observed to decrease with increasing C_0, as expected. From the expression of C_0, we assume that the applied mechanical force decreases the equivalent thickness of the static capacitance, which may seem consistent and since other parameters like relative permittivity and surface area are constants. Furthermore, the applied mechanical force disturbs the vibration of piezoelectric layer during the resonance, and therefore impacts the generation and propagation of the acoustic wave, leading to a decrease of k_t^2 and of the resulting acoustic energy.

Annex Chapter 4

The thickness influences of the 3R-MoS_2 flakes on the performance of SMRs

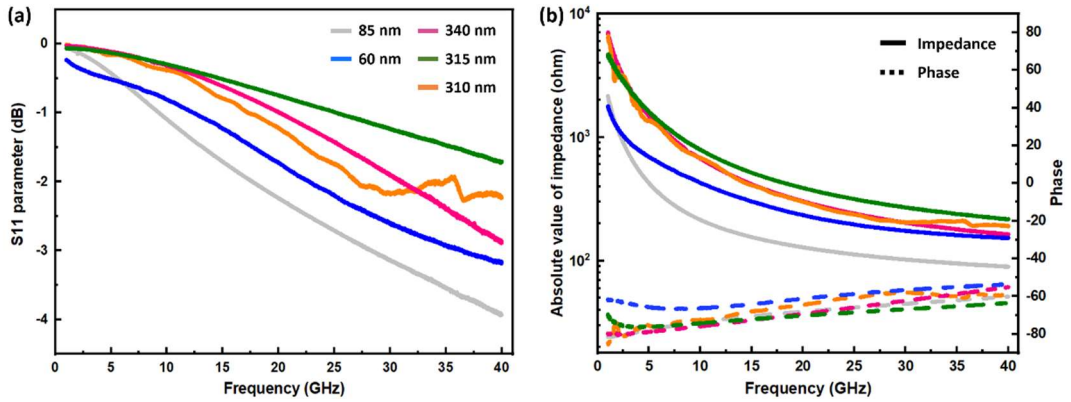

Figure A.8 (a) S_{11} measurement results and (b) absolute value and phase of the impedance of several SMRs with different thick 3R-MoS_2 flakes

The Bragg reflectors in the devices were designed and fabricated for resonance under the frequency around 25 GHz according to the mechanical properties and thickness of multilayers of W and SiO_2. We transferred 3R-MoS_2 flakes with thickness from 60 nm to 340 nm to the bottom electrodes/Bragg reflectors. It was found that the SMRs which showed strong resonance from 20.3 GHz to 27.5 GHz had 210 nm - 290 nm thick 3R-MoS_2 flakes. Beyond this thickness range no resonance was observed, due to the mismatch between the 3R-MoS_2 and the Bragg mirror. Figure A.4 (a) and (b) show the typical S11 measurement result and the absolute value and phase of the impedance of several SMRs with 3R-MoS_2 thickness less than 210 nm or larger than 290 nm. From Figure A.4 (a,b), no resonance was detected in S_{11} responses. The phase diagram exhibits the capacitive characteristics of these SMRs, and no phase conversion can be observed.

Simulation based on a “compact” 3R-MoS_2 structure

The acoustic theory is commonly based on bulk materials, FEM simulations also consider the elasticity theory. A FEM simulation with such layered structure to study further the wave propagation behaviour would have need huge calculation resources and was not possible in the frame of this work. We thought of proposing a retro-simulation based on FEM method as previously, still with a bulk material but “compacting” the atomic layers, thus with a thickness neglecting the “voids”, Van der Waals force field and interfaces between them.

On this basis, we performed a retro-simulation related to the 210 nm thick $3R - MoS_2$ flake SMR, considering an effective acoustic wave path of thickness 98 nm and assuming an effective C_{33} increased by 30% with a value of 130 GPa.

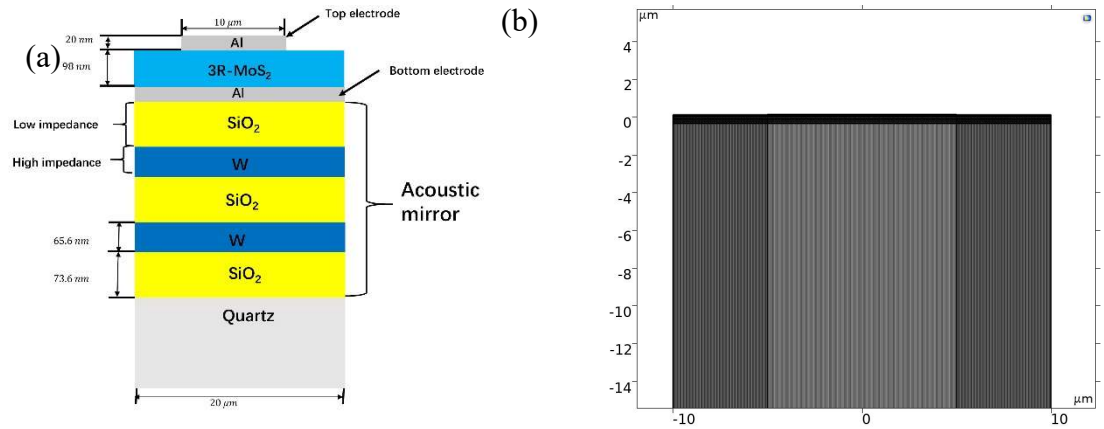

Figure A.9 (a) The cross-section of 3R- MoS_2-SMR for retro-simulation; (b) The mesh structure of FEM model.

This 2D model is shown in Figure A.9 (a). The structure of the acoustic Bragg mirror is the same as the previous model. The mesh structure of this model is shown in Figure A.9 (b), the same quadrangular elements are applied, the total number of elements is 7150, a Perfectly Matched Layer (PML) is also used.

The condition limits are the same as for the other 2D models, the physics of solid mechanics and electrostatics are added. A mechanical damping of 0.001 and a dielectric loss of 0.01 are added to the piezoelectric layer $3R - MoS_2$. The frequency ranges from 18000 to 28000 MHz, the step size is 1 MHz, the calculation time is 3 h 14 minutes.

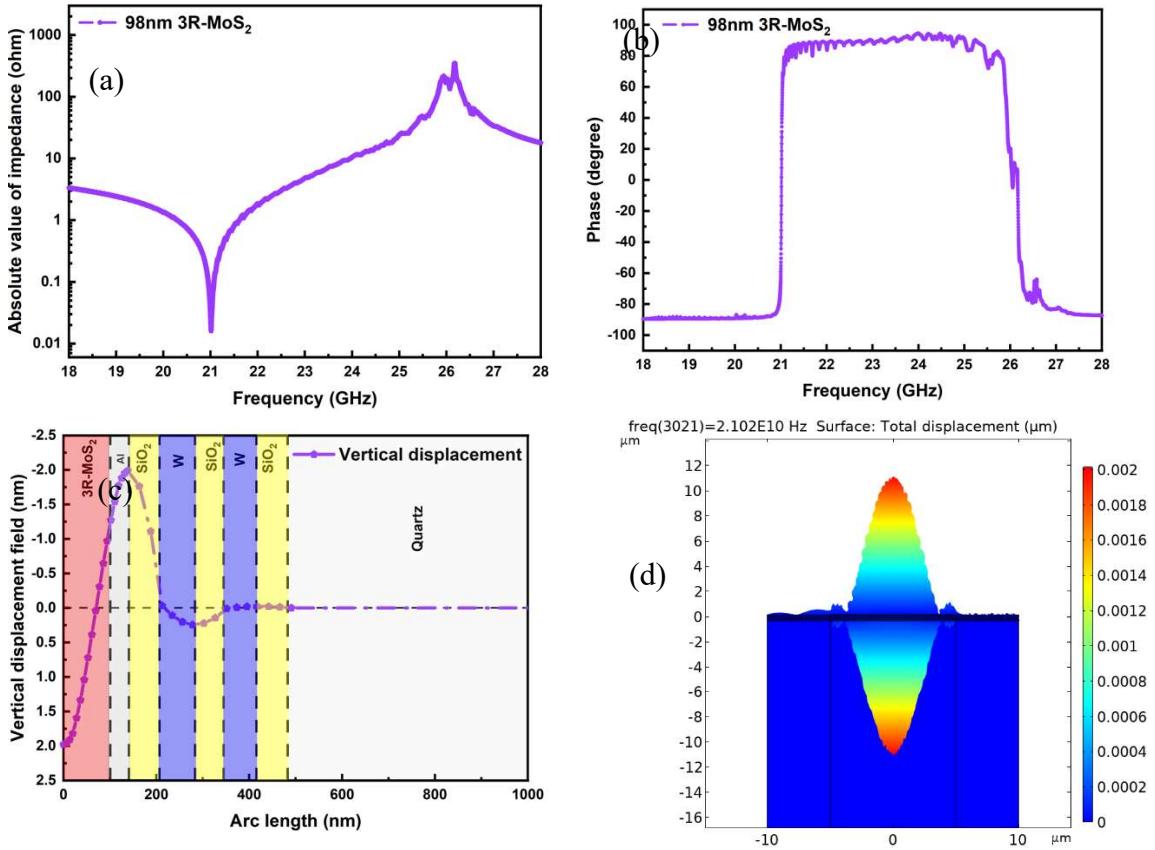

Figure A.10 2D model simulation results: (a) Electrical impedance; (b) Impedance Phase; (c) Mechanical vertical displacement and (d) mode shape at the resonance frequency f_r.

The simulation results of this strategy to figure out the wave propagation in the layered 2D nanomaterials by considering a compacted homogeneous equivalent film, are presented in Figure A.10. From the curve of the electrical impedance as a function of frequency, the

minimum of the electrical impedance is observed at 21.01 GHz, resonance frequency f_r, and the maximum at 26.16 GHz, anti-resonance frequency f_a. The minimum and maximum of the electrical impedance are at 0.1 and 450 ohms, respectively. The electromechanical coupling coefficient k_t^2 is calculated to be 47.5%, which is not far from that of our characterization results.

Figure A.10 (b) shows the phase of impedance as a function of frequency. The same bandwidth as in Figure A.10 (a) can be observed with a phase of 90° between f_r and f_a, -90° out of this band.

Again, the same analysis of mechanical performance is performed. From the displacement field in Figure A.10 (c), and the mode shape in Figure A.10 (d), the existence of a thickness extension (longitudinal) acoustic mode can be clearly observed.

From the above results, though spurious modes are still visible on the electrical spectra, the mechanical mode shape at the resonance exhibits a nice regular lobe with a maximum at the centre of about 2 nm instead of about 1 nm for the previous model with a C_{33} of 900 GPa. The resonance frequency is also closer to that of the characterization results. However, there are still some discrepancies between the simulated and experimental results, that may originate from inhomogeneity of the 3R-MoS_2 flakes, material losses, relatively weak mechanical coupling between the 3R-MoS_2 flakes and the bottom and top electrodes. The internal stress in 3R-MoS_2 may also play a more important role in the elastic constant C_{33}, more than 30%. Besides, since most of the simulation parameters were taken from DFT calculations [24, 25], there might be large discrepancies as many factors were not considered such as impurity, internal stress, temperature, etc. For a better understanding of the acoustic propagation in such a layered material, an in-depth study on the 3R-MoS_2 material properties will be required.

References

1. Cédric, M. and T. Mohammed. *Cellular RF Front-End Technologies for Mobile Handset 2021*. 2021; Available from: https://www.i-micronews.com/products/cellular-rf-front-end-technologies-for-mobile-handset-2021/.
2. Gao, X., et al., *Development of Wireless and Passive SAW Temperature Sensor with Very High Accuracy.* Applied Sciences, 2021. **11**(16): p. 7422.
3. Nicolay, P., et al., *A LN/Si-based SAW pressure sensor.* Sensors, 2018. **18**(10): p. 3482.
4. Müller, A., et al., *GaN/Si based single SAW resonator temperature sensor operating in the GHz frequency range.* Sensors and Actuators A: Physical, 2014. **209**: p. 115-123.
5. Rodríguez-Madrid, J., et al., *High precision pressure sensors based on SAW devices in the GHz range.* Sensors and Actuators A: Physical, 2013. **189**: p. 364-369.
6. Yu, F., et al., *Investigation of Ca3TaGa3Si2O14 piezoelectric crystals for high temperature sensors.* Journal of applied physics, 2011. **109**(11): p. 114103.
7. Chiu, K.-H., H.-R. Chen, and S.R.-S. Huang, *High-performance film bulk acoustic wave pressure and temperature sensors.* Japanese journal of applied physics, 2007. **46**(4R): p. 1392.
8. Mansfeld, G., et al. *BAW microwave temperature sensor*. in *SENSORS, 2004 IEEE*. 2004. IEEE.
9. Hribšek, M.F., D.V. Tošić, and M.R. Radosavljević, *Surface acoustic wave sensors in mechanical engineering.* FME transactions, 2010. **38**(1): p. 11-18.
10. Hallil, H., et al., *Passive resonant sensors: trends and future prospects.* IEEE Sensors Journal, 2021. **21**(11): p. 12618-12632.
11. Wang, W., et al., *Surface acoustic wave acceleration sensor with high sensitivity incorporating ST-X quartz cantilever beam.* Smart Materials and Structures, 2014. **24**(1): p. 015015.
12. Pohl, A., et al. *Monitoring the tire pressure at cars using passive SAW sensors*. in *1997 IEEE Ultrasonics Symposium Proceedings. An International Symposium (Cat. No. 97CH36118)*. 1997. IEEE.
13. Oh, H., et al., *Gyroscopes based on surface acoustic waves.* Micro and Nano Systems Letters, 2015. **3**(1): p. 1-10.
14. Kurosawa, M., et al., *A surface-acoustic-wave gyro sensor.* Sensors and Actuators A: Physical, 1998. **66**(1-3): p. 33-39.
15. Varadan, V., et al., *Design and development of a MEMS-IDT gyroscope.* Smart Materials and Structures, 2000. **9**(6): p. 898.
16. Lee, S.W., et al., *A micro rate gyroscope based on the SAW gyroscopic effect.* Journal of Micromechanics and Microengineering, 2007. **17**(11): p. 2272.
17. Oh, H., S. Yang, and K. Lee, *Development of surface acoustic wave-based microgyroscope utilizing progressive wave.* Japanese journal of applied physics, 2010. **49**(6S): p. 06GN16.
18. Oh, H., et al., *Enhanced sensitivity of a surface acoustic wave gyroscope using a progressive wave.* Journal of Micromechanics and Microengineering, 2011. **21**(7): p. 075015.
19. Zhang, S.-y. and L.-p. Cheng, *Surface acoustic wave motors and actuators: mechanism, structure, characteristic and application.* Acoustic waves. InTech, 2010: p. 207-232.
20. Kurosawa, M., M. Takahashi, and T. Higuchi, *Friction drive surface acoustic wave motor.* Ultrasonics, 1996. **34**(2-5): p. 243-246.

21. Kurosawa, M.K., H. Itoh, and K. Asai, *Elastic friction drive of surface acoustic wave motor.* Ultrasonics, 2003. **41**(4): p. 271-275.
22. Destgeer, G. and H.J. Sung, *Recent advances in microfluidic actuation and micro-object manipulation via surface acoustic waves.* Lab on a Chip, 2015. **15**(13): p. 2722-2738.
23. Logan, D.L., *A first course in the finite element method*. 2016: Cengage Learning.
24. Konabe, S. and T. Yamamoto, *Piezoelectric coefficients of bulk 3R transition metal dichalcogenides.* Japanese Journal of Applied Physics, 2017. **56**(9): p. 098002.
25. Tan, D., M. Willatzen, and Z.L. Wang, *Prediction of strong piezoelectricity in 3R-MoS2 multilayer structures.* Nano Energy, 2019. **56**: p. 512-515.